

**THERMAL AGING INVESTIGATIONS OF
MEDIUM-VOLTAGE EXTRUDED
POWER CABLES**

Xufei Ge

A thesis submitted for the degree of Doctor of Philosophy to the
Department of Electronic and Electrical Engineering

University of Strathclyde

Glasgow, United Kingdom

5th May 2024

DECLARATION OF AUTHENTICITY AND AUTHOR'S RIGHTS

This thesis is the result of the author's original research. It has been composed by the author and has not been previously submitted for examination which has led to the award of a degree.

The copyright of this thesis belongs to the author under the terms of the United Kingdom Copyright Acts as qualified by University of Strathclyde Regulation 3.50. Due acknowledgement must always be made of the use of any material contained in, or derived from, this thesis.

Signed: _____ Xufei Ge _____

Date: _____ 05/05/2024 _____

Abstract

Medium Voltage (MV) extruded power cables play a vital role in electric power transmission and distribution systems. Insulation of power cables is essential for cables' lifetime, effectiveness, and reliability within the power cable system. However, insulation materials degrade progressively due to thermal, electrical, mechanical, and environmental stresses experienced during cables operation. This ageing of power cables poses potential safety concerns for power system operators and leads to increased maintenance and replacement costs.

This research focuses on the thermal ageing of MV extruded power cables. In order to investigate electrical performance degradation of entire extruded power cables (comprising semi-conductor layers) under thermal ageing, there are four single-core extruded MV cables with cross-linked polyethylene (XLPE) insulation are subjected to accelerated thermal ageing in a chamber. Standard measurements of Insulation Resistance (IR), Polarization Index (PI), Dielectric Absorption Ratio (DAR) and Dielectric Loss ($\tan\delta$) are carried out on the specimens periodically through the thermal ageing process. It was found that IR and $\tan\delta$ measurements are susceptible to Relative Humidity (RH), while PI variations are weak relative to RH changes. In addition, the annealing effect, which existing in extruded cable with semi-conductor layer through thermal ageing processes, has a significant influence on IR and $\tan\delta$.

To better evaluate degradation of cable insulation caused by distributed thermal stresses, a methodology combining Finite Volume Method (FVM) and Artificial Neural Network (ANN) models are developed to determine spatial temperature profiles of the cable insulations in the experimental environment. The thermal modelling temperature distribution results from FVM provide temperature distribution on cross-section of cables and align well with the experimentally measurement results. A much more detailed and reliable temperature distribution profile of cable insulation estimated from ANN model, which is trained by FVM resulting data, holds significant benefits for estimating thermal degradation of extruded power cables.

IR degradation models for extruded power cables under thermal ageing are established by using of dichotomy and discretization models. Cable cylindrical insulation is first divided into sufficiently small segments, and then simulated by dichotomy models that randomly sample fully degraded segments based on an overall (or layer) ageing condition estimation and discretization models that estimated the gradual degradation of individual segments, respectively. Furthermore, uniform and non-uniform temperature profiles are incorporated into

dichotomy and discretization models, respectively, for a comparison. The IR simulation results are not only compared between different models, but also discussed around the sensitivity of IR simulation to segment size and degradation rates. Among the four developed IR degradation models, the discretization model with non-uniform temperature distribution is recommended, as it more comprehensively accounts for the effects of temperature distribution during the aging process and treats the IR of the material as a bulk property. However, the limitation of this model is its need for more accurate degradation rates as a function of aging temperature.

Finally, in accordance with IEEE Standard 1407, Finite Element Method (FEM) thermal modelling works of power cable accelerated ageing in a tank filled with water is proposed. Simulation investigates there are temperature gradients across cable length and temperature difference among cables in tank, which are influential for ageing rate of cables in experiment based on IEEE standard 1407. To achieve a uniform temperature distribution, a forced circulated system with different rotating speed and at different location in a tank are simulated and compared. Based on the simulation results, it is highly recommended that IEEE Standard 1407 include guidelines for using forced water circulation with a fan speed of 50 rpm to create a more uniform artificial aging environment for all cables in the tank.

List of Publications

Journal paper:

Ge. X., Fan. F., Given. M. J., Stewart. B. G. Insulation resistance degradation models of extruded power cables under thermal ageing. *Energies*, 17(5), 1062. **2024**. DOI: 10.3390/en17051062

Conference papers:

1. Ge. X., Fan. F., Given. M. J., Stewart. B. G. Insulation Resistance Measurements of Medium-Voltage Cross-linked Polyethylene Cables under Thermal Stresses. In *2024 IEEE Electrical Insulation Conference (EIC)* (pp. 34-37), IEEE. **2024, June**. DOI:10.1109/EIC58847.2024.10579459
2. Ge. X., Fan. F., Given. M. J., Stewart. B. G. XLPE cable insulation resistance modelling under annealing and thermal ageing effects. In *2023 IEEE Conference on Electrical Insulation and Dielectric Phenomena (CEIDP)* (pp. 1-4). IEEE. **2023, October**. DOI: 10.1109/CEIDP51414.2023.10410560.
3. Ge. X., Given. M., Stewart. B. G. A power cable thermal aging insulation resistance degradation model. In *2022 IEEE Conference on Electrical Insulation and Dielectric Phenomena (CEIDP)* (pp. 53-56). IEEE. **2022, October**. DOI: 10.1109/CEIDP55452.2022.9985388.
4. Ge. X., Given. M. Stewart. B. G. Determining accelerated aging power cable spatial temperature profiles using Artificial Neural Networks. In *2022 IEEE International Conference on High Voltage Engineering and Applications (ICHVE)* (pp. 1-4). IEEE. **2022, September**. DOI: 10.1109/ICHVE53725.2022.9961792.
5. Ge. X., Given. M., Stewart. B. G. FEA simulation studies of accelerated aging of power cables in water tanks. In *2020 IEEE Electrical Insulation Conference (EIC)* (pp. 465-468). IEEE. **2020, June**. DOI: 10.1109/EIC47619.2020.9158746.

Acknowledgements

I would like to express my heartfelt gratitude to my supervisor, Prof. Stewart, whose patience, dedication, and expertise guided me onto the path of research and provided me with invaluable direction throughout my PhD journey. Prof. Stewart provided crucial help in the whole process of my PhD, leveraging his connections to obtain the necessary cables for my experiments, offering valuable guidance based on his experience for my simulations, and ensuring comprehensive considerations for the constructed models. His meticulous guidance throughout the completion of my thesis, from topic selection and outlining to the culmination of the research work, reflects his immense dedication and effort.

Despite his busy schedule, Prof. Stewart consistently made time to provide me with meticulous guidance and support through on-line calls, emails, and other means, helping me overcome challenges and obstacles encountered during my research, thus enabling me to navigate my academic pursuits more efficiently. The outbreak of the pandemic during my PhD studies posed significant hurdles to the progress of my experiments. During this challenging period, his care and patient guidance provided me with the strength to overcome these obstacles successfully. He is not only a supervisor in my academic pursuits but also a respected elder figure in my life.

I would also like to extend my gratitude to my co-supervisor, Dr. Martin John Given, for his valuable insights and guidance provided throughout the research during my doctoral studies, and I am truly grateful for his dedication and mentorship. Furthermore, I would like to extend my heartfelt appreciation to Dr. Fulin Fan for his invaluable guidance and collaborative efforts in the writing and publication process of my papers. His expertise and support have significantly contributed to the quality and success of these publications.

Additionally, I am grateful to the workshop technicians and Maureen Cooper, as well as my families and friends, for their support and assistance.

Lastly, I want to express my deepest appreciation to my wife Yumeng Xu for her unwavering support throughout my PhD journey. Our relationship began as partners at the outset of my doctoral studies, and as my PhD journey draws to a close, we embark on the journey of marriage. Her support has been indispensable to me every step of the way.

Xufei Ge

Contents

DECLARATION OF AUTHENTICITY AND AUTHOR’S RIGHTS	II
Abstract.....	III
List of Publications	V
Acknowledgements.....	VI
Contents	i
Chapter 1. Introduction.....	1
1.1. Background.....	1
1.2. Research objectives	3
1.3. Main contributions.....	4
1.4. Organization of the thesis	6
Chapter 2. Background Information and Literature Review	8
2.1. Introduction.....	8
2.2. Background information	9
2.2.1. History of power cable development	9
2.2.2. The main characteristics of extruded power cables	12
2.2.3. Major insulation material for extruded power cables	15
2.3. Thermal ageing of extruded cable.....	18
2.3.1. Introduction.....	18
2.3.2. Previous research	21
2.3.3. Discussion.....	23
2.4. Condition monitoring techniques.....	24
2.4.1. Introduction.....	24
2.4.2. Insulation Resistance	25
2.4.3. Polarization Index and Dielectric Absorption Ratio	29
2.4.4. Dielectric Loss	34

2.4.5. Other techniques	36
2.5. Accelerated thermal ageing of extruded cables	38
2.5.1. Introduction.....	38
2.5.2. Previous research	39
2.5.3. Discussion.....	41
2.6. Thermal modelling of extruded cables	42
2.6.1. Introduction.....	42
2.6.2. Previous research	43
2.6.3. Discussion.....	44
2.7. Thermal degradation models of extruded cables	45
2.7.1. Introduction.....	45
2.7.2. Previous research	49
2.7.3. Discussion.....	50
2.8. Conclusion	51
Chapter 3. Accelerated thermal ageing experiment for MV XLPE cables	54
3.1. Introduction.....	54
3.2. Cable specimens	55
3.3. Experimental setup and equipment.....	57
3.4. Temperature monitoring setup and results	62
3.5. Condition monitoring results	68
3.5.1. Calculation of equivalent ageing hours.....	68
3.5.2. IR tests results.....	69
3.5.3. DAR tests results	73
3.5.4. PI tests results	76
3.5.5. Capacitance and $\tan\delta$ tests results.....	77
3.6. Discussion.....	79
3.6.1. Influence of environmental relative humidity.....	79

3.6.2. Fitting PI variation curves.....	81
3.6.3. Annealing effect.....	85
3.6.4. Correlations analysis.....	87
3.7. Conclusion.....	90
Chapter 4. Modelling of power cable spatial temperature profiles under accelerated thermal ageing.....	92
4.1. Introduction.....	92
4.2. FVM modelling	94
4.2.1. Model geometry.....	95
4.2.2. Model meshing	97
4.2.3. Material properties.....	100
4.2.4. Simulation setup	101
4.2.5. Modelling results	105
4.3. ANN modelling.....	118
4.3.1. Construction and Training of ANN.....	119
4.3.2. Performance of ANN	123
4.3.3. Application of ANN	124
4.4. Conclusion.....	125
Chapter 5. IR degradation models of power cable under thermal ageing.....	127
5.1. Introduction.....	127
5.2. IR degradation models.....	130
5.2.1. Dichotomy model with uniform temperature distribution	134
5.2.2. Dichotomy model with radial temperature gradients.....	136
5.2.3. Discretization model with uniform temperature distribution.....	138
5.2.4. Discretization model with non-uniform temperature distribution	138
5.3. Application of IR Degradation Models.....	139
5.3.1. Degradation model parameters estimation.....	139

5.3.2. Comparison of estimated results by IR degradation models.....	143
5.4. Sensitivity Analysis	150
5.4.1. Influence of segment size	150
5.4.2. Influence of degradation rate	152
5.5. Conclusion	154
Chapter 6. Modelling of extruded cables under accelerated thermal ageing in tank filled with water.....	157
6.1. Introduction.....	157
6.2. Modelling of cable loops in water tank without forced circulation system	159
6.2.1. Simulation setup	159
6.2.2. Simulation results	163
6.2.3. Discussion.....	164
6.3. Modelling of cable loops in water tank with forced circulation system	166
6.3.1. Simulation setup	166
6.3.2. Simulation results	169
6.3.3. Discussion.....	170
6.4. Conclusion	173
Chapter 7. Conclusions and future work	175
7.1. Conclusions.....	175
7.1.1. Chapter 3.....	175
7.1.2. Chapter 4.....	176
7.1.3. Chapter 5.....	177
7.1.4. Chapter 6.....	178
7.2. Future work.....	179
Reference	182
Appendix A (reference section 3.4)	190
Appendix B (reference section 3.5.1)	192

Appendix C (reference section 3.5.4)	194
Appendix D (reference section 4.2).....	196
Appendix E (reference section 4.3.2)	199

Chapter 1. Introduction

This research investigates the thermal ageing of Medium Voltage (MV) extruded power cables through a combination of laboratory testing and software modelling methodologies. This introductory chapter provides background information on the research topics, outlines the research objectives, highlights the main contributions of this study, and presents an overview of the thesis structure.

1.1. Background

Electric power is at the core of modern society and the economy. As advanced technologies continue to develop across various industries, they have significantly enhanced the convenience of people's lives, thereby increasing both the demand for electricity and the importance of its stable supply. According to the “Electricity Market Report 2024-2026” published by the International Energy Agency (IEA), the global electricity demand growth rate in 2023 is 2.2%, slightly lower than the 2.4% in 2022, but still exhibiting strong overall growth [1]. Despite facing numerous challenges, such as energy crises, climate change, and economic pressures, global electricity demand is expected to be driven by the expansion of emerging economies, the rise of new demand sources, and the advancement of energy transitions over the next few years. The average annual growth rate of global electricity demand is projected to accelerate to 3.4% in the coming three years. Additionally, renewable energy has gained significant attention across various regions of the world, and by early 2025, it is expected that the share of renewable energy in global electricity generation will surpass that of coal, reaching 37%.

The primary function of an electric power system is ensuring the reliable supply of electrical power to consumers, playing a crucial role in the overall well-being and stability of society. The uninterrupted operation of this system is imperative, as any disruptions or failures can have serious consequences. When a power system fails, it can easily lead to large-scale blackouts, causing significant economic losses and even threatening the safety of residents. In recent years, several major blackout incidents have occurred worldwide, with equipment failure being one of the primary causes [2]. Globally, the transmission and distribution of electric power are heavily depended on expansive networks comprising High Voltage (HV) and MV power cables. These cables serve as the lifelines of the power grid, facilitating the efficient and secure transfer of electricity across long distances. HV cables are used for transmitting electricity over distances of 50 to 500 km or more, while MV cables generally cover distances ranging from a few kilometers up to about 50 km [3]. According to statistics

from the State Grid Corporation of China, as of 2019, cable failures accounted for 19.3% of all power failures, with 51.7% of these failures attributed to the aging of the main insulation layer of cables [4]. The reliability and performance of these cables are crucial in maintaining a stable and resilient power infrastructure.

Power cable systems subjected to several stresses throughout their service life, encompassing electrical, thermal, mechanical, and environmental stresses. Thermal stress generated from cable working processes and extreme operational conditions, is considered as one of the primary factors for the reduction in cable lifetime and the degradation in cable performance [5]. The insulation system, a critical component tasked with safeguarding conductors against external threats and shielding adjacent layers from the voltage stress of the conductor[6], is particularly susceptible to degradation. The degradation of insulation, when coupled with suboptimal maintenance and installation practices, introduces the risk of developing cable defects and eventually leading to failures. Such consequence occurrences not only inconvenience customers but also translate into substantial financial losses for power system operators [7].

In order to understand ageing effects and mechanisms on extruded power cables caused by thermal stresses, electrical properties are used to monitor health condition variation of cables insulation. A MV extruded power cable typically comprising multiple components, which undergo interaction during the thermal ageing processes and eventually lead to cable failure. The execution of Insulation Resistance (IR) measurements on full-scaled extruded cables, inclusive of semi-conductor shield layers, during the thermal ageing processes is rarely illustrated in the existing literature. Past research has provided partial indications on parameters such as Dielectric Loss ($\tan\delta$), Dielectric Absorption Ratio (DAR) and Polarization Index (PI) concerning insulation materials. However, investigations of these electrical properties related to integral extruded power cables are quite rare.

As cable assets progress in degradation, it is essential to make appropriate strategic decisions concerning maintenance, repair, renovation, or potential replacement of cables. Relying exclusively on the designed cable lifetime for guiding decisions related to asset maintenance and replacement might prove unnecessary and economically burdensome [8]. The accelerated thermal ageing of cables serves as a crucial method for simulating the long-term effect of thermal stresses on power cables, providing insights into their performance and durability over time. A power cable system normally spans a long distance, and the service environments of power cables could significantly vary along their length. Furthermore, differences in power demand at different times of the day will result in a time variation in the

cable load. Aging mechanisms of non-uniform and time-varying thermal fields are not taken into account in previous research.

Due to the variation in the health condition and lifetime of power cables with their service conditions, there arises a critical demand for cable asset managers and maintenance engineers to develop more reliable and accurate diagnostic tools and predictive indicators. These tools aim to provide comprehensive insights into the health condition of power cable systems, with a particular emphasis on the insulation component [5]. While previous researchers focused on utilizing the hot spot temperature of cables for estimating insulation performance degradation and predicting remaining cable lifetime [9], precise temperature distribution holds importance in the enhancement of power cable utilization efficiency. There is a lack of investigations considering temperature distribution along length and across radius of a power cable, as well as temperature cycles during practical operating processes.

In addition, thermal degradation models are helpful for researchers and engineers to understand the changes of extruded power cable properties resulting from prolonged exposure to thermal stresses conditions. These models facilitate the quantification and predication of alterations in key cable characteristics over time. Despite various studies having explored aspects of cable insulation degradation and ageing, a gap exists in the literature regarding the absence of effective estimation models for IR degradation specifically to cable insulation cylindrical geometry.

1.2. Research objectives

Degradation of extruded power cables under thermal ageing conditions poses a significant challenge in the reliability and maintenance of electrical power systems. Understanding the mechanisms of cable degradation and developing effective diagnostic and prognosis techniques are crucial for ensuring the long-term reliable performance of power cables. The overall goal of this thesis is to advance the understanding of extruded power cable degradation under thermal ageing conditions and develop novel estimation models using IR techniques.

To investigate the influence of thermal stresses induced by elevated conductor temperatures on the electrical properties of extruded power cables, the first objective of this research is to design and implement an accelerated thermal ageing experiment that accounts for time dynamic temperature distributions varying with cable length and radius. The relationship between thermal ageing and electrical performance are sought to be elucidated through this experiment.

IR, PI, DAR and $\tan\delta$ tests have the advantages of being non-destructive in nature, simplicity and ease of implementation, and cost-effectiveness. The PI test, in particular, is excellent for detecting the gradual deterioration of insulation due to ageing or contamination. Because these tests have been used for decades, they allow for the easy accumulation of historical data, which can be used to track trends over time. This long-term data can be crucial for predictive maintenance strategies [10].

Thus, this research aims to carry out in IR, DAR, PI, and $\tan\delta$ measurements on complete extruded XLPE cables and examine the variation of these values throughout thermal ageing processes, understand the trends in as they evolve during the thermal ageing of extruded cross-linked polyethylene (XLPE) cables. Effective monitoring techniques for assessing the condition of XLPE cables and predicting their remaining service life are desired to be developed by gaining insights into these trends, thereby contributing to the reliability and longevity of power cable systems in diverse applications.

Furthermore, establishing spatial temperature distributions of cables under designed experimental conditions through advanced modelling methods is expected in this research. Developed models that can accurately simulate and predict temperature variations along the length and radius of cables subjected to specific operating conditions, aids in the optimization of cable thermal degradation models.

Finally, this research looks forward to developing novel estimation models for assessing insulation degradation in cables under thermal ageing conditions using IR techniques. Through developed models, a more precise and efficient monitoring and predicting of cable health could be achieved.

1.3. Main contributions

The research contributed a novel artificial thermal accelerated ageing methodology for MV extruded power cables. This methodology could effectively simulate the practical temperature variations experienced across the cable's length and radius, as well as the thermal cycling effects induced by daily time-varying loading cycles. Through the utilization of four XLPE insulated cable samples within a chamber equipped with thermal insulation, powered by a current transformer, the method successfully elevated cable temperatures to meet accelerated thermal ageing requirement. The thermal ageing in a day was divided into three phases, including a heating phase, a high-temperature phase, and a cooling-down phase. The assessment of temperature distributions on both cable surfaces and conductor surfaces, were facilitated by type T thermocouples.

Throughout the thermal ageing process, an evaluation of various electrical properties, including IR, DAR, PI, capacitance, and $\tan\delta$ of the cables, has been conducted and trended. Testing voltage levels ranging from 1kV to 10kV have been applied, exerting an influence on the measurement results of IR and $\tan\delta$. Along with the thermal ageing process, the IR values displayed a obvious pattern of fluctuations, characterized by alternating phases of decrease and increase. Similarly, corresponding variations are observed in the $\tan\delta$ values, prompting an in-depth analysis of the influences induced by Relative Humidity (RH) and annealing effect. Nevertheless, a relatively consistent downward trend was observed in the global variation of PI, exhibiting a correlation with the progression of thermal ageing degrees.

The integration of Finite Volume Method (FVM) and Artificial Neural Network (ANN) models presented a contribution towards estimating the spatial temperature profile of MV extruded power cables undergoing thermal accelerated ageing conditions. The FVM modelling accurately reproduced temperature distributions on cable surfaces and conductor surfaces, aligning closely with experimental measurements, thus demonstrating a high level of agreement. Furthermore, the FVM model enabled the assessment of the temperature distribution across cable cross-sections at different lengths. To address the limitations of FVM in providing detailed temperature profiles along the model meshing structure, a 3-layer ANN model was developed. This combination of FVM and ANN modelling approaches achieved a more precise evaluation of temperatures at specific locations within the cable under varying operating conditions, thereby enhancing the accuracy and comprehensiveness of thermal ageing models.

The development of IR degradation models for cylindrical insulation of extruded power cables under thermal ageing conditions constituted a significant contribution towards quantitatively assessing cable insulation degradation over time. Four distinct scenarios of IR degradation models were investigated, including dichotomy models with uniform and radial gradients temperature distributions, as well as discretization models with uniform and non-uniform temperature distributions. These models are applied and compared through using experimental data on IR degradation and the spatial temperature profile of cable insulation obtained from FVM and ANN models. The random selection of degraded segments in the dichotomy models leads to lower IR estimation results compared to the discretization model. Additionally, the discretization model with non-uniform temperature provides the highest IR estimates throughout the period of interest because it utilizes the full insulation temperature profile rather than just hotspot temperatures.

In addition, the study provided insights into the influence of segment sizes and

degradation rates on estimation results. Specifically, the comparison revealed that discretization models, which incorporate a more advanced calculation mode than dichotomy models by considering the ageing behaviours of each sub-segment, offer enhanced accuracy in predicting cable insulation degradation.

1.4. Organization of the thesis

This chapter provides a general background information about power cable systems and illustrates the objectives and main contributions of this PhD research. The thesis is structured as follows:

Chapter 2 presents literature review covering background information, thermal ageing mechanisms, condition monitoring techniques, accelerated thermal ageing methodologies, thermal modelling applications and thermal degradation models of extruded power cables.

Chapter 3 describes the thermal accelerated ageing experimental setup and results for power cable in a chamber with thermal insulation. The information on experimental samples, equipment, arrangements, temperature control and monitoring methodologies, and variations of condition monitoring tests results (IR, PI, DAR, $\tan\delta$, and capacitance) during the thermal accelerated ageing process are represented.

Chapter 4 presents the thermal modelling of temperature distribution for cables under the experimental conditions which described in Chapter 3. The variation of temperature distribution across cables' length and radius in a heating cycle, are investigated by FVM simulation. The temperature profiles obtained from the FVM simulation are validated by experimental measurements from Chapter 3. Additionally, a 3-layer ANN model was developed to estimate temperature between meshed points in FVM, a more detailed spatial temperature profiles of cable insulation thus could be assessed by the assistance of the ANN model.

IR degradation models for cylindrical insulation of extruded power cables under thermal ageing conditions are devised in Chapter 5, including four scenarios. There are two methodologies: Dichotomy models and Discretization models, are used to simulate the IR degradation of cable insulation. Furthermore, uniform and non-uniform insulation temperature profiles (or radial gradients) are introduced to models to investigate the influences of thermal ageing temperature on IR simulation. In addition, the sensitivity of IR degradation models to segment sizes and degradation rates are discussed to appropriate application of IR degradation models.

Chapter 6 illustrates the thermal simulations for accelerated ageing of MV power cables

in a tank filled with water according to IEEE standard 1407. This chapter initially comparing of water in the tank treated as solid or fluid by modelling to verify the effects of natural water convection on temperature distribution. Then, modelling works investigate the impacts of forced circulation in the tank on temperature distribution, models with different rotating speed and location of circulation fans are compared.

Finally, conclusion and recommendations for future works are discussed in Chapter 7, encompassing continuous implementing the accelerated thermal ageing experiment and monitoring electrical properties variation, further exploring the influence of environmental relative humidity on measurement of electrical indicators, recommendations on how to further develop the IR degradation models considering the annealing effects and partial discharges phenomena, and how to thorough application of FVM and ANN models.

Chapter 2. Background Information and Literature Review

2.1. Introduction

Due to the influence of thermal ageing, the long-term effectiveness and reliability of extruded power cables are hard to guarantee. The occurrence of extruded cables ageing caused by thermal stresses is marked by insulation degradation and some other related phenomenon. A comprehensive exploration of thermal aging is imperative for effectively diagnosing and prognosing the performance of extruded cables under various operational circumstances.

This chapter aims to explore the background associated with extruded power cables and review a various of literature cover crucial research about thermal ageing investigation of extruded power cables, as outlined here:

- Mechanisms and effects of thermal ageing: thermal ageing factors and chemical reactions that lead to degradations in materials at both localized and bulk levels, including both chemical and physical variations. These degradations may result in the formation of new chemical compounds, changes in material properties (such as colour, texture, or hardness), and potential alterations in the material's mechanical, thermal, or electrical performances.
- Condition monitoring techniques: highlighting approaches such as IR, PI, DAR, and $\tan\delta$ measurements. These techniques offer valuable insights into the health variation of extruded cables when they subjected to thermal ageing conditions.
- Accelerated thermal ageing methodologies: designing accelerated ageing tests to replicate real-world ageing processes. these methods enable researchers to simulate prolonged ageing effects within a shorter timeframe.
- Numerical methods for thermal modelling: by simulating cable temperature distributions under thermal stresses, these methods aid in investigating potential weakness location and developing effective maintenance strategies and lifetime estimation models.
- Thermal degradation models: Incorporating the effects of thermal ageing and thermal modelling methodologies. These degradation models contribute to predicting cable performance over long service durations.

Through a comprehensive review and synthesis of existing literature, this chapter aims to enhance the understanding of thermal ageing's impact on MV extruded cables. The research

gaps and developing new insights obtained from this chapter, are helpful to guide the research in this thesis towards better approaches for handling the impacts of thermal ageing of extruded cables and enhancing assessment and prediction methods for the health status and performances of extruded power cables.

2.2. Background information

2.2.1. History of power cable development

The development of power cables has history over a hundred years. Figure 1 demonstrates several important moments in power cables development history. The first underground power cable with jute pitch insulation called “Street Pipe” was invented by Edison and installed in 1881. The use of underground power cables became more important in electrical systems, making it easier to transmit and distribute power starting in the early 1890s [11].

The first 20kV power cable was installed in 1908 in the UK. In 1911, the first instances of HV cables incorporating impregnated paper insulation were initiated, operating at 60 kV in Germany and 50 kV in Barcelona, Spain. A 380kV Ultra-High Voltage (UHV) cable firstly laid in 1952 in Sweden initiated the start of UHV power cable applications. The first long-distance application of 500kV alternating current (AC) power cables insulated by XLPE was in 2001. The first flexible direct current (DC) transmission cable was put into use in China in 2014 [12].

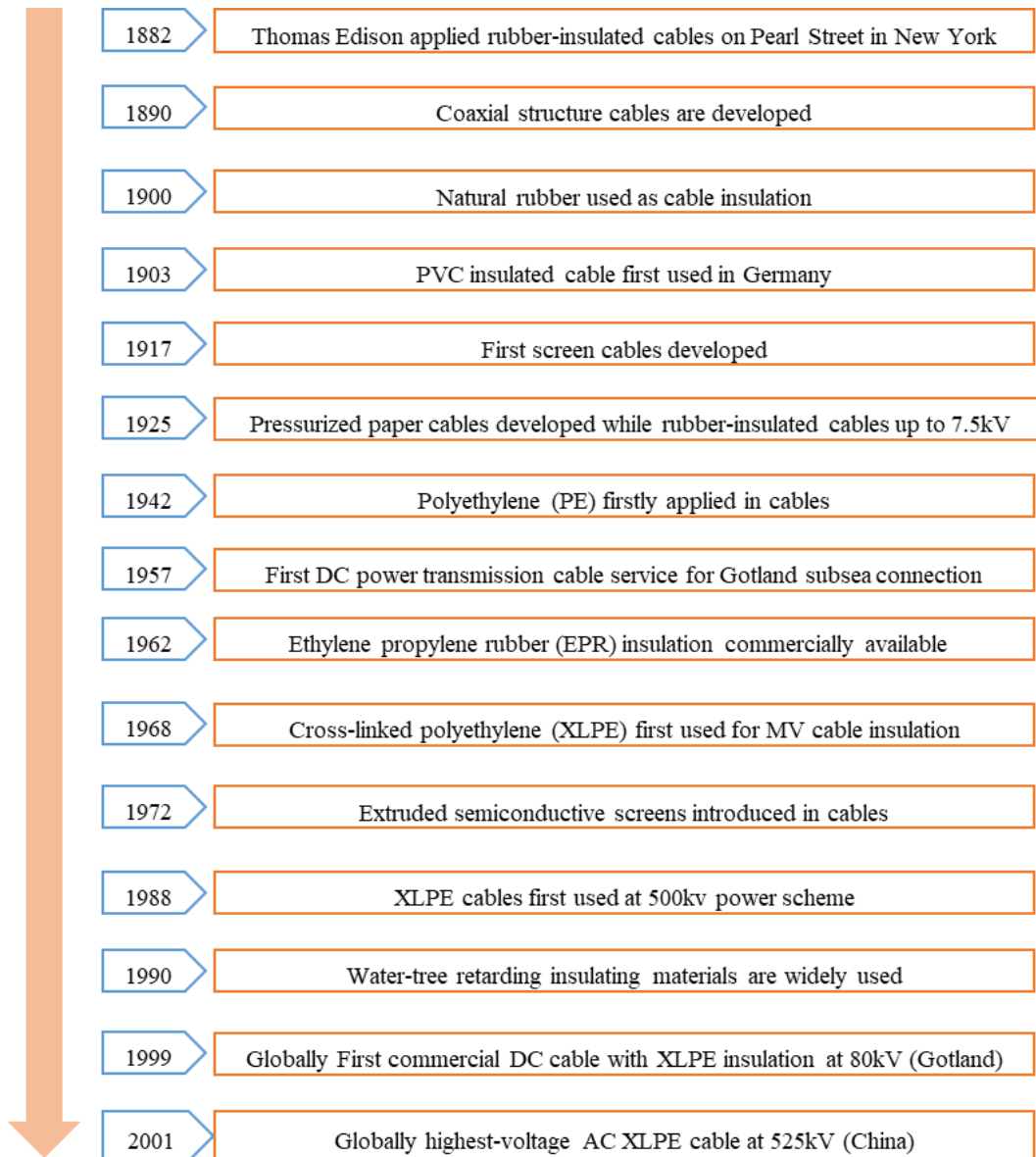


Figure 1. Significant milestones in power cable development history [12]

In 1890, Ferranti initiated the first successful program for using 10kV coaxial cables insulated by mass impregnated paper in the UK and laying it for the London Electric Supply Corporation [13]. Subsequently, a significant development emerged in long-distance power distribution systems with the rise of mass-impregnated paper-insulated power cables for more than 70 years [14]. These cables were characterized by paper insulation saturated with insulating oil to enhance the overall insulation properties of the cable. Insulating oil enhances cable insulation by increasing dielectric strength, improving heat dissipation and providing moisture protection, which prevents electrical breakdown and thermal ageing. It also fills voids within the insulation, suppressing partial discharges and maintain the overall integrity and longevity of the cable system [15].

Then, extruded power cables, which produced through the extrusion process of pushing plastic insulation material through a die to make a continuous shape, gradually replaced mass-impregnated paper-insulated cable systems. This phenomenon was mainly because of economic considerations and application benefits of extruded power cables.

Extruded power cables possess several advantages over mass-impregnated paper-insulated cables, including superior dielectric properties, higher voltage capabilities, reduced size and weight, easy installation, resilience to environmental factors, decreased maintenance, lower risk of partial discharge, improved environmental impact, and advancements in manufacturing processes and technology [12].

Introduced in Germany in 1903, polyvinyl chloride (PVC) insulated cables found application in cable manufacturing. Production started before and during World War II, with remarkable progress in the 1950s across Europe [12]. After World War II, the cable industry embraced various synthetic elastomers, including butyl rubber silicone rubbers, Ethylene Propylene Rubber (EPR) et.al. Despite higher manufacturing costs, cables using these materials became competitive due to potential savings in conductor cross-sectional area or increased permissible current-carrying capacity [14].

XLPE insulation material was firstly developed by the General Electric Company in 1963. It was processed through the irradiation of low-density polyethylene (LDPE) or via chemical processes involving organic peroxides. The resultant crosslinks establish intermolecular connections among carbon atoms, inducing a transition of the initially thermoplastic LDPE into an elastomeric state. This transformative characteristic gives these cables significant mechanical strength even at high temperatures, which greatly improves their operational capabilities. The use of XLPE cables has experienced a very fast development from 1960 in the United States, in Japan, and in the Scandinavian countries. Since then, other countries are increasingly using XLPE [13].

In contemporary times, the fundamental architecture of power cables remains akin to its early stage from a century ago; however, considerable development has been undertaken in the enhancement of dielectric materials. This pursuit aims to render cables economically more tenable while concurrently enabling their operation at significantly augmented voltage levels.

In developing countries, the cable network infrastructure is relatively new and continuously growing. Taking China as an example, it's clear that cables installed during the first ten years of the century make up a significant majority, accounting for more than fifty percent of the overall cable inventory [16]. In contrast, the majority portion of MV distribution cables and their fundamental associations within the United Kingdom's networks underwent

installation throughout the decades encompassing the 1950s and 1960s [17]. Considering their typical design lifespan of 40 to 70 years, these components are currently approaching or have already exceeded their expected operational duration. A more detailed approach is required, which highlights the importance of monitoring the condition and predicting the lifespan of power system cables.

2.2.2. The main characteristics of extruded power cables

The extruded technique provides a precise combining of insulation and semi-conductor screen layers for power cables. Metallic materials such as copper and aluminium are generally used for manufacturing cable conductors. Manufacturers choose between copper and aluminium for cable conductor(s) based on the specific needs of the application, balancing factors like electrical conductivity, weight, cost, mechanical strength and environmental conditions. Copper is often chosen for its superior conductivity and mechanical properties, while aluminium is preferred for its cost-effectiveness and lighter weight in large-scale and weight-sensitive applications. Cable conductors then are enveloped by insulation and semi-conductive screen layers through a simultaneously extruding process. This simultaneous extrusion process ensures uniformity in insulation quality and thickness, enhancing both the durability and electrical efficiency of the cable.

In order to meet specific requirements including voltage specifications, environmental conditions and regulatory standards, different models are designed for the extruded power cables. The conductor of extruded power cables could be designed to single-core or multi-core, and the insulation could be made from materials like XLPE, EPR. The use of the extrusion method allows for precise control over cable characteristics like conductor size, insulation thickness and overall quality.

The foundational architecture of an extruded power cable is typically characterized by a central conductor, manufactured from copper or aluminium strands, enveloped by a layer of polymeric electrical insulation, and subsequently encased within a protective plastic jacket. It is common for shielding layers to be introduced between these three main components. An example of a single-core underground cable configuration is shown in Figure 2.

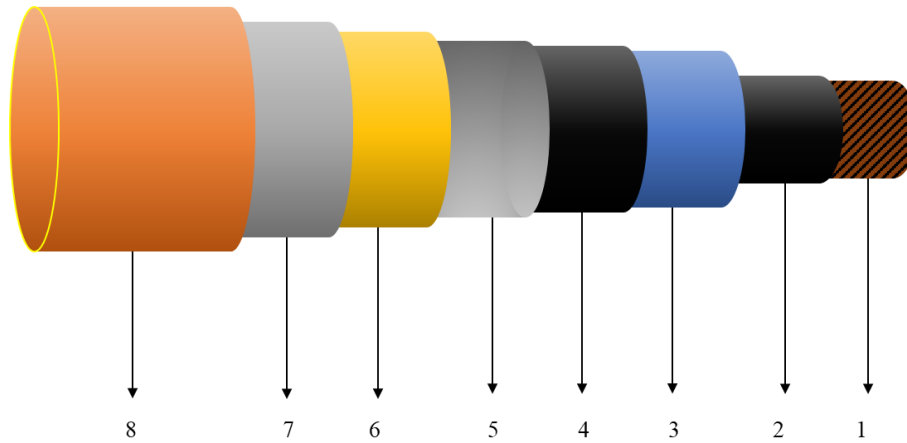


Figure 2. Schematic representation of a single core extruded power cable

1. **Conductor:** A power cable conductor is the core element that carries electric current within the cable. Typically made from highly conductive materials like copper or aluminium, the conductor's design, and material influence key cable attributes such as current capacity and efficiency. The conductor's properties directly affect the cable's overall electrical behaviour and function.

2. **Conductor screen:** This refers to a semi-conducting layer extruded a smooth surface on the conductor. Its primary role is to smooth out the electric field generated by the conductor. When an electric current passes through a conductor, it creates an electric field around it. Without a conductor screen, this field would be uneven and concentrated around sharp edges or surface imperfections, leading to localized electrical stress. This could result in partial discharges, insulation degradation, or even breakdown. The semi-conductive conductor screen helps distribute the electric field more evenly, smoothing out irregularities and ensuring a uniform field across the insulation layer. This uniform distribution reduces the risk of electrical stress concentrations that could cause insulation failure. Additionally, the conductor screen improves bonding between the conductor and the insulation, decreasing the likelihood of voids or gaps that could lead to partial discharge and subsequent insulation deterioration.

3. **Insulation:** Insulation in extruded power cables refers to the protective layer enveloping the conductor. This layer prevents current leakage and ensures secure electricity transmission. Insulation acts as a barrier against external factors, prevents shorts, and regulates electric field distribution, reducing stress-related issues. Effective insulation is crucial for the cable's longevity, efficiency, and safety within the power cable system.

4. **Insulation screen:** An insulation screen is a semi-conductor layer above the insulation. The layer made from semi-conductivity material. Its primary role is to control electric field within the insulation and to provide a smooth transition between the high-dielectric insulation

and the ground metallic sheath or armour. Similar to the conductor screen, the insulation screen ensures a uniform electric field within the insulation layer, aiding in the smooth transition of the electric field from the high-dielectric insulation to the cable's outer grounded layers. The insulation screen prevents abrupt termination of the electric field at the insulation boundary, thereby avoiding the buildup of electrical stress at the interface between the insulation and the outer sheath. This reduction in stress helps to extend the life of the insulation and improve the cable's overall reliability. Additionally, the insulation screen helps prevent partial discharges at the insulation boundary by maintaining a controlled electric field and ensuring there are no sudden changes in potential that could lead to dielectric breakdown.

5. **Metallic sheath:** A metallic sheath is an external layer of metal (like aluminium or lead) encasing the insulation and core of cable. It provides mechanical protection, shields against electromagnetic interference, and guards against environmental factors like corrosion and moisture. This enhances cable durability, safety, and performance.

6. **Bedding sheath:** This layer ensures a smooth surface for the Armor and aids in distributing mechanical stresses during installation and operation, enhancing cable integrity and longevity.

7. **Armouring:** It provides mechanical protection, enhancing the cable's resistance to physical damage, environmental stress, and external interference. Armouring is particularly beneficial in challenging conditions, providing strength and reliability to the cable.

8. **Outer sheath:** An outer sheath in extruded power cables serves as the protective layer, shielding the cable from environmental and mechanical challenges, preserving its integrity, and conveying important information about the cable's characteristics by colour.

Table 1 presents that extruded power cables are organized into different categories based on their rated voltage. This important parameter determines their appropriateness for specific voltage levels. This classification framework encompasses several discernible classes [18]:

Table 1. Power cable rating voltage classification[18]

	AC	DC
Low Voltage	$U < 6 \text{ kV}$	
Medium Voltage	$6 \text{ kV} \leq U \leq 35 \text{ kV}$	$U < 30 \text{ kV}$
High Voltage	$35 \text{ kV} \leq U \leq 330 \text{ kV}$ (Overhead line)	$30 \text{ kV} \leq U \leq 600 \text{ kV}$
	$35 \text{ kV} \leq U \leq 220 \text{ kV}$ (Cable)	
Extra High Voltage	$330 \text{ kV} \leq U \leq 1000 \text{ kV}$ (Overhead line)	
	$220 \text{ kV} \leq U \leq 500 \text{ kV}$ (Cable)	

This methodical categorization based on rated voltage ensures the careful choice and use

of extruded power cables that align with specific voltage requirements. By matching cable specifications with the specific voltage demands of various application, this classification system supports the achievement of both safety and operational effectiveness in electricity transmission and distribution networks.

Due to the intrinsic relationship between voltage classification and operational parameters, such as electrical stress and thermal resilience, it is important to understand voltage classification of power cables. This understanding is helpful for identifying vulnerabilities and weak points that leads to performance decline or failure and effectively determining health condition and predicting remaining lifetime of power cables.

2.2.3. Major insulation material for extruded power cables

The selection of appropriate insulation materials is a crucial factor that greatly influences the performance and reliability of extruded power cables. The insulation materials employed significantly influences the cable's electrical properties, thermal behaviours, resistance to environmental factors, and overall suitability for diverse voltage levels and application requirements.

Among the various of insulation materials available, three primary contenders take precedence: XLPE, EPR, and PVC. These materials, each possessing distinct attributes and advantages, play a key role in determining the ability of extruded power cables to perform well in different operational situations. An exploration of these insulation materials reveals their unique characteristics and contributions to the field of thermal ageing of extruded cables insulation.

XLPE is a general accepted insulation material for extruded power cables, known for its complex molecular structure and remarkable dielectric, thermal and mechanical properties. XLPE is a type of polyethylene that has undergone a cross-linking process to enhance its thermal, chemical and mechanical properties. Polyethylene is a polymer made up of long chains of the ethylene monomer (C_2H_4). In its linear form (low-density polyethylene), the polymer chains are flexible, but not interconnected. Polyethylene has good dielectric properties, low cost and ease of processing, but its thermal stability is limited [19]. The cross-linking process transforms the thermoplastic polyethylene into a thermoset material with a three-dimensional network of covalent bonds. The cross-linking process imparts enhanced thermal stability, mechanical strength, chemical resistance, and improved dielectric properties, making XLPE suitable for high-temperature and high-voltage applications. [20].

Due to the long-term thermal ageing characteristics of the XLPE insulation, the normal

operation temperature limit of XLPE-insulated cables is 90°C. Continuous exposure to temperatures above this limit can accelerate the chemical and physical degradation of insulation material, leading to embrittlement, loss of dielectric strength, and reduced mechanical properties. This degradation can shorten the cable's lifetime and compromise its reliability and will be discussed in detail in section 2.3.

In emergency situations like short-term extremely high loading, the cable can be exposed to higher temperature such as 140°C for short periods. At this temperature, the insulation experiences accelerated ageing, but the cable can generally withstand this without immediate failure. However, frequent or prolonged exposure to such temperatures can significantly reduce the cable's overall service life. Moreover, these cables possess a conductor short-circuit capability assessed at 250 °C.

The thermosetting nature of XLPE empowers it with a distinctive capacity to sustain its form even when subjected to high temperatures for extended periods, making it suitable for applications demanding endurance under thermal stress. Additionally, XLPE exhibits a low dielectric loss tangent and high IR, translating into efficient power transmission and limited energy dissipation across the insulation[21]. A partial set of properties for XLPE is presented in Table 2. It worth noting that the electrical resistivity and DC breakdown strength of XLPE decrease with increasing temperature, the DC Breakdown strength decreases to >200kV/mm at 70-90°C and increases to 340kV/mm at 30°C [22].

Table 2. Partial properties of XLPE [23]

Properties	XLPE
DC volume resistivity ($\Omega \cdot m$)	0.9×10^{15}
DC breakdown strength (kV/mm)	300
Operation temperature (°C)	70-90
Thermal nature	Thermoset
Mechanical property	Soft and flexible

XLPE's strong resistance to moisture, chemicals, and environmental elements protects the cable's electrical quality and lifespan, enabling it to deliver consistent performance in different situations [24][25]. Moreover, XLPE's mechanical properties, such as flexibility and tensile strength, contribute to the cable's strength during installation and operation, further enhancing its reliability.

Because of its outstanding electrical properties and thermal stability, XLPE insulation is suitable for a broad spectrum of voltage levels, including low, medium, and high-voltage applications. Its successful application extends to power distribution networks, underground installations, and power transmission systems. In these contexts, its ability to reduce partial

discharge, improve insulation integrity, and withstand challenging environmental conditions is of paramount significance.

While XLPE offers good thermal stability, it may have lower resistance to extreme temperatures compared to some other specialized insulation materials, limiting its suitability for extremely high-temperature applications. XLPE-insulated cables would be in larger size than some alternatives due to its thicker insulation layer to provide sufficient electrical insulation and maintain breakdown strength, especially under high voltage conditions. This increased size may impact their installation in tight spaces or require adjustments in cable pathways [26]. Furthermore, while the process of cross-linking improves the qualities and advantages of XLPE, the technical complexities and necessities tied to achieving ideal cross-linking can make the manufacturing process more intricate. This could lead to higher production expenses compared to simpler insulation methods.

In conclusion, XLPE material is widely recognized as an excellent option for insulation of extruded power cables. Its complex molecular structure, impressive electrical properties, thermal stability, resistance to environmental factors, and suitability for different voltage levels make XLPE an essential component in enhancing the effectiveness and dependability of contemporary power cable systems. In addition, there are some other insulation materials that are often used in extruded power cables, such as EPR and PVC.

EPR is a multifunction insulation material known for its exceptional elasticity, durability, and electrical properties. Its elastomeric nature allows it to withstand mechanical stresses, making it ideal for complex installations. EPR also offers outstanding temperature resistance, ensuring stable electrical performance in extreme conditions. Like XLPE, EPR has a maximum continuous operating temperature at 90°C. With superior dielectric properties, it enables efficient power transmission and reduced energy losses. While well-suited for medium and high-voltage applications, it may not be optimal for extremely high-voltage scenarios. Additionally, considerations regarding raw materials and recycling pose environmental challenges. In summary, EPR insulation is another good choice for extruded power cables, contributing to their efficiency, reliability, and durability [25]-[30].

PVC insulation is a cost-effective choice for extruded power cables. Processed from vinyl chloride monomers, PVC offers a balance between thermal resilience and flexibility, making it suitable for low and medium-voltage applications. Although PVC is not ideal for extreme temperatures, its dielectric properties and resistance to moisture and chemicals ensure efficient power transmission and durability. Flame-retardant PVC variants enhance safety. However, limitations include a restricted temperature range and potential for plasticizer migration. In

summary, PVC insulation, renowned for its adaptability and affordability, caters to a wide range of applications, especially in low and medium-voltage scenarios.

The adoption of right insulation materials is contingent upon multifarious criteria, encompassing voltage specifications, operational environment, and targeted performance benchmarks, thereby dictating their suitability to specific applications.

Understanding the properties of major insulation materials in extruded cables is essential for effective condition assessment and accurate life estimation research. These properties provide a baseline for normal functioning, aiding in identifying anomalies or deviations during assessment. They also support degradation analyses, model development, and data interpretation, ensuring informed decision-making. Predictive models and mitigation strategies rely on these properties for accurate projections and targeted maintenance. In sum, grasping insulation material properties enhances the precision of both condition assessment and life prediction efforts for extruded power cables.

2.3. Thermal ageing of extruded cable

2.3.1. Introduction

Ageing of extruded power cables refers to the gradual deterioration and alteration of the cable's physical, chemical, and electrical properties over time due to various stresses. This ageing process can result in a gradual reduction in the cable's performance, insulation integrity, mechanical strength, and overall reliability. Factors such as temperature variations, exposure to moisture, chemical interactions, mechanical stresses, and electrical loading contribute to the ageing process, potentially leading to decreased cable effectiveness and increased risk of operational failures or breakdowns [31][32]. Understanding and managing cable ageing is essential for ensuring the continued safe and reliable operation of power cable systems.

Ageing mechanisms involve a range of influential factors, including thermal, electrical, mechanical, and environmental stresses, which could impact individually or synergistically. These factors can cause variations in the component materials of cable insulation systems, thereby influencing material properties. These ageing stresses interface with contaminants, defects, protrusions, or voids (CDPVs) present within insulation materials or at interfaces between semiconductor screens and conductors or insulation, leading to degradation. These CDPVs may accidentally arise during phases such as material processing, cable and accessory manufacturing, transportation, installation, or during service[33].

The ageing mechanisms caused by thermal ageing stresses, along with the corresponding effects may lead to failures, are summarized and presented in Figure 3. Thermal stress is

considered one of the primary factors contributing to the ageing of extruded power cables in service. The principle source of thermal stresses arises from the resistive heating of the heavily loaded cable core conductor. The resistive heat generated in the core conductor propagates throughout the cable insulation and might increase the insulation temperature beyond its designed limit. Furthermore, excessively high ambient temperature conditions can also contribute to thermal ageing of the cable insulation. In addition to the cable temperature itself, the thermal degradation of extruded power cables is closely related to the polymer structure and the effectiveness of antioxidants [34]. Thermal degradation of polymer insulation materials can lead to embrittlement, cracking or crazing, discoloration, melting, and alterations in the mechanical and electrical properties that are crucial for the cable.

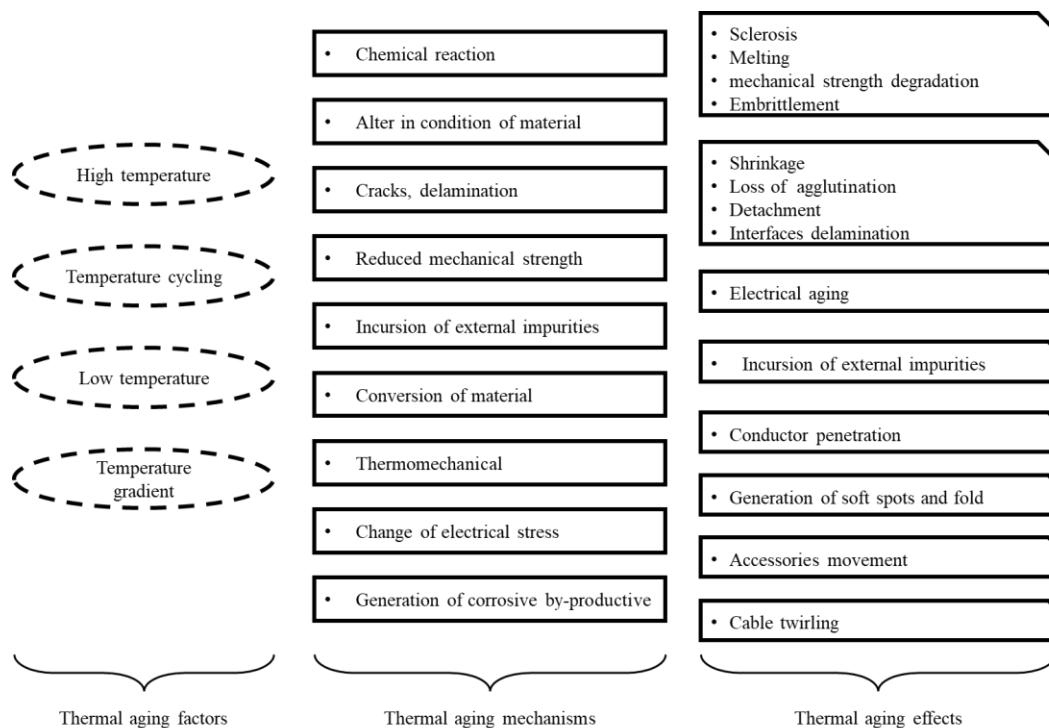


Figure 3. Ageing mechanisms and effects of cable insulation caused by thermal stresses [34].

When polymers absorb thermal energy, it triggers various chemical reactions within the material. One of the immediate effects is an increase in molecular excitation. Since organic materials are typically held together by covalent bonds (electron sharing), this increased excitation can easily damage these bonds. In solid polymers, the formation of free radicals can occur, leading to further chemical reactions. The most significant of these reactions, in terms of their impact on mechanical properties, are crosslinking and chain scission [35].

Crosslinking involves the covalent bonding of long polymer chains, which generally

leads to greater tensile strength and hardening of the material, though it often results in reduced flexibility and decreased elongation-at-break. On the other hand, chain scission breaks these long chains into smaller fragments, typically leading to reduced tensile strength. Depending on the type of polymer and the level of degradation, chain scission may cause elongation to increase, decrease, or remain relatively unchanged.

Additional processes that can occur in polymers include crystallization and chain depolymerization. Crystallization, often induced by high temperatures or rapid temperature changes, is generally not considered an aging phenomenon, though scission processes can sometimes enhance crystallinity. Chain depolymerization, a specific form of chain scission, involves molecules "unzipping" sequentially due to free radicals at the ends of the broken chains. This process can occur to varying degrees during normal aging, depending on the material type and the aging conditions.

When the XLPE material experiences thermal ageing, its physical and chemical reaction types can be mainly divided into two types: pyrolytic reaction and thermal oxidation reaction. Pyrolysis reaction refers to the process of breaking molecular bonds and random rearrangement or recombination of small molecule groups of XLPE molecules in the absence of oxygen under the action of heat, as illustrated in Figure 4 [36].

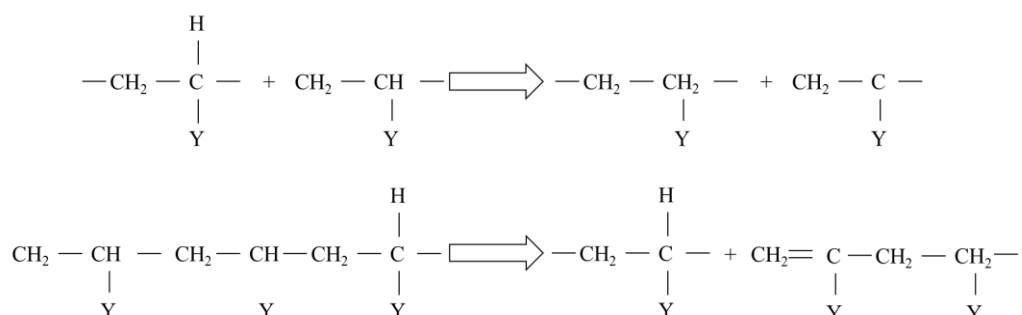


Figure 4. Molecular structure variation of XLPE under pyrolysis reaction

Thermal oxidation reaction refers to the combination of small broken molecules of XLPE and oxygen molecules into peroxide or oxygen-containing groups in the state of oxygen, and at the same time causes other chain reactions, resulting in the change of XLPE color, the increase of hardness and brittleness, and the significant changes in mechanical and electrical properties. The main forms of thermal oxidation reactions are as follows in Figure 5 [37].

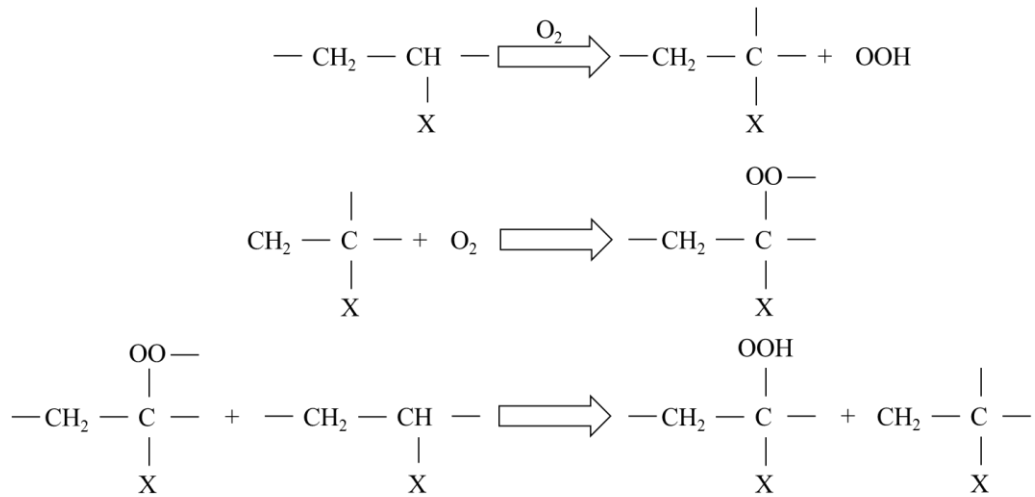


Figure 5. Molecular structure variation of XLPE under thermal oxidation reaction

It is generally believed that the thermal cracking reaction occurs first to produce a large number of small molecule groups, and at the same time, with the participation of high thermal energy and oxygen, the thermal oxidation reaction can occur [38].

The rate of thermal degradation generally follows the Arrhenius model, which states that the degradation rate increases exponentially with temperature. This means that even a small increase in operating temperature can significantly accelerate the ageing process of the insulation material, reducing the effective lifetime of cables [35]. Different degradation mechanisms have different activation energies, which is the energy required to initiate the degradation process. As temperature rises, mechanisms with lower activation energy become prominent, leading to rapid degradation. This is particularly relevant for cables operating in environments with fluctuating or consistently high temperatures. A much more detailed and comprehensive discussion of the Arrhenius model and activation energy will be introduced in section 2.7.

2.3.2. Previous research

Previous research has confirmed that the thermal degradation of the insulation made from polymer materials encompasses multifarious influencing factors, including morphological characteristics and their correlated transition temperature [39], effects of oxidation under conditions of restricted diffusion, manifesting at elevated temperatures [40][41], as well as the solubility and volatility traits of stabilizing agents [42][43], along with certain additional instances of kinetic heterogeneity, which refers to the variation in the oxidation rate and mechanisms within different regions or centers of a material, rather than a uniform, homogeneous reaction throughout the entire sample [44].

According to the investigation works by Bowler and Liu, physical state of a polymer is

inherently related to temperature considerations [46]. As temperatures rise and approach the crystalline melting point, crystalline structures gradually diminish, leading to variations in the polymer's degree of crystallinity. Furthermore, both XLPE and the majority of EPR exhibit characteristics of semi-crystalline polymers, involving both amorphous and crystalline domains. Within these amorphous regions, free radicals are likely to get involved in chemical reactions, including oxidation, which catalyses polymer deterioration. At lower temperatures, free radicals within the crystalline regions remain constrained. However, with increasing temperature, crystallites melt, releasing free radicals and enabling their participation in various chemical reactions.

The energy required to activate thermo-oxidative degradation shows variation within the temperature range spanning from 100 to 120 °C for both XLPE and EPR materials [47]. This phenomenon can be attributed, as previously stated, to changes in the crystalline structure and dimensions of crystallites within this temperature range. These changes prompt the release of unbound molecular components when the temperature closely approaches the polymer's melting point. Furthermore, the quantity of antioxidants diminishes as the materials undergo accelerated ageing, owing to vaporization in instances of thermal ageing [48]. Antioxidants encompass a variety of organic compounds that can be categorized into groups such as phenol, amine, sulfur, and phosphine [49]. In the formulation of cable polymers, the inclusion of antioxidants typically ranges from 0.5 to 1.0 parts per hundred resin (phr) for crystalline polymers and 1.0 to 2.0 phr for rubbery polymers [50].

One way that antioxidants slow down the breakdown process has been suggested, by Conley and Osawa in their respective studies [51][52], to be by joining in with peroxy radicals and hydro-peroxide. In this situation, the role of the antioxidant is to stop free radicals or break down hydro-peroxides in the damaged polymer chains. However, more recently, other researchers looked at groups of XLPE samples with different amounts of a certain antioxidant [53]. They found that the antioxidant worked well to protect against heat-caused breakdown. This is different from the earlier idea that the antioxidant stops free radicals like peroxy radicals in polymer chains. Instead, the effect of the antioxidant seems to be about slowing down the start of radical formation in polymer chains when the temperature goes up.

The study conducted by Kurihara, T. et.al involved subjecting XLPE sheets to thermal degradation at 180°C for a maximum of 100 hours in atmospheric air [54]. The resulting oxidation levels were measured using micro-Fourier Transform Infrared (FTIR) spectroscopy, revealing a non-uniform distribution of oxidation degree across the sheet's depth. This oxidation was most pronounced on the upper surface due to ample air exposure during heating,

while the lower surface in contact with a metal plate exhibited the lowest oxidation. An abrupt decline in the mechanical properties takes place when the content of antioxidant decreases below a critical value.

2.3.3. Discussion

Previous scholarly investigations illustrate the complexity of thermal degradation for polymer insulation materials in power cables. Temperature, crystalline structure, antioxidants and stabilizing agents play critical roles in maintaining the integrity and performance of cable insulation materials. Prolonged exposure to high temperatures can cause chain scission, leading to the loss of mechanical integrity. Over time, exposure to oxygen (particularly at elevated temperatures) can lead to oxidation of polyethylene chains, resulting in the formation of carbonyl groups (like ketones, aldehydes and acids). This process is accelerated by higher temperatures.

In earlier studies on the performance changes of insulation materials due to thermal aging, tests conducted at temperatures above the material's melting point were selected [54]-[56]. While some trends might be observed within the experimental temperature range, these studies fall short of accurately explaining the material's degradation mechanism at typical operating temperatures [57]. The ageing mechanism occurring at temperatures exceeding the melting point of insulation materials exhibits a marked divergence from the ageing process at temperatures below their melting point. Consequently, when investigating the lifetime of semi-crystalline cable insulation materials through accelerated ageing experiments conducted at elevated temperatures, it is advisable to choose ageing temperatures below the melting point of materials, to make sure the accuracy of reliable lifetime predictions [58]. This consideration is essential in the context of this research, particularly in the design of accelerated thermal ageing experiments for extruded cables.

Several studies have focused on the thermal aging of cable insulation under controlled, uniform temperature conditions. These studies often conclude that the aging rate increases exponentially with temperature, as predicted by the Arrhenius model. However, fewer studies have addressed the impact of temperature gradients within the insulation material itself. For example, researchers like Mazzanti [59] and Zhang et al. [60] have highlighted the need for more detailed studies on the spatial variations in temperature within power cables, particularly under operational conditions that deviate from the idealized, uniform temperature assumptions. The degradation behaviours of whole scale extruded power cables' electrical performances under non-uniform temperature distribution conditions constitutes another significant research gap, as understanding these distributed thermal effects is essential for accurately assessing the

degradation patterns and ultimately, for formulating effective strategies for the maintenance and replacement of cable systems.

Furthermore, the existing body of research often lacks comprehensive investigations into how interfaces, which exist between multiple different layers (insulation-shielding, conductor-shielding, etc.), contribute to thermal degradation on performance of insulation material, and whether they act as initiation points for degradation, is an area that requires further investigation.

2.4. Condition monitoring techniques

2.4.1. Introduction

Condition monitoring techniques for extruded cables includes a range of methodologies and procedures utilized for the sustainably or periodically evaluation of the effectiveness, health and functioning condition of cables. These approaches cover the collection, analysis, and interpretation of parameters and information to spot difference from the standard or projected performance. The fundamental objective of condition monitoring involves the early detection of signs indicating degradation, defects, or abnormalities, thereby enabling prompt maintenance or treatment measures to prevent breakdowns, ensure safety, and enhance operational productivity. An ideal condition monitoring technique would possess the following attributes[10]:

1. It should be non-destructive and non-intrusive, meaning that disturbance or disconnection of the cable is not required.
2. It should be capable of measuring a property change that can be monitored with time for trend analysis and reliably correlated with functional performance during normal service.
3. It must be applicable to the cable types and materials commonly used in existing power systems.
4. It should provide reproducible results that are uninfluenced by, or adjustable for, the test environment (e.g., temperature, humidity, et al.).
5. It should be cost-effective and easy to implement under service conditions.
6. It should be able to locate any defects in the cable.
7. It should allow for the establishment of a well-defined end condition.
8. It should provide enough time before initial failure for proper actions to be taken.
9. It should be readily available to industry.

Condition monitoring involves the continuous or periodic assessment of various

parameters within the cable system. By systematically tracking these parameters over time, even small deviations from expected values can be detected. The monitoring and recording of data over a long duration allow for trend analysis. This entails consideration how specific parameters change over time. By recognizing patterns or trends in the data, engineers can glean insights into the gradual degradation of the cable system. This information proves valuable in predicting the system's remaining useful life and strategically planning maintenance or replacement protocols. The data amassed through condition monitoring also serves the purpose of validating ageing models and predictions.

A literature review of condition monitoring techniques to be employed in this research is provided in this section.

2.4.2. Insulation Resistance

2.4.2.1 Introduction

The IR test is a fundamental and non-invasive methodology generally employed within the industrial domain to evaluate the prevailing state of cable insulation integrity. This method offers the capacity to identify the presence of contamination attributed to factors such as moisture infiltration, carbonization, or particulate matter, many of which are linked to thermal aging. Moisture can enter the insulation due to environmental exposure or damage, with thermal aging further compromising the insulation's integrity. Carbonization occurs when organic materials break down at high temperatures, a process accelerated by thermal aging. Although particulate matter contamination is generally caused by external factors, thermal aging can increase the insulation's vulnerability to such infiltration by making it brittle or cracked. The IR measurement is one of typical techniques within the spectrum of cable condition monitoring techniques, demonstrating a significant ability to directly reveal the current state of cables. The manifestation of good condition insulation is inherently associated with a heightened resistance to current flow[61].

The determination of cable IR through the application of a DC voltage between the cable conductor and the ground reference. A small current, potentially as low as 10^{-12} A depending on the quality of insulation, will traverse the insulation from conductor towards the ground, this assessment procedure seeks to quantify the insulation integrity. The applied voltage and duration vary depending on cable's rating: LV cables typically use 500V-1kV DC, MV cables use 1-5 kV DC or more, and HV cables use 5-10kV DC or more. Measurements are usually taken after 1 minute and monitored over longer periods. While this is a common application method, there is no specific standard for power cables. Expected IR levels are at least several G Ω per kV of the cable's rating, with higher resistance level expected for higher voltage cables.

Regular implementation of IR tests on cables should be accompanied by systematic recording for the purpose of comparison. A persistent downward trend in IR values, even if these values remain above the set limitations, signifies potential deterioration in cable insulation due to several physical mechanisms. Moisture ingress can occur through micro-cracks or poor sealing, water molecules leading to increased conductivity within the insulation [24]. Thermal aging degrades the insulation material, causing micro-cracks and carbonization. Continuous electrical stress may induce defects like voids or treeing, while chemical degradation from exposure to harsh substances weakens the insulation. Additionally, mechanical damage can create conductive paths through the insulation. These factors collectively contribute to the gradual decline in IR values over time.

According to the IEEE standard 43, the attainment of accurate measurements necessitates the adjustment of readings to a reference temperature due to the marked sensitivity of IR measurement outcomes to temperature variations [62]. The inverse correlation between temperature elevation and IR values is evident, with a reduction in IR values as temperature rises. A mere 10°C temperature rise can yield a 5 to 10-fold reduction in IR, and this generally applies more significantly at higher temperatures, though it can be relevant across a range of temperatures depending on the materials. Temperature increases typically accelerate molecular activity and can lead to higher leakage currents in insulation materials. At higher temperatures, the reduction in insulation resistance is often more pronounced due to the material's decreased ability to prevent the flow of electrical current. However, the exact relationship between temperature and insulation resistance can vary based on the type of insulating material, the environment, and other factors [56]. It is pertinent to underscore that the conventional temperature correction method may lead to an overestimation of cable IR [63].

Furthermore, it is worth mentioning that dry air is an excellent insulator. Clean and dry cable insulation thus might be reported with acceptable IR values even if the insulation is severely degraded and damaged. Consequently, a comprehensive evaluation of cable condition necessitates the supplementation of IR results with complementary condition monitoring techniques [62].

2.4.2.2 Previous research

Most research related to power cable ageing has placed an emphasis on the increase of conductivity or the decrease of resistivity throughout the ageing processes [64]-[67]. Mecheri et al. delved into the impacts of prolonged thermal ageing on dielectric and mechanical properties of XLPE insulation of HV cables [65]. To ascertain the degree of material deterioration resulting from thermal ageing and prevent potential failures, an extensive

examination was conducted by encompassing volumetric resistivity assessments and additional condition monitoring evaluations over a duration of 5000 hours based on both dumb-bell and circular-shaped probes composed of XLPE. The findings revealed a significant reduction in resistivity, amounting to several hundredfold, caused by the concurrent decrease in polymer viscosity which is believed to increase the mobility of charge carriers within XLPE [66]. Nedjar [67] examined the influences of thermal ageing on the electrical characteristics of XLPE employed in HV cables, demonstrating that the thermal ageing induced modifications in the electrical properties of polymer. In particular, elevating the thermal ageing temperature leads to a faster reduction in resistivity, aligning with the principle outlined by the Arrhenius law. With the thermal ageing process going further, molecular bonds exhibited weakening, resulting in an augmentation of free volume. This phenomenon subsequently heightened the mobility of charge carriers, accompanied by a decline of volumetric resistivity.

Mecheri et al. performed a comprehensive investigation into the impacts of thermal ageing conditions on the performance of XLPE for 18/30 kV cables[24]. XLPE specimens of the same material were subjected to thermal stresses under a controlled environment facilitated by a forced air-circulating oven. The assessments on XLPE thermal degradation were carried out through the volumetric resistivity testing under a DC voltage of 500 V at 85 °C. After 1350 hours of thermal ageing at 90 °C, XLPE resistivity was observed to significantly decrease from around $7 \times 10^{14} \Omega \cdot \text{cm}$ to $2.5 \times 10^{12} \Omega \cdot \text{cm}$. Discernible resistivity reductions were further pronounced at higher ageing temperatures of 135 °C and 150 °C, where the volumetric resistivity values declined to $4.6 \times 10^{11} \Omega \cdot \text{cm}$ and $2 \times 10^{11} \Omega \cdot \text{cm}$, respectively, after 1350 h thermal ageing.

Zhang et al. investigated the impacts of thermal ageing temperatures and durations on the DC electrical conductivity of XLPE insulation materials for HVDC cables by using Fourier transform infrared (FTIR) spectra [55]. The experimental findings and subsequent analysis revealed a sequential pattern in the DC electrical conductivity of thermally aged XLPE insulation, which initially declined below the level observed on unaged XLPE insulation and then exhibited a gradual increase over the entire ageing period due to the combined effects of thermal decomposition, post-crosslinking and the diffusion of low molecular weight substances. In addition, it was observed that higher thermal ageing temperatures induced more pronounced changes in the electrical conductivity of XLPE insulation. When XLPE is subjected to ageing duration of 700 hours at temperatures of 130, 140 and 150°C, the variation of the DC electrical conductivity with ageing temperature complied well with the Arrhenius equation.

Kang and Kim implemented a comprehensive assessment on IR properties of low voltage cables, subjecting them to external flame exposure, over-current conditions and accelerated degradation trials [56]. The results revealed a significant reduction in cable IR from a peak of 7.5 TΩ to 0.008 TΩ during direct flame contact. However, it demonstrated a complete recovery to its initial state following the cooling period. In accelerated degradation experiments conducted at an aging temperature of 130°C for 22 to 89 hours, which simulates 10 to 30 years of cable aging under normal operational temperatures, no significant decline in insulation resistance (IR) was observed at room temperature. Nevertheless, upon reaching an induced ageing equivalent to 40 years, a rapid IR reduction was observed at room temperature. The discussion of accelerated ageing experiment methodologies will be presented in section 2.5.

2.4.2.3 Discussion

In theory, the insulation resistance characteristics of materials can indicate the degradation caused by thermal aging. However, insulation resistance testing faces challenges during measurement, which means the data collected is not effectively used to assess the material's thermal aging condition.

The study by Ghorbani et al. found that the chemical composition and electrical properties of the samples were affected by production variables such as temperature, pressure, time, and the protective film used during preparation [68]. As a result, it is crucial to assess these factors when selecting and maintaining a consistent sample preparation method throughout experimental studies. Additionally, since heat treatment impacts the conductivity of polymer insulation materials, the thermal history of the samples must be carefully controlled [69]. Therefore, it is recommended to prepare new samples for each measurement rather than reusing them, as variations in thermal history could render result comparisons irrelevant.

While there has been significant development in understanding how the volume resistivity of insulation materials variation during extruded cables thermal ageing processes and its mechanisms, there remains absences of scholarly exploration into the dynamic changes in the IR of integral cables throughout thermal ageing processes. Investigating how IR of power cables including semi-conductor layers under the influence of thermal ageing is a critical research gap. This study aims to elucidate IR variations under thermal ageing conditions, as it could provide valuable insights into the long-term performance and health assessment of cables.

In addition, A significant challenge of comprehending the dielectric insulation condition lies in developing a quantitative approach to assessing insulation degradation over time. Research about developing IR degradation models under thermal ageing of power cables thus

become necessary.

2.4.3. Polarization Index and Dielectric Absorption Ratio

2.4.3.1 Introduction

The Polarization Index (PI) test is a way to assess the integrity and health for the insulation of power cables and equipment. The PI test is particularly important for evaluating the potential for insulation breakdown, which can lead to electrical faults or failures. The PI test is derived from IR test, involving measuring IR at two different time intervals (usually 10 min). The formula for calculating the Polarization Index is:

$$PI = \frac{IR_{10}}{IR_1} \quad (1)$$

where:

- IR_1 is the IR value measured after 1 minutes.
- IR_{10} is the IR value measured after 10 minutes.

The theory behind this test is that the registered current within the IR test encompasses a composite of distinct current components, which include:

- Capacitive charging current (I_C)
- Conduction current (I_G)
- Leakage current (I_L)
- Polarization current (Dielectric absorption current) (I_A)

the variations of these current components with respect to the DC test voltage and over time are graphically depicted in Figure 6. For instances involving dry or intact insulation conditions, the I_C is often negligible, and the I_L tends to be minimal. Consequently, the I_A and I_G predominately contribute to the total current measured. These currents commence with a relatively high magnitude upon the application of DC voltage to the test cable conductor. Notably, the I_A and I_G of the tested cable insulation exhibit distinct decay rates contingent upon the degree of insulation degradation. The conduction current arises from the movement of electrons between the conducting material and the insulating material, creating a galvanic current through the ground wall. This current can occur if the ground wall has absorbed moisture, a condition that can develop in older thermoplastic insulation systems.

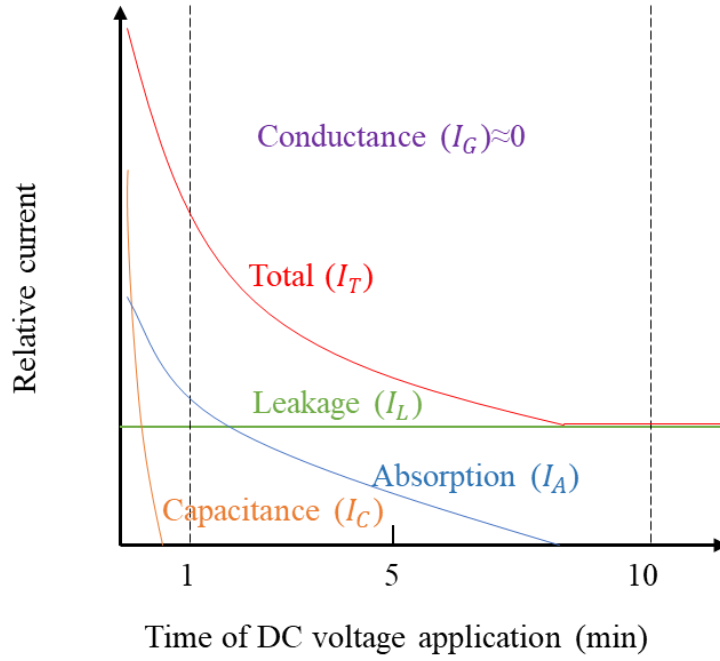


Figure 6. Magnitude of current component flowing through insulation vary with time after voltage applied (in scenario of low conduction current) [62]

The polarization current component emerges from three underlying factors:

- 1) A general migration of free electrons throughout the insulation material, driven by the exerted electric field.
- 2) Molecular distortion, whereby the application of an electric field induces the deformation of electron shells encircling the nucleus towards the voltage source.
- 3) Alignment of polarized molecules within the applied electric field. Initially randomized in a neutral state, these polarized molecules exhibit an alignment response proportional to the intensity of the electric field.

In typical scenarios, capacitive currents generally attenuate to zero within a span of 1 minute, with the current measured at this interval denoted as I_{1min} and described by Equation (2). Correspondingly, the I_A diminishes to zero within a period of 10 minutes, thus culminating in the composite current observable at the 10-minute mark, designated as I_{10min} , as elucidated in Equation (3).

$$I_{1min} = I_G + I_L + I_A \quad (2)$$

$$I_{10min} = I_G + I_L \quad (3)$$

The I_L will maintain at a steady value which is related to insulation condition. Insulation that is degraded, contaminated, or penetrated by moisture, will have a greater I_L . Consequently, the total current flowing through the insulation will start from a high value when a test voltage

is firstly applied and decrease in different rates in the following several minutes based on the insulation state.

A common set of criteria for cable PI is presented by Table 3. If PI is about 1, I_L and I_G are large enough that electrical tracking will likely occur. A PI less than 1 suggests either that the insulation is not effectively absorbing and storing charge over time, or is indicative of the presence of moisture, dirt, or other contaminants within the insulation, which is a sign that the insulation has deteriorated to the point where it no longer provides adequate electrical insulation. If the I_L and I_G are low compared to I_A , then typically the PI value is greater than 2.

Table 3. Criteria of PI for cable insulation health condition [62]

Polarization Index	Insulation condition
<1	Poor
1-2	Questionable
2-4	Acceptable
>4	Excellent

The specific acceptable range for PI values can vary depending on the type of insulation, the equipment being tested, and the industry standards. It is important to consult relevant standards and guidelines when interpreting PI test results.

PI as a variation of the IR test, is a more consistent and repeatable indicator for cable insulation condition because it reveal time-dependent current components performance as previous described. It is often assumed that both IR10 and IR1 are measured at the same cable insulation temperature, so PI measurement is less sensitive to temperature. The PI test is a valuable tool for preventive maintenance, allowing technicians and engineers to identify potential insulation problems before they lead to operational issues or failures in electrical systems [10].

A Dielectric Absorption Ratio (DAR) test is similar to a PI test in that measurements of resistance over time are presented by a ratio of resistance at time t_1 over resistance at time t_2 . The DAR and PI are both used to assess the condition of electrical insulation, but they differ in test duration and focus. DAR, the ratio of insulation resistance at 60 seconds to that at 30 seconds, provides a quick snapshot of insulation quality, making it useful for initial assessments, especially in newer equipment. PI is more reliable for assessing long-term aging and the ability of the insulation to withstand electrical stress, whereas DAR is better suited for quick diagnostics. The Dielectric Absorption Ratio is calculated as:

$$DAR = \frac{IR_{60}}{IR_{30}} \quad (4)$$

where:

- IR_{60} is the IR value measured after 1 minutes.
- IR_{30} is the IR value measured after 30 seconds.

The criterias of power cable DAR are presented by Table 4.

Table 4. Criteria of DAR for cable insulation health condition [62]

DAR value	Insulation condition
<1	Insufficient
<1-1.4	Acceptable
>1.4-1.6	Excellent

The DAR test, along with other insulation testing methods like IR and PI tests, contributes to the comprehensive assessment of cable insulation health and helps identify potential issues before they lead to operational problems or failures [70].

2.4.3.2 Previous research

The existing body of research has predominantly focused on PI and DAR as key indicators for assessing the health status of electrical machinery and Paper-Insulated Lead-Clad (PILC) cables because these materials have been widely used in the industry for many decades, and their aging mechanisms are well-understood, while XLPE insulation is a relatively newer material with different chemical and physical properties.

Research work by Huzainie et al. delved into the computation of severity indices derived from PD and PI testing outcomes [71]. The PD severity calculation takes into account discharge voltages, density, and magnitudes. Specific severity levels are assigned and categorized based on these ranges. The two severity indices are then combined into a single condition assessment index by applying weighting factors, which aids in the decision-making process for cable maintenance. Three-core PILC cable samples, rated at 22kV, with service time ranging from 7 to 15 years were studied. It was found that PI testing is instrumental in evaluating cable insulation condition. The cable's overall state concerning leakage current from DC testing could be comprehensively evaluated. Low PI values were suspected to result from moisture or carbonization effects, forming substantial leakage paths. The integration of severity indices aided in establishing a unified condition assessment index, facilitating informed decision-making in cable maintenance. The synergy between PI and PD mapping were considered as a potent diagnostic tool, providing a comprehensive understanding of insulation quality and pinpointing localized defects in PILC cables.

In their investigation of the efficacy of PI and DAR on evaluating the insulation health condition of Electrical Submersible Pump (ESP) Cables, Juan David et al. conducted a

thorough analysis based on data collected from 50 different wells within the Colombian Llanos basin [72]. The study aimed to ascertain whether the application of PI and DAR indexes could offer more detailed insights into insulation quality compared to conventional IR measurement. The research revealed that low IR values did not consistently indicate poor insulation properties, challenging conventional assumptions, as these values can be influenced by various factors. Temperature changes can temporarily lower resistance, and transient conditions such as moisture exposure may lead to reduced readings that improve once the issue is addressed. Additionally, the test voltage applied can affect resistance measurements. However, findings underscored the importance of incorporating PI and DAR metrics to enhance the assessment of insulation quality, particularly when IR measurements might be insufficient. The analysis further demonstrated that monitoring PI and DAR values provided valuable information for distinguishing between mechanical damage and issues related to moisture and dirt along the motor-cable circuit. The study emphasized that the correlation of leakage current, IR, DAR, PI, and downhole gauge measurements enabled the identification of mechanical stress, motor damage, or circuit cleanliness problems, providing a comprehensive understanding of the insulation system's status during electrical testing.

In the research carried out by Jagriti et al., a novel approach based on Detrended Fluctuation Analysis (DFA) was introduced for estimating insulation condition-sensitive parameters within the context of the oil-paper insulation system [73]. The study revealed that one of the DFA coefficients establishes clear and consistent relationships with key insulation condition-sensitive parameters, including dissipation factor, paper moisture content, PI, and DAR. The identified correlations between DFA coefficients and established insulation parameters contributed to the advancement of techniques for accurately assessing and monitoring the health of oil-paper insulation systems, showcasing the potential of DFA as a valuable tool in insulation condition estimation.

2.4.3.3 Discussion

Despite the significant advancements in the theory of the PI and DAR, there is a gap in the literature regarding the fluctuations in PI and DAR values exhibited by extruded cables during practical thermal ageing processes. This research gap is of particular significance because it hinders a comprehensive understanding of PI and DAR as indicators of cable health condition. Consequently, there is a compelling need for further investigation to unravel the dynamics of PI variations during thermal ageing, ultimately enabling the practical utilization of these variations in the condition monitoring of extruded cables. Closing this gap holds great promise for enhancing cable health assessments and ensuring the reliability of electrical distribution systems.

2.4.4. Dielectric Loss

2.4.4.1 Introduction

Integral degradation can be reflected by the Dielectric loss (DL) measurement, which is also called $\tan\delta$ test. This method is an in-situ and non-destructive test. The tests can be executed under various voltage frequencies. However, localized defects and degradation are not able to be indicated and located by DL tests. A $\tan\delta$ measurement consists of two relevant tests: the dissipation factor test and the power factor test. The principle of this measurement is a total current (I) that comprises a capacitive current (I_C) dependent on the capacitance of cable insulation and a leakage current (I_R) produced when a steady-state ac test voltage is applied across cable insulation [10]. The equivalent circuit of measurement operation is presented by Figure 7 (a). The correlations among the test voltage and the produced current components as Figure 7 (b) shown.

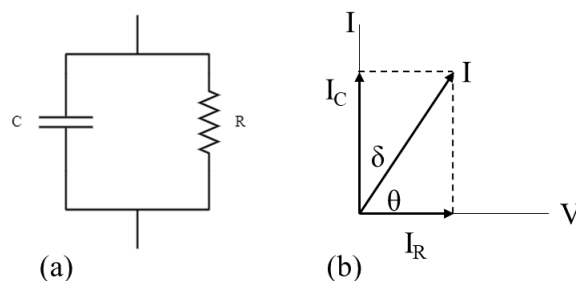


Figure 7. (a) Equivalent circuit and (b) diagram for currents and voltage of insulation under $\tan\delta$ tests

where:

- I : Total measured current
- I_C : Capacitive component of I
- I_R : Loss component of I
- V : Applied ac voltage
- θ : Dielectric phase angle
- δ : Dielectric loss angle

For cable insulation in ideal conditions without defects like trees, moisture and voids, I_R is relatively low ($0.1\mu\text{A}$ to $1\mu\text{A}$ for MV cables), due to the insulation properties being more like a good capacitor. In a capacitor, the voltage has 90-degree phase shift with the capacitive current through the cable insulation. In the case of contaminations incurring in the insulation and thus capacitance increases, or insulation is degraded due to ageing, resistive current

through insulation grows as the IR degradation occurs, while I_C is approximately fixed. The voltage and current phase will shift less than 90 degrees. The magnitude of angle moving away from 90 degrees is called “loss angle (δ)” which is related to insulation quality.

As a result, the health of an electrical insulator can be determined by the ratio of resistive component to the capacitive component as shown in (5). This ratio is commonly known as $\tan \delta$, sometimes also referred to as dissipation factor which is usually used as a measure of dielectric degradation.

$$\tan \delta = \frac{I_R}{I_C} = \frac{\frac{V}{R}}{V \times 2\pi f C} = \frac{1}{2\pi f R C} \quad (5)$$

For a proficient insulator, this ratio tends to be relatively low (below 0.1%), exhibiting minimal variation as the applied voltage increases. Conversely, when dealing with cables featuring subpar insulation, the DL values surpass the standard range (0.1% to 0.5%). Additionally, the correlation between these values and the applied voltage level is more pronounced. Similarly, the dielectric power factor ($\cos\theta$) serves as an indicator of dielectric loss.

2.4.4.2 Previous research

As cable ageing time progresses, there is a variation of the dielectric loss values. This pattern serves as evidence of a change in the cable's insulation capacity. The research conducted by Dragan revealed that cable capacitance remains virtually constant throughout the ageing period, while resistance experience gradual deterioration when subjected to increased levels of stress, whether of an electrical or thermal nature [74]. It is worth to note that the impact of temperature on $\tan\delta$ is more pronounced compared to the influence of electrical stress. It was found that the $\tan\delta$ can serve as an indicative measure of cable insulation conditions relevant to the ageing phenomenon. Moreover, the study conducted by Asmarashid and Muhammad focuses on underground XLPE cables ratings of 11kV and 22kV also found similar conclusions [75]. The $\tan\delta$ values exhibited a direct correlation with the ageing duration of the cables. In contrast, the analysis of capacitance measurements indicated a lack of relationship in their values.

Fothergill et al. conducted a study on the dielectric behaviour of extruded power cables with XLPE insulation and both inner and outer semi-conductive layers [76]. This investigation encompassed a frequency span of 10^{-4} to 10^4 Hz and temperatures ranging from 20 to 100°C. Their findings revealed that subjecting the cables to thermal ageing at 135°C for a duration of 60 days led to substantial increases in $\tan\delta$ value. This outcome suggests that these measurements could serve as a sensitive means of quantifying the extent of electrical

degradation resulting from thermal ageing. Kocatepe et al. analyzed the $\tan\delta$ changes in a 5 kV high voltage cable under varying voltage and frequency conditions using a digital measurement device. They found that $\tan\delta$ values increased with higher voltage levels and were significantly elevated at higher frequencies [77].

2.4.4.3 Discussion

While prior studies have indicated the significance of $\tan\delta$ testing outcomes, the correlation between these variations and data obtained from other monitoring technologies for power cables remains relatively unexplored in academic literature. This study aims to address an existing research gap concerning the relationship between the changes observed in $\tan\delta$ values and the trends identified through IR and PI tests to comprehensively evaluate the thermal degradation of cable insulation performance.

2.4.5. Other techniques

2.4.5.1 Introduction

In addition to the above reviewed IR, PI, DAR and $\tan\delta$ techniques, a variety of other techniques are employed for monitoring the condition of cables. While IR, PI and $\tan\delta$ are widely recognized for their simplicity and effectiveness in assessing the general health of cable insulation, other methods provide more specialized insights into different aspects of cable integrity. There are techniques that focus on assessing the mechanical properties and chemical stability of the insulation materials. Elongation at Break (EaB) testing is particularly valuable for evaluating the physical durability of the insulation, helping to detect issues like embrittlement or cracking that might not be apparent through electrical tests alone. On the other hand, oxygen monitoring is crucial in environments where oxidative degradation poses a risk, providing early warnings of chemical changes that could compromise the insulation's performance. These techniques offer a more comprehensive approach to cable condition monitoring by addressing different failure modes and degradation mechanisms.

2.4.5.2 Elongation at Break (EaB) Testing

EaB testing is a crucial method for evaluating the mechanical resilience and flexibility of a cable's insulation material. Specifically, it measures the extent to which the insulation can stretch before it fractures and is defined as percent increase in elongation at the time of fracture by Equation (6), providing a direct assessment of the material's ductility and tensile strength. The test is particularly important in determining the insulation's ability to withstand physical stress, such as bending, stretching, or environmental factors like thermal expansion and contraction.

$$EAB(\%) = \frac{\text{Final length} - \text{Original length}}{\text{Original length}} \times 100 \quad (6)$$

One of the primary advantages of EaB testing is its ability to detect mechanical degradation in insulation materials that might not be apparent through electrical tests alone. Insulation materials that have been subjected to harsh environmental conditions, such as extreme temperatures, UV exposure, or chemical contamination, may become brittle or develop micro-cracks over time. EaB testing effectively identifies these issues by measuring the material's ability to stretch before it breaks. A significant reduction in elongation at break indicates that the insulation has lost its flexibility, which is often a precursor to complete mechanical failure.

EaB testing is also valuable in assessing the ageing of polymeric insulation materials. By measuring how much the insulation can elongate before breaking, EaB testing provides a clear indication of the material's aging process. This information is critical for predicting the remaining useful life of the cable and scheduling maintenance or replacements before a catastrophic failure occurs.

While many cable condition monitoring techniques focus on electrical properties, EaB testing provides a material-focused perspective, offering insights that complement electrical tests like IR and PI. By focusing on the physical properties of the insulation, EaB testing helps build a more complete picture of cable health, addressing potential failure modes that might be missed by purely electrical assessments.

However, the most significant drawbacks of EaB testing is that it is destructive. The test involves physically stretching a sample of the insulation material until it breaks, which means the section of cable tested is permanently damaged and can no longer be used in service. As a result, EaB testing is often limited to laboratory settings or used on representative samples rather than the actual cable in use. Besides, the need for careful sample preparation and the lack of real-time monitoring capabilities limit its use under service conditions.

2.4.5.3 Oxygen Monitoring

Oxygen monitoring is typically used to detect the presence and concentration of oxygen that can indicate the degradation of cable insulation materials, especially in environments where the cable is exposed to oxidative conditions. Elevated levels of oxygen can lead to oxidation. Oxygen monitoring can also detect production of other gases, such as carbon dioxide or carbon monoxide, which can be by-products of insulation degradation processes. This provides additional insight into the chemical stability of the insulation material and the progression of degradation.

Oxygen monitoring systems typically use gas sensors to detect the concentration of oxygen and other relevant gases within the insulation or in the vicinity of the cable. These sensors can be placed in strategic locations where they can effectively monitor the cable's environment. In some cases, a small amount of gas is extracted from the cable's environment and analyzed using gas chromatography or other analytical methods to determine the composition of gases present.

Oxygen monitoring is typically non-invasive, meaning it does not require direct contact with the insulation material. This makes it suitable for continuous monitoring without interrupting the operation of the cable system. By detecting increase in oxygen or other by-product gases, this technique can provide early warnings of insulation degradation before it progresses to a critical stage.

However, effective oxygen monitoring requires sensitive and often specialized gas detection equipment, which can be more complex and costly than other cable condition monitoring techniques. While oxygen monitoring can indicate the presence of degradation, it does not provide a direct measurement of the mechanical or electrical properties of the insulation, so it typically needs to be used in conjunction with other testing methods for a comprehensive assessment.

2.5. Accelerated thermal ageing of extruded cables

2.5.1. Introduction

It is widely acknowledged that the time needed to age cable insulation materials under normal working conditions is impractical for experimental studies. Given that the designed lifetime of a power cable typically reaches to 30-40 years, conducting experiments over such prolonged periods becomes challenging [78]. In addition, obtaining aged samples directly from the field for essential testing and evaluation objectives is impracticable. Predicting the failure times or estimating the long-term performance of extruded power cables constitutes a quandary [79]. In light of this challenge, scholars have turned their attention towards the adoption of accelerated ageing methodologies.

Accelerated thermal ageing tests conducted at elevated temperatures speeding up the ageing process of power cables. This acceleration facilitates the examination of alterations in insulation properties, including dielectric strength and conductivity, within a compressed timeframe [80]. Furthermore, the methodologies employed in accelerated ageing tests could simulate the stressors and environmental conditions that power cables are projected to undergo during their operational lifespan [81].

Accelerated thermal ageing for insulation materials of extruded cables is frequently carried out using material samples shaped into dumbbells or circles [82]. Thermal accelerates the ageing process by increasing the rate of chemical reactions within the polymer. Most accelerated thermal ageing experiments involving XLPE, the ageing temperature has been kept below 130°C. This temperature choice is consistent with the maximum allowable operating temperature for conductors under overload conditions [83].

As reviewed in section 2.3, there are physical and mechanical properties variations occur when the polymer insulation material degrades, these alterations can influence the overall mechanical strength and flexibility of the extruded cables. Accelerated thermal ageing could serve as a quality control tool to validate the stability and performance of extruded power cables. Manufacturers can identify potential issues with insulation degradation early in the development or production process. Thermal accelerated ageing offers insight into the response of insulation material to prolonged exposure to high temperatures.

2.5.2. Previous research

Subjecting sheet-shaped flame-retardant cross-linked polyethylene (FR-XLPE) to thermal ageing at temperatures of 100°C, 135°C, and 155°C for durations ranging from 800 to 2000 hours was observed to progressively influence its performance characteristics [84]. It is important to note that this study operates within a high-temperature range where melting can occur, potentially making the findings less representative of behavior at lower or service temperatures. The ageing phenomenon exhibited a three phases progression based on the analysis of correlation between the conduction current and the indenter modulus (IM). The turning points among these three aging stages are at about 22 and 45 N/mm in IM. During the initial phase, a rise in cross-linking density within the material led to a concomitant reduction in both conduction current and the imaginary component of the complex permittivity. Subsequently, the second phase manifested oxidative degradation as the dominant mechanism, resulting in an escalation of conduction current as well as augmented real and imaginary components of the permittivity. In the final phase, stabilization of the conduction current occurred, yet the complex permittivity exhibited sustained augmentation.

The research program conducted by Lofaro et al. sought to address challenges in the Environmental Qualification (EQ) process for low-voltage instrumentation and control electric cables in nuclear power plants by evaluating three commonly used cable types: XLPE insulation with a Neoprene jacket, EPR insulation with an unbonded Hypalon jacket, and EPR insulation with a bonded Hypalon jacket [10]. The study involved testing both unused cables, which were subjected to accelerated aging to simulate 20, 40, and 60 years of service life

through cyclic loading at 90°C and three times the standard operational stress in water-immersed conditions over 60, 120, and 180 days, and naturally aged cables from two nuclear plants. Multiple condition monitoring techniques were applied at each testing stage to assess the cables' condition and the effectiveness of these methods. EPR-insulated cables exhibited a clear trend of decreasing IR and PI, indicating deteriorating dielectric strength as the insulation material degraded. Similarly, XLPE-insulated cables also showed a decline in IR and PI with increasing degradation during pre-aging. This trend was consistent in measurements taken both from conductor-to-conductor and from conductor-to-ground. Therefore, IR measurements, especially when compared to baseline measurements, are considered an effective electrical condition monitoring technique for these cable materials. For the Dielectric loss measurements, EPR-insulated cables consistently showed an increasing power factor, indicating deteriorating dielectric strength, as the insulation material degraded. Similarly, XLPE-insulated cables exhibited the same trend of increasing power factor with greater degradation during pre-aging. This trend was most pronounced and consistent at applied AC test voltage frequencies between 10 and 500 Hz, and it was most effectively observed in measurements taken from conductor-to-ground.

To examine the operational condition of polypropylene, a thermal accelerated ageing experiment was conducted on polypropylene materials intended for 10kV cables by Li et al [85]. Given that the melting point of the modified polypropylene was approximately 140 °C, an accelerated ageing test was performed on 1mm thick polypropylene samples at 110°C for 10, 20, and 30 days, as well as at 135°C for 7, 14, 21, and 28 days. A state assessment method considering carbonyl index, activation energy, medium loss and melting enthalpy, which are measured by thermogravimetric analysis (TGA), differential scanning calorimetry (DSC) and Fourier-transform infrared spectroscopy (FTIR) methods, was established to calculate performance index of cable samples. The results indicated a substantial deterioration in the performance index of polypropylene after 28 days at 135°C.

In a study conducted by Mustafa et al., an examination of the behavior of low voltage unshielded power cables utilized in nuclear power plants was carried out under thermal stress conditions [86]. The cable samples, featuring a 0.762mm outer jacket and 1.143mm XLPE insulation, were subjected to thermal stress in an oxygen-controlled oven set at 120°C. The accelerated ageing periods were determined using the Arrhenius model and were specified as 176, 338, 512, 784, 912, 1056, 1248, and 1464 hours. The Arrhenius model will be discussed in detail in section 2.7. Additionally, Zhang et al. conducted accelerated thermal ageing of XLPE specimens in a chamber filled with 99.99% inert nitrogen gas at atmospheric pressure,

at temperatures of 130, 140, and 150°C, respectively [55]. Following defined ageing time intervals, the specimens were cooled to room temperature and removed from the thermal ageing chamber for FTIR and DC electrical conductivity measurements, results and conclusions of this study as already discussed in section 2.4.2.

2.5.3. Discussion

Within the existing body of literature, substantial progress has been achieved in the methodologies related to the accelerated thermal ageing of extruded power cables and applied into thermal behaviour investigations of extruded cables. A reasonable designed thermal accelerated ageing experiment holds significance for researchers. The data derived from thermal accelerated ageing tests can be extrapolated to understand thermal ageing processes and mechanisms of cables and predict the anticipated service life of cables under typical operating temperatures.

Nonetheless, there persist significant gaps that necessitate further investigation, encompassing the consideration of elevated cable temperatures resulting from load currents, thermal ageing of whole scaled-extruded power cables with semiconductor screen layers, the effects of cyclic temperature fluctuations over time, and the temperature distribution across cable length and cross-section. Additionally, in practical scenarios, power cables often experience temperature gradients both along their length and across their radius. These gradients arise from several factors, including uneven loading, environmental conditions, thermal resistances at material interfaces, and the dissipation of heat generated by electrical losses. For instance, the outer layers of a cable might be cooler due to contact with ambient air or soil, while the inner layers, closer to the conductor, could be significantly hotter. The non-uniform temperature distribution can lead to localized differences in aging rates within the same cable. For example, the hotter regions near the conductor may undergo faster thermal degradation, including oxidation, chain scission, and cross-linking changes, while cooler regions may age more slowly. This differential ageing can result in a non-uniform degradation profile, potentially leading to early failure in the most thermally stressed regions of the insulation.

The addressal of these gaps holds utmost importance, as it not only contributes to a more comprehensive understanding of the thermal ageing mechanisms of extruded cables within practical operating conditions but also holds the potential to estimate cable lifetimes and assess property variations under typical service environments. Consequently, this study designs a novel accelerated thermal ageing method, involving the application of elevated load currents within a thermally insulated chamber, with the intent of bridging these recognized research

gaps and advancing the existing knowledge within this field. The design and application of accelerated thermal ageing experiments in this research will be further elaborated upon in Chapter 3.

2.6. Thermal modelling of extruded cables

2.6.1. Introduction

The distribution of temperature profiles in extruded power cables are significantly influenced by the heat dissipation into surroundings of cable conductors. The accurate computation of both temperature distribution and the distinctive thermal processes of extruded power cables highly holds significance in the design of power cable construction and the enhancement of power cable utilization efficiency [87]. The temperature distribution profiles of power cable in different working conditions could be obtained through experimental measurement or calculated by thermal analytical or numerical methods. The IEEE and IEC have provided their standards based on the analytical methods [88][89]. While the numerical approaches are mainly developed according to Finite Difference Method (FDM), Finite Element Method (FEM) and Finite Volume Method (FVM) [90][91].

The cable installation modes and the ambient environment have significant influence on the temperature calculation accuracy of power cables, the methods provided by IEEE and IEC Standards are not able to properly handle the coupling effects of these factors [92]. The numerical calculation methods have a good adaptability to complex and uneven field so that it can provide an accurate simulation of the installation mode and physical field of the cable and treat the coupling effects [93].

FVM is numerical technique used for solving Partial Differential Equations (PDEs) in various fields of science and engineering. The most excellent characteristic of the FVM lies in its capacity to result solution by conservation of fundamental quantities, including mass, momentum, energy, and species, within the computed solutions. This conservation principle remains strict satisfied for every individual control volume, spanning the entirety of the computational domain, and irrespective of the number of discretized cells employed [94]. FVM is particularly well-suited for problems that involve conservation laws, such as fluid dynamics and heat transfer.

Furthermore, FVM typically uses a structured or unstructured grid system, which makes it more adaptable to complex geometries and irregular domains. This flexibility can be advantageous when dealing with problems that have varying geometries or require adaptive mesh refinement. As a result, the FVM has emerged as one of the predominant research

approaches for analysing the temperature distribution of cables in recent years[95].

2.6.2. Previous research

In the research by Vahidi and Mahmoudi, FVM was applied to analyse the heat generation and transfer within a three-phase 145kV underground cable branch, considering both homogeneous and non-homogeneous soil conditions [96]. The study revealed a marked disparity of over 10% in cable ampacity calculations between these environments. Consequently, employing ampacity values determined in homogeneous soil conditions for cables in routes with non-homogeneous soil can lead to cable overloading, emphasizing the critical importance of FVM in cable design and deployment to ensure operational safety and reliability.

Boukezzi et al. presented the findings of their study focused on the radial temperature distribution within XLPE cables [97]. The investigation involved a detailed analysis of the distribution characteristics utilizing the FVM. The results illustrated that the radial temperature distribution within the XLPE cable does not exhibit a uniform pattern due to variations in thermal conductivity across its different layers. Specifically, the highest radial temperature distribution is observed within the conductor region, while regions near the cable's insulation and grounding exhibit comparatively lower temperature distributions, consistent with the prescribed boundary conditions. From a methodological perspective, the application of the FVM is an effective tool for addressing heat transfer phenomena in extruded power cables.

Hwang et al. focused on thermal analysis of underground cables enclosed in PVC conduits. Their findings indicated that cables buried directly exhibited notably lower temperatures than those within conduits [98]. They employed a comprehensive approach, coupling multiple physical domains in an electromagnetic-thermal model for subterranean power cables. This method, based on the numerical method, addressed limitations inherent in the IEC standard.

Furthermore, the numerical methods were harnessed to explore the heat transfer dynamics within submarine cables, as studied in the [99], wherein the discerned impact of submarine soil temperature upon cable temperature was highlighted. Hughes et al. substantiated the significant role of permeability in influencing submarine cable temperatures through numerical simulations in [100].

Zhang etc. focused on a 220 kV three-core AC submarine high-voltage cable and employed a multi-physical coupling model encompassing electromagnetic, fluid, and heat transfer fields [101]. The study iteratively computed the cable's temperature distribution and

ampacity. It was found that the landing section experiences the highest operating temperatures, exceeding insulation limits, and impacting ampacity. Under various laying methods, conductor temperature increases linearly with seawater temperature, while ampacity decreases linearly. The sub-sea laying method, which is in direct contact with seawater, is most affected by seawater temperature, showing the highest increase rate in conductor temperature (1.072) and the greatest reduction rate in ampacity (2009.7222). In comparison, pipe laying and direct burial laying methods experience smaller increases in conductor temperature and decrease rates in ampacity (0.66654 and 991.42667 for pipe laying, and 0.6989 and 1149.16222 for direct burial laying), due to medium blocks limiting direct seawater contact. There is a positive correlation between temperature and laying depth: as depth increases, the temperature rise diminishes and eventually stabilizes. Conversely, cable ampacity decreases with increasing laying depth, as shallower depths benefit from better seawater heat dissipation due to its high convection coefficient and thermal conductivity. Additionally, as seafloor soil heat conductivity increases, submarine cable ampacity improves, although the rate of ampacity increase gradually slows [101].

2.6.3. Discussion

The previous thermal modelling research of power cables has shown the efficacy of numerical methods in offering a high level of accuracy in predicting the spatial temperature distribution of cables under specific operational conditions. Through numerical computations, FEM and FVM could effectively simulate the heat transfer processes occurring within power cables, accounting for the varying thermal properties of different cable components and their interactions. This capability offers spatially accurate temperature profiles across the cable's length and cross-section. For researchers, a more precise estimation of the cable's operational lifetime thus could be conducted, ultimately enhancing the ability to forecast thermal degradation and ageing processes.

While the previous studies have made considerable contributions to the field, several research gaps and areas for further investigation exist. The identified research gaps can be broadly categorized as follows:

1. Thermal cycling effects: There's a gap in the existing research about how temperature distribution changes in cables due to repeated load cycling, which occurs during cable operation. Addressing this gap, it is necessary to develop models that account for the dynamic temperature distribution over time due to cyclic loading variations.
2. To validate and enhance the credibility of numerical models, a combination of laboratory experiments and field measurements need to be conducted. In the

laboratory setting, real cables will be utilized to gather data on temperature distributions, heat dissipation, and other related parameters. On-site measurements in real-world cable installations will be undertaken to corroborate numerical models.

3. Modelling approach and prediction enhancement: In the numerical modelling approach, a model is divided into numerous small elements to facilitate calculations using mathematical models of thermal conduction and natural fluid convection, following common numerical methodologies. This process allows for the extraction of temperature data from specific points within the mesh. Nonetheless, the temperatures spanning the entirety of the cable structure, especially those between mesh points, aren't directly derived from simulation outcomes. To address this limitation and enhance the predictive capabilities concerning the spatial temperature profiles of extruded cables, integration of Artificial Neural Network (ANN) techniques with numerical methods are intended.

These gaps show opportunities for future research to extend and enhance understanding of thermal modelling of extruded cables. It would not only enhance the understanding of cables behaviour but also hold significant meaning for cable design and reliability assessments in dynamic operating environments. Furthermore, a more comprehensive and detailed assessment of temperature distribution throughout the cable structure, improving the overall accuracy and precision of thermal models used for ageing phenomena.

2.7. Thermal degradation models of extruded cables

2.7.1. Introduction

Thermal degradation models refer to mathematical or computational models that are designed to simulate and analyse the process of deterioration or breakdown of cables under the influence of thermal stresses. Thermal degradation models could help researchers and engineers understand the change of cable insulation material properties as a result of it prolonged exposure to elevated temperatures. By incorporating factors such as heat transfer, chemical reactions, and material behaviours, these models aim to predict the degradation mechanisms and estimate the remaining useful life of the cables.

Around the year 1890, there existed a general awareness that elevated temperatures induce a rise in chemical reaction rates, typically leading to a doubling of the rate for every approximate 10-degree increment, yet the underlying rationale behind this phenomenon remained elusive. This widely accepted understanding persisted until Svante Arrhenius combined the principles of the Boltzmann distribution law and activation energy in 1899. This

synthesis culminated in the establishment of one of the most prominent relationships in the realm of physical chemistry, as denoted by (7) [102]:

$$k = Ae^{-\frac{E_a}{K_B T}} \quad (7)$$

where:

- k represents the rate constant (1/h),
- E_a signifies the activation energy (J),
- K_B denotes the Boltzmann constant (J/K),
- T is the absolute temperature (K), and
- A stands for a constant denoted as the Arrhenius factor.

The activation energy (E_a) represents the energy needed to initiate a specific endothermic reaction within the material. This parameter is directly related to the rate of degradation, meaning that materials with higher activation energies will undergo thermal degradation more slowly than those with lower activation energies. The term " $K_B T$ " embodies the concept of average kinetic energy, while the exponent " $E_a / K_B T$ " is subject to the interplay between the activation energy " E_a " and the average kinetic energy " $K_B T$ ". A higher ratio of " E_a " to " $K_B T$ " engenders a reduction in the rate constant due to the negative sign inherent in the exponent. Consequently, it follows that smaller activation energies in conjunction with elevated temperatures yield greater rate constants, thereby accelerating the progress of the chemical reaction.

Equation (7) can also be alternatively expressed in a non-exponential format, specifically in natural logarithm form. This transformation serves to enhance the interpretability of outcomes. Consequently, the resulting formulation assumes the structure of a linear equation, taking the form of (8):

$$\ln(k) = \ln(A) - \frac{E_a}{K_B T} \quad (8)$$

Generating a plot of the natural logarithm of the rate constant $\ln(k)$ against the reciprocal of temperature ($1/T$) yields a linear relationship characterized by a slope of $-E_a/K_B$ and an intercept on the y-axis. The slope magnitude is indicative of the coefficient of activation energy over the Boltzmann constant (K_B), while the y-intercept pertains to the value of the natural logarithm of the frequency factor $\ln(A)$. This linear representation permits the utilization of k acquired from distinct temperature points for the purpose of deducing the activation energy. This graphical representation is visually depicted in Figure 8, illustrating the correlation between $\ln(k)$ and $1/T$.

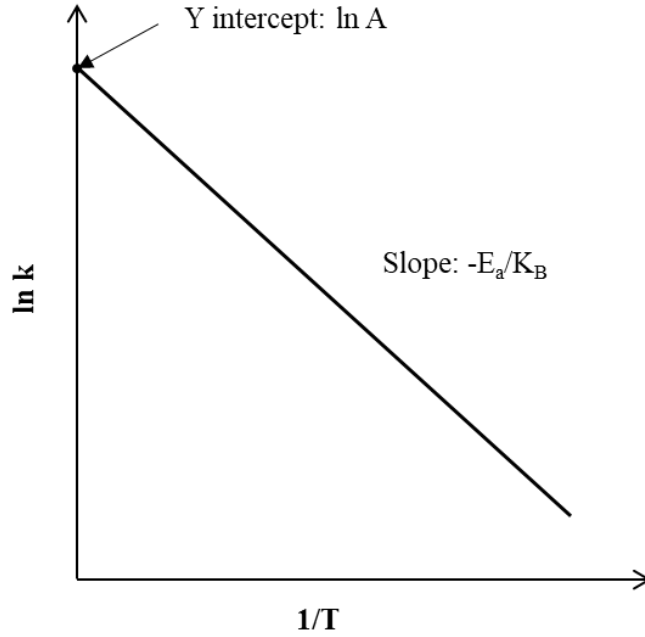


Figure 8. Logarithm representation of Arrhenius plot (ln k vs. 1/T)

Hence, the Arrhenius model establishes the connection between the thermal lifespan of extruded cable insulation at one temperature and its counterpart at a different temperature, as depicted by (9) [35]:

$$t(T) = t_R \exp \left[\frac{E_a}{K_B} \left(\frac{1}{T} - \frac{1}{T_R} \right) \right] \quad (9)$$

where $t(T)$ is the service lifespan in h, T is the service temperature in K, t_R is the reference lifespan, T_R is the reference temperature. In particular, the lifespan $t(T)$ and t_R represent the thermal lifespans respectively associated with the temperature T and T_R . The values for E_a , t_R , and T_R could be taken from the appropriate experimental data.

The Arrhenius model has both theoretical and practical limitations, such as: (1) the possible difference in reactions and aging mechanisms between high temperatures and normal service temperatures, indicating that activation energy (E_a) may change with temperature rather than remain constant; (2) difficulties in extrapolating data through a material's phase transition region, like the crystalline melting point; (3) the use of regressed statistical data, which can produce varying activation energy values depending on the chosen endpoint criterion; and (4) the possible lack of specific activation energy data for certain material formulations, as this information is usually provided only for general material categories[35]. Miner's cumulative damage law, also known as Miner's law, expressed mathematically as (10). Miner's rule is a concept widely used in fatigue analysis and engineering. The law suppose that the total accumulated damage in a material subjected to repetitive loading is proportional

to the sum of the fractions of loading cycles at each level of stress. In simpler terms, it predicts the cumulative fatigue damage experienced by a material when subjected to repeated stress cycles of different levels [103].

$$D = \sum \frac{N_i}{N_{i,max}} \quad (10)$$

where:

- D represents the cumulative damage
- N_i is the number of cycles at stress level i
- $N_{i,max}$ is the number of cycles at stress level i that would cause failure if applied alone

Miner's law assumes that each cycle contributes to the overall fatigue damage, regardless of its magnitude, and that the material fails once the cumulative damage exceeds a critical value (usually taken as 1). This approximation is suitable for cases where the stress amplitudes are not significantly different from each other.

Derived from Miner's Law, the service lifespan ($t(T)$) of an extruded power cable, in hours, transforms into the cumulative thermal lifespan ($L_{tot}(T)$) in hours, operating under the premise of an inverse relationship with the thermal ageing rate ($R_a(T)$) expressed as a percentage per hour [104]. Therefore, the expression for the thermal ageing rate ($R_a(T)$) is obtained as (11):

$$R_a(T) = \frac{A_{max,p}}{t(T)} = \frac{100}{L_{tot}(T)} \quad (11)$$

where, $L_{tot}(T) = t(T)$ represents the total thermal lifespan at a particular service temperature T , as estimated using (8), and $A_{max,p} = 100\%$ signifies the highest conceivable fraction of $L_{tot}(T)$.

A portion of $L_{tot}(T)$ utilized within a specific operational span t_{op} can be approximated by employing an appropriate array of thermal ageing rates $R_{a,i}(T)$ that correspond to the given temperature profile. Variations in a temperature profile align with variations in the associated load diagram and can be evaluated through the thermal modelling techniques. Through the division of the known temperature profile of a specific operational duration t_{op} into K intervals, each interval's thermal ageing rate $R_{a,i}(T)$ and duration $t_{D,i}$ can be employed to compute the fraction of $L_{tot}(T)$ attributed to that interval, denoted as $A_{F,p,i}(T)$ [105]. The aggregate proportion of $L_{tot}(T)$ in percentage expended over the entire operational duration $t_{op} = K \cdot t_{D,i}$ is established by the Miner's cumulative damage law [104]:

$$L_{tot,p} = \sum_{i=1}^K L_{F,p,i}(T) = \sum_{i=1}^K R_{a,i}(T) t_{D,i} \quad (12)$$

where, $L_{F,p,i}(T)$ signifies the portion of $L_{tot}(T)$ expended within the i th interval, expressed as a

percentage. $R_{a,i}(T)$ denotes the thermal ageing rate occurring at the designated service temperature T throughout the i th interval, measured in percentage per hour, and $t_{D,i}$ represents the duration of this i th interval in hours. In accordance, $L_{tot,p}$ represents the overall loss of $L_{tot}(T)$ across the complete operational duration t_{op} .

2.7.2. Previous research

The research undertaken by Abdulsalam and Rayan employing an accelerated thermal ageing coupled with the implementation of the Arrhenius model [106]. Within the accelerated life testing, the investigation showcased the establishment of a clear and well-supported relationship between cable lifespan and stress factors. The investigation encompassed the examination of two distinct variants of XLPE material used for extruded medium voltage and high voltage power cables, subjected to varying elevated temperatures spanning the range of 95°C to 105°C. The findings of this research were succinctly depicted through the graphical representation of an Arrhenius plot, facilitating the projection of long-term performance trends and the calculation of cable lifetimes. The study highlighted the projected lifespan of XLPE material, within the operational conditions of 90°C, spanning a range of 40 to 60 years. Furthermore, the research identified a prediction of cable longevity, situating the expected operational span between 7 to 30 years across a temperature spectrum of 95°C to 105°C.

Jelena et al. introduced a utilization of the PLAN-DO-CHECK-ACT (PDCA) approach for the management of thermal ageing in underground power cables within electricity distribution networks [107]. They employed thermal modelling in conjunction with the Arrhenius model to calculate the uncharted temperature of cable conductors during operational conditions. This combination allowed the FEM-based Arrhenius model to encompass additional thermal factors such as external heat sources, wind, solar irradiation, etc., within the assessment protocols for qualifying underground power cables. The efficacy of their proposed method was corroborated through successful validation with established experimental data on cross-linked polyethylene insulation.

The study by Dardan etc. successfully employed the Arrhenius model and numerical thermal model to analyse the thermal effects of a heating pipeline and various pavements on the thermal lifespan of a 110 kV underground cable line insulated with XLPE [108]. The study demonstrated that the analysed thermal effects can substantially reduce the expected service lifespan of XLPE-insulated cables near a heating pipeline. The greatest thermal impact occurred when the 110 kV cables are closest to the heating pipeline. The parallel installation of the 110 kV cables and heating pipeline did not lead to a hotspot due to the cable bedding's high thermal conductivity in a dry state.

2.7.3. Discussion

The Arrhenius equation is widely used to model the thermal aging of cable insulation like XLPE. It relates the rate of a chemical reaction (or degradation process) to temperature, providing insights into how materials will perform over time under different thermal conditions.

The Arrhenius model allows for accelerated thermal aging tests by exposing cables to higher temperatures than they would experience in service. This can predict the material's lifespan under normal operating conditions without having to conduct long-term tests. By knowing the activation energy and pre-exponential factor, the Arrhenius equation enables extrapolation of aging data from high temperatures to lower, operational temperatures, giving a theoretical estimate of service life.

The equation provides a relatively simple mathematical relationship between temperature and aging rate, which makes it easy to apply in practical scenarios. The Arrhenius equation is based on empirical data, and for many materials, it has been shown to provide reasonable predictions of aging behaviours under various thermal conditions.

However, The Arrhenius equation assumes that the activation energy is constant over the range of temperatures considered. In reality, the activation energy may vary at different temperatures, especially if different degradation mechanisms become dominant at different temperatures, leading to inaccurate predictions.

The Arrhenius equation is a useful tool for predicting thermal aging in cable insulation, offering a straightforward and effective method for estimating service life under varying thermal conditions. However, its utility is limited by its assumptions, particularly the constancy of activation energy and the oversimplification of complex aging processes. For accurate predictions, the Arrhenius model should be used with caution, ideally in conjunction with other models and empirical data that account for the full range of environmental and operational factors affecting cable aging. Thus, certain research gaps persist and required further investigation:

1. Temperature profiling for enhanced thermal degradation models:

It is widely acknowledged that long-distance distribution and transmission extruded power cables undergo non-uniform temperature distributions under actual operational conditions, potentially resulting in localized hotspots. Although hotspot temperatures are conventionally employed to assess thermal ageing and degradation, relying solely on these temperatures may lead to premature estimations of cable failure. Therefore, there exists a

significant research gap in the need for a more comprehensive and detailed temperature profile of cable insulation. Developing models that consider this detailed temperature profile could significantly enhance the accuracy of thermal degradation assessments for cables.

2. Development and validation of specific indicator-based degradation models:

A crucial area of future research lies in the development and validation of thermal degradation models based on specific indicators like IR and $\tan\delta$. Practical experimental works can play an essential role in establishing and validating these models. Such efforts would not only contribute to a deeper understanding of cable health conditions during service but also provide engineers with valuable tools for effectively monitoring and evaluating cable performance. Closing this gap holds immense promise for ensuring the reliability and safety of power distribution systems.

2.8. Conclusion

This chapter provided a comprehensive investigation of information and previous research works in thermal ageing of extruded cables. Through an examination of a multitude of studies and findings, several key insights and trends have emerged:

The thermal ageing mechanisms of extruded cables insulation is a complex process influenced by several critical factors such as transition temperature, crystalline structure, stabilizing agents, antioxidants. Understanding thermal ageing effects and mechanisms of extruded power cables is beneficial for an array of critical applications for researchers, including the formulation of accelerated ageing tests to simulate real-world ageing phenomena, as well as the appropriate selection of condition monitoring tests that enable the discernment of the health status of power cable insulation.

Theoretical framework and previous studies of condition monitoring techniques for extruded cables including IR, PI, DAR and $\tan\delta$ were introduced. Condition monitoring of extruded cables is of paramount importance as it enables early detection of potential issues, ensures reliable operation, enhancing the efficiency and safety of electrical distribution systems. Condition monitoring is crucial for formulating effective strategies for predictive maintenance and ensuring the long-term reliability of power cable systems.

Then accelerated thermal ageing methodologies of extruded power cable used in previous research were reviewed. Accelerated thermal ageing of extruded power cables at elevated temperatures offers a controlled and accelerated platform for investigating insulation degradation, emulating enduring impacts, projecting performance under thermal stresses. This knowledge plays an important role in the anticipation of cables' longevity and dependability

in practical situations.

The utilization of the numerical methodologies for thermal modelling were presented as a significant tool that enriches the arsenal of researchers and engineers in the power cable domain. Research works of thermal modelling for extruded cables by numerical methods are examined, by providing accurate spatial temperature insights, this technique lays the foundation for improved decision-making and lifetime estimation.

Finally, thermal degradation modelling methodologies of extruded cables including Arrhenius and Miner's models are significant for predicting the lifetime of extruded power cables were reviewed. Their integration with thermal modelling techniques has elevated the precision of these predictions.

However, there are research questions and objectives have arisen from identified gaps and unaddressed needs in the field:

- Exploring the long-term effects of thermal ageing on full-scale extruded power cables, particularly those incorporating semi-conductor layers—a dimension that has received limited attention. While [10] investigated the thermal ageing and condition monitoring tests on full-scale power cables, the samples were of low-voltage cables used for instrumentation and control (I&C) applications, rather than MV/HV power cables.
- Designing and executing non-uniform and time-cycling accelerated thermal ageing experiments to extruded cables. This approach enables the examination of interactions among cable components and the effects of dynamic thermal stress.
- Inquiring into the variation of IR, PI, DAR and $\tan\delta$ with the progression of thermal ageing, contributing to an enhanced understanding of insulation degradation dynamics.
- Critically examining, comparing, and validating thermal simulation results against experimental data to establish the accuracy of modelling techniques.
- Investigating the spatial temperature profile of extruded cables through simulation, offering insights into the influence of temperature gradients on cable performance and ageing.
- Developing thermal degradation models of extruded cable insulation using spatial temperature profiles.

In conclusion, this chapter has provided essential background knowledge on the thermal

aging of extruded power cables, covering thermal aging mechanisms, condition monitoring techniques, accelerated thermal aging methodologies, thermal modelling applications, and thermal degradation models. Representative studies in each domain were reviewed to identify research gaps in the field. This literature review chapter helps in clarification of the significance of the new research subsequently presented in this thesis.

Chapter 3. Accelerated thermal ageing experiment for MV XLPE cables

3.1. Introduction

In order to investigate the thermal degradation of extruded cables caused by elevated cable temperatures resulting from load currents, thermal ageing of whole scaled extruded power with semiconductor screen layers, the effects of cyclic temperature fluctuations over time, and the temperature distribution across cable length and cross-section, this chapter describes the specifics of the experimental setup for accelerated thermal ageing of extruded cables. It covers methodologies of temperature elevation, control and monitoring. The detailed description encompasses the following aspects:

- Preparation of cable specimens to be subjected to accelerated thermal ageing.
- Methodologies employed for heating and thermal cycling.
- Arrangement of specimens within a thermally insulated chamber.
- Installation of thermocouples on cable and conductor surfaces for temperature monitoring.
- Analysis of temperature distribution across cables length and their variations within thermal cycles.

The artificial aging accelerated thermal cycling methodology used in this experiment was based on IEEE standard 1407, which provides guidelines for accelerated aging tests on extruded medium-voltage (MV) cables using water-filled tanks [109]**Error! Reference source not found.** While IEEE standard 1407 considers multiple aging factors in a single experiment, this study focused solely on thermal stresses generated by the conductor's joule heating. These stresses were applied to cable samples in an air-filled chamber to examine the thermal aging effects on full-scale MV power cables caused by non-uniform temperature distributions.

Condition monitoring of extruded cables could provide valuable information on predicting their remaining useful lifetime and strategically managing maintenance or replacement. Specific electrical properties including IR, PI, DAR and $\tan\delta$ have been proved associating with health condition of extruded cables in previous research, there existing gaps in exploration of variations of these electrical properties during thermal ageing processes. In addition, their sensitivity to environmental factors like RH and annealing effect generated from semi-conductor layers have not been investigated. Furthermore, correlations among variations

of these properties were lack of consideration. Thus, following works are implemented and presented in this chapter.

- Results of condition monitoring tests including IR, PI, DAR, Capacitance and $\tan\delta$ are presented.
- Influence of environmental relative humidity on testing results is discussed.
- PI variations of cables under 10kV testing voltage are fitted into three phases.
- Influence of annealing effect on measured results is considered and analysed.
- Correlations among testing results are investigated.

3.2. Cable specimens

The cross-sectional view of a single-core MV extruded power cable that underwent accelerated ageing in the experiment is illustrated in Figure 9. These MV power cables, produced by Cabelte S.A., are utilized in electrical power distribution networks [110]. The structure of cable specimens comprises 8 layers:

1. Circular conductor using solid aluminium material, class 1 according to BS EN 60228.
2. Semi-conducting compound conductor screen.
3. Cross-linked polyethylene (XLPE) insulation.
4. Semi-conducting compound insulation screen, fully bonded.
5. Copper wires helically applied.
6. Copper tape applied in an open counter helix.
7. Tape preventing water ingress: Semi-conductive tape preventing water ingress under the metallic screen; Water blocking tape over the screen.
8. Medium Density Polyethylene (MDPE) red outer sheath.

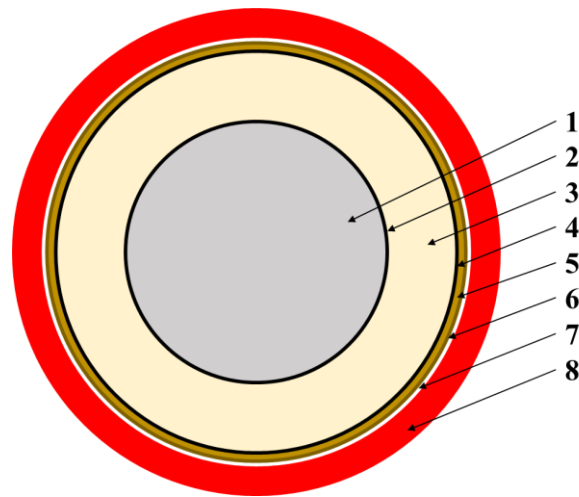


Figure 9. Cross-section view of MV extruded XLPE cable [110]

The manufacturing of the power cable adheres to standards BS EN 60228, CAB-03-020, and BS 7870-4.10. The rated voltage U_0/U is 6.35/11 kV. The cable conductor exhibits a maximum DC resistance (at 20°C) of $1.64 \times 10^{-4} \Omega/\text{m}$, and a maximum AC resistance (at 90°C) of $2.11 \Omega/\text{m}$. The current carrying capacity of the cables, depended on its installation environment, spans from 368 A to 446 A [110].

The dimensions of cable specimens are outlined in Table 5. The complete configuration of the cable specimen is visualized in Figure 10. It can be discerned from the illustration that the terminal of the cable specimen are meticulously prepared, allowing the cable core to connect to the power supply while the metal sheath serves as the grounding connection. To safeguard the exposed insulation from moisture and potential environmental impurities, a thin layer of black polymer material envelops it. The sectional view of the prepared cable specimen with terminals for connection is depicted in Figure 11.



Figure 10. Whole scale of cable specimen with prepared terminals

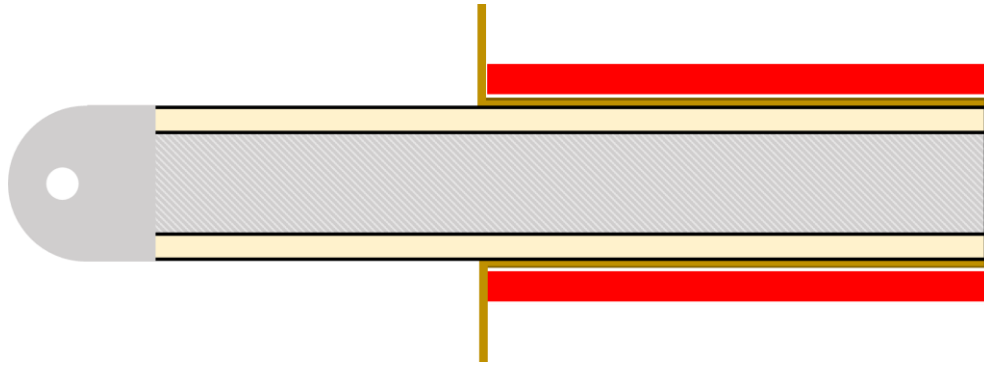


Figure 11. Section view of prepared cable with terminals

Table 5. Dimensions of cable specimens

Characteristics	Dimensions
Cable specimen length	3.3 m
Area of cable conductor	185 mm ²
Conductor screen thickness	0.3 mm
Insulation thickness	3.4 mm
Insulation screen thickness	0.3 mm
Cross-section area of metal shield	35 mm ²
Outer sheath thickness	1.9 mm
Overall diameter of cable	33 mm

It worth note that the prepared cable specimens stored at room temperature for approximately 500 days, which could be helpful for degassing further. Following this period, the presence of by-products in the cable insulation (XLPE) layer, including acetophenone (AP) and dimethyl benzyl alcohol (DMBA), which are generated during the manufacturing process, is notably reduced to a negligible level [111].

3.3. Experimental setup and equipment

Four cable specimens were prepared and parallelly arranged within an aluminium chamber, which is encapsulated with thermal insulation made from polystyrene material. The primary objective behind this arrangement is to facilitate the execution of the thermal accelerated ageing experiment and simulating the non-uniform temperature profile of power cables under authentic operational scenarios. The architectural and cross-sectional perspectives of the chamber are graphically represented in Figure 12. The gaps between adjacent cable cores are 100 mm, same as the distance from the cable core to both the upper and lower walls. Meanwhile, the lateral walls maintain a separation of 50 mm from the nearest cable core. The chamber's length spans 2.5 m, a slightly shorter length compared to the cable specimens, as the cables need to extend beyond the chamber's confines to establish connections with each other and the power supply. The walls of the aluminium chamber exhibit a 2 mm thickness. These dimensions were chosen based on the limitations of the experimental site and

equipment, as well as the outcomes of relevant simulations conducted prior to the experiment. The selection of the 100 mm gap between cable samples, along with the other specified distances in the experimental setup, is the result of the need to accurately simulate thermal conditions experienced by power cables in real-world scenarios and preventing overheating.

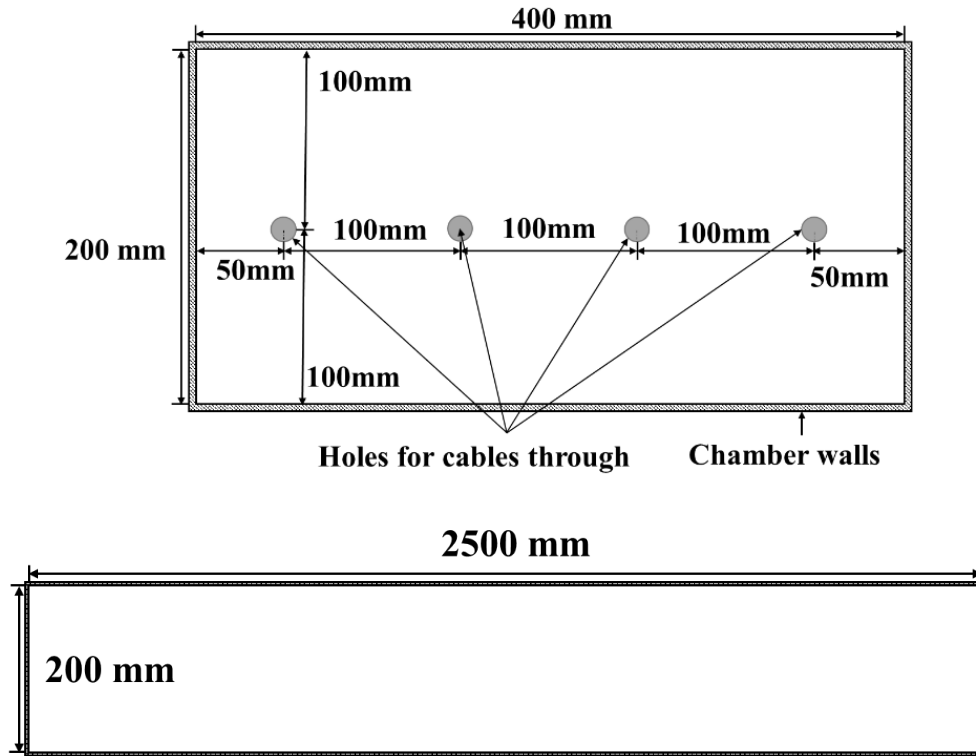


Figure 12. Dimensions and section views of chamber used for experiment

To replicate the temperature distribution of power cables under real-world operational scenarios and elevate the temperature of power cables to achieve the intended accelerated thermal ageing conditions, the temperature increase is accomplished by connecting the cable conductors to a high current transformer, which serving as the power supply. The induced current leads to joule loss of the cable conductors and generates substantial heat. Generated heat subsequently dissipates into the surrounding environment through the cable structures, thus elevate cable temperature to meet accelerated thermal ageing requirements.

Additionally, the aluminium chamber incorporates a 20mm-thick thermal insulation layer, which effectively prevents heat escaping from the chamber. The experimental configuration depicting the connection of power cables to the power supply is outlined in Figure 13. Within the chamber, the cables are interconnected in a series arrangement, facilitated by aluminium connectors, to the power source.

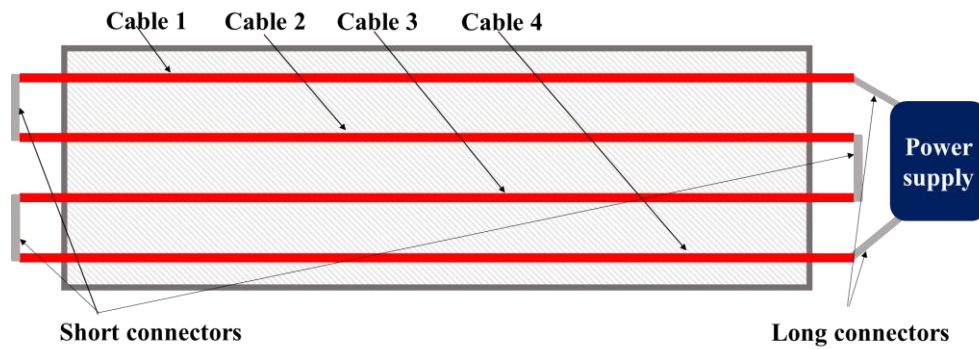


Figure 13. Schematic of experiment platform

The practical experimental setup is depicted in Figure 14. The aluminium chamber, equipped with thermal insulation, is elevated above the ground by four horse trestles to weaken its heat losses transfer to the ground. By raising the chamber above the ground using a horse trestle, direct conductive heat transfer between the chamber and the ground is minimized. The air gap between the chamber and the ground provides a thermal resistance of approximately 21 K/W. As a result, convection becomes the primary mode of heat transfer, which is less efficient than conduction through solid materials. Cable specimens, as illustrated in Figure 8, are carefully arranged and positioned within the chamber. The current transformer is grounded using a copper wire. The connectors, constructed from short or long aluminium bars, are affixed to the cables and the power supply unit through the use of screws.



Figure 14. Practical cables accelerated thermal ageing experiment platform

The current transformer is displayed in Figure 15. It is capable of producing an output voltage of up to 4 V, with an output current reaching 10 kA. The black knob situated atop the current transformer serves the purpose of regulating the output voltage within the range of 0%

to 100%. Positioned in front of the transformer are two meters that display the current output and voltage values. The current output of the current transformer undergoes calibration using an RS ICM 139R multi-tester.



Figure 15. The current transformer as experiment power supply

Under realistic operational conditions, the temperature of a power cable is subject to temporal variations due to fluctuations in power demand throughout both daily and yearly cycles. Moreover, the thermal cycling component also significantly contributes to the cable ageing process. According to IEEE standard 1407 recommendation [109], in the context of this experiment, the temperature of power cables across a 24-hour period is managed through the output of the current transformer. This controlled manipulation is designated as one heating cycle, thereby simulating the temporal temperature fluctuations in practical working circumstances. Each heating cycle is further divided into three distinct phases:

1. a 2-hour heating up phase,
2. a 6-hour high-temperature phase, and
3. a 16-hour cooling down phase.

This methodology encapsulates the comprehensive spectrum of temperature dynamics in the simulation.

The output voltage of the current transformer is graphically depicted in Figure 16 (a). Within this illustration, the maximum temperature on the cable surfaces quickly ascends from 20°C to 100°C by virtue of a comparatively higher voltage during the culmination of the heating up phase. Throughout the high-temperature phase, the maximum temperature on the

cable surfaces is effectively sustained at 100°C through the application of a relatively lower voltage. During the ensuing cooling down phase, the temperature of the cables undergoes reduction to ambient levels, achieved by the cessation of power supply and the removal of voltage from the conductors. The maximum surface temperature of 100°C was selected to ensure that the internal temperature of the cable does not surpass the melting point of the XLPE insulating material. This helps to more accurately simulate the thermal aging mechanism of the cable insulation under normal operating conditions. The setup for temperature monitoring on cables by applying thermocouples will be described in section 3.4.

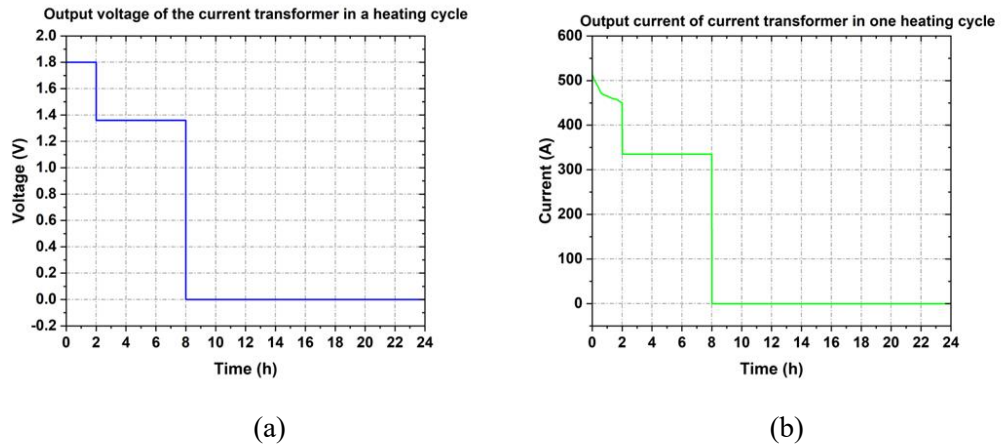


Figure 16. Output (a) voltage and (b) current of current transformer within one ageing cycle

The output current of the current transformer within a single heating cycle is visually represented in Figure 16 (b). During the heating up phase, the current experiences a decline over time while maintaining a constant output voltage. This phenomenon arises from the escalating temperature of the cable conductor in this interval, resulting in an increase in resistance. The output current remains consistent throughout the high-temperature phase, owing to the stable temperature of the cable conductor. This cycle of heating is enacted five days a week, thus forming a recurrent procedure for the thermal ageing of cables.

As detailed in section 2.4, condition monitoring techniques were periodically applied to the cable samples in this experiment to study how their performance changed throughout the thermal aging process. Before conducting measurements on the cables in the chamber, the connecting bars were firstly removed to allow the instruments to be connected to each individual cable sample.

For the IR, PI, and DAR tests, a Megger MIT1025 was utilized at test DC voltage levels of 1kV, 2.5kV, 5kV, 7.5kV, and 10kV. This instrument can measure IR values up to 10kV with a maximum resistance of 20 TΩ and an accuracy of $\pm 5\%$ from 1 MΩ to 2 TΩ, and $\pm 20\%$ from 2 TΩ to 20 TΩ. IR values were taken between the conductor and ground, recorded at 1 minute

and 10 minutes after applying the test voltage. The temperature at the time of testing was also controlled at 20°C. These readings provided direct IR values at two-time intervals, enabling the calculation of the insulation's polarization index. Appendix B includes the connection diagrams for the MIT1025.

For the $\tan\delta$ and capacitance tests, a WGS-4C Automatic Capacitance & Dissipation Factor Test Set was employed, using 50Hz AC voltage intervals similar to those used in the IR tests. This instrument offers capacitance measurement accuracy of $\pm (\text{reading} \times 1\% + 1\text{pF})$ and dissipation factor accuracy of $\pm (\text{reading} \times 1\% + 0.00040)$. The instrument and connection diagrams for the capacitance and $\tan\delta$ measurements are provided in Appendix C.

3.4. Temperature monitoring setup and results

To monitor the temperature distribution along the length of each individual cable as it evolves through heating cycles, temperature sensors are positioned on the cable surfaces. The more detailed information about thermocouple and instrument used for temperature monitoring could be found in Appendix A.

The spatial arrangement of these temperature sensors is shown in Figure 17. There are 20 temperature sensors are affixed to the cable surfaces, each cable accommodating 5 sensors. The assigned temperature sensors are named as the following format: "CableX Y" to clear identification and differentiation of each temperature sensors, where X represents the serial number of the cable, and Y indicates the serial number of the temperature sensor on individual cable.

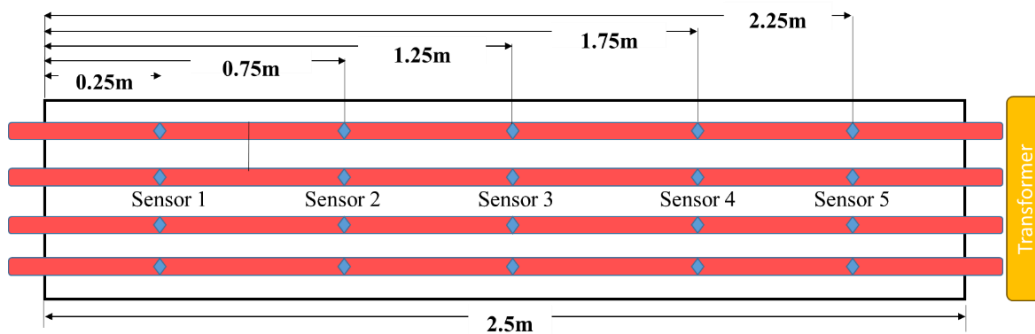


Figure 17. Locations of temperature sensors on the cable surfaces in the chamber

The interior composition of the chamber is depicted in Figure 18. The cables are securely upheld by nylon frames, chosen for their capability to withstand the elevated temperatures within the chamber. On the upper surfaces of the cables, type T thermocouples are affixed. These type T thermocouples are characterized by their operational temperature range spanning from -75°C to +260°C. Type T thermocouples have a class 1 tolerance as stated in IEC standard

60584 [112], with a tolerance of $\pm 0.5^{\circ}\text{C}$ from -40°C to $+125^{\circ}\text{C}$, and $\pm 0.4\%$ of the measured temperature from $+125^{\circ}\text{C}$ to $+260^{\circ}\text{C}$.



Figure 18. Internal arrangement within the chamber

An instance of thermocouples is firmly affixed to the cable surfaces using adhesive, as demonstrated in Figure 19. The selected adhesive possesses thermal conductivity properties, thereby ensuring precise and accurate temperature measurements.



Figure 19. Example of temperature sensor fixed on the cable surface

Three TC-08 thermocouple data loggers, as displayed in Figure 20, are employed to gather temperature data. Each data logger offers 8 input channels, amounting to a cumulative total of 24 channels. Among these, 20 channels are specifically for measuring temperatures on the cable surfaces within the chamber. Out of these, two channels are assigned for gauging the

temperatures of the short connectors on both sides, one channel for one of long connectors temperature, and an additional one for measuring the cable surface temperature external to the chamber. These data loggers are interconnected with a laptop, enabling continuous monitoring and recording of temperature variations.



Figure 20. TC-08 thermocouple data logger

The TC-08 setup operates with a sampling rate of 1 sample per minute, with a Filter factor, which returning to average value of number of collected samples, is set to 6. Consequently, the actual sampling rate equates to 1 sample measurement per 10 seconds. Within each minute, an average value calculated from 6 samples is recorded. This configuration results in the accumulation of 1440 samples throughout a single heating cycle.

Figure 21 illustrates the temperature distribution on different position of each cable surface variation within a single heating cycle. During the initial hour of the heating up phase, all sampled points on each cable surface demonstrate a similar upward trajectory in temperature. However, during the subsequent hour, the temperature escalation rates at location 1 and location 5 are comparatively slow in comparison to the other three locations.

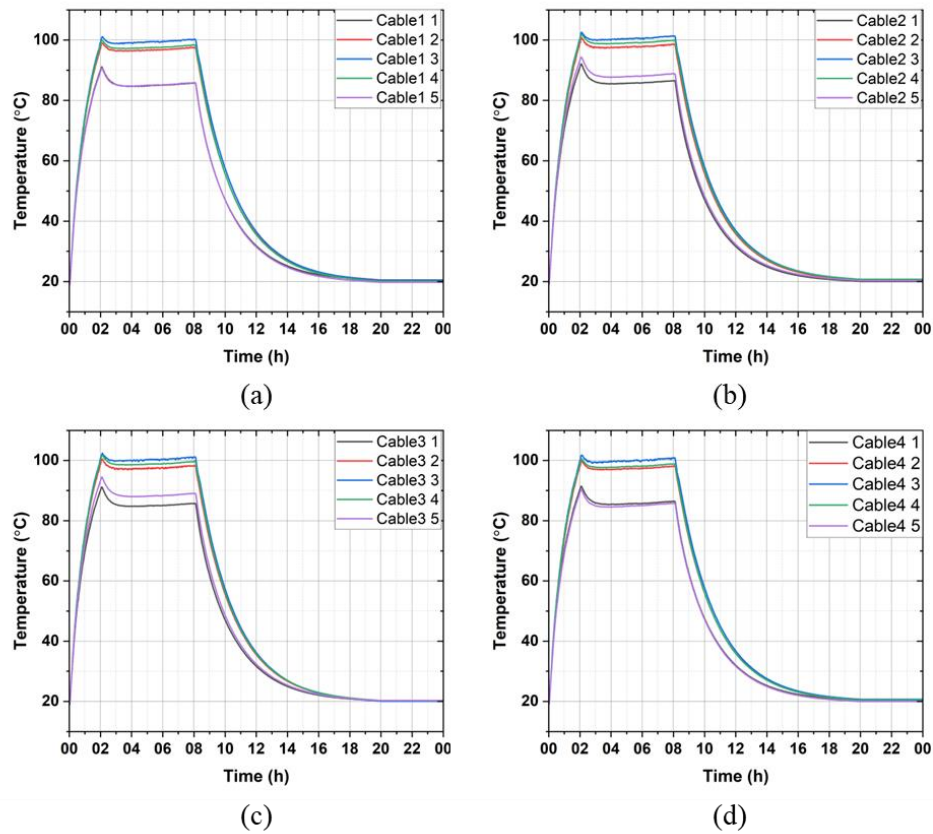


Figure 21. Temperature distribution on cable surface along with cable length for **(a)** Cable1; **(b)** Cable2; **(c)** Cable3 and **(d)** Cable4, variation within one ageing cycle of the experiment

In the high-temperature phase (2-8h), location 3 consistently registers the highest temperature, while for the remaining locations, location 2 and location 4 exhibit considerably higher temperatures than location 1 and location 5. At the start of the high-temperature phase, a brief temperature decrease is observed (obvious on location 1 and 5), attributed to the initial reduction in power supply current. Subsequently, the temperature stabilizes and remains constant as the current diminishes. Once the elapsed time exceeds 8 hours, the power supply is disengaged, initiating the descent of temperature of power cables toward ambient levels.

Additionally, despite the approximate temperature distribution and trends across all cable surfaces, Cable 2 and Cable 3 exhibit higher overall temperatures in comparison to Cable 1 and Cable 4. This disparity arises due to the positioning of Cable 1 and Cable 4 near the two side walls of the chamber. Although the temperature distinction remains minimal during the heating up and cooling down phases, the maximum temperatures (location 3) of Cable 1 and Cable 4 lag behind those of Cable 2 and Cable 3 by approximately 1.5°C within the high-temperature phase.

The temperature distribution on the cable conductor surface, along with the cable length, is observed through the utilization of a dummy cable. This process involves the insertion of thermocouples onto the conductor surface after drilling holes, a depiction of which is rendered in Figure 22. This dummy cable solely serves the purpose of monitoring temperature variations across the cable conductor surface during heating cycles. It is important to note that this dummy cable does not undergo periodic condition monitoring tests as the cable integrity has been diminished due to the inserted hole.



Figure 22. Demonstration of a hole on the dummy cable

At the end stage of this experiment, Cable 2 is replaced with a dummy sample, while the remaining cables are retained within the chamber. The holes on the cable conductor surface, aligned precisely with the sensor placements, mirror the configuration displayed in Figure 23.

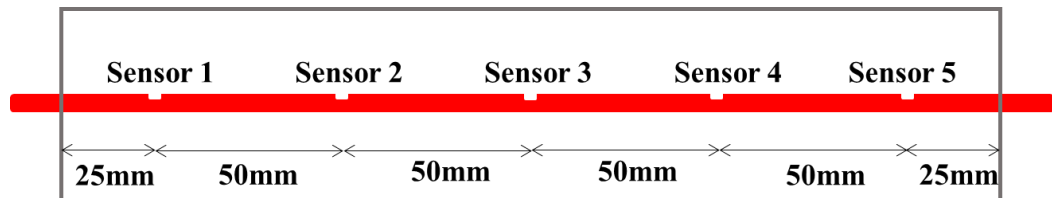


Figure 23. Location of holes on Cable2 for placing thermal sensors

The temperature distribution on the conductor surface of the dummy cable, at different positions in cable length throughout a heating cycle, is illustrated in Figure 24. Notably, the maximum temperature experienced on the cable conductor surface at the end of the heating up phase reaches approximately 110°C. Subsequently, this temperature gradually recedes to around 107°C during the high-temperature phase.

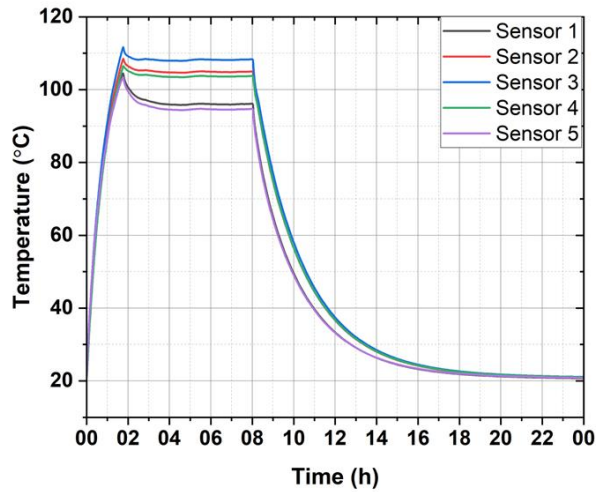


Figure 24. Temperature distribution on the conductor surface of dummy cable along with cable length variation within one ageing cycle

The temperature distribution across connector surfaces, and variation within a single heating cycle, is also subject to measurement and depicted in Figure 25. The long connector (Bar in Figure 25) registers a notably lower temperature in comparison to the short connectors (connector 1&2 in Figure 25). This distinction in temperature arises from the larger surface area of the long connectors that come into contact with the surrounding ambient environment.

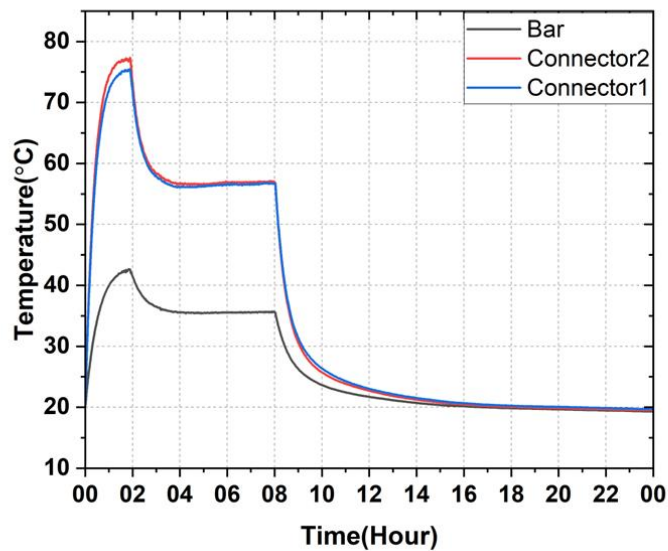


Figure 25. Temperature distribution on connectors' surface within one ageing cycles

3.5. Condition monitoring results

3.5.1. Calculation of equivalent ageing hours

To understand the fluctuations of condition monitoring indicators related to the ageing process of cables within practical operational scenarios, it becomes imperative to compute equivalent hours under normal service temperatures from the ageing cycles conducted in the experiment. For this purpose, the Arrhenius model and Miner's law are commonly invoked, as elaborated upon in section 2.7.

The Arrhenius equation, originally employed in chemical kinetics to forecast the rate of a process, has been extended to thermal degradation equivalent of materials, with the assumption that the activation energy of the material in the tested temperature range is constant and reliable. This extension aids in estimating the Time-To-Failure (TTF) at a given temperature. The Arrhenius model is presented as (9) and could be used for calculating equivalent ageing hour at different ageing temperatures through the following form:

$$\frac{t_1}{t_2} = \exp\left(\frac{E_a}{K_B}\left(\frac{1}{T_1} - \frac{1}{T_2}\right)\right) \quad (13)$$

where, t_1 and t_2 are the time in hours ageing at temperature T_1 and T_2 in K respectively, K_B is the Boltzmann constant (1.38×10^{-23} J/K), and the activation energy E_a is 1.0623×10^{-19} J taken from references[113][114].

Following Miner's law, each heating cycle in this experiment is subdivided into 12 segments in this research. Within each of these segments, the equivalent ageing time, denoted as t_{0-i} (where i ranges from 1 to 12), is computed utilizing the Arrhenius equation. Table 6 shows the equivalent ageing times for each section, specifically considering a normal working temperature of 50°C.

Table 6. Equivalent ageing time for one heating cycle in the experiment

Section No.	Time (h)	Average Temperature (°C)	Equivalent working time t_{0-i} (h) at normal working temperature
1	0-2	70	2 x 8.015=16.03
2	2-4	100	2 x 119.71=239.42
3	4-6	100	2 x 119.71=239.42
4	6-8	100	2 x 119.71=239.42
5	8-10	80	2 x 20.77=41.54
6	10-12	45	2 x 0.32=0.64
7	12-14	30	2 x 0.095=0.19
8-12	14-24	20	10 x 0.026=0.26

The cumulative summation of all these individual section ageing times yields the total

equivalent hours experienced at 50°C during one heating cycle could be calculated by (14). The total equivalent ageing hours t_0 at 50°C for one ageing cycle is yield as (15):

$$t_0 = \sum_{i=1}^{i=12} t_{0-i} \quad (14)$$

$$t_0 = 776.92h = 32.37\text{days} \approx 0.08869\text{year} \quad (15)$$

Table 7 presents equivalent ageing time at normal working temperature corresponding to different accelerated ageing cycles. Given that the design lifetime of a MV power cable can be 30 to 40 years, this artificial accelerated thermal aging experiment has brought the cables close to the lower end of their expected lifespan, yet no failures have occurred.

Table 7. Equivalent ageing time for the experiment

Accelerated ageing cycles number	Equivalent working time (h)	Equivalent working time (year)
50	38846	4.43
100	77692	8.87
150	116538	13.3
200	155384	17.73
250	194230	22.17
300	233076	26.607

3.5.2. IR tests results

The IR measurement results of power cables under different testing voltage levels along thermal ageing process are presented and compared in this section. The instrument used for IR, PI and DAR tests as well as the connection diagrams are displayed in Appendix B for reference. This instrument can measure IR values up to 10kV, with a maximum resistance of 20 TΩ and an accuracy of ±5% for measurements ranging from 1 MΩ to 2 TΩ, and ±20% for measurements between 2 TΩ and 20 TΩ.

Before conducting measurements on the cables in the chamber, the connecting bars were removed to ensure the cables were de-energized and to allow instruments to be connected to each individual cable sample. After selecting the measurement modes and voltage levels, the positive lead was connected to the conductor of the cable sample, while the negative lead was attached to the metal shield. IR values were then measured between the conductor and ground, and recorded at both 1 minute and 10 minutes after the test voltage was applied. Since the cable samples have a rated voltage of 6.35/11kV, the testing DC voltage levels were chosen to be 1kV, 2.5kV, 5kV, 7.5kV, and 10kV to determine the IR variations. The temperature during testing was also controlled at 20°C. When subjected to a testing voltage of 5 kV, the variations in IR1 for each power cable, synchronized with the ageing cycles, are described in Figure 26. Error bars of data points are visualized throughout in Figure 26 by calculating the standard

deviation of 5 samples at every measurement to reflect fluctuations in data points. The developmental trends of IR1 are found to be non-constant throughout the ageing process, characterized by distinctive stages observable in the figures.

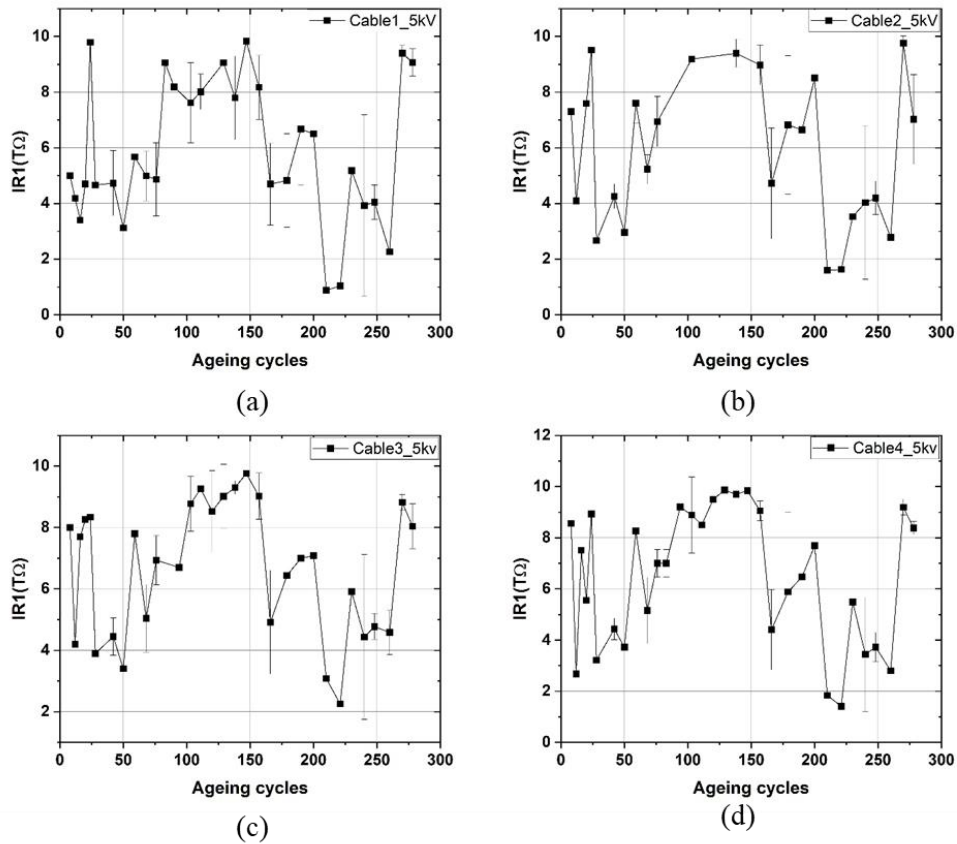


Figure 26. Variation of the IR1 measured at 5 kV versus ageing cycles for (a) cable1; (b) cable2; (c) cable3 and (d) cable4

During the initial 50 ageing cycles, the IR1 values exhibit obvious fluctuations, expressing a pattern of fluctuating curves that alternate between descending and ascending trends. Following this initial phase, the IR1 values commence a raise trend with the progression of ageing cycles, reaching in peak values at approximately 150 ageing cycles. Subsequently, a decrease in IR1 values occurs after the 150 ageing cycle, reaching their minimum at around 220 ageing cycles. Thereafter, a resurgence in IR1 values occurs after the 220 ageing cycles, signifying a renewed upward trend.

The resulting IR1 measurement outcomes at 7.5 kV for each power cable, along with ageing cycles, are represented in Figure 27. Given the Megger instrument's current range of 0.01 nA to 6 mA, applying higher voltage to the cable conductor increases the current flow through the insulation layers. Consequently, certain IR values that could not be measured at 5kV were successfully obtained at 7.5kV. Therefore, the datasets under the 7.5 kV testing

voltage each consist of a greater number of data points. During the initial 50 ageing cycles, the IR1 values exhibit a downward trend with oscillations, unlike the pattern observed under the 5 kV testing voltage, which is a remarkable absence of the distinct down-up-down variation. Post the first 50 ageing cycles, the variation trends in IR1 under 7.5 kV are similar to those identified under 5 kV.

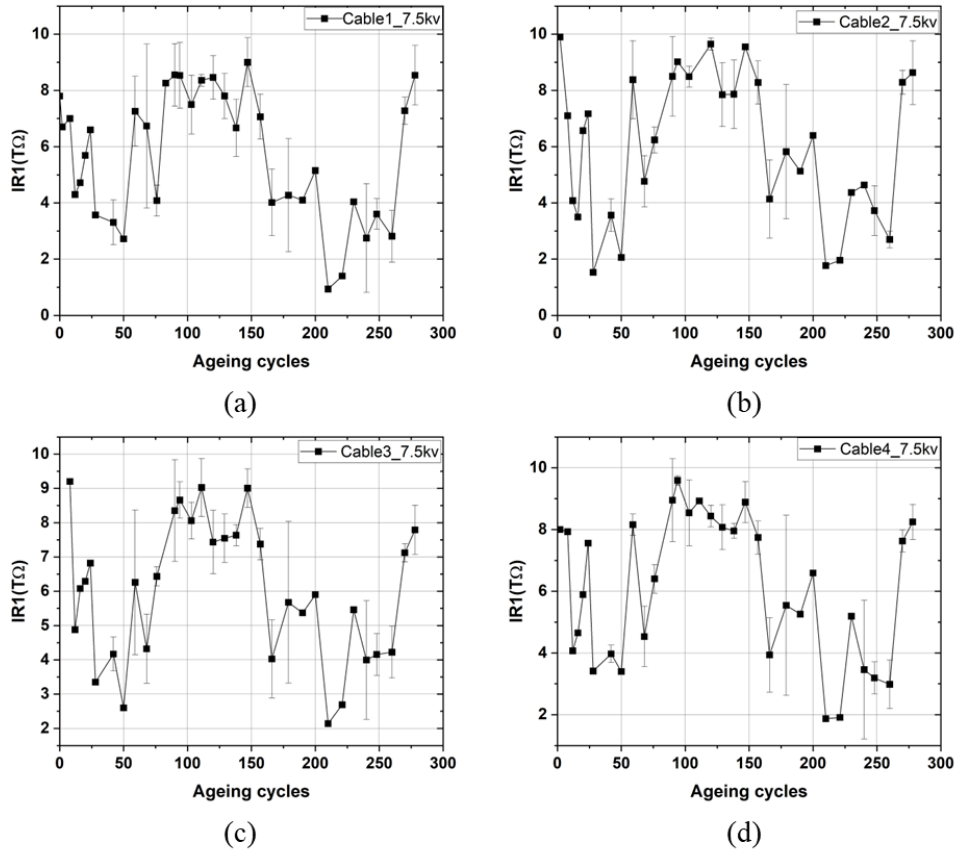


Figure 27. Variation of the IR1 measured at 7.5 kV versus ageing cycles for each cable sample

The variations in IR1 for each power cable, subject to a testing voltage of 10 kV, are shown in Figure 28. In the initial 50 ageing cycles, there is an obvious decline in IR1 values from their initial values. The occurrence of peak IR1 values under the 10 kV testing voltage transpires earlier than in the preceding two scenarios (5kV and 7.5kV). For Cable 1 and Cable 4, their respective IR1 values reach their peaks at approximately 9.3 TΩ and 10 TΩ after approximately 80 ageing cycles. Cable 2 and Cable 3 attain their peak IR1 values at 10.5 TΩ and 9.2 TΩ after approximately 110 ageing cycles. The minimum of IR1 values for all four cables surfaces at 210 ageing cycles, aligning with the time frame observed under the 7.5 kV testing voltage. An upward trajectory characterizes the IR1 plots after 210 ageing cycles.

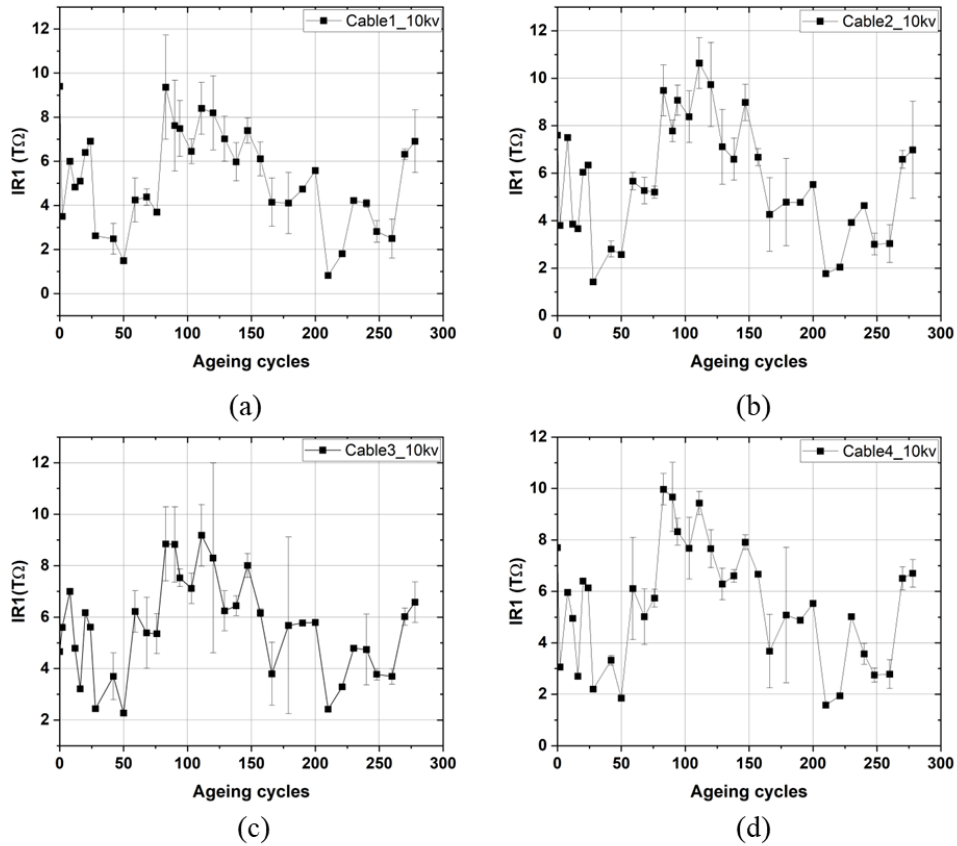


Figure 28. Variation of the IR1 measured at 10 kV versus ageing cycles for each cable sample

In Figure 29, the changes in IR10 for each power cable under a 10 kV testing voltage are visually represented. The description of IR10 variations under the 5 kV and 7.5 kV testing voltages is omitted due to the shortage of available IR10 data, a result of the capable of current measurement range limitations inherent in the Megger instrument range at these voltage levels. It is evident that IR10 values are significantly higher than IR1 values. This difference arises because measured current only includes resistive leakage currents that persist after the application of a DC voltage on the cable conductors for a duration of 10 minutes.

Similarly, the IR10 values of the cables exhibit a decline within the initial 50 ageing cycles. The lowest value of Cable 3's IR10 value is recorded at 5.1 TΩ at the 50 ageing cycles. For Cable 1 and Cable 4, their respective IR10 values reach their maximum values at around 19.5 TΩ and 19 TΩ after approximately 110 ageing cycles. Cable 2 and Cable 3 attain their peak IR10 values, also at 19.5 TΩ and 19 TΩ, but at 150 ageing cycles. After reaching these peak values, the IR10 values of all four cables initiate a subsequent decline. After 210 ageing cycles, the lowest IR10 values are observed for Cable 1, Cable 2, and Cable 4, measuring 1.5 TΩ, 3.28 TΩ, and 2.55 TΩ, respectively.

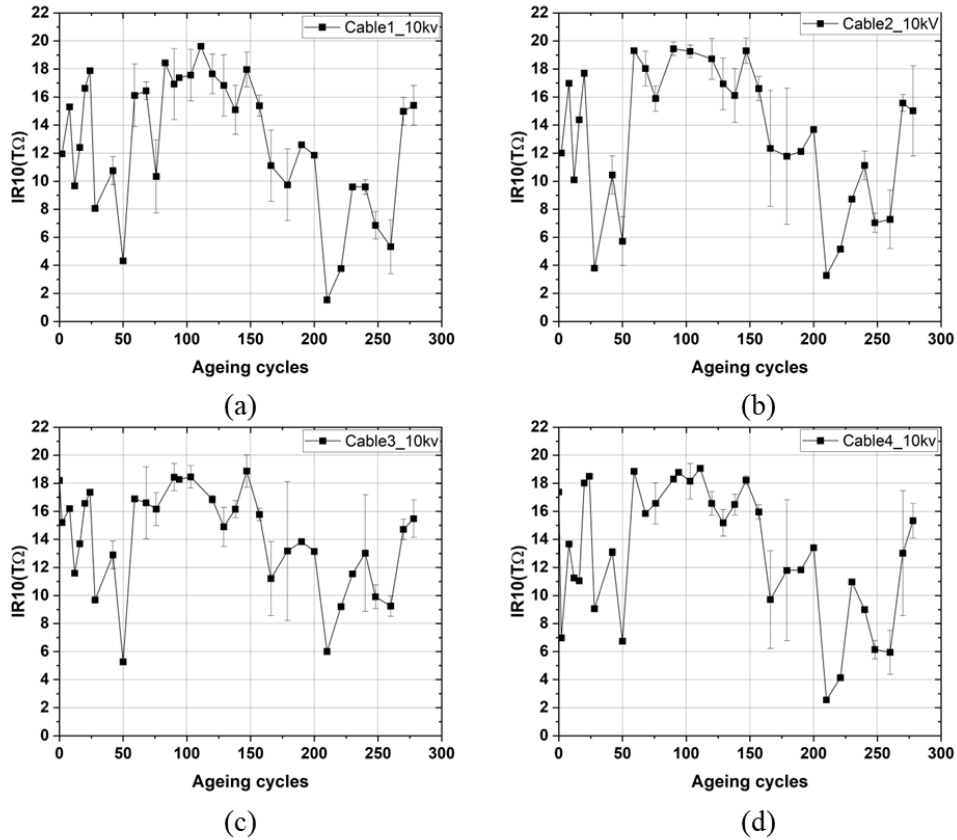


Figure 29. Variation of the IR10 measured at 10 kV versus ageing cycles for each cable sample

Additionally, it is observed that the IR1 and IR10 curves exhibit varying rates of change. As explained in Chapter 2, during IR testing of power cables, the current passing through the cable insulation comprises several distinct components. The magnitudes of these current components evolve over the duration of the applied testing voltage. At 10 minutes, leakage current constitutes the primary component of the measured current, whereas at 1 minute, the measured current encompasses both polarization and leakage currents. This dissimilarity in the rates of change between IR1 and IR10 contributes to the fluctuations observed in PI, which will be expounded upon in the subsequent discussion.

3.5.3. DAR tests results

The progression of DAR values under 5kV testing voltage for each power cable, corresponding to ageing cycles, is illustrated in Figure 30. The initial DAR values for Cable 1, Cable 2, and Cable 4 hover around 1.4, while Cable 3 commences with a DAR of 1.6. Subsequently, at approximately 30 ageing cycles, the DAR values for Cable 1, Cable 2, Cable 3, and Cable 4 reach their respective peak values of 3.1, 2.3, 2.9, and 2.7. During the interval of 30 to 50 ageing cycles, an obvious decline in DAR values is evident. Post 50 ageing cycle

mark, the DAR values exhibit slight fluctuations within narrow ranges around 1.6.

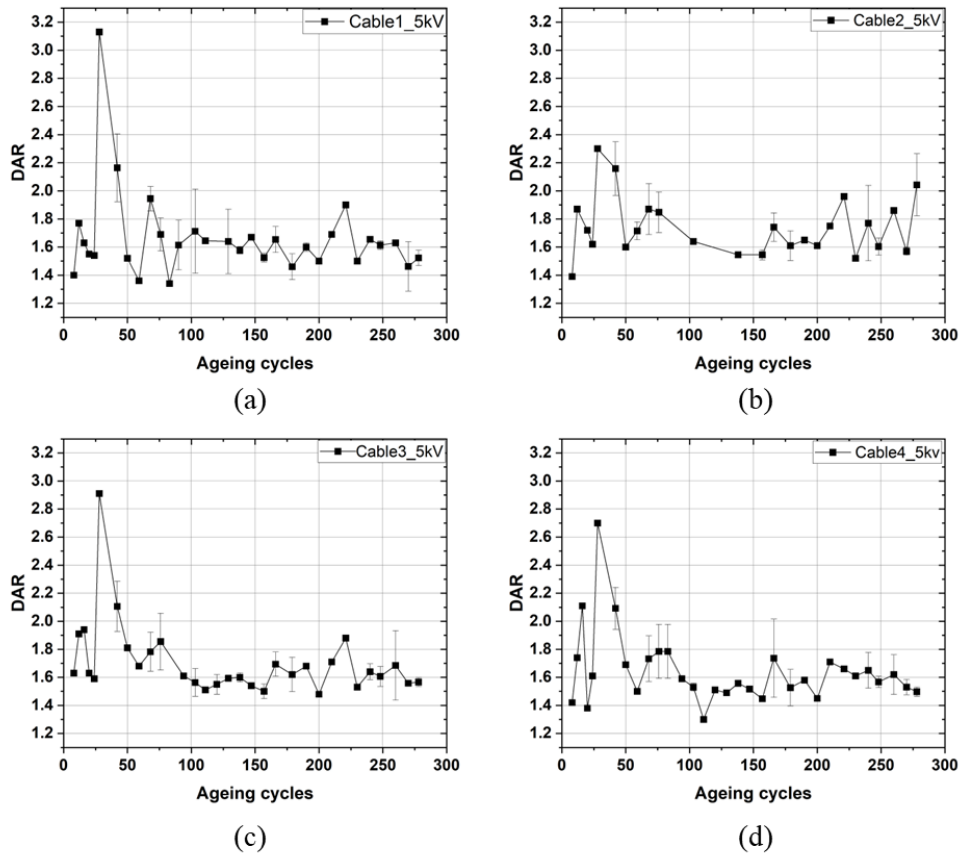


Figure 30. Variation of the DAR measured at 5 kV versus ageing cycles for each cable sample

The fluctuations in DAR values for the four power cables under the 7.5 kV test voltage are depicted in Figure 31. Significantly more data points are acquired under the 7.5 kV conditions. The trends in DAR variations mirror those observed under the 5 kV conditions: an initial rise in the first 30 ageing cycles, a subsequent decline from 30 to 50 ageing cycles, and eventual stabilization post the 50 ageing cycle threshold.

Furthermore, it is evident from the figure that the magnitude of DAR undulation is smaller for Cable 1, Cable 2, and Cable 4 compared to Cable 3. Additionally, the peak DAR values for Cable 1 through Cable 4 decrease to 2.35, 2.25, 2.9, and 2.45, respectively.

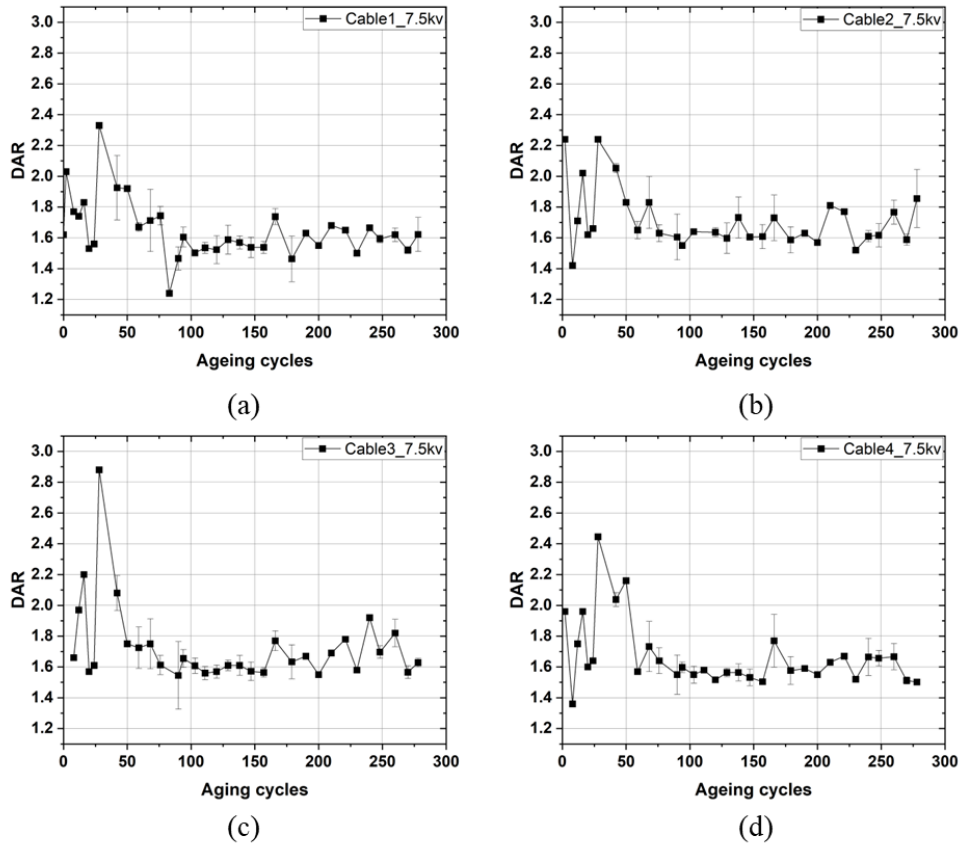


Figure 31. Variation of the DAR measured at 10 kV versus ageing cycles for each cable sample

Figure 32 graphically illustrates the alteration in DAR values for the four cables across ageing cycles, derived from the 10 kV testing voltage. Remarkable, the peak DAR values for Cable 1 and Cable 2 experience reductions with the testing voltage increase, reaching 2.2 and 2.1, respectively. Conversely, the peak values for Cable 3 and Cable 4 remain unchanged. As for the stable phase of DAR (post 50 ageing cycles), all cables exhibit fluctuations that cluster around 1.6.

Throughout the thermal ageing process of power cables, the peak DAR values are subject to the influence of varying test voltage levels. However, following a specific ageing duration, the consistent ranges of DAR variation exhibit only marginal alterations across different test voltage levels.

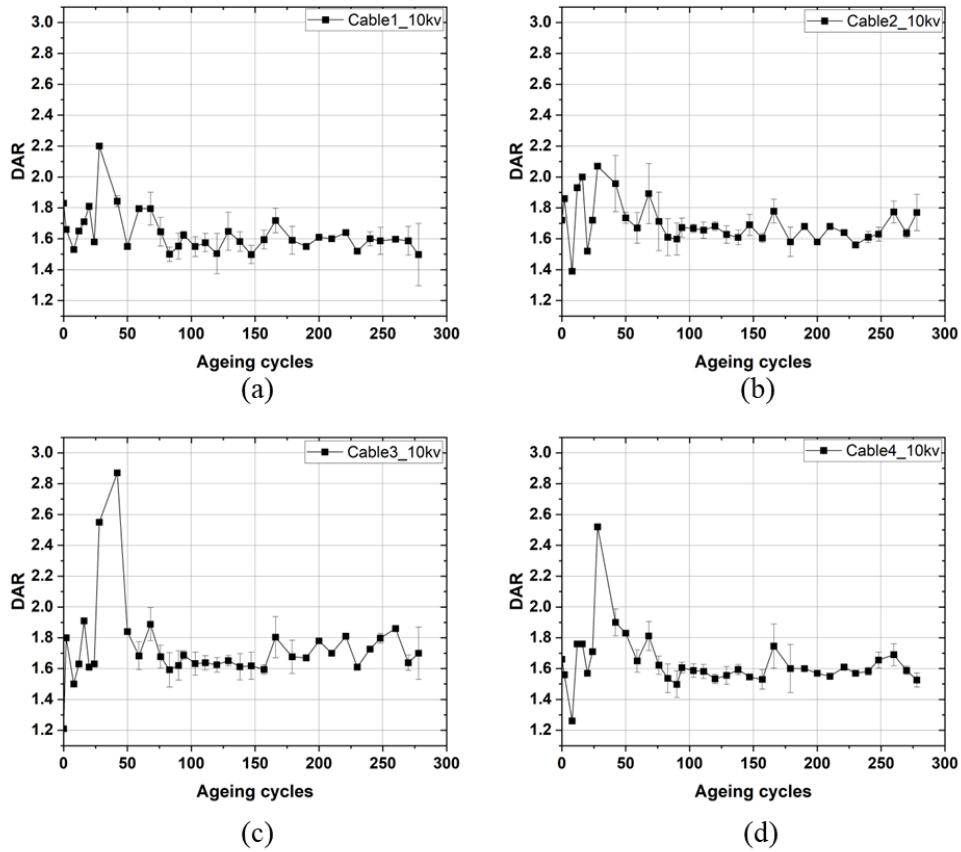


Figure 32. Variation of the DAR measured at 10 kV versus ageing cycles for each cable sample

3.5.4. PI tests results

Figure 33 presents a comprehensive comparison of the PI values for each cable measured at 10 kV, tracing their variation throughout the thermal ageing process. The overall trend is characterized by a gradual decrease in PI values; However, this general trajectory can be subdivided into three-time durations. Commencing from the initial baseline values, the first part involves a decline in PI over the initial 20 ageing cycles, followed by a subsequent upward trend until approximately 40 ageing cycles. The durations of the first two phases are notably shorter in comparison to the third part. Subsequent to the 40 ageing cycles mark, PI values for the cables undergo a gradual reduction in tandem with the ageing process.

It is important to note that the variations in PI values do not monotonously decrease or increase even within each individual phase. Rather, certain levels of volatility persist during these time durations.

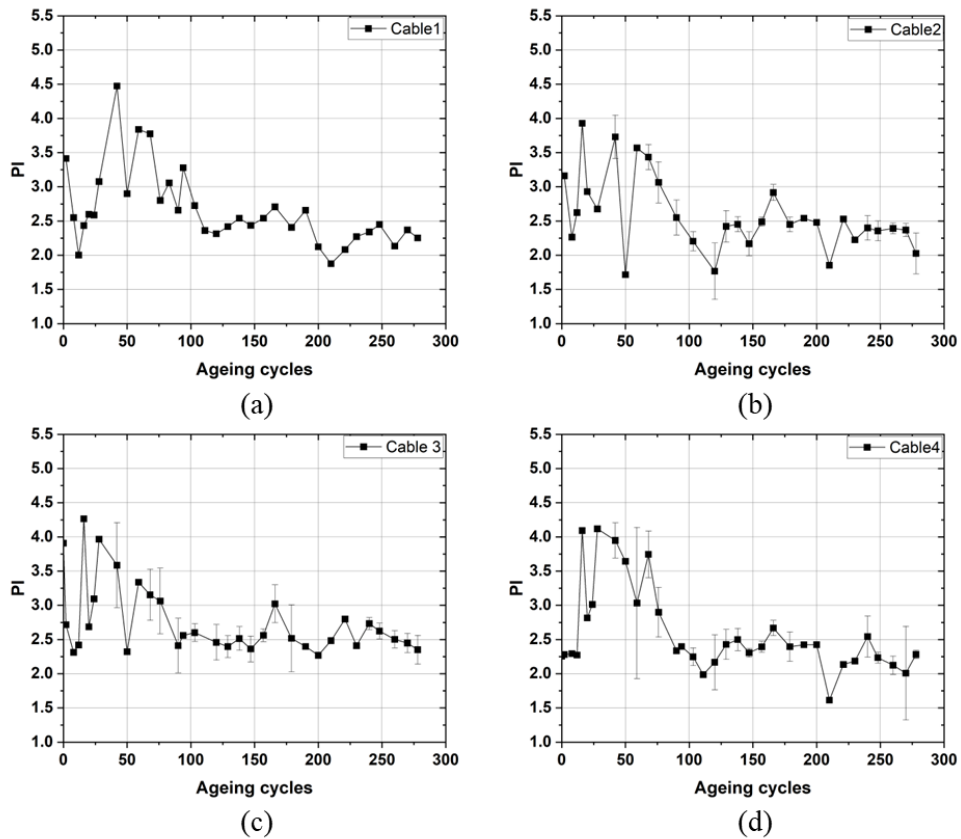


Figure 33. Variation of the PI measured at 10 kV versus ageing cycles for each cable sample

3.5.5. Capacitance and $\tan\delta$ tests results

The instrument and connection diagram for capacitance and $\tan\delta$ measurements are presented in Appendix C for reference. The data depicted in Figure 34 represent the measured capacitance variations of each cable throughout the thermal ageing cycles. In range of testing voltages (1kV to 10kV) at 50 Hz, there is no difference was shown on measured capacitance. Across the entirety of the ageing process, the capacitance values of Cable 2 consistently surpass those of Cable 1. Conversely, the capacitance of Cable 3 is akin to that of Cable 4, with both being marginally smaller than Cable 1's capacitance.

Throughout the ageing process, the capacitance values of all cables exhibit a very slight decline from their initial phase values to their final states. It was found that the capacitance of Cable 1 remains at approximately 1.027 nF, Cable 2 at around 1.044 nF, Cable 3 at around 1.021 nF, and Cable 4 at around 1.019 nF.

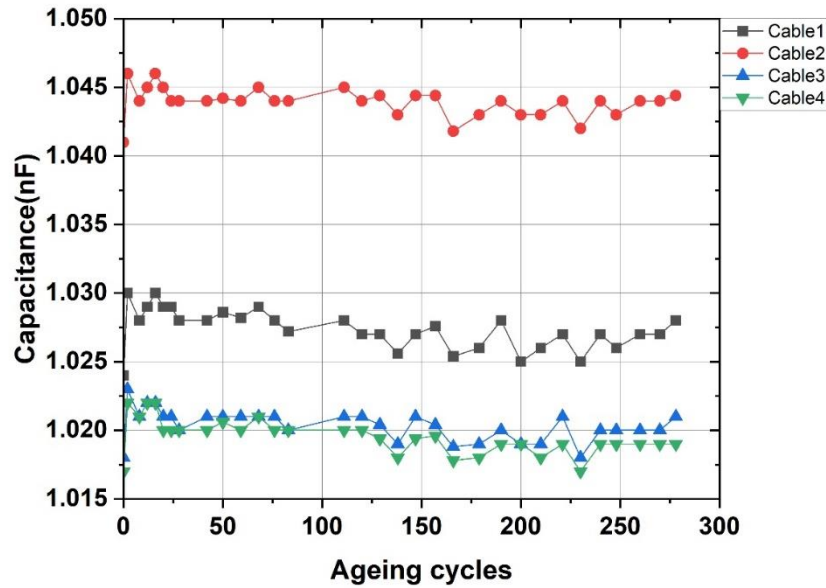


Figure 34. Variation of cable capacitances during thermal ageing process

The outcomes illustrated in Figure 35 delineate the variation of $\tan\delta$ for cables, as measured at different testing voltage levels at 50Hz, across ageing cycles. The $\tan\delta$ curves for cables can also be divided into three distinct phases. Over the initial 150 ageing cycles, the $\tan\delta$ values of cables under diverse testing voltages exhibit a general downtrend. Given that the observed capacitance remains within a consistent range, the variations in $\tan\delta$ values for the cable are primarily influenced by resistive current. Hence, the variation of $\tan\delta$ is correlated to IR values. The initial decrease in $\tan\delta$, as opposed to the initial increase in IR values, is logically coherent. This observation aligns with the expected behaviour based on the underlying electrical properties of the cable. Subsequently, there is a rise in the $\tan\delta$ values between 150 and 200 ageing cycles. Following this, there is another drop in the $\tan\delta$ curves after the 200 ageing cycles. It could be observed from Figure 33 that testing voltage levels have impact on measured $\tan\delta$ value: a higher $\tan\delta$ value could be obtained at with the increase of testing voltage levels.

It should be noted that the tape preventing water ingress of Cable 3 failed at around 220 aging cycles, allowing environmental moisture to penetrate the insulation. This likely resulted in the sharp increase in the $\tan\delta$ value for Cable 3 at that point. After the tape was repaired, the $\tan\delta$ value returned to the normal range.

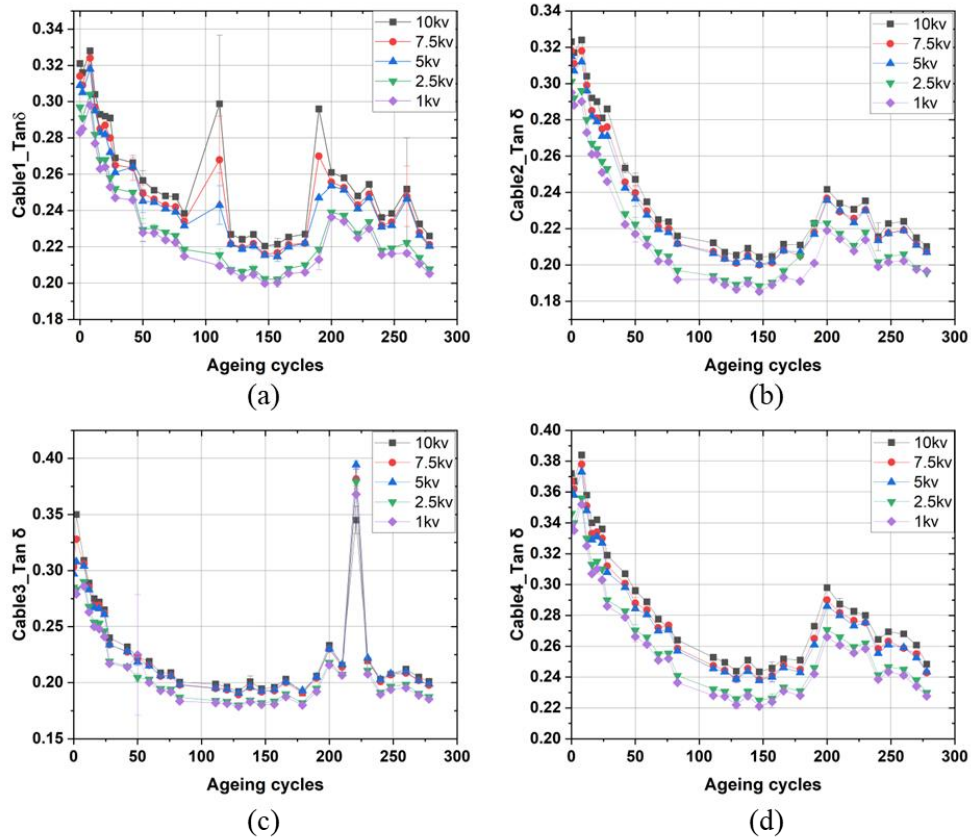


Figure 35. Variations of $\tan\delta$ for (a) Cable1; (b) Cable2; (c) Cable3 and (d) Cable4 versus ageing cycles at different testing voltage levels

3.6. Discussion

3.6.1. Influence of environmental relative humidity

The IR1 values, observed at different testing voltage levels throughout the thermal ageing process, do not exhibit a consistent downward trend. Instead, there are periods characterized by a decrease followed by upward trends. These fluctuation patterns are also evident in both IR10 values and $\tan\delta$. To delve into the underlying causes of these variations, which are likely not attributed purely to thermal ageing, this section delves into the influence of environmental RH on IR and $\tan\delta$ values.

Figure 36 shows the average RH values during the time frame of 9:00 to 17:00 in Glasgow (the city conducting the experiment) during all tests' date across this experiment process. Around the 210th ageing cycle, a period characterized by elevated RH corresponds to lower measured IR values in the cables. Conversely, at approximately the 150th ageing cycle, a period marked by lower relative humidity aligns with higher measured IR values in the cables. However, it's noteworthy that other turning points in the trends of IR values do not align with the turning points in RH values.

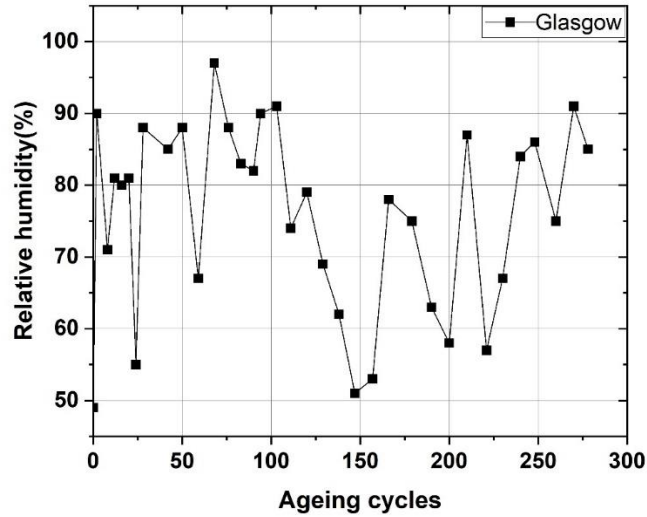


Figure 36. Relative Humidity variation in Glasgow

In this study, it is observed that IR1 and IR10 values of each cable shows a relatively more noticeable correlation with RH compared to other variables. As per (5), the $\tan\delta$ value can be expressed as the ratio of resistive current to capacitance current. Given that the capacitance of the cables remains relatively constant, the capacitance current also remains stable. In such a scenario, any increase in resistive current would generally result in a proportionate increase in the measured $\tan\delta$ value. Additionally, the turning points in the variations of $\tan\delta$ values are evident at approximately 150 and around 200 ageing cycles during testing.

In contrast to IR measurements, both PI and DAR exhibit a greater degree of independence from environmental RH variation. This distinction arises due to the measurement procedures of PI and DAR. Since PI and DAR are ratios derived from timed IR measurements, the effects of transient factors like variations of temperature and environmental RH tend to cancel out to some degree. The critical assumption here is that the moisture content within the cable insulation remains constant during the relatively short duration of the measurement. Therefore, even if RH fluctuates slightly, its influence on the PI and DAR is minimized compared to its impact on raw IR readings. Consequently, the alterations in PI and DAR values are more closely associated with the extent of ageing rather than changes in RH levels.

The correlation coefficients between the testing results of IR1, IR10, PI, and $\tan\delta$ for each cable sample and all RH values on the measurement dates have been calculated, although the specific values are not presented. This is because the correlation coefficients did not

demonstrate strong correlations that could be collected from the results. A more comprehensive explanation of the correlation coefficients will be provided in section 3.6.4 to elucidate the relationships among the testing results.

It is important to note that the RH values shown in Figure 34 are sourced from Glasgow's city weather records. These values only partially reflect the humidity conditions during testing and do not represent the actual humidity levels measured in the laboratory. This discrepancy limits the accuracy of the analysis regarding the impact of humidity on the measurement results. As additional RH data would be gathered in the future through real-time measurements at the experimental location, the correlation coefficients between variables and RH may differ from the current findings. Furthermore, the impact of time length exposure to high humidity on the moisture content within the cable insulation should be paid attention. Moreover, the depth of moisture infiltration into the cable insulation is also likely to enhanced by the long-term of cable exposure to humid conditions.

3.6.2. Fitting PI variation curves

Figure 35 presents the results of a three-phase fitting for the PI variation of each power cable carried out by Origin, the start and end points of each phase are marked on figures. In phase 1 and phase 2, linear fittings equation as (16) are applied to the experimental data points.

$$y = a \times x + b \quad (16)$$

where, a is slope and b is intercept of fitting lines. Table 8 presents the fitting parameters of phase1 and phase2 for the PI variation of each power cable. In these linear fitting results, statistical parameters, including "Residual Sum of Squares (RSS)", " Pearson Correlation Coefficient (R)" and "R-square (COD)", are measures used to evaluate the quality of the fit and the strength of the relationship between variables.

The Residual Sum of Squares (RSS) measures the total deviation of the observed data points from the values predicted by the linear model. It is calculated by summing the squares of the residuals, which are the differences between the observed values and the predicted values. A smaller RSS indicates a better fit, as it means the model's predictions are closer to the actual data points.

The Pearson correlation coefficient (R) stands as a fundamental statistical measure widely employed to quantify the strength and direction of a linear relationship between two continuous variables. Its value serves as a numeric indicator of the degree to which two variables are linearly associated, thereby enabling researchers to assess the extent of dependency between them. The Pearson correlation coefficient offers a numerical measure

ranging from -1 to +1. A value of -1 signifies a perfect negative linear relationship, +1 indicates a perfect positive linear relationship, and 0 denotes no linear relationship. Additionally, R values falling between 0 and 0.2 indicate no or very weak correlation, while values between ± 0.2 and 0.4 suggest a weak correlation. Values ranging from ± 0.4 to 0.6 indicate a moderate correlation, ± 0.6 to 0.8 point to a strong correlation, and ± 0.8 to 1 indicate a very strong correlation.

R-square (Coefficient of Determination, COD) measures the proportion of the variance in the dependent variable that is explained by the independent variable(s) in the model. It is the square of Pearson's R in the case of simple linear regression. A higher R-square value indicates a better fit of the model to the data, meaning that a larger proportion of the variability in the dependent variable is accounted for by the model.

Table 8. Fitting parameters of PI variations for each cable in phase 1 and phase 2

Samples	Phase	Slope	Intercept	RSS	R	COD
Cable1	1	-0.14	3.69	1.89×10^{-4}	-0.9999	0.9998
	2	0.08	0.98	0.17	0.9769	0.9544
Cable2	1	-0.06	3.13	0.22	-0.6835	0.4671
	2	0.02	2.78	1.33	0.33	0.11
Cable3	1	-0.17	3.54	0.39	-0.85	0.72
	2	0.06	2	2.27	0.57	0.32
Cable4	1	0.004	2.27	1.34×10^{-4}	0.9	0.8
	2	0.07	1.81	1.99	0.65	0.42

Phase 1, represented by a dashed line in the figure, shows a negative slope for Cable 1 Cable 2 and Cable 3, indicating a linear decrease in PI with thermal ageing cycles. Phase 1 linear fitting result of Cable 4's PI with a very small positive slope which is different from other three cables. This is possible as a result of the crosslinking by-products in the Cable4 XLPE insulation is lower than other cables, due to degassing of Cable 4 XLPE insulation during the manufacturing process is better than other three cables and some other possibilities. It worth noting that all four cable samples were supplied by the same manufacturer. It is not known if they all came from the same reel. It may be that in this research that the sample was taken from a different reel or at the end of a different reel and may have undergone a different degree of degassing. However, this is just a hypothesis, and the actual reasons could be more complex.

Phase 2 depicted as dotted lines, demonstrates a positive slope for all cables, signifying an increasing trend in PI until the end of this phase. The third phase, denoted by a chain line, employs an exponential decrease fitting as (17) presented. Notably, the rate of PI decrease in Phase 3 is generally lower as the thermal ageing time progresses, a distinct pattern of

exponential decrease in PI is evident, starting from a peak value. This behaviour can be attributed to the effects of thermal ageing on the XLPE insulation, leading to a systematic decrease in PI values and a variation in the rate of decrease as ageing time progresses.

$$y = A_1 e^{\left(\frac{-x}{t_1}\right)} + y_0 \quad (17)$$

Table 9 presents the fitting parameters of phase 3 for the PI variation of each power cable. Statistical parameters Reduced Chi-Sqr and COD are used to assess the goodness of fitting. Reduced Chi-Sqr helps to determine whether the model appropriately represents the data by considering both the residuals and the uncertainties in the observations. A reduced Chi-Square value near 1 generally indicates a good fit, while significant deviations from 1 suggest potential issues with the model or the data.

Table 9. Fitting parameters of PI variations for each cable in phase 3

Sample	y_0	A_1	t_1	Reduced Chi-Sqr	R-Square (COD)
Cable1	2.25	4.69	44.88	0.1	0.74
Cable2	2.33	32.16	18.82	0.08	0.65
Cable3	2.55	3.94	27.38	0.07	0.62
Cable4	2.19	4.34	40.75	0.09	0.79

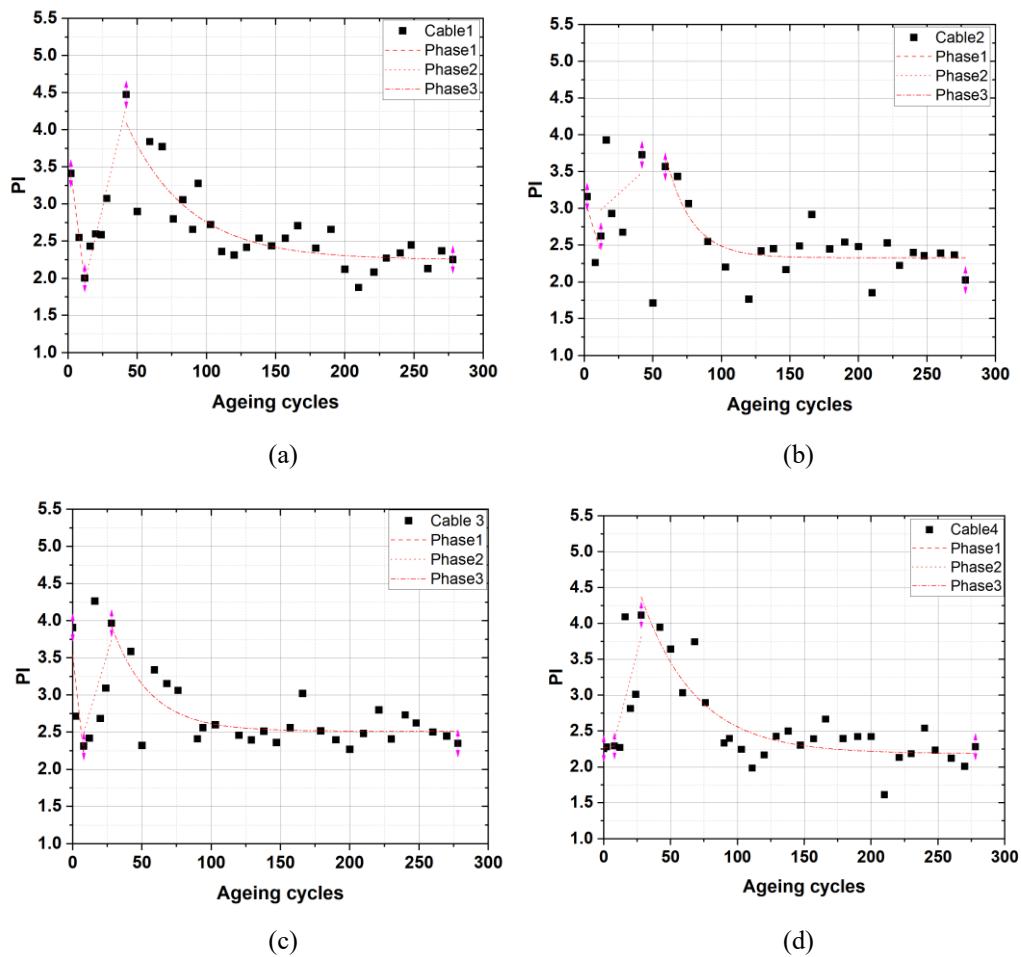


Figure 37. Fitting of PI variation for each power cable(start and end points of each phase are identified by the purple arrows)

The statistical parameters in the Tables 8 and 9 reveal that while the errors of each fitting curves are different with each other, the overall trend and variation at each stage remain consistent. This phenomenon may potentially be attributed to the ageing mechanisms of cable samples being consistent, but there exists a certain degree of difference in the generation and volatilization of crosslinking by-products within the XLPE insulation. The later factor may play a significant role in causing the observed decrease in PI during phase 1 and the subsequent increase in phase 2 [84].

According to the criteria of PI provided by IEEE standard 43 [62], a PI value between 1 and 2 indicates health condition of insulation is questionable, warranting close monitoring and more frequent testing to track any further deterioration. A PI value smaller than 1 means health condition of insulation is poor, and the cable should be considered for immediate replacement or decommissioning. Despite the PI value is still above the critical value within the current

thermal ageing cycles, the fitting curves in phase 3 of PI could be used to estimate the failure point of power cable, thus assists the cable system manager in maintaining the cable. Due to the PI data available for fitting Phase 3 of each cable is not sufficient, the current fitting curve suggests that the PI value remains above 2 even after 1,000 ageing cycles. Therefore, further investigation into the variation of PI as the ageing cycle progresses is necessary to optimize the fitting curve for more accurate state prediction. The ongoing nature of the thermal ageing experiment on MV power cables is expected to yield additional data in the future, enabling further investigation into the PI variation trends under these conditions.

3.6.3. Annealing effect

Nath et al. applied the band theory to analyse current-voltage (I-V) characteristics of LPDE. They developed a mathematical model centred on carrier hopping within amorphous regions [115]. Recent studies, building on this theory, have concurred that electronic transport primarily involves thermally activated hopping, which is facilitated by a low activation energy due to an electric field [116].

Moreover, Diego et al. conducted conductivity measurements on XLPE cable samples using the Absorption Resorption Current method (ARC) [117]. Their findings indicated that the conductivity of XLPE cables is significantly affected by the thermal treatment of the samples in the presence of the cable's semiconducting shields (SC). This process is based on a hopping mechanism.

In the context of the annealing process, infrared spectroscopy observations have indicated that certain chemical particles originating from semi-conductor layers diffuse into the XLPE insulation layer. The process of carrier hopping is enhanced by the diffusion of components from semiconducting shields and other by-products generated during the cross-linking process, as this leads to the formation of internal charges and trapping centres [118].

Additionally, the analysis of thermally stimulated depolarization and intensity-current measurements reveals that the importance of this diffusion process diminishes as the annealing time progresses beyond the point of maximum conductivity. It is a widely recognized fact that crosslinking by-products tend to dissipate over extended annealing periods due to their volatile nature. However, while the presence and dissipation of crosslinking by-products do play a role, they are not the primary factor behind the subsequent decrease in conductivity observed in XLPE cable insulation following an initial increase. Instead, it is the reduction in the diffusion of components from the semi-conductor shields into the XLPE insulation that contributes to the observed decrease in conductivity [118].

In summary, the process of diffusion from the semi-conductor shields leads to an increase in trap density within the cable insulation. This initial increase in trap density contributes to the rise in conductivity in XLPE insulation. Nevertheless, as annealing time extends, the diffusion rate gradually decreases, resulting in a subsequent decrease in conductivity over longer periods.

Figure 38 (a) illustrates the insulation conductivity (σ) in (S/m) of XLPE cable samples, as measured in [118], during heating at 90°C over various duration. The characteristic hump shape in σ is primarily attributed to the accumulation and subsequent depletion of chemical species diffused from the semi-conductor layers, which augment hopping conduction. By fitting a function of the gamma distribution (Γ) to the σ measurements, the variation of σ with time (t) at 90°C, influence by the combined effects of annealing and thermal ageing, is approximated by (18), as described in Figure 38 (a).

$$\sigma(t, 90^\circ\text{C}) = 9.31 \cdot 10^{-15} + 3.26 \cdot 10^{-13} \cdot \Gamma\left(\frac{t+20.55}{1.179}; 13.65, 3.17\right) \quad (18)$$

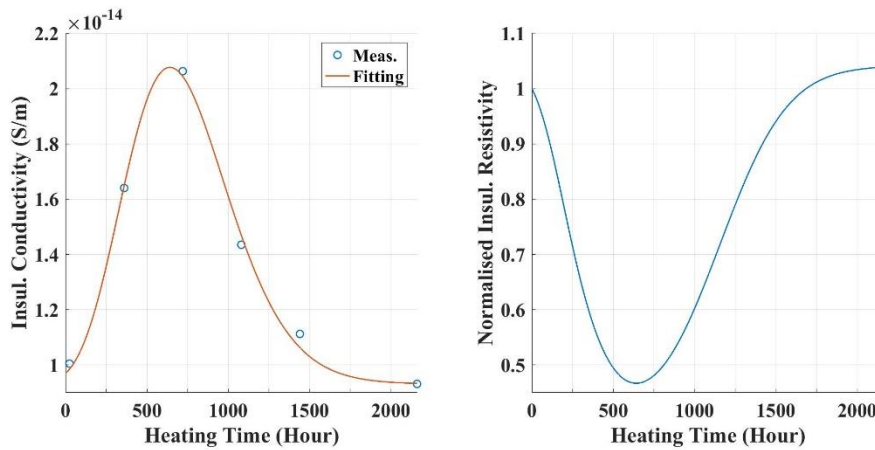


Figure 38. (a) Insulation conductivity measurements and their fitted values (S/m) of XLPE insulation samples heated at 90°C over various durations (hour) with the presence of SC layers and (b) the corresponding insulation resistivity normalized by the initial level.

It worth noting that by-products of cross-linking formed during manufacturing can also enhance hopping conduction, consequently elevating the initial σ . However, after a duration, when these by-products along with the chemical species from SC shield layers are consumed, the resultant σ (e.g., at 2160 hours) may be even smaller than the initial σ .

Considering the reciprocal relationship between conductivity (σ) and resistivity (ρ), the alteration of normalized insulation resistivity relative to its initial level is deduced from the fitting of σ , as shown in Figure 36(b). It is important to note that both the intensity of hopping conduction and the diffusion of chemical species are impacted by temperature[117][118]. The

contribution of the hopping mechanism between traps to the conductivity of the cable sample exhibits a linear relationship with temperature to the power of negative one-quarter [119]. Diffusion rate of chemical species would be increased as temperature raise.

As indicated in Figure 38 (b), the resistivity of the XLPE cable, when viewed as a function of annealing time at 90°C, exhibits its lowest value between 600 to 650 hours. It is important to note that there are variations in temperature along both the cable's radius and length dimensions in the accelerated ageing experiment conducted in this thesis.

For the experiment in this research, temperature monitoring on the cables reveals that the temperature range on the cable conductor's surface spans from 95 to 107°C. On the outer surfaces of cables, the temperature range extends from 85 to 100°C. This implies that for the inner and outer semi-conducting shield layers, the maximum temperature difference could reach up to approximately 22°C. This discrepancy in temperature could consequently lead to varying annealing effects rates on the semi-conducting shields at different locations.

Given that the conductor surface experiences higher temperatures, the semi-conducting shield around the conductor undergoes the annealing process more rapidly and concludes earlier. Consequently, for the measured IR1 and IR10 values at 10kV testing voltage, as they vary along with ageing cycles in this experiment, they exhibit an initial decrease in the first 50 ageing cycles, followed by an increase between approximately 50 to 100 ageing cycles. However, the insulation semi-conducting shields, with lower temperatures compared to the conductor surfaces, undergo the annealing process at a slower rate and concludes later. This leads to another subsequent increase in IR values from around 210 ageing cycles.

The $\tan\delta$ values of the cables, in relation to resistivity, also display an observable up-down-up trend due to the influence of the annealing effect. However, it's worth noting that the variation in PI values appears to be less affected by the annealing effect, as per the measured results.

3.6.4. Correlation analysis

In this chapter, various condition monitoring techniques have been employed to measure different electrical indicators of power cables throughout the thermal ageing processes. It's worth noting that there exist intrinsic correlations among these indicators based on their underlying principles. For instance, there are correlations between $\tan\delta$ and IR, as well as between PI and IR. To assess the degree of correlation among the results of these testing indicators, the Pearson correlation coefficient (R), alongside other pertinent statistical tools, are employed in this section.

The Pearson correlation coefficient (R) has been discussed in section 3.6.2. The p-value is a measure of the strength of evidence against the null hypothesis. In the context of a Pearson correlation, the null hypothesis states that there is no significant correlation between the two variables. A low p-value (typically less than 0.05) indicates that there is strong evidence against the null hypothesis, suggesting that there is a significant correlation between the variables. Conversely, a high p-value suggests that the observed correlation could easily occur by chance alone, and there is not enough evidence to reject the null hypothesis.

The 95% confidence interval provides a range of values within which we can reasonably expect the true population correlation coefficient to fall, with 95% confidence. It is computed using a formula that takes into account the sample size and the standard error of the correlation coefficient. The confidence interval helps in understanding the precision of our estimate. A wider interval indicates more uncertainty about the estimate, while a narrower interval indicates the estimate of the correlation coefficient is more reliable.

The confidence interval is typically expressed as two values: the lower boundary and the upper boundary.

- Lower Boundary: This is the lower limit of the range, below which we would expect the true correlation coefficient to be only 2.5% of the time if we were to take many samples.
- Upper Boundary: Conversely, the upper boundary is the upper limit of the range, above which we would expect the true correlation coefficient to be only 2.5% of the time.

In essence, a 95% confidence interval provides us with an understanding of the probable range within which the actual population is likely to fall.

Table 10 presents Correlation coefficients between IR1 and IR10 for the cables. R values are in the range of 0.8 to 1, which indicates there is a strong correlation between IR1 and IR10, while p values are all significantly smaller than 0.05 also suggesting this is a significant correlation.

Table 10. Correlation between IR1 and IR10 at 10kV testing voltage for each cable

Cable	R	p	Lower boundary	Upper boundary
Cable1	0.9105	8.1×10^{-14}	0.827	0.9547
Cable2	0.8939	4.9×10^{-13}	0.7985	0.9455
Cable3	0.8682	1.4×10^{-11}	0.7528	0.9319
Cable4	0.9017	1.4×10^{-13}	0.8126	0.9496

Table 11 shows the correlation coefficients, p values, 95% confidence interval lower and upper boundaries for IR1 and $\tan\delta$ for each cable sample, with data measured at 10kV. R values for IR1 and $\tan\delta$ of all cables are in the range of 0.2 to 0.4 which indicates a weak correlation. The correlation between IR1 and $\tan\delta$ for Cable 4 is the strongest among cables, it has the maximum R value and minimum p value, while the cable 2 shows the lowest correlation coefficient.

Table 11. Correlation between IR1 and Tan δ at 10kv testing voltage for each cable

Cable	R	p	Lower boundary	Upper boundary
Cable1	0.2944	0.0860	-0.0431	0.5716
Cable2	0.2433	0.1589	-0.0978	0.5333
Cable3	0.3372	0.0476	0.0045	0.6027
Cable4	0.3596	0.0338	0.03	0.6187

The correlation coefficients between PI and $\tan\delta$ of each cable samples are presented in Table 12. Absolute values of R are even smaller than for IR1 and $\tan\delta$, and negative signs could be found for all R values. Thus, the correlation between PI and $\tan\delta$ is very weak.

Table 12. Correlation between PI and Tan δ at 10kv testing voltage for each cable

Cable	R	p	Lower boundary	Upper boundary
Cable1	-0.1249	0.4816	-0.4443	0.2227
Cable2	-0.0203	0.9151	-0.3778	0.3424
Cable3	-0.2024	0.2665	-0.5148	0.1574
Cable4	-0.1871	0.2972	-0.4984	0.1669

Moreover, the results obtained from DAR testing exhibit a correlation with the results of PI testing over the course of 50 ageing cycles. Within this span of 50 ageing cycles, it is observed that DAR and PI values demonstrate a synchronous yet inversely proportional trend. After the initial 50 ageing cycles, the DAR values of cables subjected to various testing voltages remain within narrow ranges. The PI values of these cables exhibit a gradual reduction concurrent with the progression of thermal ageing processes.

3.7. Conclusion

In this chapter, an experiment focused on the accelerated thermal ageing of MV cables has been carried out. A novel artificial thermal accelerated ageing methodology for MV extruded power cables has been devised. This method has the capability to replicate the temperature variations experienced along the cable's length and radius. Additionally, it effectively emulates the thermal cycling effects induced by repeated loading cycles.

Four XLPE insulated cable samples were placed within a chamber equipped with thermal insulation. A current transformer was employed as the power source to elevate the cable temperature, meeting the criteria for accelerated thermal ageing. To simulate the temperature fluctuations experienced by cables in real-world operating conditions, one ageing cycle (equivalent to 24 h) was divided into three phases: a 2h heating phase, followed by a 6h high temperature phase, and finally a 16h natural cooling down phase.

Temperature distributions on both the cable surfaces and conductor surfaces were assessed using Type T thermocouples. During the heating up phase, the cable surfaces temperature experienced a rise from room temperature (20°C) to a maximum of 100°C. In this phase, no significant temperature difference was observed along the length of the cables. However, the temperature on the conductor surface was notably higher, with a difference of approximately 10°C compared to the cable surface.

As the experiment transitioned into the high-temperature phase, the maximum temperature on the cable surfaces remained at 100°C. Notably, the temperature difference along the length of individual cable surfaces increased to 15°C. Additionally, the maximum temperature on the cable conductor surface was also recorded at 107°C.

The equivalent ageing hours, derived from thermal ageing cycles and translated into normal working conditions, are computed using the Arrhenius model and Miner's law. Based on the current experimental procedure, the equivalent ageing duration for the cables stands at approximately 25 years. Throughout the thermal ageing process, various electrical properties of the cables have been monitored. These include IR1, IR10, DAR, PI, capacitance, and $\tan\delta$. Testing voltage levels have been induced within the range of 1kV to 10kV, and found exerting a significant influence on the measurement results of IR1, IR10, and $\tan\delta$.

As the thermal ageing process progresses, the IR values exhibit a pattern of fluctuations characterized by down-up-down-up trends. Likewise, similar variations are observed in the $\tan\delta$ values. In order to probe the underlying causes of these fluctuations, the impact of RH on the testing results is examined. Survey results reveal that lower IR testing values are observed

under relatively high RH conditions. Nevertheless, further data is needed to solidify this relationship.

Furthermore, the interplay between chemical reactions and particle diffusion from semiconductor layers, commonly referred to as the annealing effect, on the electrical properties of cables during the process of extruded cable thermal ageing has been considered and investigated. According to Nath et al.'s research [115]-[118], the changes in cable insulation conductivity are influenced by the annealing effect, leading to alterations in the trends of IR and $\tan\delta$ values.

Based on temperature measurements, it was observed that the conductor SC shield experiences higher temperatures than the insulation SC shield layer. These temperature discrepancies along the length and radius of the cables contribute to variations in the rate of the annealing effect. There are two humps of IR curves, this manifests in the initial upturn of IR curves attributed to the annealing effect of the conductor SC shield layer during service, followed by a subsequent upturn of IR curves attributable to the annealing effect of the insulation SC shield layer during service.

The variation in PI values for the cables has been subjected to fitting, revealing three distinct phases in relation to the thermal ageing process. For Cable 1, Cable 2, and Cable 3, the first phase exhibits a short-term linear decrease in the fitting curve, only for Cable 4 the first phase displays an increasing straight line with a very slight slope. The second phases of PI fitting for all cables also follow a linear trend, with positive slopes. In the third phase of PI fitting, an exponential decrease trend is observed. This indicates that the rate of PI decrease during the thermal ageing process is generally lower. It is worth emphasizing that a PI value falling below specified thresholds, such as 2 or potentially even lower than 1, could serve as a significant indicator of potential insulation issues, prompting consideration of maintenance or replacement measures for the cable in question.

Finally, correlation coefficients among the testing results, along with their respective P-values and 95% confidence intervals, have been computed. The analysis reveals a strong correlation between IR1 and IR10, whereas the correlation between other indicators is comparatively weak. The $\tan\delta$ changing is correlated to IR changing as well based on the principle of $\tan\delta$ measurement, but the correlation coefficient between them is relatively lower.

Chapter 4. Modelling of power cable spatial temperature profiles under accelerated thermal ageing

4.1. Introduction

Power cables often experience non-uniform temperature distributions under practical working conditions due to varying current loads, environmental conditions, and installation configurations. Insulation materials such as XLPE or EPR undergo various thermal degradation processes, including oxidative degradation, chain scission and crosslinking, as detailed in section 2.3. These processes are temperature-dependent and accelerated as temperature increases. Temperature variations along the length and radius of a cable result in localized differences in degradation rate. Accurate modelling of these temperature profiles allows engineers to predict where and how quickly ageing will occur, leading to more accurate estimations of the cable's operational lifespan.

The experiment described in chapter 3 involved the accelerated thermal ageing of MV extruded cables within a thermally insulated and air-filled chamber. The temperature distribution along the length of each cable during heating cycles was assessed through the placement of thermocouples on the cable surfaces and conductor surface. However, this physical measurement approach only provides a primitive assessment of the temperature distribution across the cable surfaces and conductor surface in relation to their respective lengths. Ageing and degradation of cables are highly sensitive to temperature variation. Small differences in temperature can significantly affect the rate of degradation. To construct a more reliable lifetime estimation model for cables subjected to such accelerated thermal ageing conditions, a higher degree of precision in the temperature profiles of the power cables is desired. The validity of the estimated temperature profiles could be verified through practical measurements from chapter 3. This validation process ensures that the simulation yields a reliable and nuanced comprehension of the temperature profiles, enabling advanced thermal ageing evaluations of cable insulation.

FVM as one of numerical calculation approaches has been chosen for simulating the temperature distribution in cables due to its superior functionality and cost-effectiveness in addressing the specific physical conditions of this problem [97], as indicated in the literature review of thermal modelling methodologies. Additionally, an integrated approach has been employed, wherein the FVM modelling technique is complemented with the application of an ANN model. This integrated methodology is employed to estimate the spatial temperature

profiles of the cables within the experimental framework. Subsequently, these profiles can be utilized for advanced thermal modelling evaluations of insulation degradation.

Initially, ANSYS Fluent is utilized to implement a three-dimensional FVM modelling approach, with the objective of simulating the temperature distribution within both the power cables and the fluid (air) domain of the chamber. To ascertain the reliability of the FVM simulation results, a comparison is conducted between the temperature profiles derived from the simulations and the actual temperature profiles recorded from the cables during the experimental phase. The FVM-based simulation model discretizes into numerous finite-size cells, each possessing a geometrically straightforward shape. Subsequently, temperature values at designated mesh points can be extracted from the results of the FVM simulation.

The temperature profiles along the cable structure, particularly between meshed points, cannot be directly ascertained from the results of the FVM simulation, because FVM provides temperature values only at discrete locations (the mesh nodes or control volume centers). The continuous temperature distribution between these points must be interpolated, and the accuracy of this interpolation depends on the mesh density, the complexity of the temperature field, and the specific interpolation methods used. Therefore, the temperature profiles acquired at this stage do not offer adequate precision in forecasting the ageing conditions of cable insulation. Given the presence of natural air convection within the chamber, the correlation between specific points along the cable and their corresponding temperatures is inherently non-linear and intricate. In contrast to interpolation polynomial techniques that could be applied, ANNs demonstrate the potential to deliver heightened computational capacity and enhanced efficiency in determining temperature profiles of cable insulation at any designated position.

To facilitate the estimation of temperatures at any positions within the power cable, thereby enabling the establishment of a more precise ageing model contingent upon temperature variation with respect to position, a three-layer ANN trained through Bayesian regularization back-propagation methodology is subsequently constructed.

The integration of FVM simulation and the ANN model showcases effectiveness in predicting temperatures at arbitrary locations along the power cable. This proficiency is crucial for advancing more accurate ageing and degradation models, founded on temperature distributions across any positions. Traditional thermal degradation models for power cable insulation typically rely on hot-spot temperatures, the effect of the temperature difference in the cable length and radial direction on the ageing rates of the insulation at different locations is not considered. The precise and detailed spatial temperature profiles generated through the

proposed method in this study would significantly enhance the reliability of cable insulation performance estimation.

4.2. FVM modelling

FVM is widely used in computational fluid dynamics (CFD) and heat transfer simulations. The method is used in modelling heat conduction in solids, convection in fluids and even in more complex multiphysics problems where heat transfer is coupled with fluid flow or structural analysis. As reviewed in section 2.6, the FVM is a numerical technique used to solve partial differential equations, such as the heat equation, which models heat conduction in a material. In accordance with the control volume principle of analytical fluid dynamics, FVM initiates by dividing the model into discrete control volumes, which are of appropriate size and exhibit a straightforward geometric configuration, commonly referred to as cells. The variables of calculations are situated at the centroids of these cells. Subsequently, the governing PDEs are integrated over each individual cell. The resultant set of equations is denoted as the discretization or discretized form of the equations. Within the framework of FVM, this discretization contains the conservation principle for variables within the cells, which means certain physical quantities, such as mass, energy, or momentum, are conserved within a discrete control volume.

The conservation principle ensures that the total amount of a conserved quantity remains constant within each control volume over time. General conservation equations can be performed by a single generalized transport equation:

$$\frac{\partial(\rho\phi)}{\partial t} + \frac{\partial}{\partial x_j}(\rho j_j \phi) = \frac{\partial}{\partial x_j}(\Gamma \frac{\partial\phi}{\partial x_j}) + S_\phi \quad (19)$$

In this context, ϕ can denote scalars, such as speed and temperature, which serve to represent various conservation equations, including those pertaining to momentum and energy. In (19):

- The first term pertains to the unsteady component to be analysed.
- The second term denotes the convective component of flux.
- The third term encompasses the diffusive component of flux.
- The final term signifies the generation or source term.

The transport equations are initially integrated over the volume of the cell (v), as demonstrated in (20):

$$\int_{\Delta V} \frac{\partial(\rho\phi)}{\partial t} dV + \int_{\Delta V} \frac{\partial}{\partial x_j}(\rho u_j \phi) dV = \int_{\Delta V} \frac{\partial}{\partial x_j} \left(\Gamma \frac{\partial\phi}{\partial x_j} \right) dV + \int_{\Delta V} S_\phi dV \quad (20)$$

Subsequently, discretization is carried out in the ensuing stage to yield a series of algebraic equations.

The heat equation is a partial differential equation that describes the distribution of heat (or temperature) in a given region over time. In its simplest form, for a homogeneous and isotropic material, the equation is:

$$\frac{\partial T}{\partial t} = \alpha \nabla^2 T \quad (21)$$

where:

- T is the temperature as a function of space and time
- t is time
- α is the thermal diffusivity of material ($\alpha = \frac{k}{\rho c}$, where k is thermal conductivity, ρ is density and c is specific heat capacity).
- ∇^2 is the Laplacian operator, which in Cartesian coordinates expands to:

$$\nabla^2 T = \frac{\alpha^2 T}{\alpha x^2} + \frac{\alpha^2 T}{\alpha y^2} + \frac{\alpha^2 T}{\alpha z^2} \quad (22)$$

The heat equation is derived from the integral form of the conservation of energy:

$$\int_V \frac{\partial(\rho c T)}{\partial t} dV = \int_S k \nabla T \cdot dS \quad (23)$$

where:

- V is the control volume.
- S is the surface of the control volume.

The primary objective of FVM simulation in this research is to attain precise and comprehensive temperature profiles of power cables subjected to specific accelerated thermal ageing conditions, which is provided in the chapter 3. Subsequently, the ensuing stages of the modelling process encompass the formulation of the simulation model in conformity with the actual geometry and dimensions, the generation of a mesh on said model, the establishment of simulation parameters, and the computation of the solution. These steps will be clarified upon in detail within this chapter. Finally, the resulted temperature of the simulation, will be presented, discussed, and compared with the experimental measured results.

4.2.1. Model geometry

All geometries are created using the Design Modeler tool, within the ANSYS workbench environment. The configuration of the actual power cable utilized in the experiment is depicted in Figure 9. This structure comprises eight layers, enumerated as follows.

It has been determined through a series of simulation comparisons that the thermal influence of certain thin layers, such as semi-conductor composition with thickness less than 0.3mm, exerts a minimal impact on the heat absorption and propagation within the power cable. Consequently, the inclusion of these thin layers in the model geometry would excessively increase both the complexity of meshing and the computational workload for simulation purposes. Hence, for the FVM simulation, the power cable model is simplified to encompass four primary layers. Figures 39 (a) and (b) depict cross-sectional views of the cable model, tangent and parallel to its length, respectively. The layers are designated as follows: conductor, insulation, metal shield, and outer sheath.

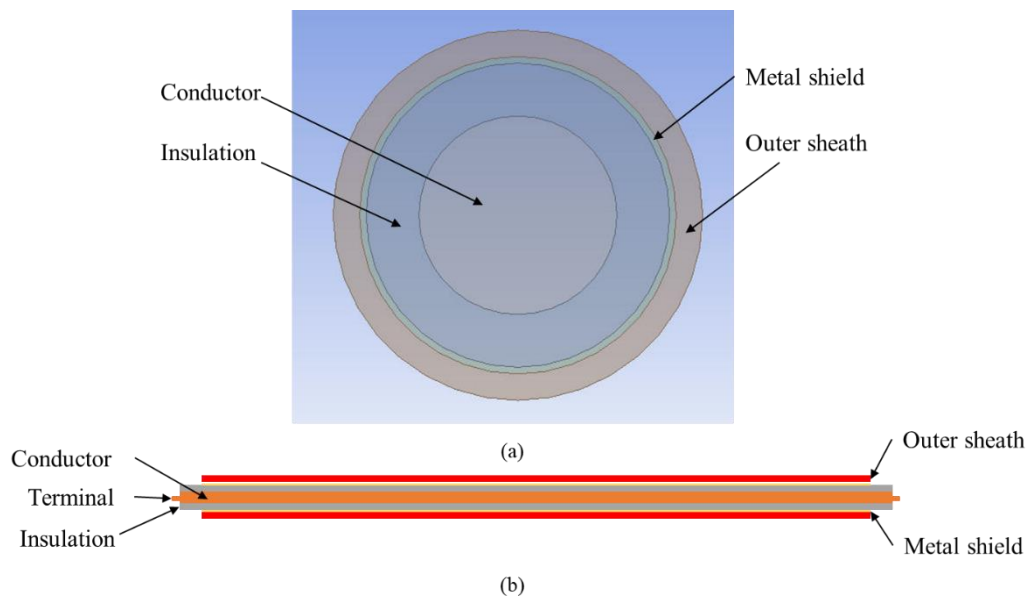


Figure 39. Cross section (a) tangent and (b) parallel to length of cable model used for FVM modelling

The specific dimensions and material attributes of each layer are outlined in Table 13. The insulation material is XLPE, while the outer sheath material is Medium-Density Polyethylene (MDPE).

Table 13. Dimensions and materials of cable model

Layer	Length	Diameter	Material
Conductor	3.2 m	15 mm	Aluminium
Insulation	3.2 m	23 mm	XLPE
Metal shield	2.55 m	24 mm	Copper
Outer sheath	2.55 m	28 mm	MDPE

The model replicates the experimental set up in chapter 3 and is presented in Figure 40. It encompasses a chamber containing air as the fluid medium. This configuration incorporates four straight power cables, two long connectors, and three short connectors. In Figure 40, the cable models are arranged in a series configuration, connected by the designated connectors.

Specifically, three short connectors facilitate the linkage of adjacent cables, while two long connectors are employed to establish connections between the cables and the power supply, represented in practice by a current transformer in the experimental setup.

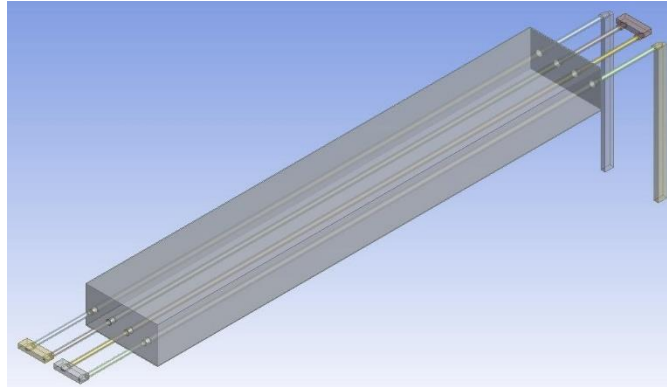


Figure 40. Constructed integral model in ANSYS for FVM thermal simulation

The dimensions of the chamber in the actual experiment serve as the basis for designing the chamber model, illustrated in Figure 41. The aluminium walls of the chamber possess a thickness of 2 mm. Positioned on the opposing shorter side walls of the chamber are four apertures, designated for the passage of power cables through the tank. The overall length of the chamber spans 2.5 m; consequently, both sides of each power cable have 0.4 m, extending beyond the chamber to make contact with the ambient environment.

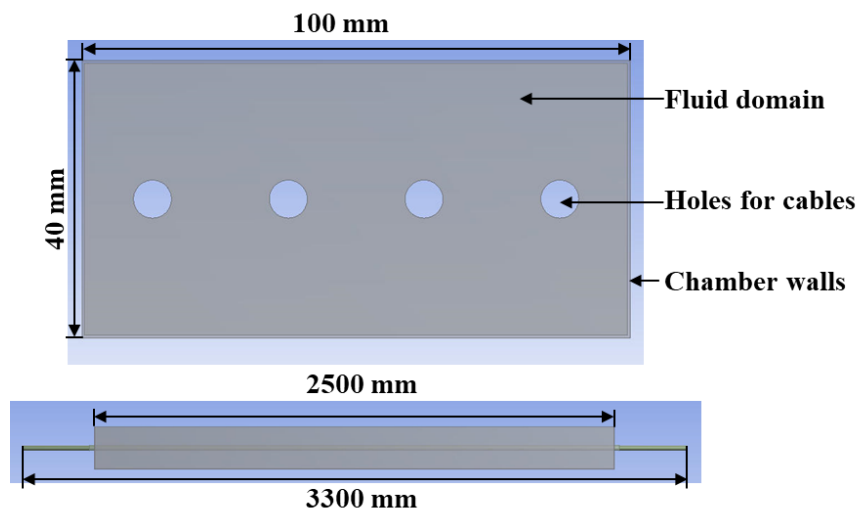


Figure 41. Chamber model for FVM modelling with chamber dimensions

4.2.2. Model meshing

Within a 3D domain, two fundamental cell types are utilized to form a surface mesh: hexahedrons (Hex mesh) and tetrahedrons (Tet mesh). Each grid cell constitutes a solution to the corresponding PDE when a FVM object undergoes discretization.

The cell types and the level of precision in the meshing results differ across various solid domains. This difference arises due to variations in their dimensions and distinct contacting boundary conditions. The quality of the meshed elements in each geometry is assessed through a composite metric, quantified by element quality values which fall within the range of 0 to 1. This metric is predicated on the ratio of the volume to the square root of the cube of the sum of the squares of the edges for three-dimensional elements. An element quality value approaching 1 signifies a more optimal cube, while a value of 0 indicates that the element possesses either zero or negative volume.

Table 14 shows the meshing results information of each component and overall model. The average quality of the overall model meshed cells is 0.8, which indicates that the overall meshing quality is good. However, the average quality of the meshed cells in the metal shield section stands at 0.25, this means that the meshing in the cable metal shields is not sufficiently refined. Such coarser meshing could potentially lead to convergence challenges in the simulation calculations. The mesh qualities between layers can influence one another. This means that refining the mesh element size to improve quality of metal shield layers will significantly increase the total number of mesh elements, leading to higher computational costs and reduced efficiency in subsequent simulations. To address this, ANSYS Fluent allows for adjustments to enhance the convergence of a distorted mesh by using a skewness correction factor in the simulation settings. This helps mitigate the impact of mesh quality issues on the simulation.

Table 14. Meshing outcomes of each component and overall model

Components	Number of cells	Cell types	Number of nodes	Average quality
Conductor	296406	Tet	66313	0.84
Insulation	84988	Tet	339211	0.82
Metal shield	27680	Hex & Tet	13820	0.25
Outer shield	48640	Tet	159892	0.72
Long connector	2645	Tet	677	0.82
Short connector	6613	Tet	1529	0.80
Overall model	9443919	Hex& Tet	1733126	0.8

Meshing results of each cable model component are represented in Figure 42. Due to sections of the insulation in Figure 42 (b) being in contact with the cable's metal shield layer, while others are exposed to the ambient air, the surface mesh for these two regions differs. The outer sheaths come into contact with the fluid domain (air in the chamber), the chamber walls, and the ambient air. As illustrated in Figure 42 (d), the mesh for these three regions varies.

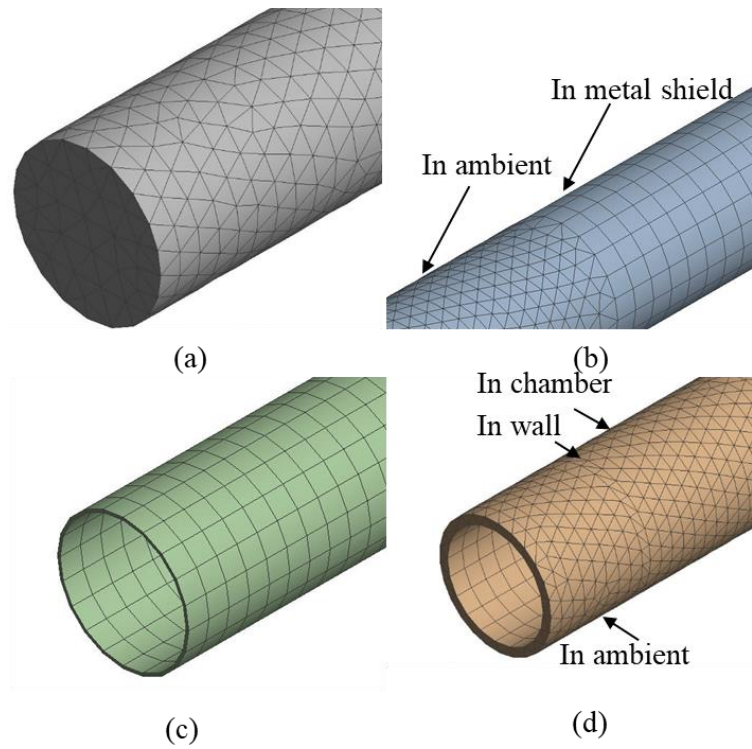


Figure 42. Mesh results of (a) conductor, (b) insulation, (c) metal shield and (d) outer sheath of cable geometries

The meshing results for the connector models are displayed in Figure 43. Two distinct types of connectors are present in the model: long connectors and short connectors.

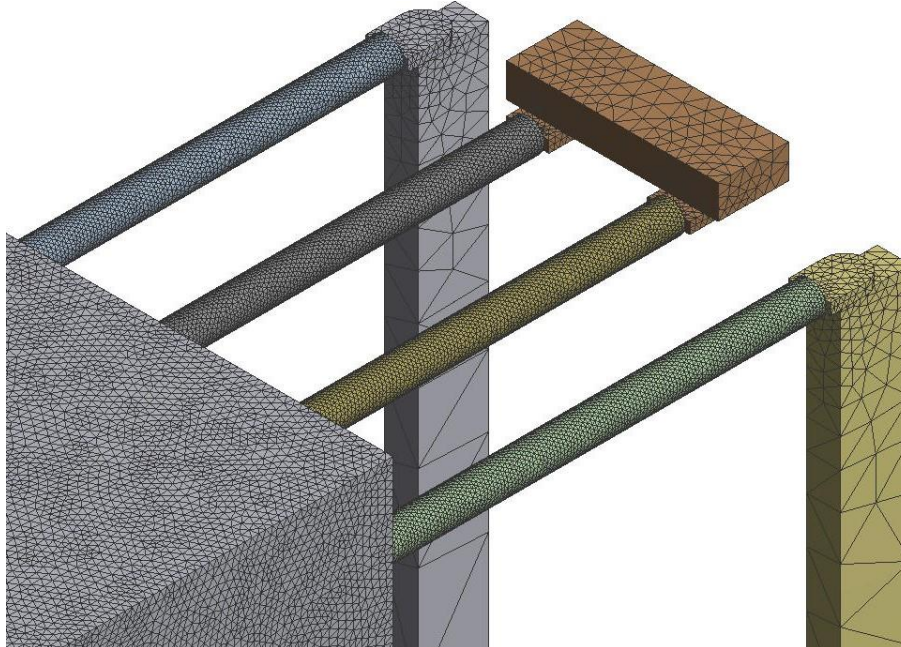


Figure 43. Meshing results of connectors

The overall model as illustrated in the sectional view of the mesh shown in Figure 44. The cable geometries are shown by coloured circles in the figure, each layer of cable structure

could be distinguished by its colour. Due to the presence of thin layers in the cable models, the cable components exhibit a finer mesh compared to the fluid domain, a feature also depicted in Figure 44.

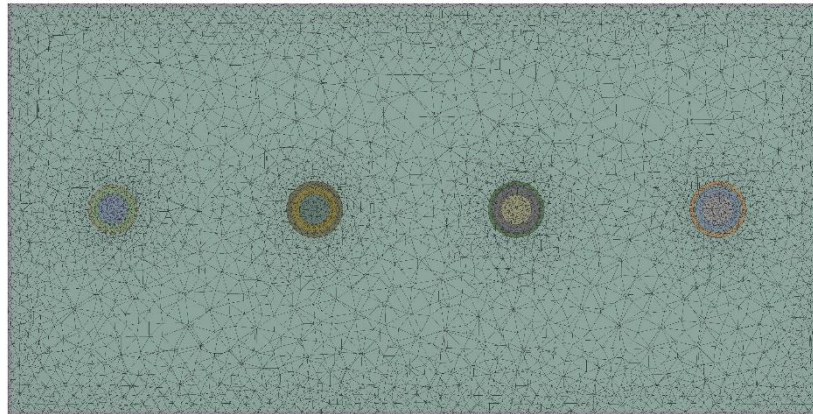


Figure 44. Overall results of meshing on sectional view (including cable, chamber and fluid domain)

4.2.3. Material properties

The materials utilized for each layer of the cable model are detailed in Table 15. The chamber walls are composed of aluminium, the thermal insulation material is polystyrene, and the fluid filling the chamber is air.

Table 15 presents the assumed constant thermal properties for the materials, including conductors (aluminium), metal shield (copper), chamber wall (aluminium), and thermal insulation (polystyrene), which are considered uniform with respect to temperature.

Table 15. Constant thermal properties of cable material

Material	Density (kg/m ³)	Thermal conductivity (W/m-K)	Specific heat (J/kg- K)
Aluminium	2719	202.4	871
Copper	8978	387.6	381
Polystyrene	40	0.029	1110

As polymer materials, the thermal properties of the insulation and outer sheath materials are subject to variation with changing temperatures. Past studies have substantiated that these properties exert a significant influence on cable thermal conduction and temperature distribution [120]. Consequently, for the simulation model, the XLPE material representing insulation and the MDPE material incorporate thermal properties that change with temperature. Table 16 furnishes the piecewise linear variations of conductivity and specific heat for XLPE and MDPE materials with increasing temperature. It is worth noting that densities are assumed to remain constant with temperature.

Table 16. Thermal properties of cable materials piecewise linear variation with temperature[120]-[122]

Material	Temperature (K)	Density (kg/m ³)	Thermal conductivity (W/m-K)	Specific heat (J/kg- K)
XLPE	293.15	965	0.223	2034
	323.15	965	0.267	2976
	363.15	965	0.28	4049
MDPE	293.15	926	0.4	1916
	363.15	926	0.48	2300

The Boussinesq approximation has been employed for modelling the flow of air within the chamber. This approximation posits that the variation in fluid density primarily impacts the buoyancy term. In this context, the reference density of air is taken as 1.204 kg/m³ at 20°C, and the thermal expansion coefficient is specified as 0.00321 (K⁻¹)[123]. It is important to note that the specific heat and thermal conductivity of air are both subject to changes with temperature, as indicated in Table 17, these changes are implemented in the air material parameters set up by piecewise linear fitting.

Table 17. Thermal properties of air changing with temperature[123]

Temperature (K)	Specific Heat C _p (J/kg · K)	Thermal conductivity (W/ m · K)
293.15	1006	0.02587
313.15	1007	0.02735
333.15	1008	0.0288
353.15	1009	0.03023
373.15	1011	0.03162

4.2.4. Simulation setup

In the setup phase, the initial step involves choosing a solver for the calculations. ANSYS Fluent offers two solver techniques: the Pressure-based solver and the Density-based solver. In both methods, the velocity field is derived from the momentum equations. Generally, when it comes to modelling low-speed, incompressible, or mildly compressible flows, the pressure-based solver is usually the preferred choice. The Pressure-based solver in ANSYS Fluent has been selected for the simulation in this research. This choice is based on the fact that the air within the chamber is supposed incompressible, and the natural convection-induced airflow is of low speed. The governing equations for continuity and momentum are expressed as (21) and (22), respectively:

$$\frac{\partial \rho}{\partial t} + \nabla \cdot (\rho \vec{v}) = 0 \quad (21)$$

$$\frac{\partial \rho}{\partial t} (\rho \vec{v}) + \nabla \cdot (\rho \vec{v} \vec{v}) = -\nabla P + \nabla \cdot (\bar{\tau}) + \rho \vec{g} + \vec{F} \quad (22)$$

where, P is the static pressure, $\rho\vec{g}$ is the gravitational body force, \vec{F} is the external force vector, and $\bar{\tau}$ is the stress tensor as (23) shown.

$$\bar{\tau} = \eta[(\nabla\vec{v} + \nabla\vec{v}^T)] - \frac{2}{3}\nabla \cdot (\vec{v}I) \quad (23)$$

where η denotes the molecular viscosity, I stands for the unit tensor, and the final term on the right-hand side of the equation accounts for the impact of volume dilation, which equals zero in the case of incompressible fluid flow.

The velocity formulation serves the purpose of reducing numerical diffusion in the solution, thereby leading to a more accurate outcome. In this simulation, the absolute velocity formulation is employed.

To capture the dynamic evolution of the temperature field within the global model system, as well as the fluid flows in the domain over time, a transient simulation approach has been employed. The natural convection of air within the chamber is influenced by gravity, acting in the negative y -direction with an acceleration of 9.81 m/s^2 .

The Energy Model has been enabled, and for the Viscous Model, the laminar model has been selected. Then, the domains within the model are established. The air fluid enclosed within the chamber is designated as the fluid domain. The solid zones encompass conductors, insulation, metal shield, outer sheath of cable models, as well as short and long connectors, along with the chamber itself.

In this model, only the Joule losses from cable conductors and connectors are considered as heat sources. This decision is based on the understanding that the dielectric loss and the sheath loss (without sheath circulating current in the experiment) are significantly smaller in magnitude compared to the conductor loss[124][125]. The power densities are applied specifically on the heat source solids: cable conductors, as well as the long and short connectors. This is done to emulate the flow of AC current in the conductive path, generating heat due to Joule loss. The heightened power load leads to elevated temperatures and temperature gradients within the insulation system of power cables. This closely replicates the conditions of accelerated thermal ageing in practical power cable experiments and results in typical thermal stress gradients within the insulation.

The equivalent power density (S_h) for each heat source solid can be determined using the equivalent power of conductors and connectors (P), and volume (V). This calculation is expressed in (24):

$$S_h = \frac{P}{V} \quad (24)$$

In the experiment, the cables are connected in series to the power supply through connectors. Following the recommendations outlined in established IEEE standard 1407 [109] and considering practical limitations of thermal ageing experiments for power cables, the equivalent load AC power in the circuit is allocated to three distinct stages. The initial stage, spanning from 0 to 2 h, corresponds to the heating-up phase. Subsequently, the period from 3 to 8 h is designated as the temperature stability stage. Finally, the span from 8 to 24 h constitutes the cooling-down stage. In this phase, the goal is to reduce the cable temperature back to ambient conditions (20°C).

The geometric shape of the cable conductors in the model conforms to a standard cylinder. As a result, the volume of the cable conductor can be computed using (25):

$$V = \pi r^2 l \quad (25)$$

where, r represents the radius of the conductor (m), and l signifies the length of the cable conductor (m).

The volume of single power conductor is calculated to be $6.105 \times 10^{-4} \text{ (m}^3\text{)}$. Additionally, the volumes of the short connectors and long connectors are determined to be $1.8 \times 10^{-4} \text{ (m}^3\text{)}$ and $9 \times 10^{-4} \text{ (m}^3\text{)}$, respectively.

The power (P) of cable conductors and connector in different phases could be calculated from the output voltage (V) and current (I), which obtained from the experimental measurements, as (26) illustrated. Figure 14 in chapter3 presents the variation of output voltage and current from current transformer within one experimental heating cycle.

$$P = V \times I \quad (26)$$

The variations in power densities applied to the conductors and connectors during one heating cycle are depicted in Table 18. It is important to note that, in the heating-up stage, the power densities should ideally change over time as the temperature increases. However, for simplifying the modelling calculations in the simulation, they were approximated as constant values.

Table 18. Power density applied on conductors and connectors in the FVM simulation

Time	0-2h	2-8h	8-24h
Conductors	204000 W/m ³	103000 W/m ³	0 W/m ³
Short connectors	70000 W/m ³	25000 W/m ³	0 W/m ³
Long connectors	12000 W/m ³	10000 W/m ³	0 W/m ³

The geometry in this model is assumed as situated in an air-filled environment, it is necessary to consider convection heat transfer between geometry surfaces and ambient air as

there is a temperature difference between the air (fluid) and the surface. Convection heat transfer takes place when there exists a temperature disparity between a fluid and a surface it passes over. Convection encompasses two types: forced convection and natural convection. Forced convection arises when the fluid flow is induced by an external force, such as a fan or pump. On the other hand, natural convection arises from density variations within the fluid, which occur due to internal temperature differences, leading to fluid motion [126].

The natural convection circumstance is set up for surfaces in this model due to the fluid flow is caused by density differences due to temperature gradients instead of external forces like pump or fan. Newton's law of cooling, expressed in (27), is extensively employed for analysing both forced and natural convection heat transfer.

$$Q = hA\Delta T \quad (27)$$

- Q represents the heat transfer rate between the fluid and the solid surface.
- A denotes the area of the surface in contact with the fluid.
- ΔT signifies the temperature difference between the fluid and the solid surface.
- h stands for the convective heat transfer coefficient.

It is the major work of convective heat transfer calculations to determine the value for the heat transfer coefficient. The calculations of natural convection heat transfer coefficient are derived from correlations of dimensionless numbers, including the Nusselt number, the Prandtl number, the Grashof number and the Rayleigh number. The convection coefficients of different boundaries are dependent on their shapes, directions, dimensions and temperature differences between ambient [127].

In this model, the upper wall surface of the chamber is characterized by a horizontal upward plate. This plane encompasses an area of 1 m² with a corresponding perimeter of 5.8 m. The average temperature of the upper wall surface is determined at 60°C through several iterative simulations. The ambient air surrounding the chamber is assumed held at a constant temperature of 20°C, which uniformly across all boundaries.

The surface type of chamber downward wall is the downward horizontal plate. This surface shares equivalent dimensions in terms of area and perimeter with the upper wall. The average temperature of the lower wall surface is established at 40°C.

The chamber's lateral surfaces are characterized by a vertical plane configuration, possessing a height of 0.1 m. These surfaces maintain an average temperature of 50°C. The exposed sections of the cables in the air are cylindrical in shape, with a diameter measuring 0.03 m. These cable segments exhibit a surface temperature of 70°C. Therefore, the convection

coefficients for the boundaries shown as Table 19, which are calculated based on (27) and validated by several iterative simulations.

Table 19. Convection coefficients of boundaries

Boundaries	Convection Coefficient (W/m ² -K)
Chamber upward wall surface	6
Chamber downward wall surface	2.5
Chamber side wall surfaces	5
Cable surfaces outside chamber	7.5
Short connector surfaces	8
Long connector surfaces	5

Furthermore, the skewness correction revises the mass flux correction to enhance convergence on distorted meshes in the current simulation, with default coefficients set to 1. Gradients are crucial for determining scalar values and velocity derivatives, the chosen methodology utilizes a least squares cell-based gradient approach. The discretization scheme is automatically determined. Viscous terms are second-order accurate, and second-order upwind discretization is used for convection terms in flow equations and scalar quantities. The transient scheme employs second-order implicit temporal discretization.

ANSYS Fluent requires the initialization of all solution variables prior to commencing iterations. In this model, the fluid domain's velocity in all directions is initialized as 0 m/s, signifying an assumption of no internal fluid flow within the chamber prior to cable heating. Additionally, the initial temperature of the overall system is set at 20°C, aligning with the experimentally measured ambient temperature.

In the calculation configuration, each time step is set at 1200s, allowing for a maximum of 20 iterations per step. Given this setup, a total of 72 steps are executed in this simulation. Consequently, the model effectively captures the temperature distribution and fluid flow over a period of 24 hours, which constitutes a complete heating cycle.

4.2.5. Modelling results

4.2.5.1 Temperature distribution on cable surfaces

The initial temperature distribution on the surfaces of the cables within the chamber is depicted in Figure 45. It is assumed that the entire system starts at an initial temperature of 20°C. The positions of each cable are also indicated on Figure 45 for reference.

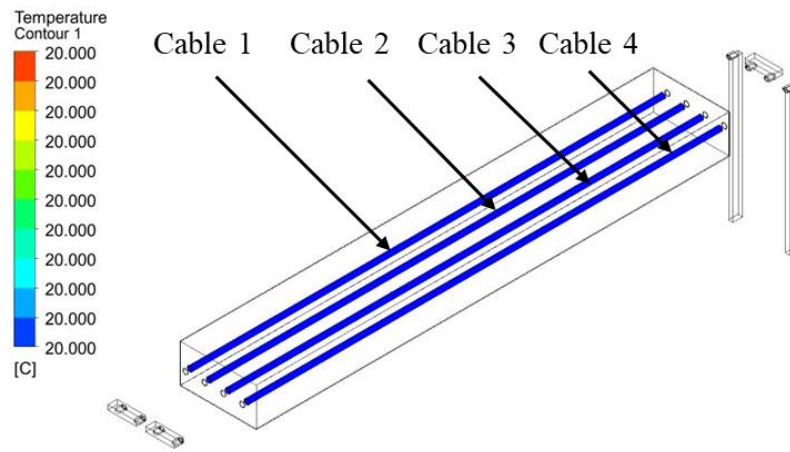


Figure 45. Temperature distribution on cable outer surfaces in the chamber (initial state) and locations of each cable

During the initial two-hour period within one heating cycle, a high-power density is applied to the cable conductors. Consequently, the temperature across the experimental system experiences a rapid increase. Figure 46 depicts the temperature distribution on the cable surfaces at the first hour of this phase. The cable surfaces exhibit a non-uniform temperature distribution along their respective lengths. The highest temperature, reaching 75.3°C, is observed at the middle sections of each cable, while temperatures diminish towards the cable ends due to their proximity to the chamber walls. The temperature difference among the surfaces of each cable, as shown in the figure, are relatively slight. Specifically, the temperatures of Cable 1 and Cable 4 are marginally lower compared to Cable 2 and Cable 3.

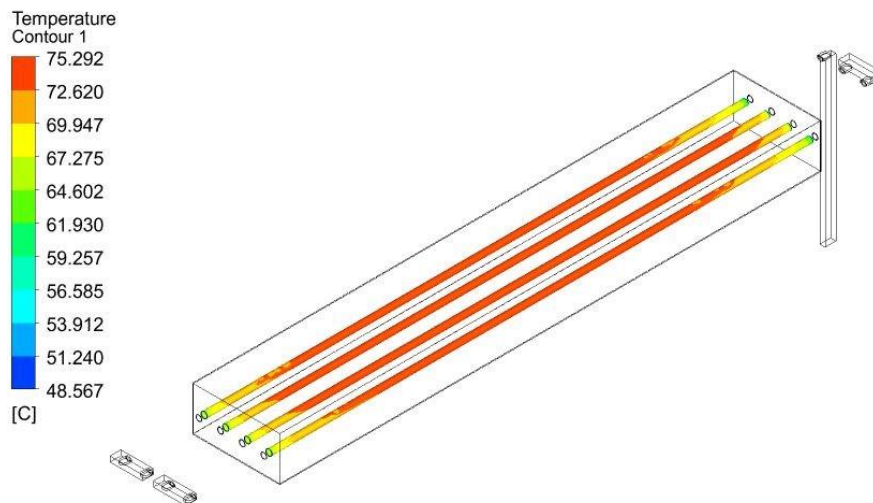


Figure 46. Temperature distribution on the cable outer surfaces in the chamber (1h)

At 2h, Figure 47 illustrates the temperature distribution on the surfaces of the cables. The highest temperature observed on the cable surfaces is approximately 100.5°C, located at the middle sections of the upper surface of Cables 2 and 3. The ends of Cables 1 and 4 register the

lowest temperatures, at around 80°C. For each individual cable, the temperature distribution along its length reveals significantly lower temperatures at both ends compared to the middle section.

At this 2h, the temperature difference between each cable becomes more pronounced than it was at the 1h. Cables 2 and 3 exhibit longer zones of elevated temperature compared to Cables 1 and 4. Furthermore, the upper surfaces of each cable record higher temperatures than their respective lower surfaces, attributed to natural convection within the chamber causing warmer air to accumulate in the upper regions.

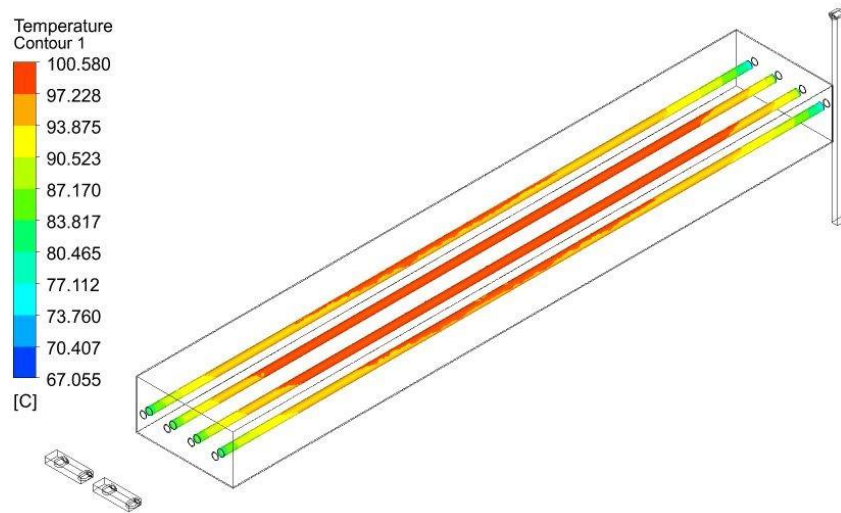


Figure 47. Temperature distribution on the cable outer surface in the chamber (2h)

During the 3 to 8h interval, the system enters a temperature stability phase within a single heating cycle. Here, the power density applied to the conductors is reduced to a lower value, effectively stabilizing the maximum temperature on the cable surfaces at approximately 100°C. Figure 48 illustrates the temperature distribution on the cable surfaces at the 8h. The air within the chamber undergoes heating due to the cables. While the temperature differences among the cables are slightly smaller than at 2h, they remain greater than those observed at 1h.

To facilitate a direct comparison between the experimentally measured temperatures and those simulated, Figure 48 depicts five lines traversing the upper surfaces of the cables. These lines serve as sampling points to capture the temperature variations along the length of each cable at different points in time. Importantly, the placement of each sampling line aligns precisely with the locations designated for experimental temperature measurements.

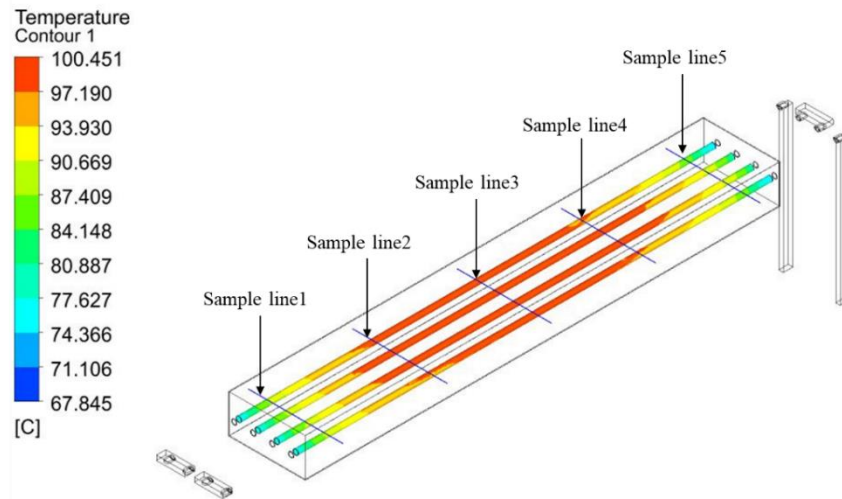


Figure 48. Temperature distribution on the cable outer surfaces in the chamber (8h), with Sampling lines for cable surface temperature at specific points

4.2.5.2 The comparison of temperature sampled from experiment and simulation

The temperature comparison between experimental and simulated data for each cable is presented in Figures 49 to 52. Specifically, temperature data collected from Cable 1 along Line 1 is denoted as "Cable1 1", while data from Cable 2 along Line 3 is labelled as "Cable2 3". In each figure, the left-hand graph represents the temperature data obtained from experimental measurements, while the right-hand graph describes the corresponding temperature data derived from simulation results.

The temperature distributions obtained from both the simulation and experiment exhibit congruence. Across all cables within the chamber, Location 3 consistently registers a higher temperature compared to other positions. Moreover, Location 2 and Location 4 demonstrate closely aligned temperatures, both of which higher than the temperatures observed at Location 1 and Location 5.

Furthermore, the maximum temperature recorded on the surfaces of Cable 1 and Cable 4 during a heating cycle is lower than that of Cable 2 and Cable 3. This difference emphasizes variations in temperature profiles across the different cables.

The temperature trends observed at all locations throughout a heating cycle, as derived from both the simulation and experiment, exhibit a strong degree of correspondence. Specifically, the maximum temperatures on the cable surfaces escalate from 20°C to approximately 100°C within the initial 2 h. Subsequently, during the 3 to 8h interval, the maximum temperatures remain stabilized. Thereafter, temperatures on the cable surfaces progressively decline from their peak values back down to ambient room temperature between

the 9 to 24 h. This observed pattern reflects the dynamic thermal behaviour of the system over the course of a complete heating cycle.

The relatively noteworthy difference between the experimental measurements and simulation results primarily arises between the 2 to 3 h. In the simulation, the temperature remains constant, whereas in the experimental data, there is an initial slight decrease followed by a rapid return to the maximum value over a brief period. This discrepancy suggests a nuanced thermal response within the system during this specific time frame, which is not fully replicated by the simulation model.

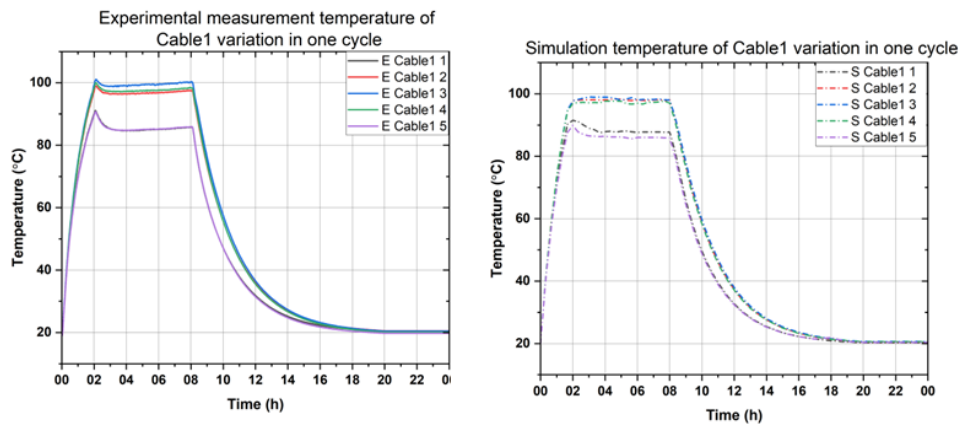


Figure 49. Comparison of cable1 temperature sampled from the simulation and experiment

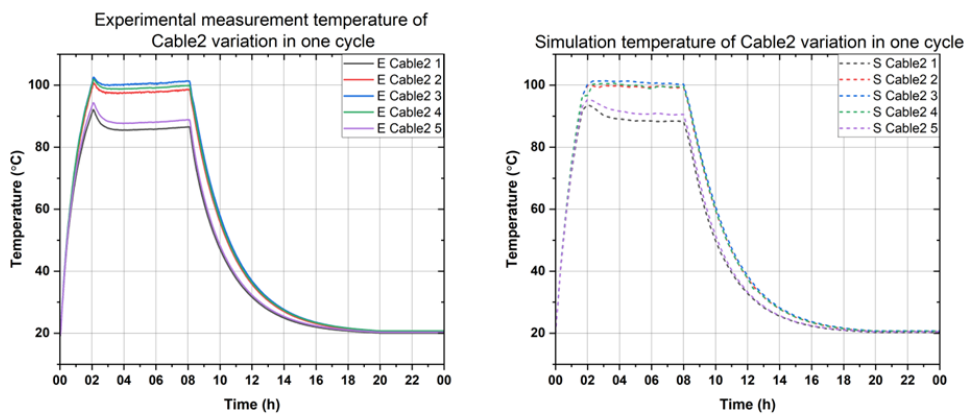


Figure 50. Comparison of cable2 temperature sampled from the simulation and experiment

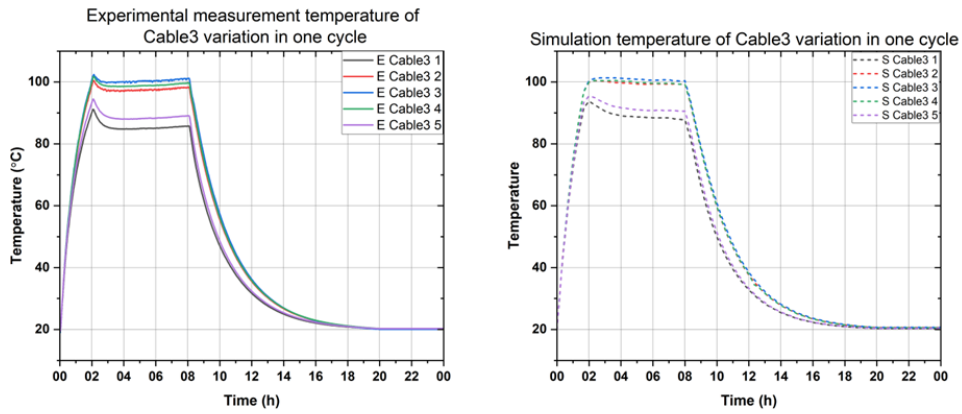


Figure 51. Comparison of cable3 temperature sampled from the simulation and experiment

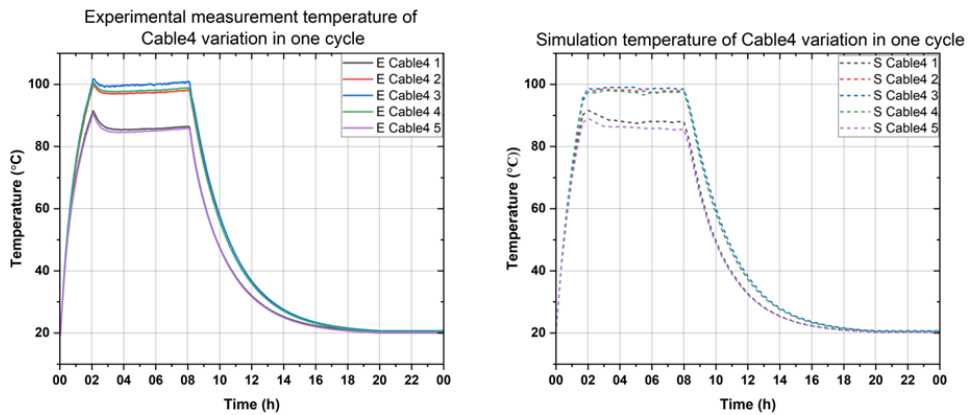


Figure 52. Comparison of cable4 temperature sampled from the simulation and experiment

4.2.5.3 Temperature distribution on cross-section at high-temperature phase

To facilitate the observation of temperature distributions across the cross-section of the model and cables, two planes perpendicular to the length direction of the cables have been generated. Figure 53 provides an illustration of the plane locations. Plane 1 is positioned at the midpoint of the chamber model, whereas Plane 2 is situated closer to the side wall of the chamber model. These planes enable a comprehensive view of temperature profiles within the chamber.

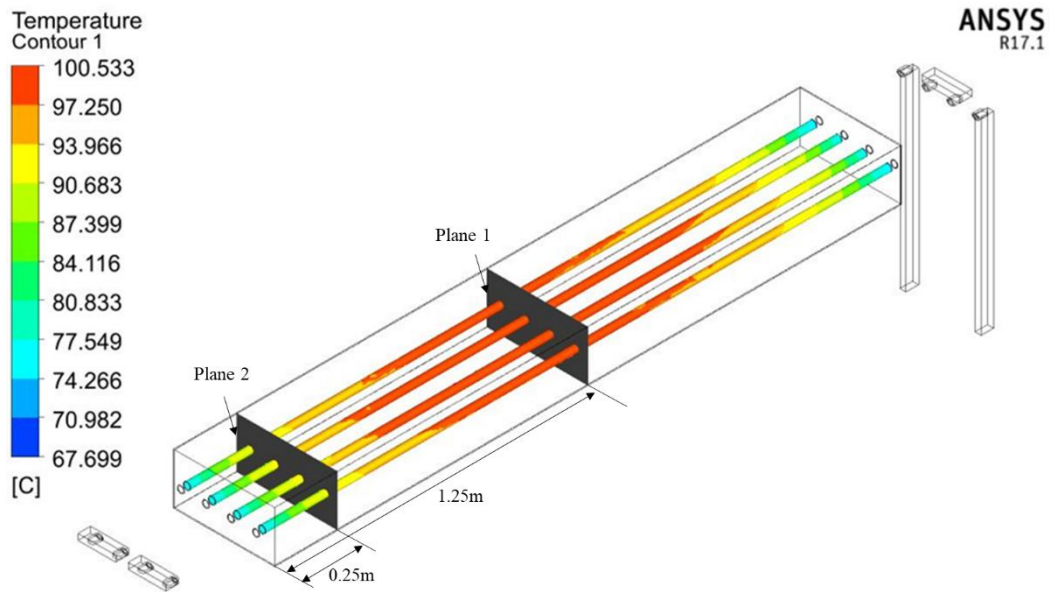


Figure 53. Temperature distribution on the cable outer surfaces in the chamber (3h), with location of planes for presenting the temperature distribution on specific cross-sections

At the high temperature phase, Figure 54 illustrates the temperature distribution across the cross-section of the chamber model at its central location (plane1). Evidently, natural air convection within the chamber is discernible from the temperature distribution within the fluid domain. Higher temperature air, being of lower density, ascends to the upper region of the chamber under the influence of gravity.

Obvious temperature gradients are observed within the cable models. Cables 2 and 3 exhibit larger areas of elevated temperature compared to Cables 1 and 4 in the cross-section. Within each individual cable model, the cable core attains the highest temperature within the cross-section, while temperatures progressively decrease towards locations nearer to the cable surface

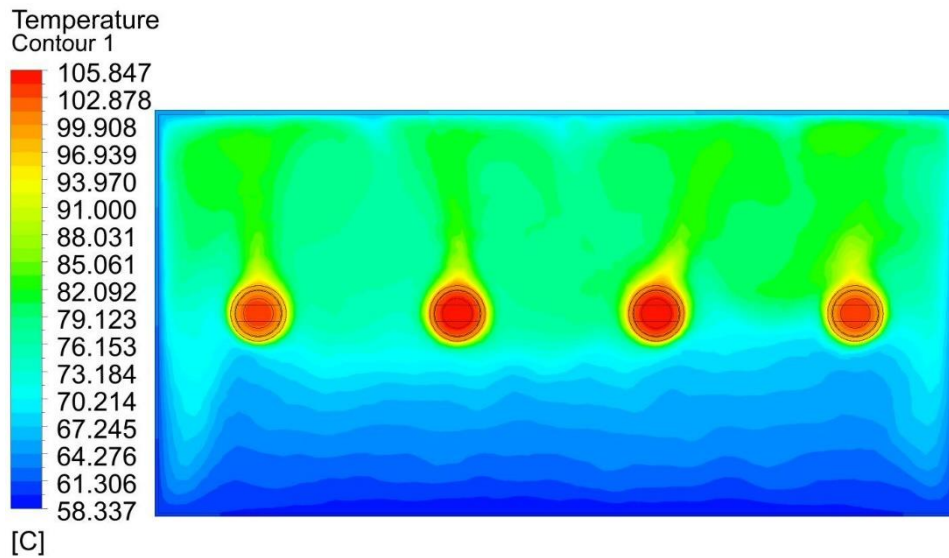
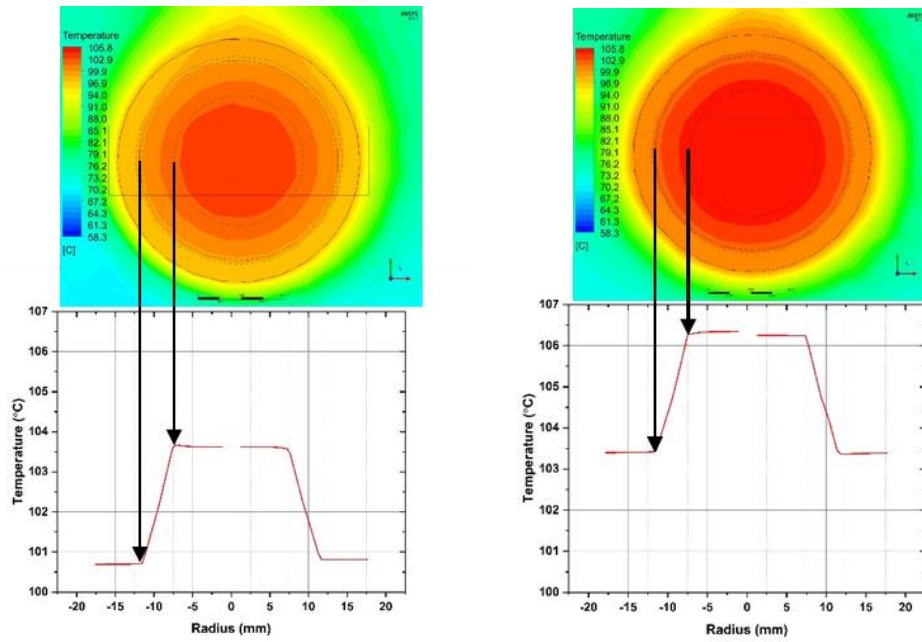


Figure 54. Cross-section temperature distribution on plane 1 (high temperature phase)

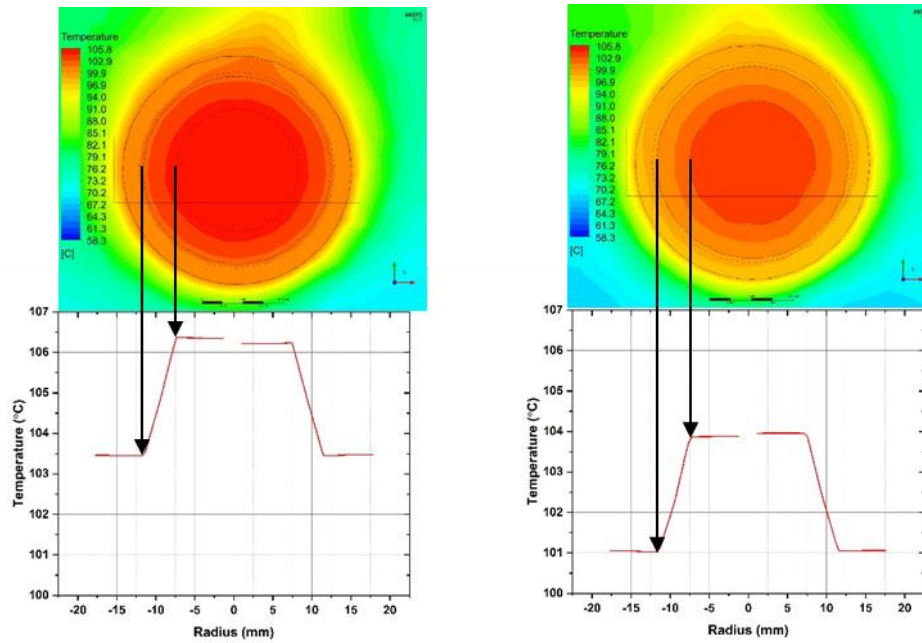
Figure 55 offers detailed, magnified views of the temperature distribution across the cross-section of each cable on Plane 1 at the 3h. Additionally, accompanying charts illustrate temperature profiles along the insulations of the cables. On the figure, surfaces of cable insulations in contact with the conductor and metal sheath are denoted by blue points. Corresponding locations on the temperature charts are identified by red points and are indicated by arrows for reference. This visual aid aids in comprehending the temperature variations within the cable structures.

The presented data in Figure 55 illustrates obvious temperature gradients across the cross-sections of the respective cables. Specifically, for cable 1, the insulation exhibits a gradient ranging from 102.4°C to 99.6°C. In the case of cable 2, this range extends from 105.2°C to 102.4°C, while for cable 3, the gradient spans from 105.4°C to 102.4°C. Similarly, for cable 4, the insulation temperature gradient is observed from 102.6°C to 99.7°C. It is evident that all cables exhibit an approximate 3°C temperature differential from the inner to the outer surface of the insulation. Although the radial temperature difference in the cable insulation is small in this case and may not significantly affect the aging rate, the simulation demonstrates that radial temperature variations do exist. These differences in temperature could potentially impact aging rates in other cables under different conditions or at different voltage levels.



(a)

(b)



(c)

(d)

Figure 55. Cross-section temperature distribution on plane 1 for (a) cable1; (b) cable2; (c) cable3 and (d) cable4 and temperature across depth of cable insulations (high temperature phase)

Figure 56 illustrates the temperature distribution across the cross-section of plane 2, which is in close proximity to the chamber's side wall. The temperature legends on the left-hand side of the Figure 54 and 56 indicate that the maximum temperature on plane 2 is lower than that on the plane 1. Additionally, this figures allow for the assessment of temperature gradients within the fluid domain, between cables, and within each individual cable. For a

more detailed view of the cross-sections of each cable on plane 2, refer to the magnified images presented in Figure 57.

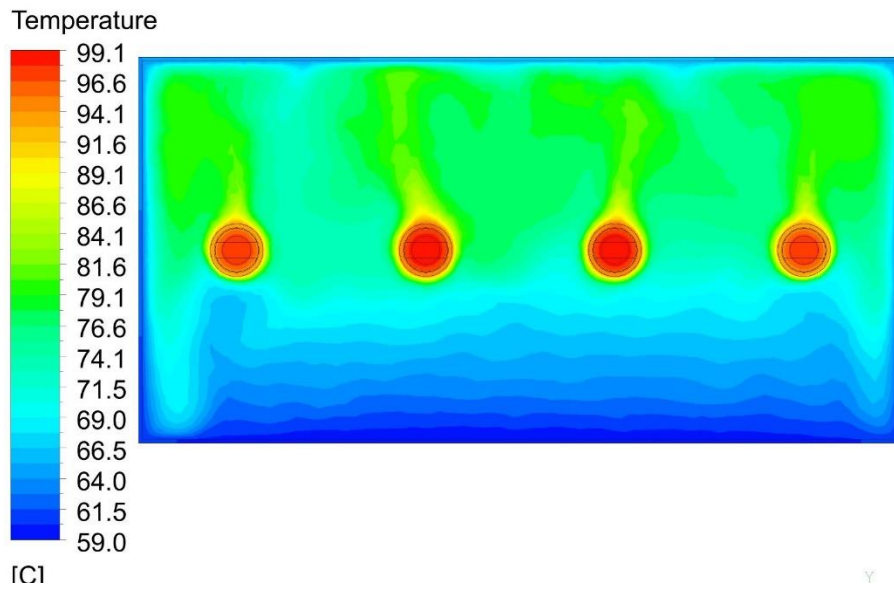


Figure 56. Cross-section temperature distribution on plane2 (high temperature phase)

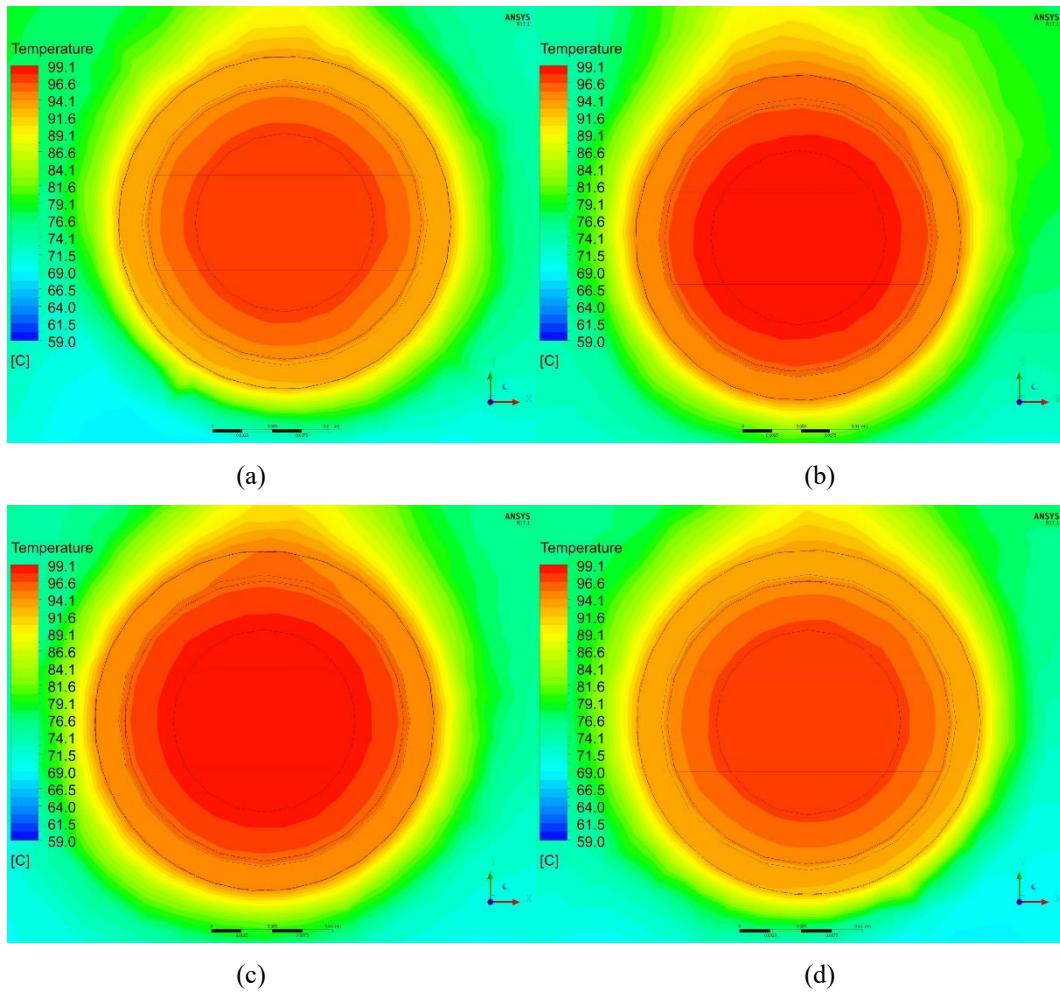


Figure 57. Cross-section temperature distribution on plane 2 for (a) cable1; (b) cable2; (c) cable3 and (d) cable4;

4.2.5.4 Temperature distribution on insulation surfaces along with length

Figure 58 shows the temperature distribution across the outer upper surfaces of the cables' insulation along their respective lengths at the 8h. The temperature distributions of Cable 2 and Cable 3 have a significant overlap, with temperatures ranging from 103°C to 79°C. In contrast, the temperature distributions of Cable 1 and Cable 4 show slight difference. Specifically, Cable 4 registers marginally higher temperatures than Cable 1. This distribution is attributed to the natural air convection occurring within the chamber, resulting in an asymmetric temperature distribution. Consequently, the temperature range for Cable 1 and Cable 4 spans from 101°C to 77°C.

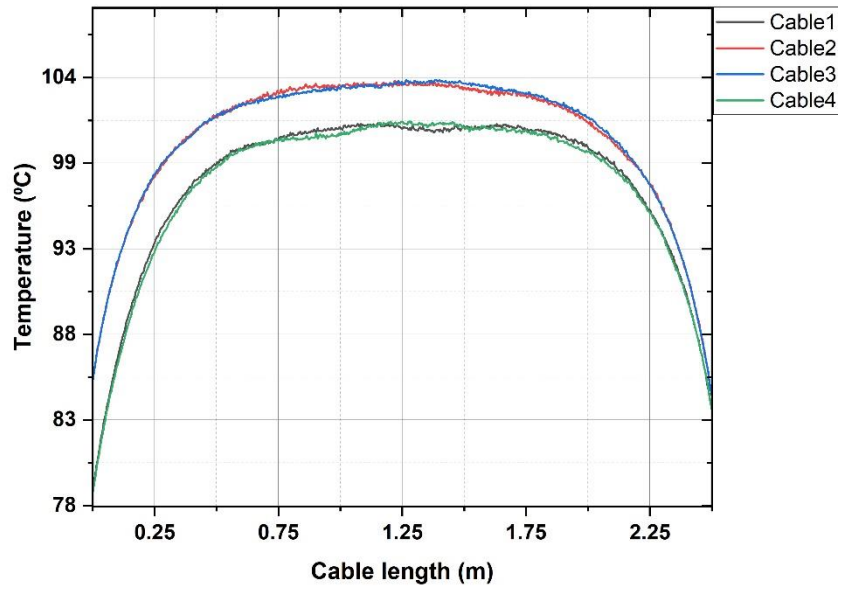


Figure 58. Temperature on cable insulation outer surfaces across cable length (high temperature phase)

Figure 59 provides a representation of the temperature distribution along the inner upper surfaces of the cables' insulation, encompassing their respective lengths at the 8h mark. Much like the outer upper surface, the temperature distributions of Cable 2 and Cable 3 exhibit a significant degree of overlap, with temperatures ranging from 106°C to 80°C. In parallel, the temperature distributions of Cable 1 and Cable 4 mirror their outer upper surface counterparts, with temperatures spanning from 104°C to 78°C.

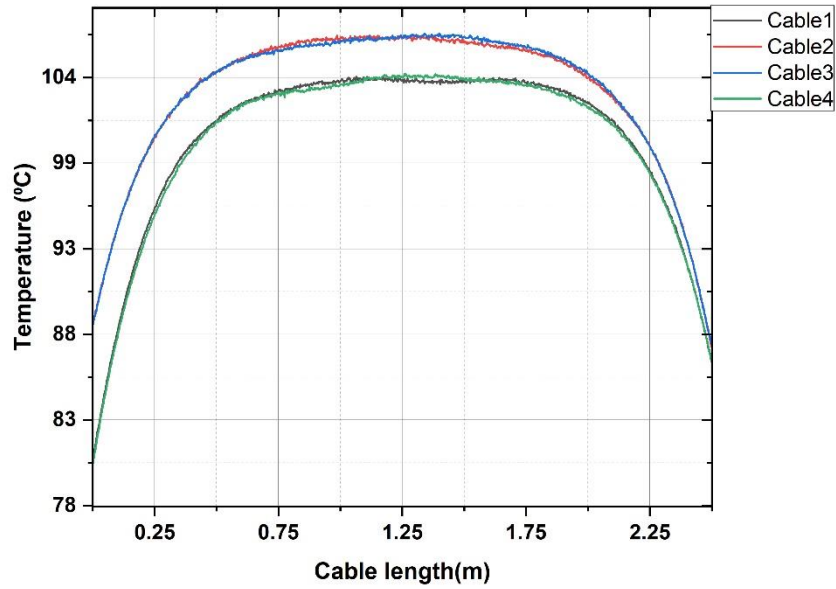


Figure 59. Temperature on cable insulation inner surface across cable length (high temperature phase)

4.2.5.5 Temperature distribution for integrity model

Figure 60 displays the temperature distribution within the integrity model at the 8h. The surfaces of the cables outside the chamber exhibit significantly lower temperatures compared to the inner parts. Additionally, Figure 60 presents the temperature distribution on the connectors. It is observed that short connectors register higher temperatures than their longer counterparts, which can be attributed to their higher power density.

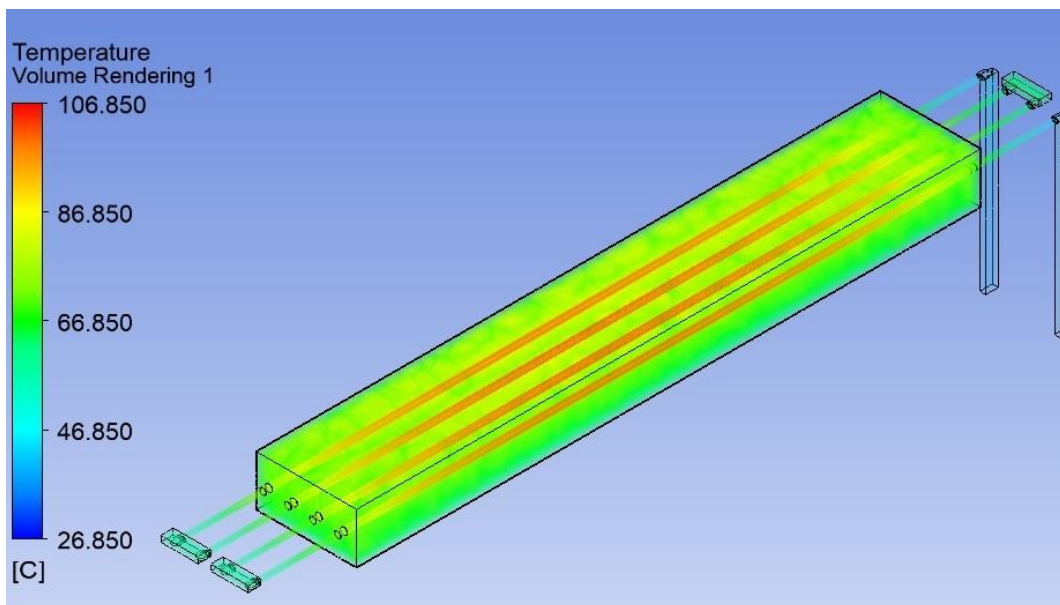


Figure 60. Temperature distribution for integrity model (high temperature phase)

4.3. ANN modelling

The temperature profiles along the cable structure, particularly between meshed points, cannot be directly determined from the FVM simulation results because FVM only provides temperature values at discrete locations, such as mesh nodes or control volume centers. To obtain the continuous temperature distribution between these points, interpolation is required. The accuracy of this interpolation depends on factors such as mesh density, the complexity of the temperature field, and the specific interpolation methods used. Consequently, the temperature profiles obtained at this stage may lack the precision necessary for accurately predicting cable insulation aging conditions. The presence of natural air convection within the chamber further complicates the correlation between specific points on the cable and their corresponding temperatures, making it inherently non-linear and complex. Unlike traditional interpolation techniques, Artificial Neural Networks (ANNs) offer greater computational power and efficiency, potentially providing more accurate temperature profiles of cable insulation at any designated position.

The temperature profiles obtained from the FVM lack the requisite accuracy for predicting cable insulation ageing conditions effectively. To enhance the precision of temperature estimation at various positions within the power cable, facilitating the development of a more accurate ageing model that accounts for temperature variations across different positions, a Bayesian regularization-backpropagation Neural Network is utilized to predict the temperature profile at any given position within the cable insulation. This prediction is based on the data obtained from ANSYS simulation results.

ANN is a powerful data analysis algorithm with high consistency, parallel processing, adaptability, and the ability to handle fuzzy data. Simulating the human brain's neural network, ANN has garnered interest for its knowledge acquisition and inference capabilities [129]-[131]. The Bayesian Regularization-Backpropagation Neural Network (BR-BPNN) integrates Bayesian regularization with Backpropagation Neural Network to tackle overfitting and uncertainty estimation challenges.

Bayesian regularization is a technique that applies principles from Bayesian statistics to the training of neural networks. The core idea is to introduce a regularization term in the training process, which penalizes overly complex models. This helps the network to generalize better to new, unseen data rather than just memorizing the training data (overfitting) [132].

Back-propagation is a standard algorithm used to train neural networks. It works by:

- Forward Pass: Calculating the output of the network for a given input by passing

it through the network layers.

- Error Calculation: Comparing the output to the desired target and calculating the error (usually using a loss function like Mean Squared Error).
- Backward Pass: Propagating this error backward through the network to update the weights using gradient descent. This is where the network learns by adjusting weights to minimize the error.

The standard objective function (F shown as Equation (28)) is modified by adding a regularization term that represents the complexity of the model, often measured by the sum of the squares of the network weights.

$$F = \alpha E_D + \beta E_W \quad (28)$$

where:

- E_D is the sum of squared errors on the training data, more detailed discussion of sum of squared errors would be given in section 4.3.2.
- E_W is the sum of squared weights (the regularization term).
- α and β are parameters that control the trade-off between minimizing the error and minimizing the complexity.

In Bayesian regularization, the weights are treated as random variables with prior distributions. The regularization term can be interpreted as a prior probability distribution over the network weights, favouring smaller (and thus simpler) weights. The training process seeks to maximize the posterior distribution of the weights given the data, which corresponds to finding the most probable model given the data. Unlike other regularization techniques where regularization parameters need to be manually selected, Bayesian regularization can automatically adjust the regularization parameters (α and β) during training. This is done using a technique called the evidence framework, where the parameters are adjusted to maximize the evidence for the model given the data. The weights are updated using a modified version of back-propagation that incorporates the regularization terms. The error gradients are adjusted by the regularization term, guiding the optimization process to avoid overly complex models. This approach enhances model generalization and offers probabilistic interpretations of predictions, supporting informed decision-making in uncertain environments [133].

4.3.1. Construction and Training of ANN

The process of constructing the temperature estimation ANN model is outlined in Figure 61. The initial step involves the implementation of a thermal field simulation for the power cables within the experimental system, as detailed in section 4.2 using the FVM model.

Subsequently, the temperature profile is extracted from the FVM simulation results. In the second stage, this collected data undergoes pre-processing in MATLAB. Here, the temperature profile (T) is transformed from its original Cartesian coordinate system (x, y, z) to a cylindrical coordinate system (r, θ, l) for each individual cable. In this context, ' r ' denotes the radius from the cable centre (m), ' θ ' represents the angle ($^{\circ}$ C), ' l ' signifies the position along the length of the cable axis (m), and ' T ' stands for temperature (K).

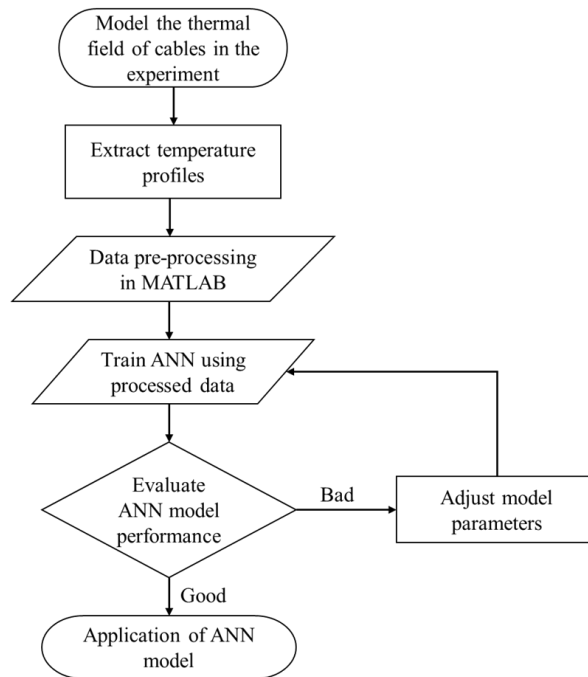


Figure 61. Flow chart of constructing a temperature estimation ANN

The pre-processed data is divided into three different groups: the first is the training data employed to train the constructed ANN model utilizing a selected training function, the second serves to validate the model, and the final group is designated for testing the model. Training data consists of input-output pairs where the input is fed into the network (r, θ, l in this model) and the output is what the network is expected to predict (T in this model). The “train” process refers to the procedure where the ANN learns from the training data. During this process, the model repeatedly processes the training data, adjusts its weights and biases based on the error between the predicted and actual outputs, and gradually improves its accuracy. The efficacy of the ANN model is assessed through various parameters, which serve to ascertain its suitability in accurately estimating temperature profiles for power cables within the experimental setup.

Figure 62 displays the temperature profiles of the insulation layers for the four power cables, extracted from the FVM simulation results in the Cartesian coordinate system. The colour bar corresponds to temperature values in K, aiding in the establishment of models for

power cable lifetime estimation and IR degradation using the Arrhenius Model. The origin point of the Cartesian coordinate system is situated at the midpoint of Cable 1's axis, and the respective cable locations are indicated in Figure 62.

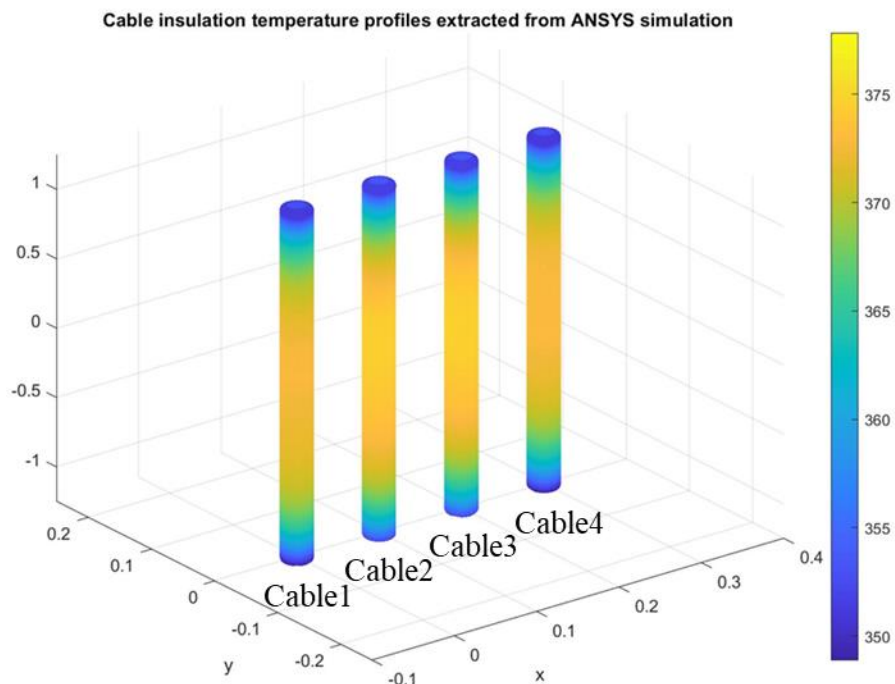


Figure 62. Original temperature profiles of cable insulations in Cartesian coordinate system

Figure 63 presents the temperature profile of the insulation layers of the cables, derived from the FVM simulation results in the cylindrical coordinate system. Here, the length axis aligns with the z axis of the Cartesian coordinate system. Notably, there are numerous positions devoid of temperature profiles. The distribution of data along the length and angle axes exhibits uniformity. However, on the radius axis, the inner surface (7.5mm) of the cable insulation displays more detailed temperature profiles compared to the outer surface (11.5mm). Additionally, temperature data is concentrated within the range of 8.5mm to 9.5mm within the interior of cables' insulation bulk.

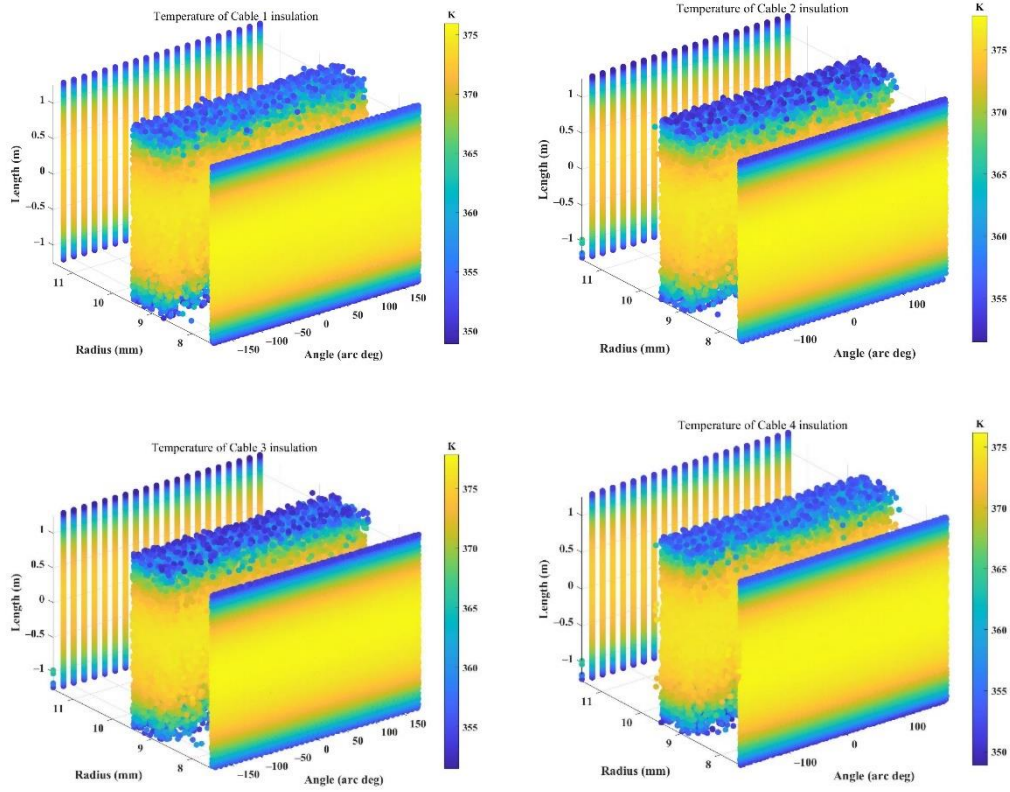


Figure 63. Original temperature profile of cables insulation in cylindrical coordinate system

The MATLAB neural network toolbox is employed to construct the ANN model. The architecture of this model is illustrated in Figure 64, comprising three layers: an input layer, a hidden layer with 10 neurons, and an output layer. The input layer handles independent variables which are then forwarded to the hidden layer for processing. Within the hidden layer, an activation function is applied, calculating the weights of the variables to assess their impact on the target variables. The prediction results are obtained within an acceptable error criterion, and the prediction process is finalized in the output layer [134].

Following the data pre-processing, the data location profile (r, θ, l) will serve as the three input variables for the ANN, while the temperature profile (T) will be the output of the ANN.

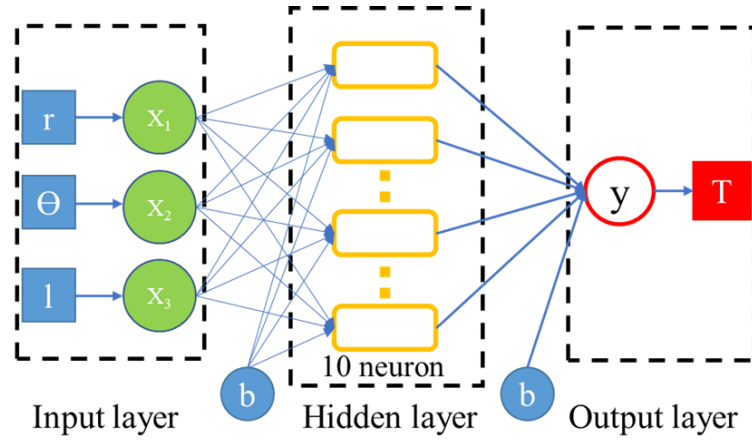


Figure 64. Architecture of ANN with 3 layers

Seventy percent of the processed data obtained from the simulation will be allocated for training the ANN. Fifteen percent of the processed data will be designated for validation, and the remaining fifteen percent will be reserved for testing.

4.3.2. Performance of ANN

The Mean Square Error (MSE) serves as a metric to assess the predicted error rate of the proposed ANN model. Additionally, the Pearson correlation coefficient (R) is employed to gauge the model's performance. R is a crucial indicator in regression analysis, signifying the correlation between the predicted results and the target outputs, as expressed in (29)[135].

$$R = \sqrt{\frac{\sum_{i=1}^N (r_{0,i} - \bar{r}_0)(r_{t,i} - \bar{r}_t)}{\sum_{i=1}^N (r_{0,i} - \bar{r}_0)^2 \sum_{i=1}^N (r_{t,i} - \bar{r}_t)^2}} \quad (29)$$

where, N is the number of samples, r_0 is the actual value and \bar{r}_0 is the average actual value, r_t is the predicted value and \bar{r}_t is the average predicted value. The range of R is between -1 and 1, while with an absolute value of R closer to 1, the better the prediction model performs[136].

The ANN models undergo training for a total of 1000 iterations. The respective performance evaluations of the ANN models for estimating the temperature profiles of each power cable's insulation are detailed in the Table 20 provided below.

Table 20. Performance of ANN model for each cable insulation

ANN model for cables	Minimum MSE value	Pearson correlation coefficient
Cable 1	0.0074971	0.99989
Cable 2	0.0080702	0.99989
Cable 3	0.0086543	0.99988
Cable 4	0.0092131	0.99988

Additional comprehensive information regarding the ANN models is available in the Appendix E. This encompasses:

1. Detailed data pertaining to MSE values of the ANN models, showcasing the fluctuations across training epochs for each power cable insulation.
2. Regression values (R) for both training and test data of the ANN models.
3. Error histograms illustrating the performance of the ANN models.

4.3.3. Application of ANN

The temperature profiles of all cable insulations, extracted from the FVM simulation results, are displayed in Figure 62 using the Cartesian coordinate system. However, it can be challenging to discern instances where cable temperature profiles are absent at specific points in this coordinate system. To address this, Figure 63 presents the temperature profiles of each cable insulation from the FVM simulation in the cylindrical coordinate system. Notably, numerous points, particularly in the radius dimension, lack calculated temperature values. This is primarily due to the fact that the simulation results only provide temperature profiles at the meshed nodes.

To fill in these gaps, developed ANN models for each cable insulation are employed to estimate temperature profiles at locations where data was not available from the FVM simulation results. Figure 65 provides examples of temperature profiles for each cable insulation, predicted by the ANN models in the cylindrical-coordinate system. This dataset comprises a total of 377,118 samples, with 41 samples on the angle axis, 73 samples on the radius axis, and 126 samples on the length axis, serving as the input location variables for the ANN models.

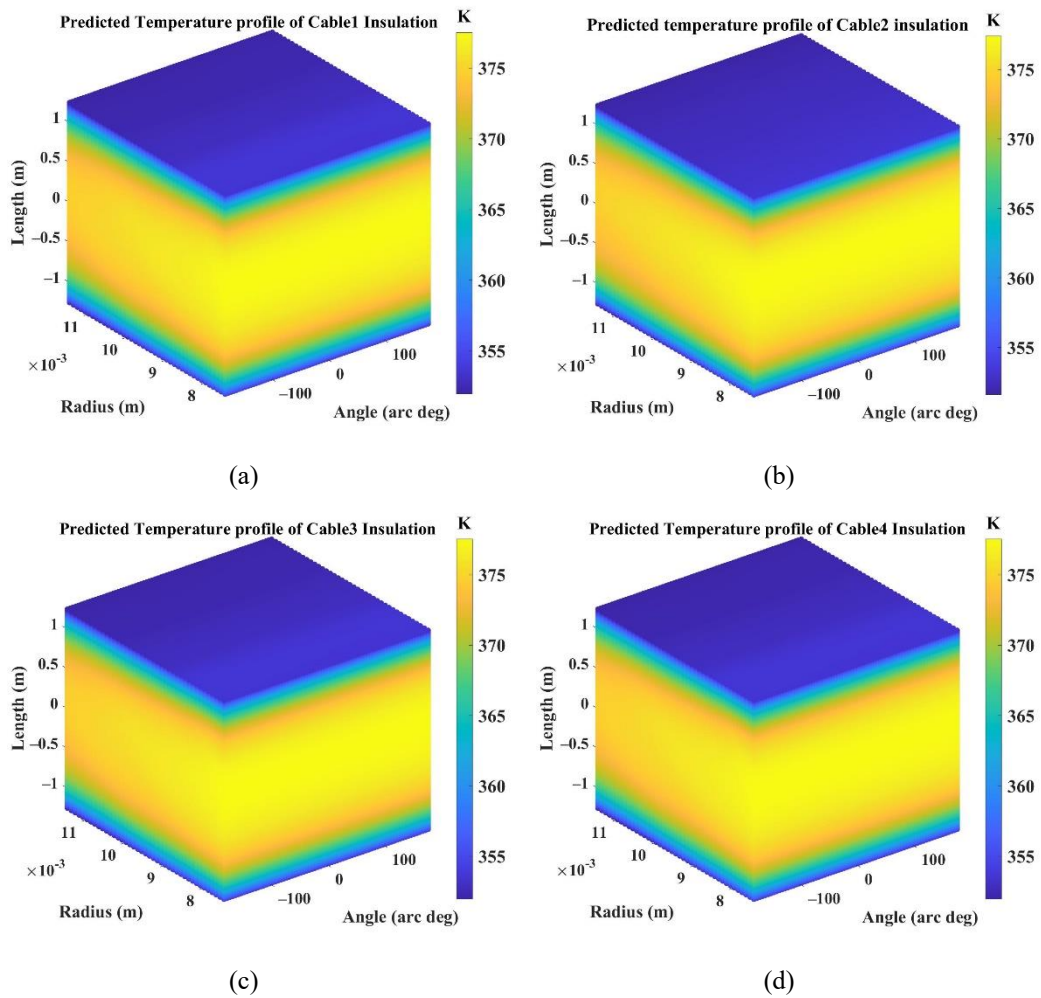


Figure 65. Example of ANN model estimates temperature profiles of the insulation of (a) cable1; (b) cable2; (c) cable3 and (d) cable4 in cylindrical coordinate system

In the context of accelerated ageing of power cables within an enclosed chamber filled with air, this study demonstrates that employing an ANN enables prediction of temperature profiles across all positions in the power cable. By doing so, the ANN introduces a more detailed analytical model capable of extracting temperature data at any given cable position. This enhancement is poised to significantly augment future effective cable bulk ageing calculations for similar scenarios in a following chapter.

4.4. Conclusion

In order to obtain a more comprehensive understanding of the spatial temperature profiles of cables under the experimental conditions outlined in chapter 3, with the aim of constructing a more reliable lifetime estimation model and thermal degradation model for cables subjected to thermal ageing, two models are developed in this chapter: a FVM model and an ANN model.

In the FVM simulation, the cable model is comprised of four layers: conductor, insulation,

metal shield, and outer sheath. There are four cables are connected in series via connectors within the model and positioned within a chamber filled with air. Details regarding the meshing results for each component of the model are also provided in section 4.2.2.

The temperature distribution on the cable surfaces and conductor surface obtained from the FVM simulation within a thermal ageing cycle closely aligns with the measurements from the experiment, indicating a high degree of correspondence. Additionally, the FVM model allows for an assessment of the temperature distribution across the cross-sections of the cables at various lengths. Notably, there is an approximate 3°C difference between the inner and outer surfaces of the cable insulations at the middle length position. This insight provides valuable data for understanding the thermal behaviour of the cables during the ageing process.

The FVM simulation results do not directly provide temperature profiles along the cable structure, especially between meshed points. To address this, a 3-layer ANN model was devised to estimate a more detailed spatial temperature profile of the cable insulation. Through this ANN model, the temperature at any position within the cable insulation under these experimental conditions could be estimated. Furthermore, this combined FVM and ANN modelling approach holds promise for achieving a more precise evaluation of temperatures at specific locations within the cable under varying operating conditions. This integrated approach enhances the accuracy and comprehensiveness of temperature assessments.

By employing the methodology elucidated in this chapter, a comprehensive temperature profile of cable insulation under the experimental conditions outlined in chapter 3 has been generated. This temperature distribution will be utilized in the subsequent chapter to formulate a degradation model for cable IR. Furthermore, the method for acquiring temperature distribution profiles holds significant applicability in predicting cable degradation across various contexts.

Chapter 5. IR degradation models of power cable under thermal ageing

5.1. Introduction

As investigated in section 2.3, thermal ageing stands as one of primary ageing mechanisms of power cables. The influence of temperature on the chemical reaction rate, as illustrated by the Arrhenius model, is significant. Over time, the performance of power cable insulation deteriorates due to thermal ageing. This degradation causes potential safety concerns for operators of power systems and increases maintenance and replacement costs for cables. In aiding preventative maintenance efforts, estimating the performance and remaining lifetime of cables proves valuable.

The predication of a good electrical cable insulation condition is inherently associated with a heightened resistance to electric current flow. Insulation Resistance (IR) testing is a widely acknowledged condition monitoring technique, extensively employed to assess the electrical state of power cable insulation, as elaborated in section 2.4. In various studies addressing power cable ageing, emphasis has been placed on the degradation of IR throughout the ageing processes[64]-[67]. For instance, in [67], it was observed that the resistivity of the tested power cable insulation decreased significantly, by several hundred times, from its initial IR value over 5000 hours, under 80 and 100°C ageing temperatures.

A significant challenge in understanding the dielectric insulation condition lies in developing a quantitative approach to assess insulation degradation over time. A dichotomy model is originally proposed by Chang et.al. to predict IR of rectangular (unit cube) insulation bulk [114][137]. It regards an entire insulation specimen cube as a combination of multiple small sub-cubes and divides them into degraded and non-degraded sub-cubes which possess disparate resistivity. The volume ratio of the two parts is estimated from thermal ageing temperature and duration. based on which the positions of degraded sub-cubes within the specimen are randomly sampled to evaluate the overall IR. According to the original dichotomy model, the electrical resistance degradation trend of the XLPE material under thermal ageing can be classified into three phases, as shown in Figure 66 [114].

- Phase 1: IR gradually decreases from an initial resistance value R_0 since thermal ageing conditions are applied on insulation till a time t_s ;
- Transition phase: IR significantly decreases within a short period from t_s to t_f , due to the percolation phenomenon occurring in the insulation bulk.

- Phase 2: After t_f , the IR gradually approaches toward a completely degraded resistance constant R_d .

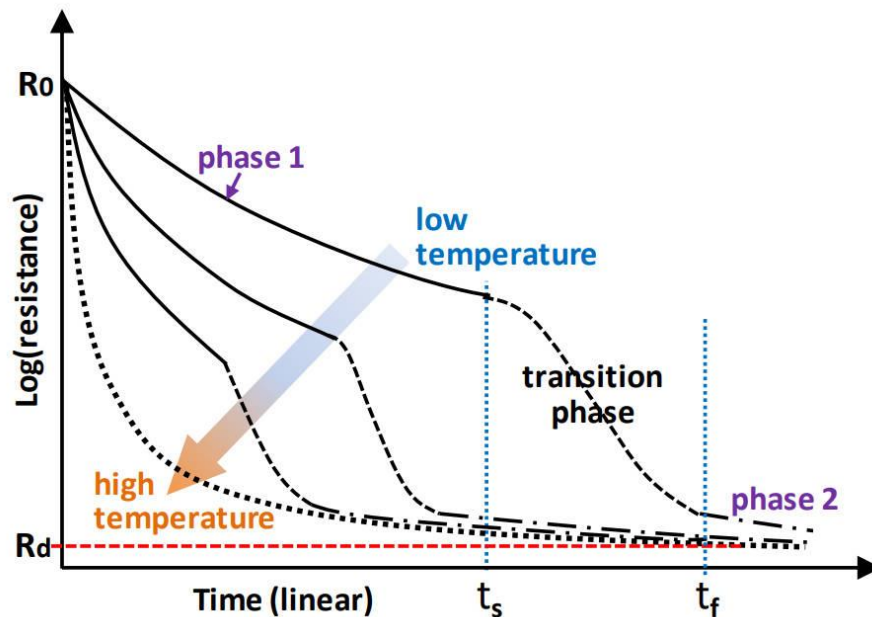


Figure 66. Temperature-dependent IR degradation of XLPE materials under thermal ageing [114]

The transition phase of Dichotomy IR degradation model as a result of taking place of percolation phenomena in the insulation bulk as Figure 67 shown. In the initial stage, insulation material without degraded parts as the Figure 67 (a) shown. The degraded parts represented by blue circles, where the electrical resistivity is much lower than that of the non-degraded portion, are gradually generated and randomly distributed within the insulation bulk with the ageing time increasing performed by (b) and (c) in the Figure 67. As discussed in section 2.4.2, the mechanism of this stage is that defects or contamination gradually appear inside the insulation with the aging process progresses. Due to the resistivity of degraded parts is much smaller than the non-degraded parts, when the volume of degraded parts reaches a certain ratio over the total volume of insulation bulk, a percolation path would be formulated at a time t_s for a current flow through the insulation via an easy path as voltage is applied on cable conductor, as presented by Figure 67 (d). A time t_s here is the starting time of transition phase.

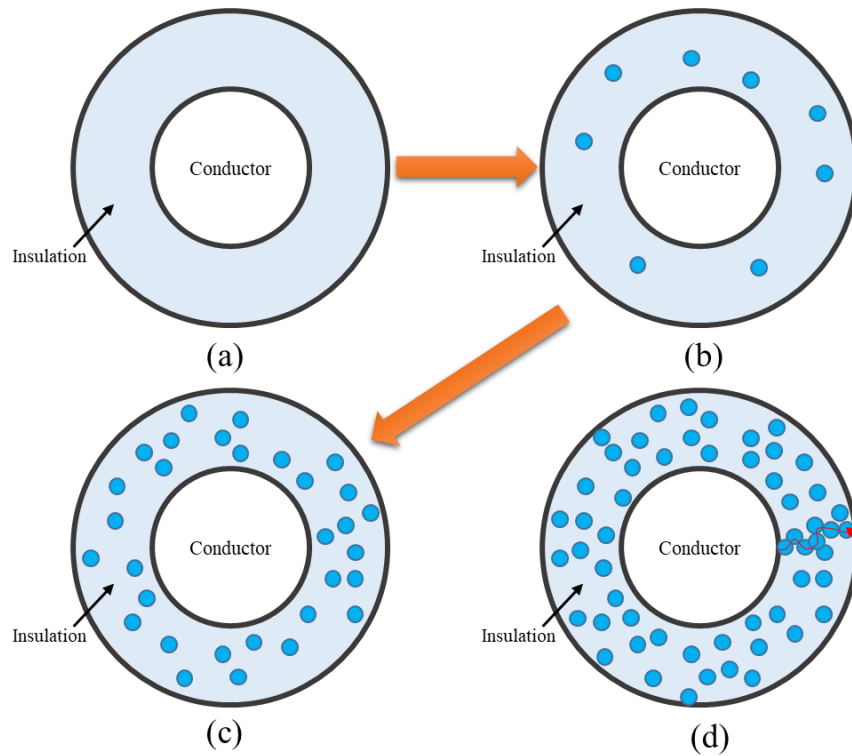


Figure 67. Demonstration of the percolation phenomenon developing process

Despite the original dichotomy model is able to describe the long-term decline of IR over thermal ageing time, it assumes that the insulation is uniform in ageing temperature and chooses the degraded sub-cubes in a random way. The contribution of this research is to extend the original dichotomy model by simulating different degradation degrees between insulation layers under radial temperature gradients and additionally propose a discretization model that simulates the degradation of individual insulation segments given a non-uniform temperature distribution.

In addition, the developed IR degradation models adapt the original unit cube insulation model to a cylindrical insulation model in order to reflect a practical cable insulation. FVM and ANN models are jointly employed to simulate the temperature distribution of cable insulation, which is then incorporated into the enhanced dichotomy model or the novel discretization model to evaluate IR degradation during Phase 1 in Figure 65. In order to perform a comparison not only between the dichotomy and discretization models but also between the uses of different temperature profiles, four IR degradation models are developed in this work:

- a dichotomy model with uniform temperature distribution
- a dichotomy model with radial temperature gradients
- a discretization model with uniform temperature distribution

- a discretization model with non-uniform temperature distribution

These models help investigate the influences of model methodologies and temperature profiles on the IR degradation simulation of power cables under thermal ageing. In addition, different segment sizes and degradation rates are applied to examine their effects on the IR degradation simulation.

The chapter 5 is structured as follows: section 5.2 describes the IR degradation model development and the temperature profile simulation under thermal ageing conditions; section 5.3 presents the application and comparison of the four IR degradation models; section 5.4 discusses the effects of segment sizes and degradation rates on IR simulation results; and section 5.5 presents conclusions and recommendations for further work.

5.2. IR degradation models

Based on the discretization methodologies [138], a sample of extruded power cable insulation can be conceptualized as a cylindrical volume made up of a substantial number of small volume segments in the dimensions of radius, angle, and length, as illustrated in Figure 68, where the inner radius, the outer radius and length of the cable insulation model are denoted by x , X and L , respectively, all in meters.

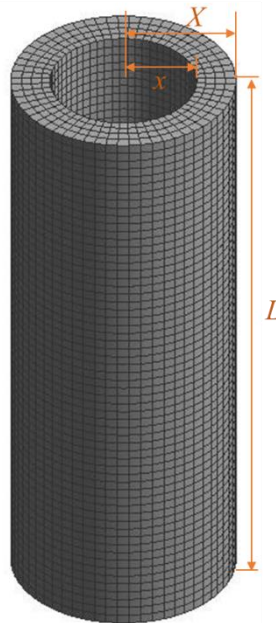


Figure 68. Model of cable insulation divided into elements

The position of the centre point of each segment is represented in a cylindrical coordinate system using the format (x_i, φ_j, l_k) , as shown in Figure 69, where x_i denotes the radial position (m) of an segment, φ_j signifies the segment's angular position (arc degree), and l_k

represents the position (meter) of the segment along the longitudinal dimension.

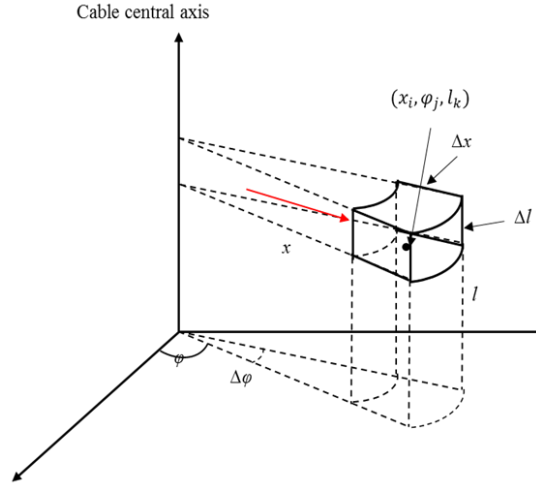


Figure 69. Shape and location of a segment in the cable insulation model

Denoting radial, angular and longitudinal sizes of each segment by Δx , $\Delta\varphi$ and Δl respectively, the resulting numbers of segments along radial, angular and longitudinal dimensions are equal to $M = (X - x)/\Delta x$, $N = 360^\circ/\Delta\varphi$ and $P = L/\Delta l$ respectively. The total number of segments in the cable insulation model is then equal to $N_t = M \times N \times P$.

The volume of a segment in the cable insulation model is dependent on its position along the radial axis. The segments located at the outer insulation layers have larger volumes than those closer to the inner insulation layers. The electrical resistance of any insulation material not only depends on its material resistivity (ρ in $\Omega\cdot\text{m}$) but also on shape and volume [139]. The integral formula of electrical resistance (R) for variable cross-section resistors with parallel curved terminals can be formulated by (30) [140]:

$$R = \frac{1}{A(l_1)} \int_{l_1}^{l_2} \frac{\rho(l)}{(1+\kappa_+(l-l_1))(1+\kappa_-(l-l_1))} dl \quad (30)$$

where l_1 or l_2 is the arc-length parameter of each terminal measured through its surface normal ($l_2 > l_1$), and $A(l_1)$ represents the cross-section area located at l_1 , $\rho(l)$ is the resistivity of the segment. The specific signed principal curvature values of κ_+ and κ_- for the cylindrical segment terminals are taken as 1 and 0 respectively.

It is assumed that the electric current flows through individual segments along the radial axis with a uniform density (i.e., radially from core conductor to any surrounding outer ground sheath) shown as the red arrow in the Figure 69. For each segment, the current flows through two parallel curved surfaces that have unequal cross-section areas. In addition, the material electrical resistivity is assumed to be uniform within an individual insulation segment given its sufficiently small volume.

The evaluation of the resistance of a given geometry can be determined using (30). The electrical resistance of a homogeneous material with parallel curved ends of cylindrical curvature, for which the electrical terminals are placed at radii x_1 and x_2 ($x_2 > x_1$), respectively is given by (31):

$$R = \frac{\rho}{K_0 \times A(x_1)} \ln(1 + k_0(x_2 - x_1)) \quad (31)$$

where k_0 is the signed principal curvature of the surface located at x_1 with area $A(x_1)$. Radii x_1 and x_2 of a segment could be expressed by its location x_i as follow:

$$x_1 = x_i - \frac{\Delta x}{2} \quad (32)$$

$$x_2 = x_i + \frac{\Delta x}{2} \quad (33)$$

The values of k_0 and $A(x_1)$ are represented by (34) and (35) respectively when the geometry of the conductive path terminals are cylindrical surfaces.

$$k_0 = \frac{1}{x_1} \quad (34)$$

$$A(x_1) = \Delta\varphi \times \Delta l \times x_1 \quad (35)$$

The material electrical resistivity is assumed to be uniform within an individual insulation segment given its sufficient small volumes. For the segment located at (x_i, φ_j, l_k) , where $i = 1, 2 \dots M$; $j = 1, 2 \dots N$; $k = 1, 2 \dots P$, with resistivity $\rho(x_i, \varphi_j, l_k)$, based on (31), its resistance $R_e(x_i, \varphi_j, l_k)$ can be formulated by (36).

$$R_e(x_i, \varphi_j, l_k) = \frac{\rho(x_i, \varphi_j, l_k)}{\Delta\varphi \Delta l} \ln\left(\frac{x_i + \frac{\Delta x}{2}}{x_i - \frac{\Delta x}{2}}\right) \quad (36)$$

It may be observed from (36) that the resistance of each individual segment in the cable insulation model is dependent on segments size (Δx , $\Delta\varphi$ and Δl), location of segment in radial axis (x_i), and specified resistivity ρ of segment located at (x_i, φ_j, l_k) , which is the center point of individual segment as illustrated in Figure 69.

The resistances of all the insulation segments are converted into the total resistance of the power cable insulation based on the equivalent resistance model for a DC circuit. The calculation of cable total IR could be generally divided into 3 steps.

Firstly, determining the series resistance of all the segments along an individual radial column at fixed angular and longitudinal locations i.e. $R_c(\varphi_j, l_k)$ in (37), making the insulation model have resistances of $N \times P$ columns as Figure 70 performed.

$$R_c(\varphi_j, l_k) = \sum_{i=1}^{i=M} R_e(x_i, \varphi_j, l_k) \quad (37)$$

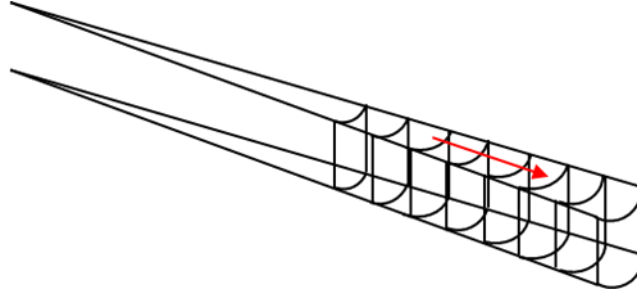


Figure 70. . Segments in individual column

Then, the total resistance of all columns within each individual plane $R_p(l_k)$ at every fixed longitudinal location shown as Figure 71. It can be calculated by parallel connection of all column resistances $R_c(\varphi_j, l_k)$ on the same length axis represented in (38).

$$R_p(l_k) = \frac{1}{\sum_{j=1}^{j=N} \left[\frac{1}{\sum_{i=1}^{i=M} R_e(x_i, \varphi_j, l_k)} \right]} \quad (38)$$

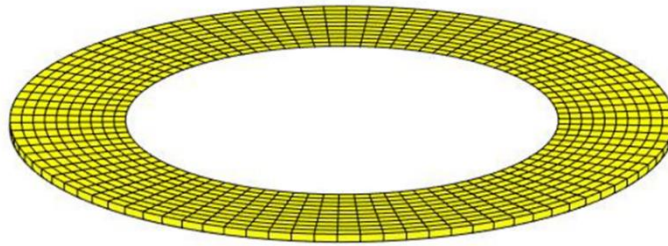


Figure 71. Segments in individual plane

Finally, the total resistance R_t of cable insulation model shown as Figure 72, is calculated by the parallel connection of all plane resistance $R_p(l_k)$ as represented in (39).

$$R_t = \frac{1}{\sum_{k=1}^{k=P} \left\{ \sum_{j=1}^{j=N} \left[\frac{1}{\sum_{i=1}^{i=M} R_e(x_i, \varphi_j, l_k)} \right] \right\}} \quad (39)$$

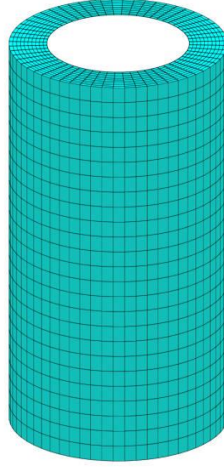


Figure 72. All segments within a power cable insulation model

The resistivity ρ estimation for individual insulation segments by the four different IR models is detailed in the following subsections, respectively.

5.2.1. Dichotomy model with uniform temperature distribution

The Dichotomy models categorize insulation segments into two types: virtually degraded and non-degraded segments which are assumed to have resistivity values of ρ_0 and ρ_d , respectively. The value of ρ_0 is considered to be much greater than the value of ρ_d .

According to (36), the resistances of virtually non-degraded and degraded segments (denoted by R_0 and R_d respectively) are formulated by (40) and (41) respectively:

$$R_0(x_i, \varphi_j, l_k) = \frac{\rho_0}{\Delta\varphi\Delta l} \log_e \left(\frac{x_i + \frac{\Delta x}{2}}{x_i - \frac{\Delta x}{2}} \right), \quad (x_i, \varphi_j, l_k) \neq (x_l, \varphi_m, l_n) \quad (40)$$

$$R_d(x_l, \varphi_m, l_n) = \frac{\rho_d}{\Delta\varphi\Delta l} \log_e \left(\frac{x_l + \frac{\Delta x}{2}}{x_l - \frac{\Delta x}{2}} \right), \quad (x_i, \varphi_j, l_k) \neq (x_l, \varphi_m, l_n) \quad (41)$$

When the ageing temperature distribution is uniform within the cable insulation and also within individual segments, the number of degraded segments N_d which are randomly sampled within the insulation model depends on the total number of segments N_t and the degradation volume ratio V_d , i.e., $N_d = N_t \times V_d$.

Assuming that the degradation rate does not change with ageing time, the value of V_d could be determined based on the cumulative distribution function (CDF) of an exponential distribution in terms of the ageing time t [141]:

$$V_d(t) = 1 - e^{-\lambda(T) \cdot t} \quad (42)$$

where $\lambda(T)$ (in 1/h) is the degradation rate of the insulation material which is a function of the

ageing temperature T depending on material properties. It must be emphasized that $\lambda(T)$ here is obtained from the IR decay tendency rather than the measurement of chemical reaction. Considering that the degradation of cable insulation is thermally activated in this work, $\lambda(T)$ is presumed to follow the Arrhenius model [137] as formulated by (43).

$$\lambda(T) = \lambda_0 \cdot \exp\left(\frac{-E_a}{k_B \cdot T}\right) \quad (43)$$

where λ_0 is a constant (1/h) obtained from experimental data, k_B is the Boltzmann constant of 1.38×10^{-23} J/K, T is in absolute temperature (K), and E_a is IR thermal degradation activation energy (J) of insulation material.

The degradation volume ratio and the number of degraded segments in the model at different temperature can then be calculated by (44) and (45) respectively:

$$V_d(t, T) = 1 - e^{-[\lambda_0 \cdot \exp\left(\frac{-E_a}{k_B \cdot T}\right)] \cdot t} \quad (44)$$

$$N_d(t, T) = N_T \cdot V_d(t, T) \quad (45)$$

Since this model assumes a uniform temperature distribution for cable insulation, the degraded segments accompanying their resistivity ρ_d are randomly placed within the insulation structure for the Phase 1 of insulation thermal degradation. Hot spot temperature of a cable insulation is applied to model bulk to predict IR degradation rate.

The resistance of each individual element contingent to the location of the segment in radial axis (x_i), segments type (degraded or non-degraded), size of segment, degraded resistivity ρ_d and non-degraded resistivity ρ_0 of insulation material which could be obtained from experimental data. A flowchart showing the IR estimation by the Dichotomy model with uniform temperature is presented in Figure 73.

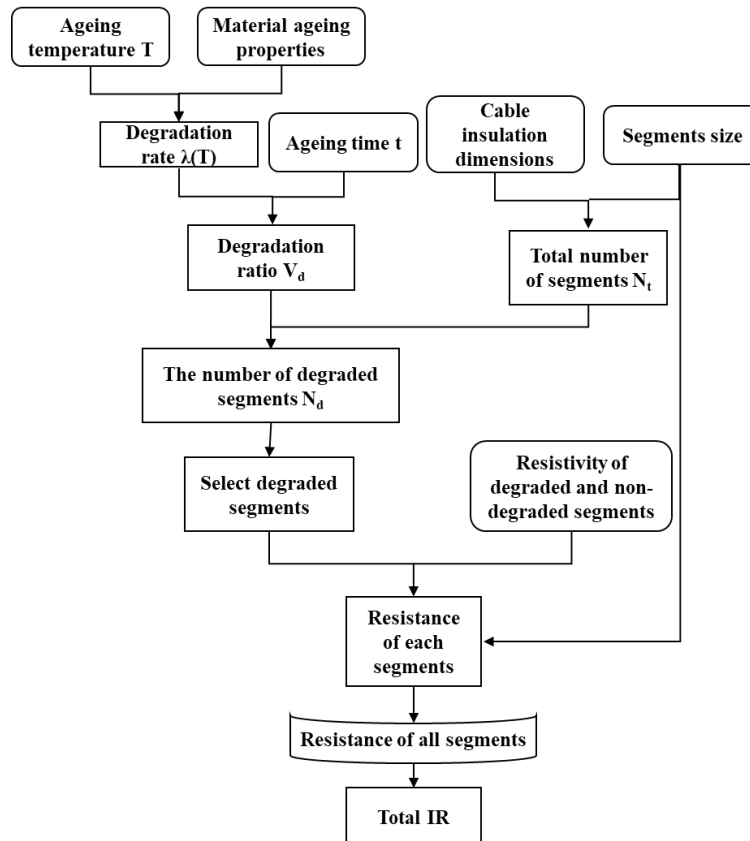


Figure 73. IR estimation process of a Dichotomy model with uniform temperature

5.2.2. Dichotomy model with radial temperature gradients

The temperature gradients along cable radius are created by the propagation of resistive heating from core conductors through insulation layers. On the radial axis, outer insulation layers closer to the ambient environment and further away from core conductors have lower temperatures than inner insulation layers, as shown in Figure 74. The introduction of insulation temperature gradients into the dichotomy model will produce more reliable IR estimation results when power cables are carrying currents.

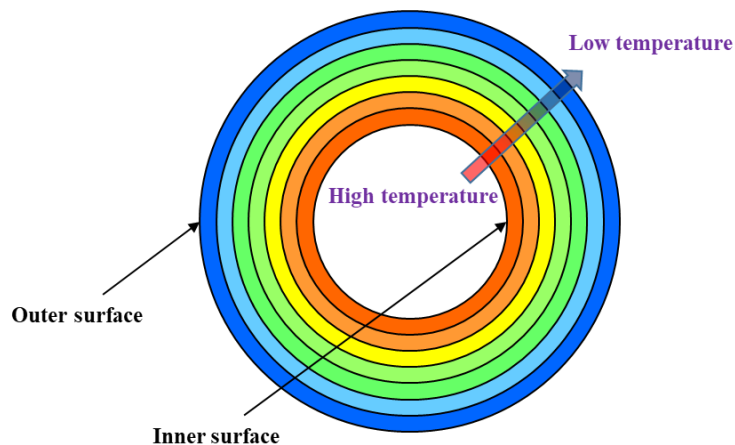


Figure 74. Schematic of insulation temperature gradients along cable radius

According to the Arrhenius Model [141], the radial temperature gradients will result in the inner insulation layers having higher degradation ratios than outer insulation layers. Given that the temperature of the i th individual insulation layer ($i = 1, \dots, M$) along the radial axis is fixed at T_i , the degradation ratio $V_{d(i)}$ and the number of degraded segments $N_{d(i)}$ of the i th layer at ageing time t can be calculated by (46) and (47), respectively:

$$V_{d(i)} = 1 - e^{-[\lambda_0 \cdot \exp(\frac{-E_a}{k_B T_i})] \cdot t} \quad (46)$$

$$N_{d(i)} = N_{t(i)} \cdot V_{d(i)} \quad (47)$$

where $N_{t(i)}$ denotes the total number of segments in the i th layer equaling $(N \times P)$. Since the model assumes a constant temperature for each individual layer, the locations of the $N_{d(i)}$ virtually degraded segments accompanying their resistivity ρ_d within each layer are randomly and uniformly selected for that layer based on the related degradation ratio $V_{d(i)}$. The IR estimation process of the Dichotomy model with radial temperature gradients is shown in Figure 75.

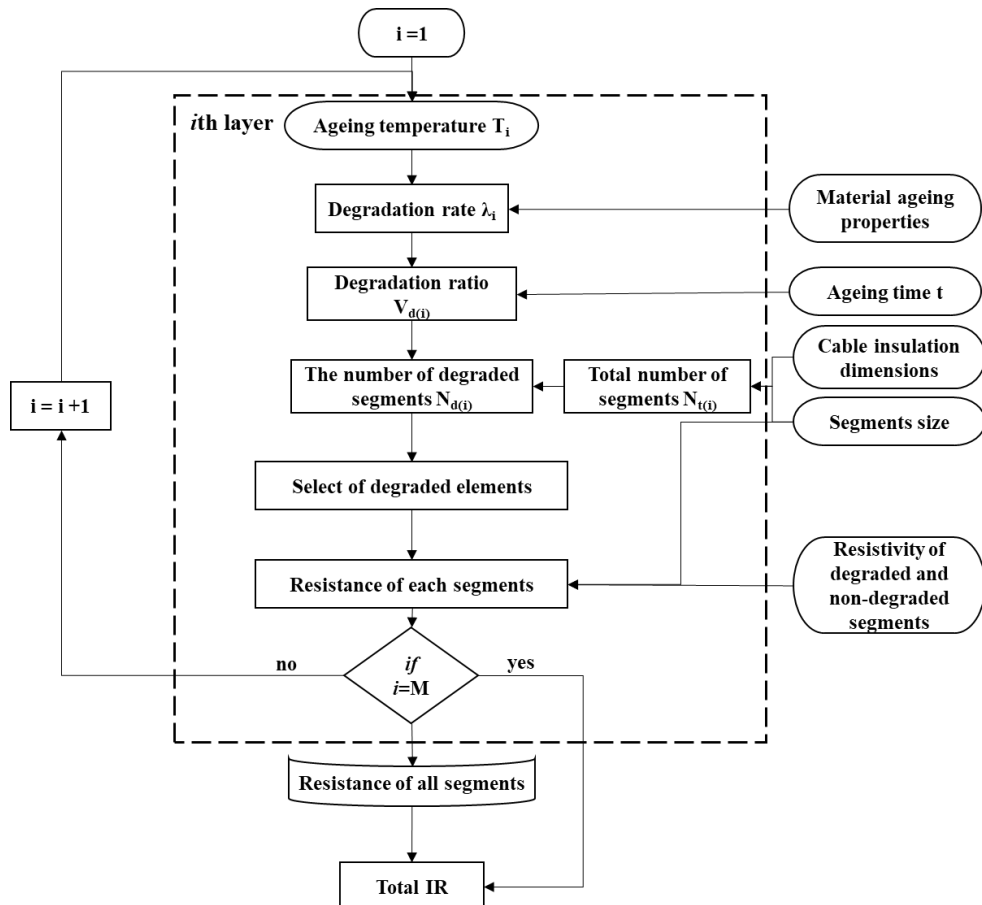


Figure 75. IR estimation process of a Dichotomy model with radial temperature gradients

5.2.3. Discretization model with uniform temperature distribution

Compared with the Dichotomy model which differentiates the segment resistivity between non-degraded ρ_0 and degraded ρ_d only, the Discretization model proposed here simulates the resistivity of individual segments by a function of thermal ageing time t and ageing temperature T . Assuming that insulation segments have consistent temperature, their resistivity is modelled to exponentially decline with t at the same degradation rate:

$$\rho(t, T) = \rho_0 \cdot e^{-\lambda(T) \cdot t} \quad (48)$$

where $\lambda(T)$ is the temperature-dependent resistivity degradation rate which complies with the Arrhenius model as formulated by (48). The resistance of each segment is then calculated by (49) based on its location along radius axis, segment dimensions and $\rho(t, T)$. The process of IR estimation by the Discretization model with uniform temperature is described in Figure 76.

$$R_e(x_i, \varphi_j, l_k, t) = \frac{\rho(t, T)}{\Delta \varphi \Delta l} \ln \left(\frac{x_i + \frac{\Delta x}{2}}{x_i - \frac{\Delta x}{2}} \right) \quad (49)$$

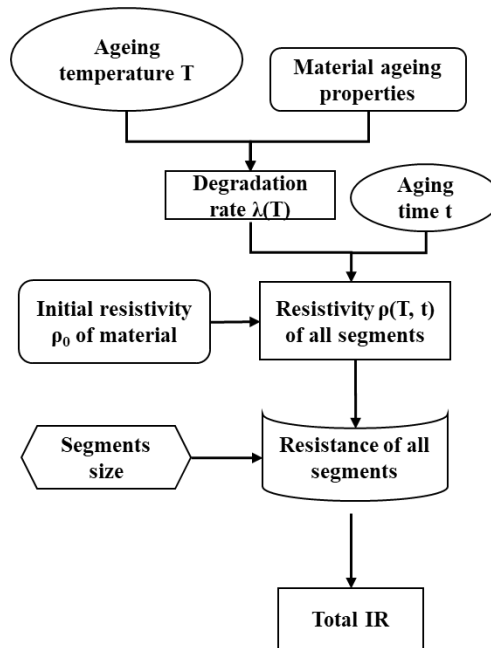


Figure 76. IR estimation process of the Discretization model with uniform temperature

5.2.4. Discretization model with non-uniform temperature distribution

As was noted in Section 5.2.2, the temperature distribution of power cable insulation is generally non-uniform along its radial axis. The cable temperature will also vary longitudinally along the cable especially when it spans a long distance with various ambient environment such as solar irradiation, wind velocity and soil moisture content [142]. The non-uniform

temperature along multiple dimensions would cause thermal ageing rates to vary with the positions within cable insulation. Given the temperature T' of a particular insulation segment locating at (r_i, φ_j, l_k) , its resistivity and resulting resistance at t can be calculated by (50) and (51), respectively. A flowchart describing the IR estimation by the discretization model with a non-uniform temperature distribution is shown in Figure 77.

$$\rho(x_i, \varphi_j, l_k, t, T') = \rho_0 \cdot e^{-\lambda(x_i, \varphi_j, l_k, T') \cdot t} \quad (50)$$

$$R(r_i, \varphi_j, l_k, t, T') = \frac{\rho(x_i, \varphi_j, l_k, t, T')}{\Delta \varphi \Delta l} \ln \left(\frac{x_i + \frac{\Delta x}{2}}{x_i - \frac{\Delta x}{2}} \right) \quad (51)$$

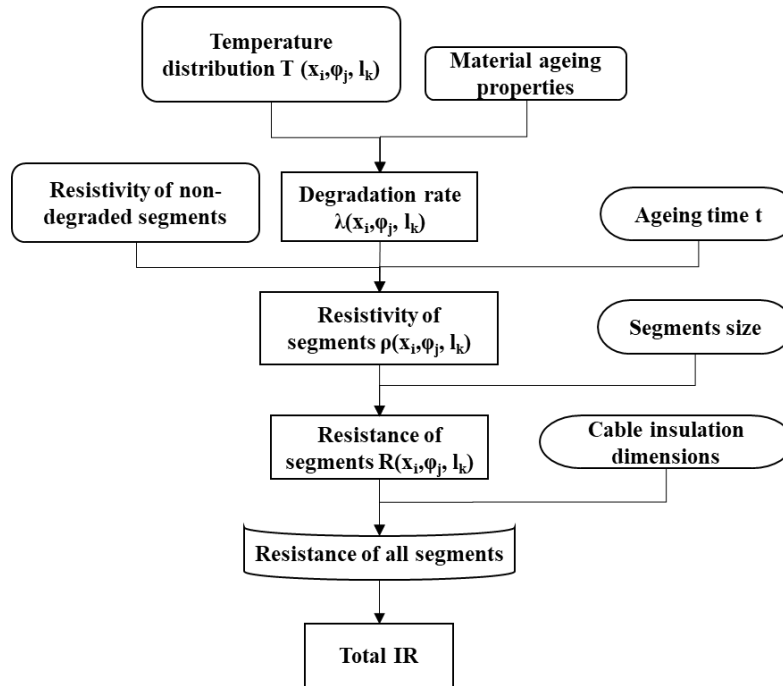


Figure 77. IR estimation process of a Discretization model with non-uniform temperature

5.3. Application of IR Degradation Models

5.3.1. Degradation model parameters estimation

The parameters of the four IR degradation models are estimated here by fitting them to the experimental data of XLPE insulation subjected to thermal degradation which is referenced from the research of Mecheri et al [24]. There are four temperature levels ranging from 80°C to 140°C are used to perform thermal ageing on XLPE insulation samples. The volume resistivity of samples variation during the thermal ageing process are measured by Megger with DC voltage at 0.5kV. As shown in Figure 78, the resistivity of XLPE insulation generally declines with the thermal ageing time, with the decline pattern being affected by the ageing temperature. To construct functions between model parameters and ageing temperature, the

resistivity degradation rates, non-degraded resistivities and degraded resistivities of the XLPE material at various temperatures will be extracted from the results of reference research.

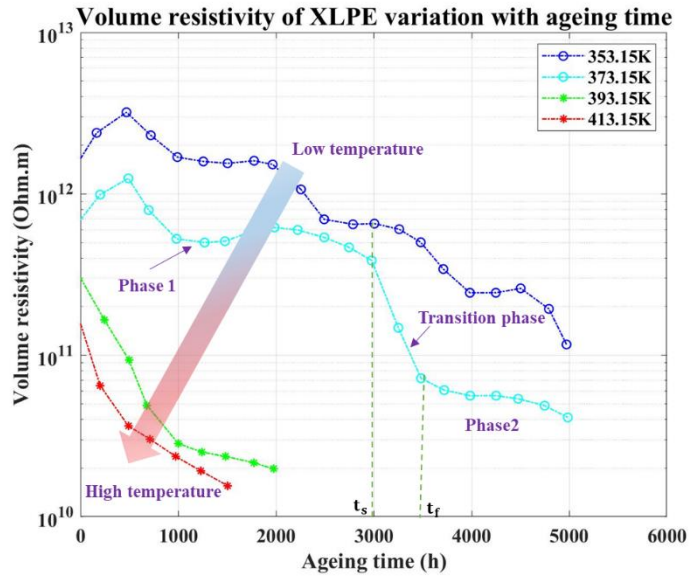


Figure 78. Variation of XLPE volume resistivity with ageing time

The degradation rates of XLPE under four temperature levels are provided in the Table 21 which is obtained by fitting experimental data. According to (48), the degradation rate at different temperature could be predicted by the Arrhenius model due to the degradation is thermally activated. The logarithmic form of Arrhenius equation is shown as (50), which could be used for estimating parameter in the (48) by fitting experimental modelled degradation rates presented in Table 21. The inverse of ageing temperature (K) versus $\ln(\lambda)$ of XLPE sample in this case are fitted and plotted as Figure 79 shown.

$$\ln(\lambda) = \left(-\frac{E_a}{k_B}\right)\frac{1}{T} + \ln(\lambda_0) \quad (52)$$

Table 21. Modelled degradation rate [114]

Temperature (K)	Degradation rate λ (1/h)
353.15	8.5×10^{-4}
373.15	1.0×10^{-3}
393.15	9.0×10^{-3}
413.15	1.4×10^{-2}

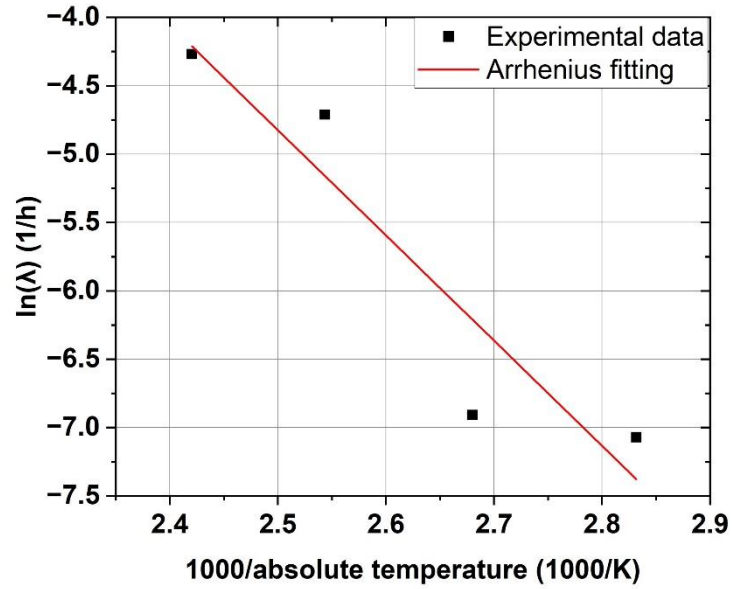


Figure 79. Arrhenius plot of XLPE sample

Based on the Arrhenius fitting result, λ_0 equals to 1.82×10^6 (1/h). the activation energy E_a of the XLPE is 1.0623×10^{-19} J, molar gas constant k_B value is 1.380649×10^{-23} J/K.

The values of ρ_0 and ρ_d at different measurement temperature could also be determined from experimental data, the values are shown in Table 22. Linear fitting of ρ_0 and ρ_d versus testing temperature are presented by Figures 80 (a) and (b) respectively.

Table 22. ρ_0 and ρ_d of XLPE at different temperature

Temperature (K)	ρ_0 ($\Omega\text{-m}$)	ρ_d ($\Omega\text{-m}$)
353.15	2.0×10^{12}	1.0×10^{10}
373.15	1.0×10^{12}	1.0×10^{10}
393.15	3.2×10^{11}	1.9×10^{10}
413.15	1.95×10^{11}	1.54×10^{10}

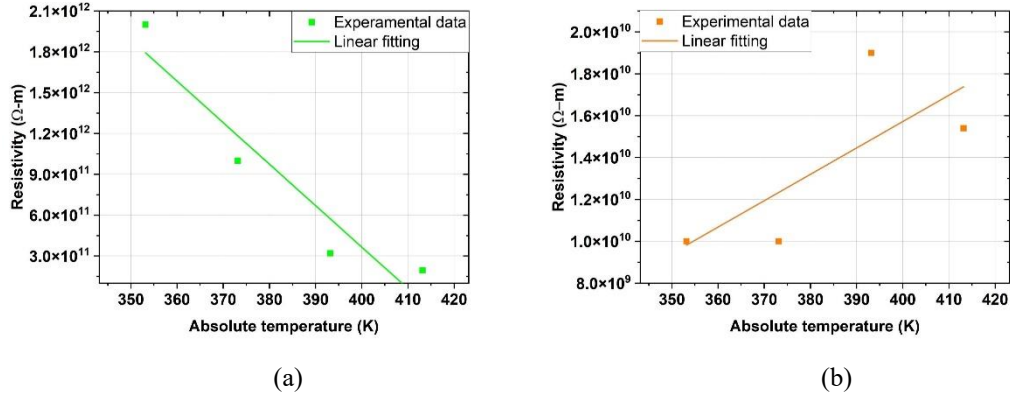


Figure 80. Linear fitting results of (a) ρ_0 and (b) ρ_d

The linear fitting result of non-degraded ρ_0 resistivity with temperature is shown as (53). The (54) is the results of linear fitting of degraded resistivity ρ_d with ageing temperature in K.

$$\rho_0 = (-3.0475 \times T + 1255) \times 10^{10} \quad (53)$$

$$\rho_d = (1.26 \times T - 346.8) \times 10^8 \quad (54)$$

For the insulation model in this case, the insulation dimensions are set to length $L = 1\text{m}$, the insulation inner radius $x = 0.0075\text{m}$, the insulation outer radius $X = 0.0115\text{m}$ (equivalent to a 0.004m insulation thickness). The total number of segments $N_t = M \times N \times P = 10 \times 180 \times 50 = 90000$, resulting in segment dimensions: $\Delta x = 0.0004\text{m}$, $\Delta\varphi = 2^\circ$ and $\Delta l = 0.02\text{m}$.

The ageing temperature distribution of the cable insulation model is the spatial temperature profile of Cable 2 obtained from the chapter 4. Figure 81 shows temperature distribution of a part length of Cable2, from its middle point to 1m away, are taken and used in the application of IR degradation models.

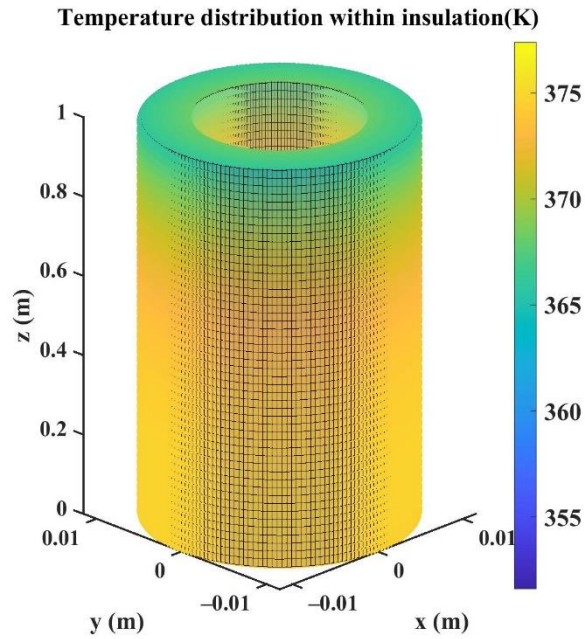


Figure 81. Spatial temperature profiles of the selected 1m cable insulation mode

5.3.2. Comparison of estimated results by IR degradation models

Given the four IR degradation models considering temperature information in different ways, the hotspot temperature of 377.26 K within the entire insulation is applied to the dichotomy or discretization model with uniform temperature, and the discretization model with non-uniform temperature uses the full insulation temperature distribution. The dichotomy model with radial temperature gradients divides the insulation sample into 10 layers along the radial dimension. Table 23 lists the hotspot temperature and related degradation rate adopted for each layer which decrease from the innermost layer #1 to the outermost layers #10. As was noted in sections 5.2.1 and 5.2.2, the degraded insulation segments are selected by the dichotomy models in a random way. To that end, the IR simulation results of the dichotomy models are calculated 50 times, though their standard deviation is found to be smaller than 0.1%. Therefore, the one-time IR calculation results of the Dichotomy models will be presented in this work.

Table 23. Hotspot temperatures and associated degradation rates of 10 insulation layers in the dichotomy model with radial temperature gradients

Layer No.	Absolute temperature (K)	Degradation rate (1/h)
1	377.26	0.002505
2	376.96	0.002464
3	376.66	0.002424
4	376.36	0.002385
5	376.07	0.002348
6	375.86	0.002321
7	375.59	0.002287
8	375.33	0.002256
9	375.10	0.002227
10	374.82	0.002192

5.3.2.1 Initial resistance distribution

The initial resistances of insulation segments estimated by the four IR degradation models are shown in Figure 82 respectively. In the main, the segments of inner layers which have relatively smaller dimensions show higher resistances than those of outer layers. Since the (non-degraded) segment resistivity at the start of thermal ageing process depends on segment temperature only, the dichotomy and discretization models which assume uniform temperature produce the same initial resistance distributions (see Figures 82 (a) and (c)) which lead to a total IR of 94.597 GΩ. When the radial temperature gradients are introduced into the Dichotomy model, the segments of outer layers with lower temperature will have higher resistivity than those that are assumed to be subjected to the hotspot temperature of the entire insulation. Therefore, the dichotomy model with radial temperature gradients produces relatively higher initial segment resistances at outer layers than the model with uniform temperature (see Figures 81 (a) and(b)) as Table 24 shown. This results in a higher total IR equalling around 97.181 GΩ. When the full insulation temperature profile is incorporated into the discretization model, the segment resistance variation with the position-dependent temperature is more accurately simulated along longitudinal and radial dimensions (see Figure 82(d)). The total IR estimated by the Discretization model at the start of thermal ageing process is around 101.316 GΩ.

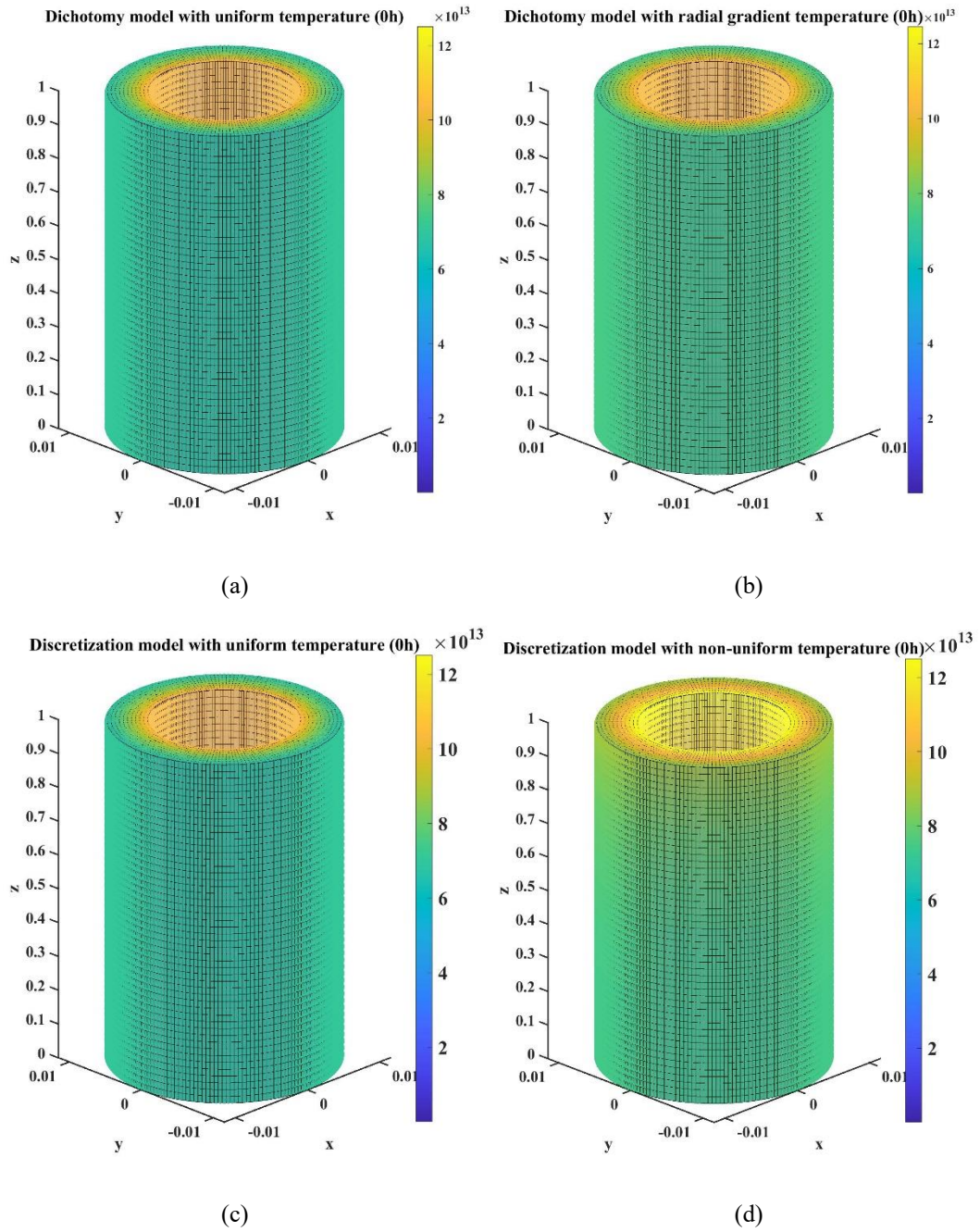


Figure 82. The segment resistances of the cable insulation at 0 h estimated by **(a)** dichotomy model with uniform temperature; **(b)** dichotomy model with radial temperature gradients; **(c)** discretization model with uniform temperature; and **(d)** discretization model with non-uniform temperature

Table 24. Information of individual segments in different insulation layers for Dichotomy model with radial temperature gradients

Layer No.	$R_0 (\Omega)$	$R_d (\Omega)$
1	1.04×10^{14}	3.54×10^{12}
2	9.92×10^{13}	3.36×10^{12}
3	9.52×10^{13}	3.2×10^{12}
4	9.15×10^{13}	3.05×10^{12}
5	8.81×10^{13}	2.92×10^{12}
6	8.48×10^{13}	2.8×10^{12}
7	8.2×10^{13}	2.68×10^{12}
8	7.92×10^{13}	2.58×10^{12}
9	7.67×10^{13}	2.48×10^{12}
10	7.44×10^{13}	2.39×10^{12}

5.3.2.2 Resistance distribution after 100h and 300h thermal ageing

Figures 83 and 84 compare the segment resistance distributions of the insulation sample modelled by the four IR degradation models for thermal ageing durations of 100 h and 300 h. Compared with the dichotomy models which assign low resistivity ρ_d to the random samples of degraded segments, the discretization models are shown to describe the gradual resistance degradation of individual segments in a more appropriate way. Table 25 tabulates the degradation ratio and resulting number of degraded segments that are randomly sampled for each insulation layer by the dichotomy model with radial temperature gradients.

The degradation ratio determined from the temperature-based degradation rate not only increases with layer temperature but also with the thermal ageing duration, which are reflected in the increasing number of degraded segment samples (see Figures. 83 (b) and 84 (b)). Since the dichotomy model with uniform temperature uses the maximum temperature of the entire insulation, the number of degraded segment samples at the outermost layer in Figure 83 (a) is greater than that in Figure 84 (a) which is simulated with the radial temperature gradients. In addition, the inclusion of the full insulation temperature profile allows the discretization model to more accurately simulate the IR degradation of individual segments which vary along both radial and longitudinal dimensions, as shown in Figures 83(d) and 84(d). It is important to recognize that IR is inherently a bulk property, reflecting the total resistance of the entire insulation material. This comparison mainly aims to highlight how temperature gradients influence the degradation process.

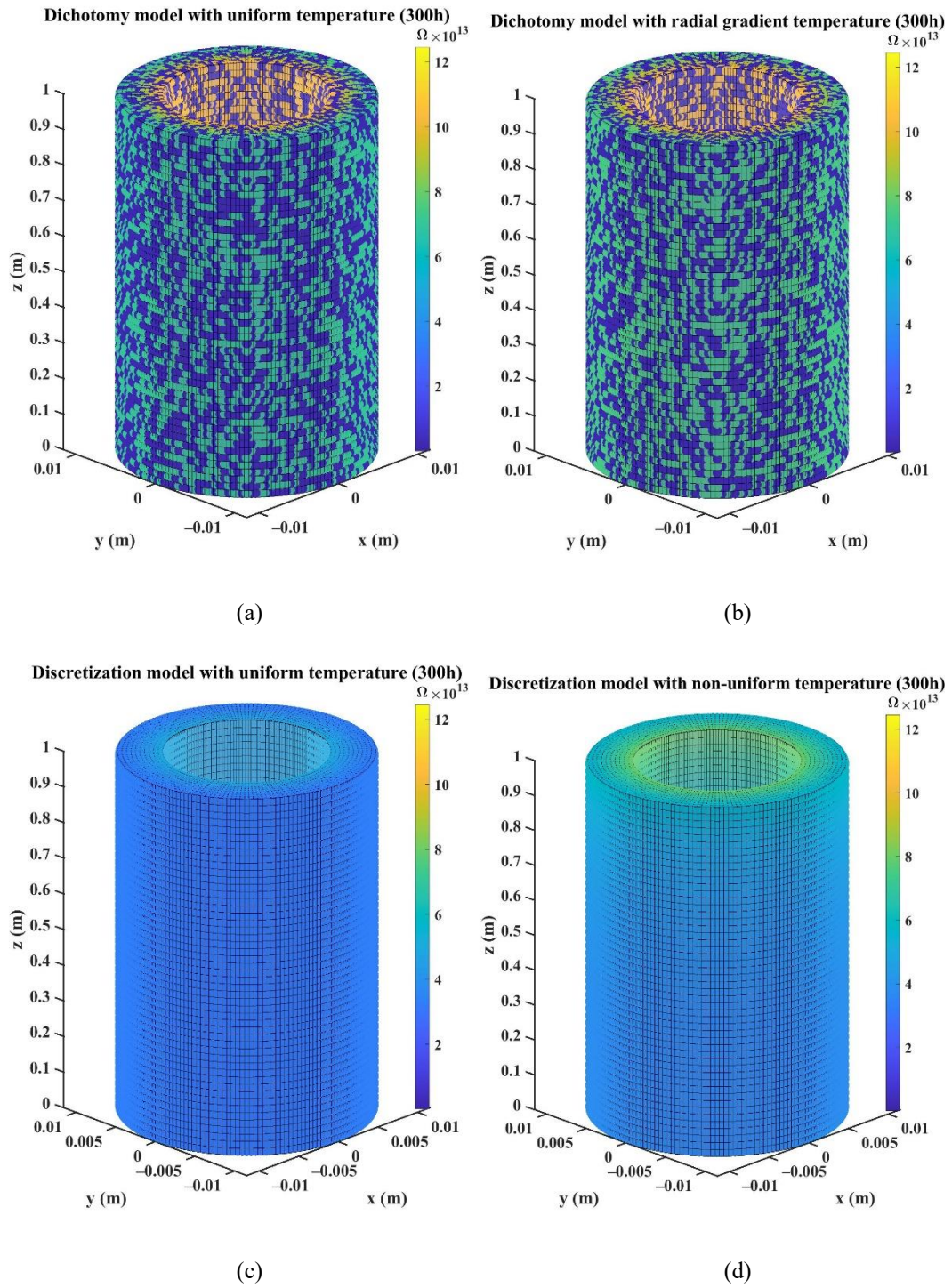


Figure 84. The segment resistances of the cable insulation at 300 h of thermal ageing estimated by **(a)** dichotomy model with uniform temperature; **(b)** dichotomy model with radial temperature gradients; **(c)** discretization model with uniform temperature; and **(d)** discretization model with non-uniform temperature.

Table 25. Degradation ratios and numbers of degraded segments estimated for 10 insulation layers by the Dichotomy model with radial temperature gradients after 100 h and 300 h of thermal ageing.

Layer	Thermal ageing for 100 h		Thermal ageing for 300 h	
	Degradation ratio	Number of degraded segments	Degradation ratio	Number of degraded segments
1	22.158%	1994	52.833%	4755
2	21.836%	1965	52.245%	4702
3	21.526%	1937	51.674%	4651
4	21.220%	1910	51.106%	4600
5	20.927%	1883	50.559%	4550
6	20.715%	1864	50.161%	4514
7	20.443%	1840	49.645%	4468
8	20.194%	1817	49.171%	4425
9	19.964%	1797	48.731%	4386
10	19.687%	1772	48.197%	4338

5.3.2.3 IR degradation curves in short term of thermal ageing

To examine the impacts of model assumptions on IR degradation simulation, the IR degradation curves generated by the four models over the initial short term (0 – 300h) of thermal ageing are compared in Figure 85. Compared with the Dichotomy model which uses the hotspot temperature of the entire insulation, the adoption of hotspot temperature for each of the 10 insulation layers under radial temperature gradients reduces the degradation rates and the numbers of degraded segments at outer layers. This not only produces relatively greater IR simulation results but also slightly reduces the speed of the simulated IR degradation. In addition, different IR simulation results between dichotomy and discretization models which use the same uniform temperature reveal the inherent differences between the two models.

The discretization model simulates the degradation of individual insulation segments, while the dichotomy model describes the overall degradation condition of the insulation sample through a degradation ratio based on which the degraded segments are randomly distributed within the insulation sample. With the degradation ratio increasing during the thermal ageing process, the column consisting of series connected segments along the radial dimension becomes more likely to have multiple degraded segments. This largely reduces the column resistance and causes more degradation in total IR. Therefore, the random selection of degraded segments by the dichotomy model results in lower IR results than the discretization model, as shown in Figure 85. Furthermore, the discretization model with non-uniform temperature is shown to give the highest IR estimates throughout the duration of interest due to it using the full insulation temperature profile instead of hotspot temperature(s).

As discussed in section 2.3, the degradation of insulation material is highly temperature-

dependent, with higher temperatures accelerating the breakdown of the material. This highlights the necessity of modelling the degradation of individual segments with detailed temperature profiles for the IR degradation simulation under thermal ageing. Therefore, the discretization model can use a non-uniform temperature profile to provide a more accurate prediction of IR over time. Additionally, this model accounts for the cumulative effect of thermal stress on sub-segments as the material ages, unlike the dichotomy model, which assumes only degraded and non-degraded segments within the insulation. The discretization model offers a more comprehensive representation of IR by considering the overall impact of thermal gradients and the material properties of the insulation.

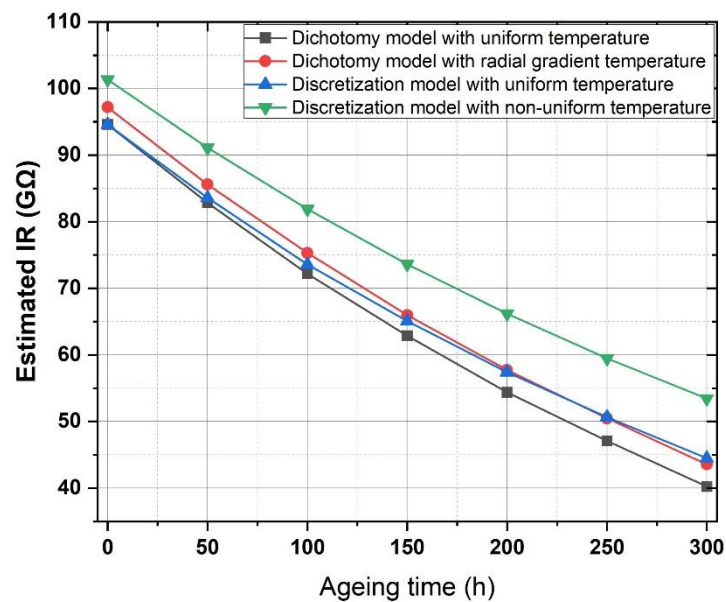


Figure 85. IR degradation curves estimated by different models within 300 h of thermal ageing

5.4. Sensitivity Analysis

5.4.1. Influence of segment size

To examine the influence of the segment size adopted for the IR degradation simulation, the IR simulation results of the four IR models are simulated based on four different segments sizes respectively, as listed in Table 26 where the size #2 is different from the size #1, #3 or #4 along the radial, longitudinal or angular dimension respectively. The material properties and related parameters are the same as those that are employed in section 5.3. To explore the IR degradation trend over a longer thermal ageing period, the IR results are simulated at every 50 hours during 2000 h of thermal ageing, as shown in Figure 86.

Table 26. Insulation segment sizes and resulting numbers of segments for comparison.

Size Index	Δx (m)	$\Delta\varphi$ (°)	Δl (m)	M	N	P	N_t
1	2×10^{-4}	2	0.02	20	180	50	1.8×10^5
2	1×10^{-4}	2	0.02	40	180	50	3.6×10^5
3	1×10^{-4}	2	0.01	40	180	100	7.2×10^5
4	1×10^{-4}	1	0.02	40	360	50	7.2×10^5

Figures 86 (a) and (b) show that the adoption of the sizes #2, #3 and #4 in the dichotomy models almost produces the same IR results, meaning that the segment size variation along the angular or longitudinal dimension examined in this work has negligible impacts on the IR simulation. When the size #1 is used by the dichotomy models, a degraded segment of $\Delta x = 0.2 \text{ mm}$ can be regarded as two degraded segments of $\Delta x = 0.1 \text{ mm}$ that are series connected in a column along the radial dimension. This increases the probability of a single column having more degraded parts and thus reducing the total IR. Therefore, compared with the sizes #2, #3 and #4 of $\Delta x = 0.1 \text{ mm}$, the size #1 of $\Delta x = 0.2 \text{ mm}$ results in the dichotomy models producing slightly lower IR values, especially during 200 – 1200 h of thermal ageing.

When the thermal ageing process approaches 2000 h, the effect of Δx on IR simulation becomes negligible due to a sufficient degradation ratio which makes the two different Δx result in similar degradation parts of single columns. For the discretization models which simulate the individual segment degradation rather than rely on the random selection of degraded segments, the use of the four different segment sizes produces very similar IR results, as shown in Figures 86 (c) and (d). This illustrates that the segment size variations examined in this work have little impacts on the IR simulation of discretization models.

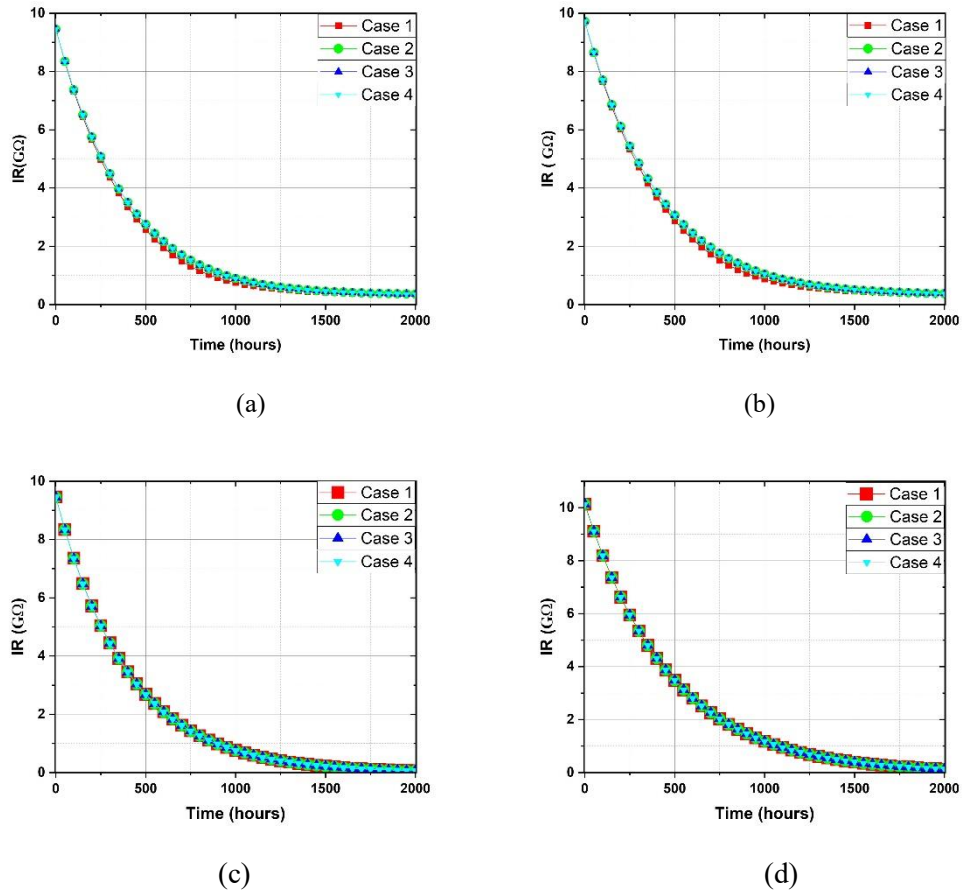


Figure 86. IR degradation trends over 2000 h of thermal ageing simulated based on different segment sizes by **(a)** dichotomy model with uniform temperature; **(b)** dichotomy model with radial temperature gradients; **(c)** discretization model with uniform temperature and **(d)** discretization model with non-uniform temperature.

5.4.2. Influence of degradation rate

The degradation rates employed in the simulation above are determined through the Arrhenius fitting of experimental data sourced from Mecheri et al. [24]. Considering the possible inherent uncertainties, a percentage error of $\pm 10\%$ is introduced in the degradation rate, denoted by 0.9λ and 1.1λ . With other model parameters remaining fixed, the IR degradation trends simulated by the four models using the smaller segment size #3 combined with the three degradation rates are shown in Figure 87 respectively. Even though the uncertainties of degradation rates do not affect the IR degradation pattern, it is estimated that the IR percentage errors are less sensitive to the λ error of $+10\%$ and vary with thermal ageing time in different ways between dichotomy and discretization models, as shown in Figure 86.

The IR percentage error amplitudes of dichotomy models increase to the maximum of about 22% for 0.9λ or 16% for 1.1λ at around 900–1000 h and then relatively slowly drop with the ageing time going further. This might be because the dichotomy randomly assigns a

constant degraded resistivity to insulation segments based on the number of degraded segments jointly determined by the degradation rate and ageing time. The variation in the number of degraded segments induced by the λ percentage error of $\pm 10\%$ increases at the beginning of thermal ageing process and then decreases at certain ageing time when the number of degraded segments approaching to the total number of degraded segments.

In an extreme case where all the segments are fully degraded after a sufficiently long thermal ageing process under any degradation rate, the dichotomy models will give the same IR results independent of degradation rates. For the discretization models which simulate the gradual degradation of individual segments, the IR percentage error amplitudes increase with the ageing time throughout the thermal ageing process and reach the maximum of about 60% for 0.9λ or 40% for 1.1λ at the end of 2000 h. However, the corresponding IR absolute errors at the end of 2000 h are insignificant due to the fact that the IR simulation results are very small after a long thermal ageing time compared with initial IR levels. The modelling of the impact of deviation of degradation rates on IR values provides confidence intervals for IR degradation models.

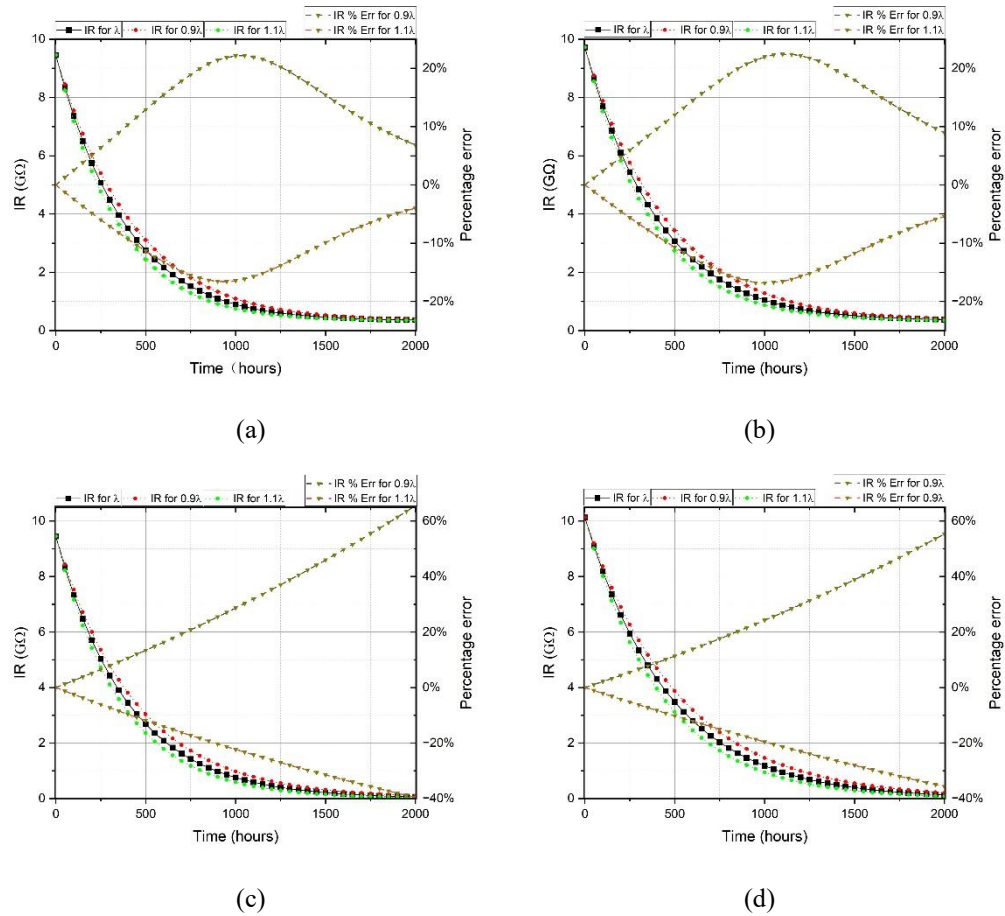


Figure 87. IR degradation trends with upper and lower percentage errors over 2000 h of thermal ageing simulated based on different degradation rates by **(a)** dichotomy model with uniform temperature; **(b)** dichotomy model with radial temperature gradients; **(c)** discretization model with uniform temperature and **(d)** discretization model with non-uniform temperature.

5.5. Conclusion

To quantitatively assess cable insulation degradation over time under thermal ageing condition, the insulation of heavily loaded power cables is subjected to varying extents of thermal ageing that causes the degradation of the dielectric properties, including IR. In this chapter, IR degradation models for cylindrical insulation of extruded power cable under thermal ageing conditions are developed. These models encompass four distinct scenarios:

- dichotomy model with uniform temperature distribution,
- dichotomy model with radial temperature gradients,
- discretization model uniform temperature distribution,
- discretization model with non-uniform temperature distribution.

The fundamental modelling approach for all these scenarios involves dividing the cylindrical cable insulation model into massive and sufficiently small segments. Subsequently, the resistance of each sub-segment is determined, culminating in the calculation of the total IR of the model. This methodology provides a comprehensive framework for evaluating IR degradation in power cable insulation subjected to thermal ageing conditions.

The dichotomy models categorize sub-segments into two groups: non-degraded segments and degraded segments. The proportion of degraded segments in the insulation model (denoted as V_d) increases with thermal ageing time, and this increase is determined by the CDF of an exponential distribution. The rate of increase is correlated with the ageing temperature, following the principles outlined in the Arrhenius model. This modelling approach accounts for the evolving proportion of degraded segments over time due to thermal ageing effects.

In the dichotomy model with uniform temperature distribution, based on the maximum temperature of cable insulation, the whole insulation model with same ageing rate. On the contrary, the radial layers in the dichotomy model with radial temperature gradients have different ageing rate due to the ageing temperature of each layer obtained from FVM and ANN models are utilized in this scenario.

In the discretization models, the resistance of each sub-segment decreases over the course of the thermal ageing process from its initial value based on its individual temperature. In the discretization model with uniform temperature distribution, the maximum temperature of cable insulation is employed for all segments. It means all segments with the same maximum ageing rate.

For the discretization model with non-uniform temperature, the temperature profile of sub-segments at different positions, obtained through the approach which combines FVM and ANN modelling, is employed to calculate the degradation rate of each sub-segment in accordance with the Arrhenius equation. This modelling approach takes into account the evolving resistance of sub-segments as a function of its individual ageing temperature and ageing time, providing a more dynamic representation of the insulation degradation process.

The application and comparison of the IR degradation models are carried out by referencing the experimental data of IR degradation and the spatial temperature profile of cable insulation obtained in FVM and ANN models. This empirical data serves as a basis for validating and evaluating the performance of the IR degradation models. By aligning the models with real-world observations, their accuracy and effectiveness can be assessed, providing valuable insights into the insulation degradation process under thermal ageing conditions.

The study also delves into the influence of segment size and degradation rate on estimation results. It is observed that in dichotomy models, segment size exerts a more pronounced impact on the estimated IR compared to the discretization models. Additionally, the confidence intervals of each degradation model are assessed by considering degradation rates at both 110% and 90% of the standard rate.

Comparing these four IR degradation model scenarios, the discretization models with a more advanced calculation mode than the dichotomy models, because the ageing behaviours of each sub-segments are considered in the discretization models. The characteristic of the discretization models means that it could be further developed to involve more thermal ageing factors. Additionally, the discretization models are less affected by the segments sized than the Dichotomy models. The discretization model with non-uniform temperature distribution employing a detailed temperature profile of cable insulation, which obtained from FVM and ANN models, so that a more accuracy and reliable estimation IR degradation results could be obtained.

The future work about developing IR degradation models would be considering the U-shape variation of IR under the joint effect of annealing effect and thermal ageing. The annealing effect is the process of diffusion from the semi-conductor shields leads to an increase in trap density within the cable insulation. This initial increase in trap density contributes to the rise in conductivity in cable insulation. Nevertheless, as annealing time extends, the diffusion rate gradually decreases, resulting in a subsequent decrease in conductivity over longer periods [118]. The discretization IR model proposed here will be developed further to simulate joint effects of annealing and thermal ageing on IR variations in a physical way, and then fitted to laboratory measurements to understand the characteristics of hopping and band conduction mechanisms in insulation with the presence of semi-conductor layers over the heating process. Moreover, further development of the FVM model could enable the modelling of highly non-uniform insulation temperature profiles, potentially resulting from local partial discharges or complex installation conditions. This advancement aims to give more reliable temperature profiles for the discretization model used in estimating resistance degradation. Additionally, in future models, consideration could be given to the low-resistance current paths formed during partial discharges. This could be modelled by assigning relatively low resistance values to a specific path or region within the insulation.

Chapter 6. Modelling of extruded cables under accelerated thermal ageing in tank filled with water

6.1. Introduction

In addition to thermal ageing mechanisms, the degradation of insulation materials, which employed in extruded power cables, is also recognized as a result of the combined influence of environmental, mechanical and electrical stresses. It is imperative to acknowledge that the ageing resulting from simultaneous and combined stresses cannot be straightforwardly correlated with the damage induced by single stresses at a time, and the summation of individual stress effects does not equate to the ageing induced by the combined stress conditions [143][144]. Combined stresses typically lead to accelerated aging and failure compared to single stresses due to synergistic effects. The complex interactions between different types of stress can create conditions that cause faster and more severe degradation than would be predicted by considering each stress factor in isolation. IEEE Standard 1407 offers comprehensive guidance for conducting accelerated ageing tests on extruded MV cables utilizing water-filled tanks[109], to investigate the mechanisms underlying thermal, electrical, and moisture-induced degradation [145].

Given that thermal ageing significantly influences both the electrical and physical properties of the insulation material [65], temperature plays a pivotal role in the cable ageing process. The temperature monitoring approach advocated by IEEE Standard 1407 entails the utilization of a dummy cable loop for the acquisition of temperature data. In this configuration, multiple thermocouples (T/C) are positioned on the conductor of the cable, as illustrated in Figure 88. The dummy cable employed for temperature monitoring is subjected to roughly equivalent heating conditions as those experienced by the active cables. The stress cone in power cable termination serves to smoothly transition electrical stress from the conductor to the insulation, preventing stress concentration and insulation failure. It protects the cable's insulation from mechanical damage and environmental contaminants while providing mechanical support and stress relief. Typically, conical and layered with both insulating and conductive materials, the stress cone is designed for a snug fit through heat-shrinking or melding. It must be weather-resistant and durable, integrating seamlessly with other termination components to ensure reliable and efficient performance.

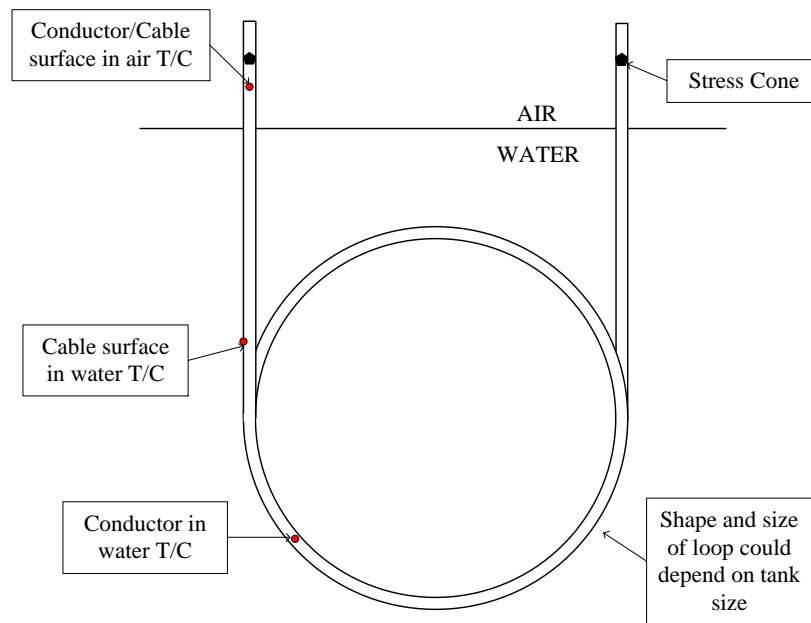


Figure 88. Dummy cable used for temperature measurement as outlined in IEEE Std 1407 [109]

Little attention has been paid to the temperature distribution along the length of cable specimens. The conventional assumption is that temperature is uniformly distributed within the water tank, resulting in consistent temperatures for the dummy loop and all other cables. However, in the absence of a circulation system and temperature control mechanism within the water tank, the temperature distribution of the cable specimens immersed in the tank can be influenced by various factors. These factors encompass the size, shape, and material composition of the water tank, the quantity of cables present, the water volume, and whether the tank is thermally insulated, among others. Consequently, the temperature profiles may exhibit variations at distinct positions within the water tank, potentially diverging even along the length of each cable.

As the temperature difference across cable structures could cause the variation of ageing rate on cable insulation, thus it is meaningful to assess the temperature distribution of power cables under the ageing conditions based on IEEE standard 1407. In the modelling work of this chapter, for the cables accelerated ageing in experiment according to IEEE standard 1407, ANSYS is employed to conduct simulations under different scenarios to assess the temperature profiles of cables within the tank. Therefore, the IEEE standard 1407 could be updated based on the findings of the research presented in this chapter.

To explore the influence of water natural convection on temperature distribution within the tank and along with cables' length, two scenarios are initially examined and compared: (a) the water in the tank is regarded as a solid material, and (b) the water in the tank is regarded

as a fluid with natural convection. This preliminary investigation is conducted without accounting for any forced circulation of water in the system.

In the subsequent phase, the simulated cable temperature distributions for scenario (b) are investigated, now incorporating forced water circulation. Five distinct scenarios are assessed and compared, namely: 1) a water tank without a rotating fan, 2) a rotating fan at 10 revolutions per minute (rpm) positioned on the middle section of the tank's side wall, 3) a rotating fan at 50 rpm located on the middle section of the tank's side wall, 4) a rotating fan at 10 rpm situated on the lower section of the tank's side wall, and 5) a rotating fan at 50 rpm positioned on the lower section of the tank's side wall. The primary objective of this part is to illustrate the influence of forced water circulation and, prospectively, to determine the optimal fan positions and rotational speeds necessary to achieve uniform temperature distribution across the cables undergoing the ageing process. The selected fan speeds of 10 rpm and 50 rpm represent a low and high range of rotational speeds to examine how varying levels of forced water circulation, corresponding to laminar or turbulent flows, influence the temperature distribution within the tank. The placement of the fan (either in the middle or lower section of the tank's side wall) is intended to explore how water movement within the tank, particularly in relation to the overall flow and heat accumulation areas, affects cooling efficiency.

6.2. Modelling of cable loops in water tank without forced circulation system

6.2.1. Simulation setup

The constructed cable model is designed consisting of a conductor and insulation, as depicted in Figure 89. These cables are designed based on typical 11kV power cable specifications. The inclusion of thin shield components, including semi-conductors, is omitted due to their negligible physical thickness, which exerts minimal influence on the thermal conductivity properties of the cable. Each cable possesses an overall diameter of 20 mm, featuring a solid copper conductor with an 8mm diameter. The thermal conductivity of the conductor is set at $386.7 \text{ W/m} \cdot \text{K}$. The insulation material is XLPE, encompassing a 6 mm thickness around the conductor. The specific heat value of XLPE is stipulated as $4000 \text{ J/kg} \cdot \text{K}$, with a thermal conductivity of $0.29 \text{ W/m} \cdot \text{K}$, and a density of 941 kg/m^3 .

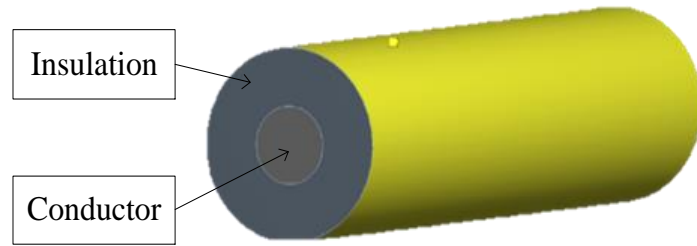


Figure 89. Local structure of cable model

The cables are presumed to be installed within the water-filled tank in accordance with standard looping procedures, where they were bent into 1.5-turn circles with a radius greater than the minimum bend radius. IEEE Standard 1407 recommends three types of tank layouts, employing either rectangular or cylindrical tank shapes. For this simulation, the rectangular water tank is employed, with the specific physical layout and constituent elements outlined in Figure 90 and Table 27, respectively. The tank walls consist of two layers: the inner stainless steel tank layer that comes into contact with the water, and the tank insulation layer utilized for heat retention. A surface covering is situated on the tank's top to prevent water evaporation and to sustain thermal boundary stability, thus ensuring the temperature of the water remains consistent.

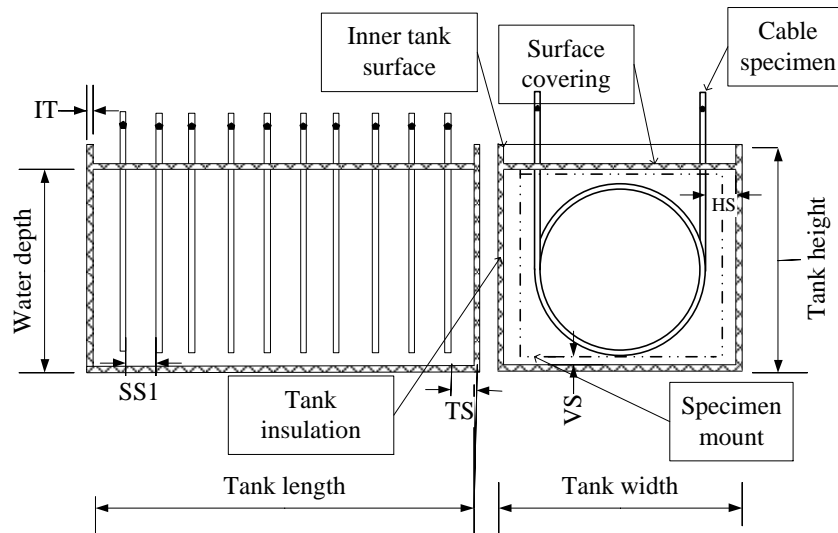


Figure 90. Tank layout according to IEEE Standard 1407 [109]

Table 27. Tank dimensions according to IEEE Standard 1407 [109]

Length (mm)	875
Width (mm)	800
Height (mm)	910
Side spacing (HS) (mm)	50
End spacing (TS) (mm)	75
Bottom spacing (VS) (mm)	50
Specimen spacing 1 (SS1) (mm)	75
Water depth (mm)	800
Specimen bend radius(mm)	350

The simplified structure of the simulation tank, featuring 10 cables according to the example provided by IEEE standard 1407, is illustrated in Figure 91. The tank is configured as an enclosed domain, completely filled with water, and its walls are constituted of steel boundaries with negligible thickness. In adherence to IEEE Standard 1407, the cable loops do not come into contact with the tank walls or bottom. Each of the 10 cable specimens is positioned within the water tank, with a presumed bend radius of 350 mm.

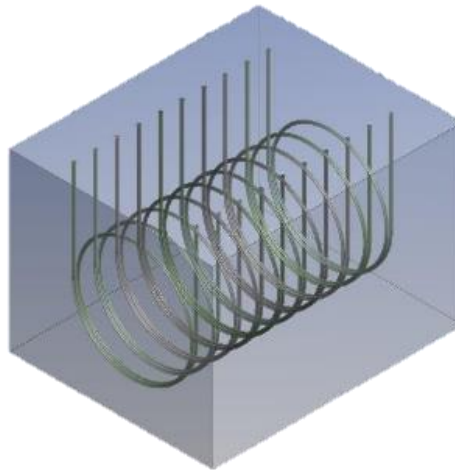


Figure 91. Overall simulation model

6.2.1.1 Water treated as solid material

The initial simulation employs a steady-state thermal analysis tool, considering the case where water is treated as a solid material. In this scenario, the water in the tank possesses only thermal and density properties, devoid of any natural fluid convection.

IEEE Standard 1407 outlines a prescribed technique for elevating the conductor temperature in order to expedite the ageing process of cables. This method entails the utilization of a current transformer to induce current into the conductors of each cable, thereby generating heat as a consequence of Joule loss. The advantage of this heating method lies in its fidelity to the actual heating experienced by cables in real-world field applications.

In the simulation, a power density is imposed on the conductors of each cable to emulate the heat generated by the flow of current within the cable. To attain a steady-state maximum temperature of approximately 90°C, in accordance with the specified maximum temperature outlined in Standard 1407, a power density of $2 \times 10^5 \text{ W/m}^3$ is applied to the conductors of each cable.

The tank walls were assigned a convection property to replicate the dissipation of heat from the steel walls to the surrounding air environment. The ambient temperature was established at 27°C, and the convection coefficient was designated as $5 \text{ W/m}^2 \cdot \text{K}$, characteristic of natural convection in air. It is assumed that the air within the tank remains stagnant, and thus, the convection coefficient is held constant with respect to temperature.

6.2.1.2 Water treated as fluid

In the second simulation, the Fluid Flow tool was employed, treating water as a fluid with inherent natural convection properties. This scenario's outcome is anticipated to closely mirror the actual cable temperature profiles, without the aid of any assisted convection methods.

In this simulation, the pressure-based solver is utilized, and absolute characteristics are defined for the velocity formulation. This is because only natural convection of water is present in the water tank domain. The energy function model is enabled during the model setup stage. Subsequently, in the setup of cell zone conditions and boundary conditions, the conductor domains are treated as a source term with one energy source exhibiting a constant power density of $2 \times 10^5 \text{ W/m}^3$.

The thermal conditions of the insulator walls and conductor walls are thermally coupled. Additionally, the thermal properties of the tank walls are configured for heat convection to the ambient air, with a heat transfer coefficient of $5 \text{ W/m}^2\text{K}$. Once again, the ambient air temperature is set at 27°C.

In the simulations, the geometry models are discretized into approximately 1.9 million and 9.8 million small elements for the Solid simulation and Fluid simulation, respectively. The precision of the meshing is determined by the results of several iterations of the simulation. Each individual element undergoes calculations, and the aggregated outcomes from these computations collectively yield the temperature distribution results.

The calculations are executed until a state of thermal equilibrium is attained, signifying that the internal heat generation rate and external wall heat dissipation rate have reached a point of balance.

6.2.2. Simulation results

6.2.2.1 Solid simulation results

The final temperature distributions in a steady state for the 10 cables are depicted on the left side of Figure 92. The highest temperature observed in the cable loops is 91°C, occurring in the middle cables. The lowest temperature within the cable loops is 58°C, localized in the cables near the tank walls. It is evident that cables situated closer to the middle of the tank exhibit higher temperatures. This temperature variation arises from the fact that cables near the tank walls have a greater propensity to dissipate heat into the ambient air, while the cable in the middle of the tank accumulates more heat and is more influenced by the thermal effects of adjacent cables.

The temperature ranges for each cable loop in the Solid simulation results are shown on the right side of Figure 91. The cables in the tank are numbered from 1 to 10, with 1 and 10 representing the loop surfaces closest to the tank walls. The blue line in Figure 92 represents the maximum temperature within each cable loop, and the orange line represents the minimum temperature within each cable loop. The temperature range for each cable loop is approximately 15°C.

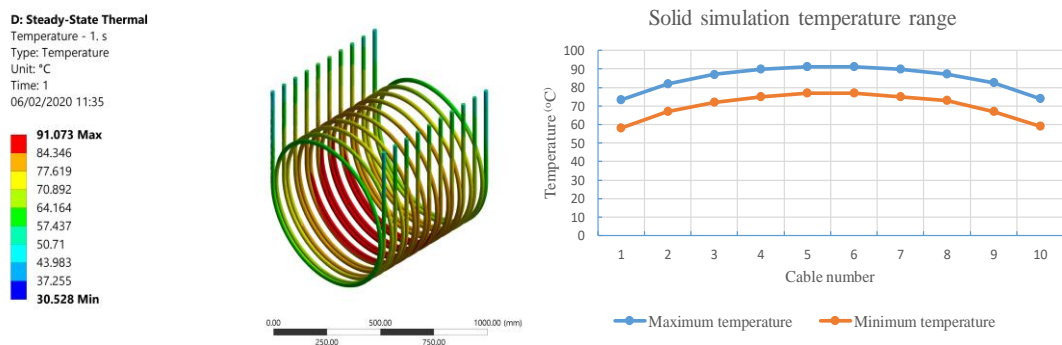


Figure 92. Solid simulation result and maximum and minimum temperatures within each of the 10 cables for the Solid simulation

6.2.2.2 Fluid simulation results

In the steady-state condition for the Fluid simulations, the temperature distributions of the 10 cables are presented in left side graph of figure 93. The maximum temperature observed in the central cable loops is 86°C, while the minimum temperature within the cable loops is 62°C. Once more, the locations of the minimum temperatures are on the cables closest to the tank walls. Notably, the central cables exhibit a lower temperature compared to the equivalent cables in the Solid simulation. The cables near the tank walls demonstrate a higher temperature than their counterparts in the Solid simulation. These results indicate that the natural convection property of the water contributes to a more uniform temperature distribution across

the cables.

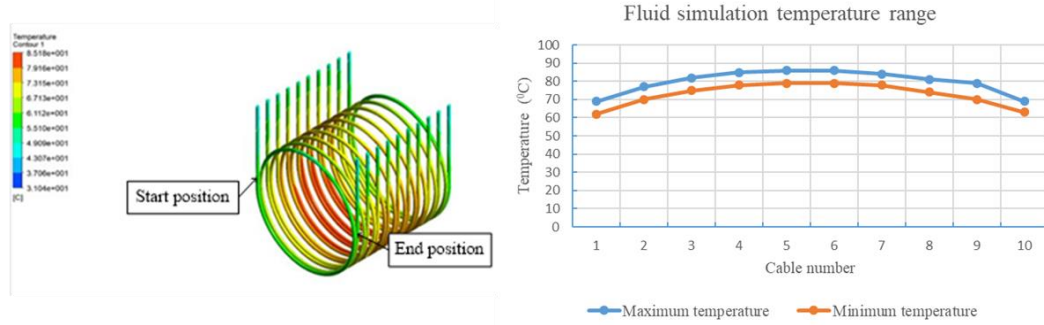


Figure 93. Fluid Simulation result (start and end position identified for later temperature comparisons) and maximum and minimum temperatures within each of the 10 cables for the Solid simulation

The right-side graph of Figure 93 illustrates the maximum and minimum temperature ranges of each cable derived from the Fluid simulation results, plotted against cable number. The blue curve represents the maximum temperature of each cable, while the orange curve represents the minimum temperature of each cable. Notably, in the Fluid simulation, the temperature range of each cable loop is only about 7°C.

6.2.3. Discussion

In the Fluid simulation, natural convection of water serves to reduce the temperature disparities between cables and within individual cables. This is primarily attributed to water's inherent ability for convection, which facilitates the dispersion of heat generated by cable conductors throughout the water tank, resulting in a more uniform water temperature than that in case of without considering water natural convection. Nevertheless, it is worth noting that temperature discrepancies still persist in the Fluid Simulation results, given that natural water convection tends to be relatively slow and gentle.

Figure 94 displays the temperature distribution along the lengths of the cables in both the Fluid and Solid simulations. To facilitate a comparison between the central and outer cables, Cable 1 and Cable 6 have been selected for this purpose. The designated start and end positions, used as reference points for temperature measurements in the simulations, are depicted in Figure 92. It is important to note that all cable loops are spiralled with 1.5 turns and possess a bend radius of 350 mm, resulting in an overlapped section in the lower half of the loop for each cable.

In the Solid simulation, both Cable 6 and Cable 1 exhibit higher temperatures compared to their corresponding values in the Fluid simulation, with an increase of approximately 5°C

to 10°C. Due to the looped configuration of the cables, the sections of the loops that fold back on each other near the tank bottom experience the highest temperatures. The top sections of the cable loops, where the cable is more exposed to the surrounding fluid material (water), undergo a reduction in temperature profile.

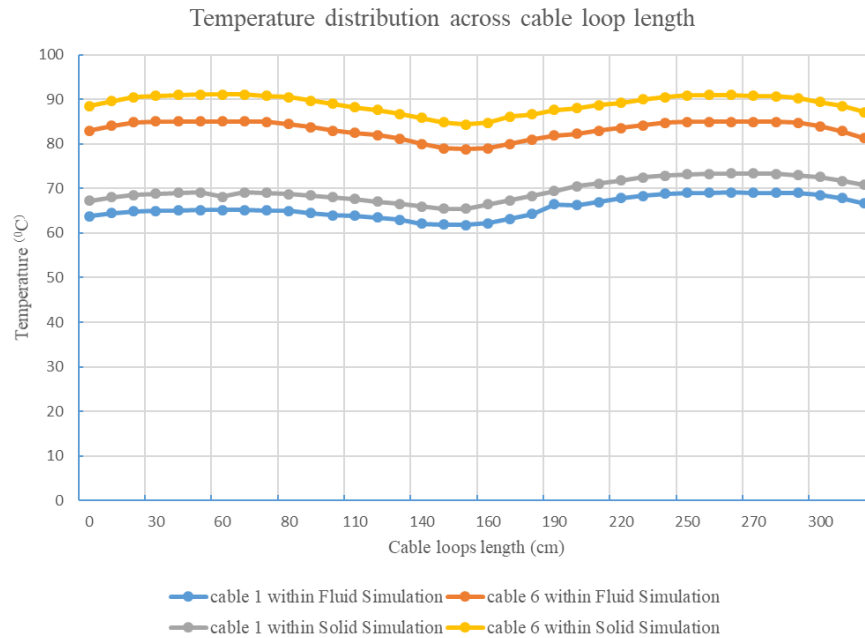


Figure 94. Temperature distribution in single cable loops

Indeed, various cable lifetime models have indicated a direct correlation between the service lifespan of cable insulation material and its operational temperature [102]. Consequently, the temperature differential among cables within the tank will impact the ageing rate of each individual cable. According to the simulation results in this section, the IEEE standard 1407 does not take into account or control the temperature differences among cables and within individual cable structures, this would cause challenges to comprehensively investigate the mechanisms governing thermally induced degradation of cable insulation or accurately predict cable lifespan with its inherent temperature dependence.

Implementing a water circulation system in the water tank stands as a plausible solution for addressing uneven ageing temperature distributions. However, it is worth mentioning that IEEE Standard 1407 does not offer specific guidance on the utilization of water pumps or fans for this purpose. In the next simulations, the addition of a circulation system within the water tank will be considered in order to comprehensively understand the effects of circulation rates on temperature distributions. Additionally, the convection coefficient of the tank walls will be examined as a function of the temperature difference between the steel walls and the ambient air.

6.3. Modelling of cable loops in water tank with forced circulation system

Previous simulation work on power cables heated by induced current in a water tank demonstrated the temperature distribution in a water tank across different cable lengths were not uniform as shown in Figure 93. This situation arises principally because the natural convection of water is not sufficient to drive a uniform distribution of heat within the tank. The cables located at the middle of the tank therefore have a higher temperature profile than the cables near the tank walls. Further the overlapped sections of each cable loop have higher temperatures due to the close nature of the loop contact.

This section delves into an examination of the simulated cable temperature distributions, now incorporating forced water circulation. Five distinct scenarios are assessed and compared, namely:

- A water tank without a rotating fan,
- A rotating fan at 10 revolutions per minute (rpm) positioned on the middle section of the tank's side wall,
- A rotating fan at 50 rpm located on the middle section of the tank's side wall,
- A rotating fan at 10 rpm situated on the lower section of the tank's side wall, and
- A rotating fan at 50 rpm positioned on the lower section of the tank's side wall.

The primary objective is to illustrate the influence of forced water circulation and, prospectively, to determine the optimal fan positions and rotational speeds necessary to achieve uniform temperature distribution across the cables undergoing the ageing process.

6.3.1. Simulation setup

The cable model remains consistent with that utilized in the preceding simulation, encompassing two layers: an aluminium conductor and XLPE insulation material. The thermal properties attributed to XLPE are established through a linear function of temperature, as outlined in Table 28.

Table 28. Thermal properties of XLPE

Temperature (K)	Density (kg/m ³)	Thermal conductivity (W/m · K)	Specific heat (J/K · kg)
300.15	965	0.33	2034
373.15	965	0.38	4000

The constructed tank geometry dimensions are provided in Table 29. The tank comprises two components: a 20 mm thick aluminium tank, with the outer surface wrapped in 10mm of

polystyrene serving as a thermal insulator, which is not considered in simulations in section 6.2. The density of the polystyrene is 20 kg/m^3 , its specific heat is $1300 \text{ J/K} \cdot \text{kg}$, and its thermal conductivity is $0.033 \text{ W/(m} \cdot \text{K)}$.

Within each tank, there are five cables, all possessing a loop bend radius of 350mm. The fan used in the model is illustrated in Figure 95. It features a diameter of 150mm and is equipped with 10 aluminium blades. To reduce the overall size of the simulation model and improve computational efficiency, the water tank's dimensions have been decreased compared to the models in section 6.2, and the number of cables in the tank has been reduced to five. However, the model dimensions still comply with the IEEE standard 1407 requirements.

Table 29. Dimensions of tank

Length (mm)	1000
Width (mm)	800
Height (mm)	800
Side spacing (HS) (mm)	50
End spacing (TS) (mm)	150
Bottom spacing (VS) (mm)	50
Specimen spacing 1 (SS1) (mm)	150
Water depth (mm)	800

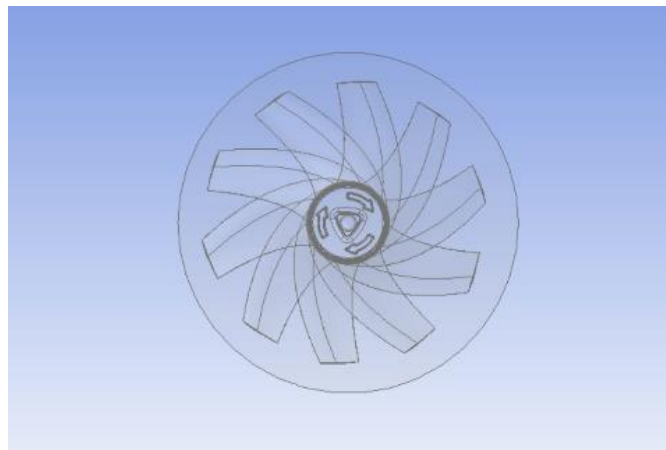


Figure 95. Fan geometry model

Three distinct cable-tank models were developed for this study. These include:

- A tank without a rotating fan.
- A tank equipped with a rotating fan positioned in the middle section of the tank's side wall.
- A tank with a rotating fan located in the lower section of the tank's side wall.

During the simulations in this section, an energy source with a power density of $400,000 \text{ W/m}^3$ was applied to simulate resistive heating in the conductors. This specific value was chosen to achieve the anticipated cable temperatures after several iterative simulations. The insulation walls and conductor walls are thermally coupled. Additionally, the tank walls

were given with a convection property to simulate the dissipation of heat from the steel walls to the surrounding air environment. For this, the ambient temperature was established at 27°C, and the convection coefficient was set to 5 W/m² · K, representing natural convection in air. It is assumed that the tank is situated in stagnant air, and hence, the convection coefficients remain constant with respect to temperature.

The effects of gravity are considered in all simulation models. The pressure-based solver was employed, with the absolute characteristic defined for the velocity formulations. Following the guidelines outlined in IEEE Standard 1407, the power cables undergo heating for 8 hours each day. Consequently, a transient model was utilized in the simulations to account for an accelerated ageing period lasting 8 hours.

To determine whether convection is simulated as "laminar" or "turbulent" in simulations, the Grashof number (Gr) is calculated. The Grashof number, denoted as Gr, is defined by (55):

$$Gr = \frac{(\beta g L^3) \times (T - T')}{\nu^2} \quad (55)$$

where:

- g = gravitational acceleration (m/s²),
- β = coefficient of volume expansion (1/K),
- T = temperature of the heater surface (°C),
- T' = temperature of fluid sufficiently far from surface (°C),
- L = characteristic length of heater geometry (m), and
- ν = kinematic viscosity of fluid (m²/s).

With a Grashof number of 186,000, the water flow condition in the tank is considered to be viscous, and thus modelled as laminar flow[146].

The Reynolds number (Re) is employed to ascertain whether the water flow state in the tank transitions into either "laminar" or "turbulent" flow when forced circulation is implemented[147]. Re is defined as follows:

$$Re = \frac{\rho v L}{\mu} \quad (56)$$

where:

- ρ = density of the fluid (SI units: kg/m³),
- v = characteristic velocity of fluid with respect to object (m/s),
- L = characteristic linear dimension (m), and
- μ = dynamic viscosity of the fluid (N · s/m²)

In the case of the 10rpm rotating fan, the Re of water flow in the tank is calculated to be 2228. Since this value is smaller than 2300, the simulation employs the viscous laminar model. However, for the 50rpm rotating fan, the Re of flow is computed to be 7388. Given that this exceeds 4500, the viscous k-ε model is implemented in the simulation[147].

6.3.2. Simulation results

The temperature distribution on the cable surfaces is depicted in Figure 96. The highest temperature recorded on the cable surface is 102.4°C, while the lowest temperature is 40.7°C. Notably, the temperature differential between all cable surfaces exceeds 60°C.

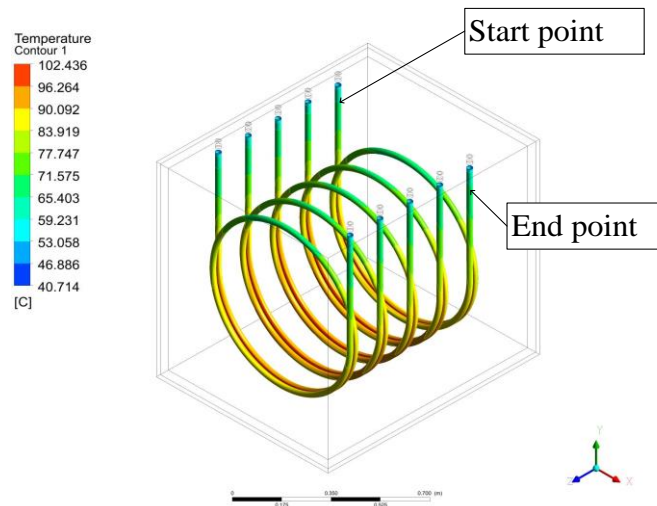


Figure 96. Scenario 1 - temperature distribution on the cable surfaces (start and end position identified for later temperature comparisons)

The temperature distribution on the cable surfaces for this scenario is presented in Figure 97(a). Here, it is evident that the maximum temperature on the cable surface is reduced to 71.8°C due to the presence of the 10rpm rotating fan. The minimum temperature experiences a slight reduction to 37°C. Consequently, the temperature differential is approximately 35°C, which is smaller than the differential observed in Scenario 1.

In Figure 97 (b), the temperature distributions for this scenario are illustrated. The maximum and minimum surface temperatures are 40.3°C and 39.7°C respectively. It is evident that the forced circulation of water at 50rpm has resulted in a significant improvement in equalizing the temperature profiles across the cable surfaces.

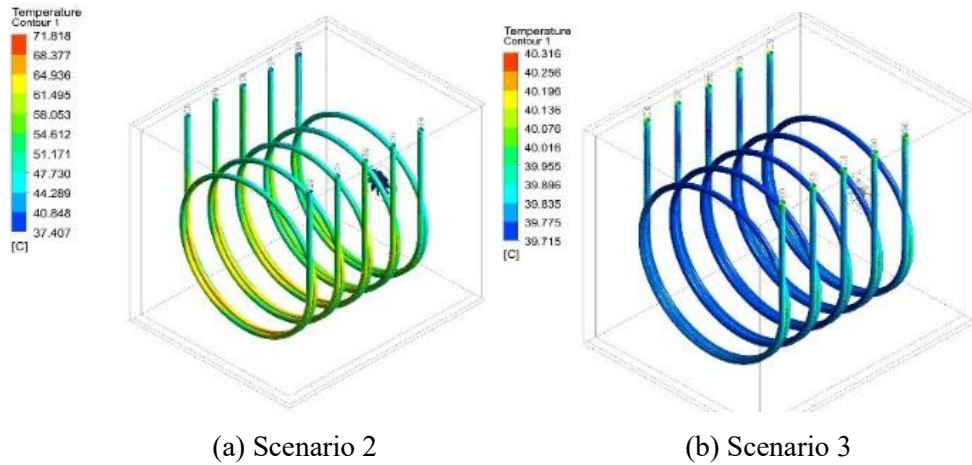


Figure 97. 10rpm temperature distributions on the cable surfaces

In Scenario 4, the temperature distributions on the cable surfaces are depicted in Figure 98 (a). Notably, the temperature differences across the cables are further reduced to 16°C in comparison with Scenario 2. Additionally, the maximum temperature on the cable surface is lowered to 56°C.

Figure 98 (b) displays the temperature distributions on the cable surfaces for Scenario 5. The results closely resemble the temperature distributions observed in Scenario 3, with a slight reduction in temperature variation across all cables, approximately 0.5°C.

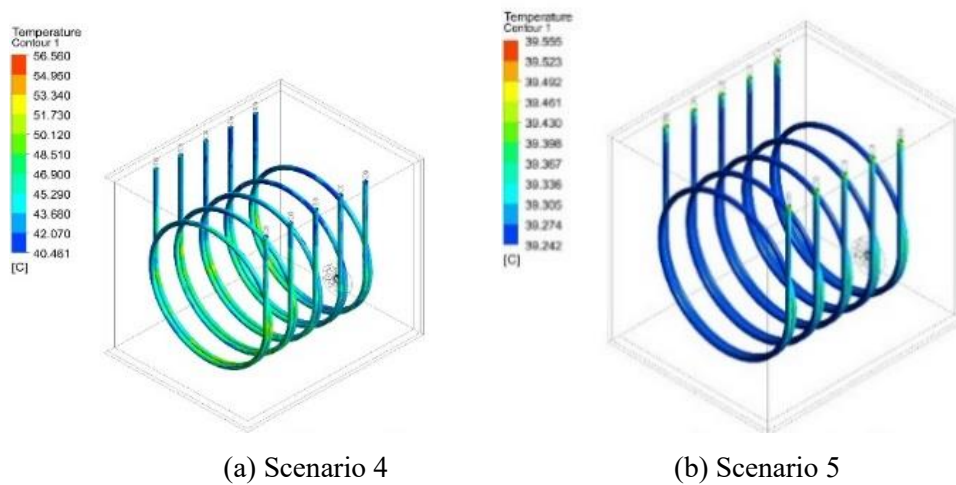


Figure 98. Temperature distributions on the cable surfaces

6.3.3. Discussion

Upon comparison, it is evident that forced water circulation systems yield a more uniform temperature distribution across all cable surfaces in contrast to natural water convection. The latter is found to be not sufficient in adequately dispersing heat within the water tank. In cases relying solely on natural convection, cable surface temperatures not only tend to be significantly higher but are also distributed unevenly along the cable, indicating non-uniform

thermal ageing across the looped cable insulation. In contrast, even at low rotating fan speeds, forced circulation proves to be quite effective in distributing heat within the tank. This results in a more efficient and evenly distributed temperature profile on the cable surfaces, attributed to the enhanced heat exchange between the cables and the circulating water.

The temperature distribution along each of the five cable loop lengths for Scenario 1, utilizing natural water convection, is illustrated in Figure 99. The designated start and end positions for temperature measurements correspond to cable 1 in Figure 96. This figure demonstrates that both cable 1 and cable 5 exhibit lower temperature profiles along their length when compared to the other cables. This can be attributed primarily to their proximity to the tank walls, resulting in higher energy dissipation. In each cable loop, the overlapped sections naturally display higher temperatures in contrast to the non-overlapped sections, as anticipated.

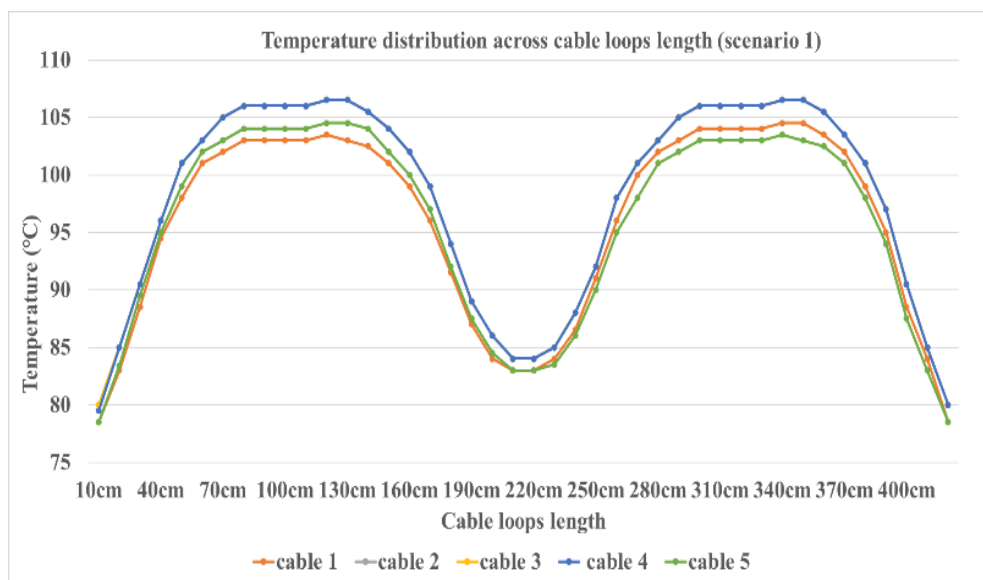


Figure 99. Scenario 1 temperature distribution across cable loops length

The temperature distribution along the length of the cable loops for the forced circulation systems in Scenarios 2 to 5 is depicted in Figure 100, where the dashed lines represent the results with the rotating fan placed in the middle of the tank's side wall, while the solid lines illustrate the results with the rotating fan positioned on the lower tank side wall.

To gain insight into the water circulation patterns within the simulations, the ANSYS water circulation stream flow patterns at 8 hours are presented in Figure 101 for both the 10rpm and 50rpm fan cases in the middle section of the wall. It is evident that water circulation significantly reduces the heat dissipation from the cable surfaces, proving to be more effective in dissipating heat throughout the entire tank. As anticipated, the maximum temperature of the cable surfaces decreases as the heat is dissipated more efficiently due to forced water circulation system.

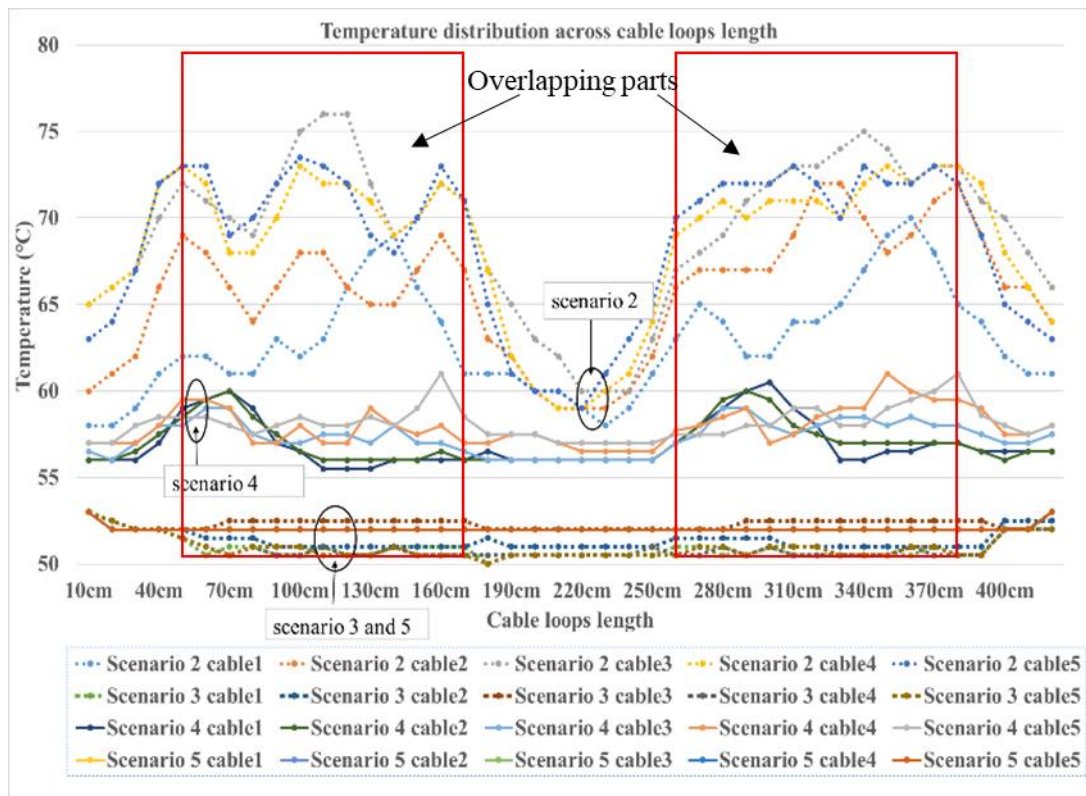
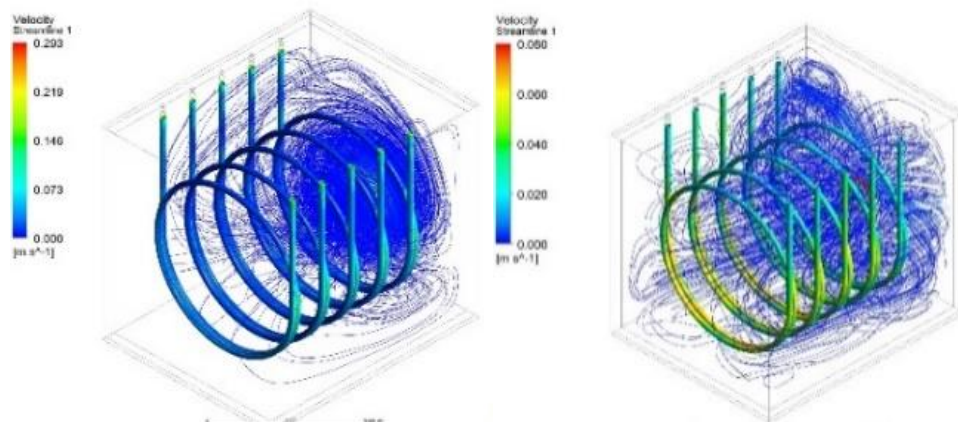


Figure 100. Cable surface temperature distributions across cable loop lengths for Scenarios 2 – 5.



(a) 50rpm fan (Scenario3)

(b) 10 rpm fan (Scenario2)

Figure 101. Examples forced circulation water flows (fans located at middle of side wall)

In comparing the scenarios with a 10rpm rotating fan positioned in the middle and lower sections (Scenario2 and Scenario4), it is evident that the lower fan placement leads to a more uniform temperature distribution on the cable surfaces. This improvement is attributed to the enhanced circulation, particularly in moving heat from the looped sections of the cables. In the case of the 50rpm scenarios, the turbulence in the flow of water intensifies, resulting in more

forceful water movement within the tank. This leads to an even more efficient distribution of heat on the surfaces of all the cables. It's worth noting that the absolute temperature differences between the 10 rpm and 50 rpm scenarios are relatively small.

6.4. Conclusion

IEEE Standard 1407 provides guidelines regarding power cable accelerated ageing in water filled tanks. Because the thermal ageing has a significant impact on the electrical and physical characteristics of cable insulation, temperature distributions are essential to be considered when conducting the cable accelerated ageing experiments according to IEEE standard 1407.

The outcome of the section 6.2 models mainly analysed from the observation that the natural convection of water is insufficient to ensure a uniform dispersion of heat within the tank but still make an improvement compared to that without natural water convection. Consequently, cables situated in the middle of the tank exhibit higher temperature profiles compared to those positioned near the tank perimeters. Additionally, the areas where each cable loop overlaps exhibit elevated temperatures owing to the close proximity of the loop sections.

The section 6.3 has investigated a simulation of the impact of forced water circulation on cable surface temperatures in a tank comprising 5 cables undergoing artificial ageing. Circulation fans with 10rpm and 50rpm were simulated and the cable temperatures compared with the situation of no forced water circulation. The 10rpm rotating fan reduces the temperature variations across each cable, providing a more even distribution of cable surface temperatures compared to the no water circulation scenario. The 50 rpm scenarios produce improvement over the 10rpm situations, producing even furthermore uniform distribution of surface temperatures for all of the 5 cables.

As a result, forced water circulation with 50rpm is a general recommendation on fan speed, which resulting in a more even artificial ageing situation for all cables in the tank. Additionally, when the fan is located at the lower part of the side wall, the situation is further improved with even lower differences in temperature across each cable and more evenly distributed surface temperature profiles across each cable.

Based upon these findings, it is recommended that IEEE Standard 1407 incorporate guidelines for implementing forced water circulation at a fan speed of 50rpm to create a more uniform artificial aging environment for all cables in the tank. Additionally, positioning the fan at the lower part of the side wall further enhances temperature uniformity across the cables,

minimizing temperature variations and ensuring more accurate aging simulations. This adjustment would result in more reliable and consistent testing outcomes, ultimately improving the accuracy of lifespan predictions for power cables.

An accelerated ageing experiment using a water filled tank based on the IEEE standard 1407 could be performed in the future, through which the results of simulations can be compared with actual experimental measurements. If the simulation results are equivalent to practical results, the temperature derived from simulation will have significance for estimating power cable lifetime under different possible accelerated ageing regimes. Detailed ageing calculation of power cables under conditions according to IEEE standard 1407 could be evaluated in the future based on simulated temperature. In addition, the cable model structure in simulations of this chapter is simplified, certain components like semi-conductor screens, metal shield and outer sheath would be considered in the future modelling.

Chapter 7. Conclusions and future work

7.1. Conclusions

The insulation of extruded power cables can be subjected to thermal stresses under working conditions due to resistive heating of the heavily loaded cable core conductor and excessively high ambient temperatures. These thermal stresses lead to insulation degradation, commonly referred to as thermal aging. The effects of thermal aging can be assessed through condition monitoring techniques, such as Insulation Resistance, Dielectric Loss, and Polarization Index. However, previous research has not fully addressed how these properties of full-scale extruded power cables (beyond just the insulation material) vary under thermal stresses in practical working conditions, and there is a lack of thermal degradation models for power cable performance in existing literature. This thesis investigated the performance variation of power cables under thermal aging conditions and developed IR thermal degradation models for medium voltage extruded power cables.

7.1.1. Chapter 3

In order to evaluate the variation of the electrical properties of extruded cables during thermal ageing processes, a novel artificial accelerated thermal ageing experiment methodology was designed and conducted for MV extruded power cables in the chapter 3. Throughout the thermal ageing process, examinations were periodically conducted on cable samples to obtain various electrical properties, encompassing IR1, IR10, DAR, PI, capacitance and $\tan\delta$.

The devised experimental methodology simulated the temperature distribution along length and radius of power cables, and thermal cycling effects induced by loading cycles in cable practical operational conditions. The yearlong artificial thermal ageing was equivalent to normal operational conditions based on the Arrhenius model and Miner's law. The calculated equivalent ageing duration for the cables approximates 25 years.

The testing voltages applied on cables ranged from 1kV to 10kV. The measurement voltage levels exerted a considerable influence on measured results of IR and $\tan\delta$, a greater $\tan\delta$ value and a smaller resistance value would be obtained when a higher testing voltage level is applied on cable samples. However, capacitance values of cables were found not to be unaffected by the applied voltage level.

During the progression of the thermal ageing, it was observed that the IRs of the cable samples exhibited two consecutive U-shape variation, followed by a rough decrease. The first

U-shape IR variations were over the first 90 thermal ageing cycles and may indicate the cumulation and subsequent exhaustion of chemical components which were diffused from semiconductor shield layers into insulation and promoted hopping conduction in insulation [115]. The variations of chemical components may have also affected the DAR and PI values which showed large fluctuations over the first 90 ageing cycles. The second U-shape IR variations which had relatively slower rates of change were suspected to be caused by the different diffusion/exhaustion rates of chemical components at inner and outer insulation layers given the radial temperature gradient along the insulation radius.

Furthermore, an investigation into the influence of environmental relative humidity (RH) on the testing results was undertaken. The findings of the survey indicated that the greater $\tan\delta$ values were evident under conditions of relatively higher RH conditions. Furthermore, a correlation was identified between the turning points of RH variation and the observed fluctuations in $\tan\delta$ values. However, it was noted that additional data are required to substantiate and further elucidate this observed relationship.

The PI values of cable samples were fitted to three-time durations in relation to the thermal ageing process. The initial phase represented as short-term linear decrease in the fitting curves for Cables 1, 2 and 3. The second phases of PI fitting for all cables follow another linear trend, characterized by positive slopes. In the third phase, exponential decrease trends were observed, suggesting generally lower rates of PI decrease during the thermal ageing processes. It is important to underscore that PI could serve as a indicator of cable health conditions. The fitting of PI variation could predict time where PI value falling below a specified threshold (generally 2), which indicates cable insulation in a questionable health condition and actions are required to be taken.

Correlation coefficients and their corresponding P-values and 95% confidence intervals, were calculated to consider the relationships among the testing results. The examination revealed a strong correlation between IR1 and IR10, signifying a significant association between these two indicators. The correlations among other examined indicators are comparatively weaker. Additionally, the variations in $\tan\delta$ demonstrate a correlation with changes in IR, indicating both indicators could reflect integral health conditions of extruded power cables.

7.1.2. Chapter 4

In Chapter4, an FVM model and an ANN model were constructed to address the detailed dynamic temperature distribution in the ageing process of cables. This method enhanced the comprehensiveness of insights into the spatial temperature profiles of cables under the

experimental conditions, and with the benefits of formulating more trustworthy lifetime estimation and thermal degradation models for extruded power cables undergoing thermal ageing.

In the FVM simulations, the geometry of extruded power cables was simplified modelled with four layers: conductor, insulation, metal shield and outer sheath. Power densities calculated from experimental current and voltage were applied on cable conductors and connectors to imitate the heat generation. The FVM model assessed the temperature distribution across the cross-sections of the cables at various lengths. An approximate 3°C difference between the inner and outer surfaces of the cable insulations existed at the midpoint length position. Furthermore, temperature distributions on both the cable surfaces and conductor surfaces derived from the FVM simulation results were closely corresponds to the measurements obtained from the experiments. This alignment underscored a high degree of agreement between the simulation and actual experimental observations.

As there is a limitation of the FVM simulation in that it did not offer direct temperature profiles between meshed points, a 3 layers ANN model was developed to predict a more detailed spatial temperature profiles for the cable insulation. The synergistic use of FVM and ANN models holds significant potential for achieving a more precise evaluation of temperatures at specific locations within the cable, accommodating variations in operating conditions. This integrated modelling approach contributed to heightened accuracy and comprehensiveness in temperature assessments.

7.1.3. Chapter 5

This chapter focussed on undertaking a quantitative assessment of cable insulation degradation over time under thermal ageing conditions. IR degradation models were formulated for the cylindrical insulation of extruded power cables subjected to thermal ageing. These models included four scenarios:

- Dichotomy model with uniform temperature distribution,
- Dichotomy model with radial temperature gradients,
- Discretization model with uniform temperature distribution,
- Discretization model with non-uniform temperature distribution.

The foundational modelling approach for all these scenarios entailed the segmentation of the cylindrical cable insulation model into sufficient small and discrete segments. Following this segmentation, the resistance of each sub-segment was determined, leading to the overall calculation of the IR for the entire model. This systematic methodology offered a more detailed

framework for the assessment of IR degradation in power cable insulation exposed to thermal ageing conditions.

The dichotomy models employed a classification system for sub-segments, segregating them into two groups: non-degraded segments and degraded segments. The proportion of degraded segments within the insulation model, denoted as V_d , exhibits an increment over thermal ageing time. This increase was governed by the CDF of an exponential distribution, with the rate of increase being correlated to the ageing temperature in accordance with the principles delineated in the Arrhenius model. This modelling approach properly accommodates the dynamic evolution of the proportion of degraded segments over time, elucidating the impact of thermal ageing effects on the cable insulation. In the dichotomy model with uniform temperature distribution, the entire insulation ages uniformly based on the maximum temperature of cable insulation. The dichotomy model with radial temperature gradients features varying ageing rates for radial layers, utilizing ageing temperature obtained from FVM and ANN models for each layer.

In the discretization models, sub-segment resistivities decreased throughout the thermal ageing process. The discretization model with uniform temperature distribution utilizing the maximum insulation temperature for all segments, resulted in an identical maximum ageing rate. The discretization model with non-uniform temperature utilizes the temperature profiles of sub-segments derived from a combined FVM and ANN modelling approach. This enabled the calculation of the degradation rate for each sub-segment based on the Arrhenius equation, reflecting the evolving resistance as a function of individual ageing temperature and time. This modelling approaches provided a more dynamic representation of the insulation degradation process, capturing the detailed effects of thermal ageing on cable insulation.

The developed IR degradation models were applied and compared using experimental data from reference on resistivity degradation, and the spatial temperature profiles of cable insulation derived from FVM and ANN models. This empirical data was crucial for assessing accuracy and effectiveness of the IR degradation models. The study also explored the influence of segmental sizes and degradation rates on estimation results, noting that in dichotomy models, segment size had more pronounced impact on estimated IR compared to discretization models. Additionally, confidence intervals for each degradation model were determined, considering degradation rates at both 110% and 90% of the standard rate. This comprehensive analysis provided enhances the understanding of the developed IR degradation models.

7.1.4. Chapter 6

Temperature distributions of cables in the accelerated ageing experiments according to

IEEE Standard 1407, which provided guidelines for power cable accelerated ageing in water-filled tank, were simulated in Chapter 6. The influence of natural water convection in the tank were initially modelled. Comparing to the scenario that without natural convection of water, the temperature differences among cables and temperature gradients along with cable lengths of scenario considered water natural convection in tank are relatively lower. However, the water natural convection mechanisms in tank is still insufficient to ensuring a uniform temperature distribution, where cables positioned in the middle of the tank are obtained higher temperature profiles than those near to the tank walls. Furthermore, elevated temperatures were noted in areas where cable loops overlap due to the close proximity of loop sections.

Then, the impact of forced water circulation on cable surface temperatures in a tank were explored by simulations. Models with circulating fans at 10rpm and 50rpm rotating speeds were conducted, and the cable temperatures were compared to a scenario that without forced water circulation. The 10rpm fan reduced temperature differences across each cable, achieving a more uniform distribution of cable surface temperatures compared to the no water circulation scenario. The 50rpm scenarios exhibited further improvement over the 10rpm situations, resulting in a uniform distribution of surface temperature for all cables in a tank. Consequently, a general recommendation for a fan rotating speed of 50rpm is established, ensuring a more even artificial ageing situation for all cables in the tank. Moreover, situating the fan at the lower part of the side wall enhances the scenario, leading to even lower temperature variations across cables and more evenly distributed surface temperature profiles. This information provided valuable insights for optimizing forced water circulation conditions to achieve uniform cable ageing in experimental settings. Based on these findings, it is recommended that IEEE Standard 1407 include guidelines for implementing forced water circulation at a fan speed of 50 rpm to create a more uniform artificial aging environment for all cables in the tank.

7.2. Future work

The accelerated thermal ageing experiment has been systematically executed on MV extruded power cables for a total of 270 ageing cycles. This experimental duration is deemed equivalent to approximately 25 years of continuous operation under normal operational conditions for cables of similar specifications. As the ageing of power cables in the experiment has not yet reached their designed lifetime, typically spanning 30 to 40 years, the ongoing implementation of the experiment becomes imperative for continued analysis. Continuous monitoring of variations in PI and $\tan\delta$ values remains essential to comprehensively assess the performance of cables subjected to thermal ageing conditions. IR measurements after more thermal ageing cycles should be performed to validate a longer-term IR reduction under the

thermal ageing effect after the two U-shape variations.

Furthermore, experimental work is required to measure the variations and diffusion depths of the chemical components in insulation over the annealing process and verify the explanation of the two consecutive U-shape IR variations. Exploration and analysis of the influence of environmental RH on both IR and $\tan\delta$ will also be crucial for an understanding of the cable behaviour and responses to varying environmental conditions.

The thermal modelling method, which combines FVM and ANN developed in this research holds the potential for further application to power cables operating in diverse environmental conditions. Its applicability could be extended and validated through practical experimental measurements, providing an opportunity to assess the reliability and accuracy of the model across various operational scenarios. This expansion of the methodology to different environments contributes to its broader utility in the analysis and prediction of power cable performance under different working conditions.

Future work on the development of IR degradation models should focus on incorporating the U-shaped variation of IR, considering the combined impact of the annealing effect and thermal ageing. The discretization model, introduced in this research, may undergo further refinement to simulate the joint effects of annealing and thermal ageing on IR variations in a more physically accurate manner. This refined model could then be fitted to laboratory measurements to identify the characteristics of hopping and band conduction mechanisms within insulation, particularly with the presence of semi-conductor layers, throughout the heating process. Furthermore, the highly non-uniform insulation temperature profiles which might be caused by local partial discharges and/or complex installation conditions could be modelled by a further developed FVM model, so that providing a more reliable temperature profiles to discretization model for resistance degradation estimation. In future model development, the low-resistance current path formed during partial discharges could be taken into account. This can be simulated by allocating relative low resistance values to particular paths or areas within the insulation.

An accelerated ageing experiment employing a water-filled tank in an accordance with IEEE Standard 1407 could be conducted in future research. This experimental setup would enable a direct comparison between simulated results and actual measurement. There is a potential for detailed evaluation of power cable ageing calculations under conditions specified by IEEE Standard 1407, utilizing simulated temperature profiles.

In addition, in the simulations of accelerated ageing based on IEEE Standard 1407, the cable model structure is presently simplified. However, in future modelling efforts, there is a

plan to incorporate additional components such as semi-conductor shields, metal shield and outer sheath. The impact of these layers on temperature distribution may not be significant, but this enhancement aims to create a more detailed and realistic representation of the cable structure, ensuring that the simulation results align more closely with the actual behaviour of power cables undergoing accelerated ageing.

Reference

- [1] IEA, Electricity 2024, IEA, Paris <https://www.iea.org/reports/electricity-2024>, 2024 Licence: CC BY 4.0
- [2] Sullivan, M. M., & Buehring, C. A., "The impact of power system failures on modern society: Economic and safety implications." *International Journal of Electrical Power & Energy Systems*, **2020**, 116, 105623.
- [3] Hammons, T. J., "Power cables in the twenty-first century." *Electric power components and systems*, **2003**, 31(10), 967-994.
- [4] State Grid Corporation of China. "Annual report on power system reliability and cable performance." **2019**.
- [5] Zhou. C., Yi. H., Dong, X., "Review of recent research towards power cable life cycle management," *High Voltage*, 2017, 2(3), 179-187.

- [6] W. Zhao, W. H. Siew, M. J. Given, "The electrical performance of thermoplastic polymers when used as insulation in cables," *48th International Universities' Power Engineering Conference (UPEC)*, 2nd– 5th, **Sept. 2013**, Dublin, Ireland.
- [7] Duan. X., Tang. M., Lin. F., Ye. H., "Analysis on breakdown of main insulation on middle joint of 220 kV power cable," *High Voltage*, **Apr. 2009**, 45(6), 142-144.
- [8] Huo. X., Pi. H., Qiu. Q., Xu. Y. "Condition evaluation for 10 kV cables of Shenzhen Bureau based on CIGRE TB 358," *In 2016 International Conference on Condition Monitoring and Diagnosis (CMD)*, IEEE **2016, September**. 631-634.
- [9] Christou, S., "Thermal prognostic condition monitoring for MV cable systems." *Doctoral dissertation*, University of Southampton, **2016**.
- [10] Lofaro. R., Grove. E., Villaran. M., Soo. P., Hsu. F., "Assessment of Environmental Qualification Practices and Condition Monitoring Techniques for Low-Voltage Electric Cables: LOCA Test Results," *NUREG/CR-6704 (Vol. 1)*, BNL-NUREG-52610). Brookhaven National Lab.(BNL), Upton, NY (United States). **2001**.
- [11] PRYSMIAN. BS6622/BS7835 "Single Core Armoured 11 kV XLPE Stranded Aluminium Conductor".
- [12] R. Black, "The History of Electric Wires and Cables," London, UK: Peter Peregrinus Ltd **1983**.
- [13] Orton. H., "History of underground power cables," *IEEE Electrical Insulation Magazine* **2013**, 29(4), 52-57.
- [14] Arrighi. R., "From impregnated paper to polymeric insulating materials in power cables," *IEEE transactions on electrical insulation*, **1986**, (1), 7-18.
- [15] Fofana, I., "50 years in the development of insulating liquids." *IEEE Electrical Insulation Magazine*, **2013**, 29(5), 13-25.
- [16] Wang. M., "State grid corporation of China's yearbook 2011". *China Electric Power Press*, China, 566. **2012**.
- [17] Walton. C., Mackinlay. R., "PD monitoring-a critical tool for condition-based assessments," *Transmission and distribution world*, **2003**, 55, 38-46.
- [18] Voltages, I. S. IEC 60038. Edition, 7, **2009-06**.
- [19] Ahmad. H., Rodrigue. D., "Crosslinked polyethylene: A review on the crosslinking techniques, manufacturing methods, applications, and recycling," *Polymer Engineering & Science*, **2022**, 62(8), 2376-2401.
- [20] Qin. S., Liu. R., Wang. Q., Chen. X., Shen. Z., Hou. Z., Ju, Z., "Study on the molecular structure evolution of long-term-operation XLPE cable insulation materials," *Energy Reports*, **2022**, 8,

1249-1256.

- [21] Boukezzi. L., Boubakeur. A., “Effect of thermal ageing on the electrical characteristics of XLPE for HV cables,” *Transactions on Electrical and Electronic Materials*, **2018**, 19, 344-351.
- [22] Wang, S., Yu, S., Xiang, J., Li, J., & Li, S., “DC breakdown strength of crosslinked polyethylene based nanocomposites at different temperatures.” *IEEE Transactions on Dielectrics and Electrical Insulation*, **2020**, 27(2), 482-488.
- [23] Hu. S., Zhou. Y., Yuan. C., Wang. W., Hu. J., Li. Q., He. J., “Surface-modification effect of MgO nanoparticles on the electrical properties of polypropylene nanocomposite,” *High Volt* **2020**, 5, 249–255.
- [24] Mecheri. Y., Nedjar. M., Lamure. A., Aufray. M., Drouet. C., “Influence of moisture on the electrical properties of XLPE insulation,” *In 2010 Annual Report Conference on Electrical Insulation and Dielectric Phenomena*, **October 2010**, IEEE, 1-4.
- [25] Crine. J. P., Lanteigne. J., “Influence of some chemical and mechanical effects on XLPE degradation,” *IEEE Transactions on Electrical Insulation*, **1984**, (3), 220-222.
- [26] Igwe. O. E., “Cable sizing and its effect on thermal and ampacity values in underground power distribution”. **2016**.
- [27] Jiang, G., Zhou, Y., Teng, C., Zhang, Y., Huang, X., Zhou, L., & Yang, D., “Synergistic improved electrical resistivity-temperature characteristics and DC breakdown strength in insulating XLPE composites by incorporating positive temperature coefficient particles.” *Polymer Testing*, **2023**, 117, 107839.
- [28] Arhart. R. J., “The chemistry of ethylene propylene insulation. II,” *IEEE Electrical Insulation Magazine*, **1993**, 9(6), 11-14.
- [29] Sriraman. A., Bowler. N. Glass, S. W., Fifield, L. S., “Dielectric and mechanical behavior of thermally aged EPR/CPE cable materials,” *In 2018 IEEE Conference on Electrical Insulation and Dielectric Phenomena (CEIDP)*, **October 2018**, 598-601. IEEE.
- [30] Lei. Z., Song. J., Geng. P., Tian. M., Lin. L., Xu. C., Li. Z., “Influence of temperature on dielectric properties of EPR and partial discharge behavior of spherical cavity in EPR insulation,” *IEEE Transactions on Dielectrics and Electrical Insulation*, **2015**, 22(6), 3488-3497.
- [31] Standard, I. E. C. Evaluation and qualification of electrical insulation systems. *IEC Std, 60505*, **2011**.
- [32] IEEE Standard, “IEEE Guide for Multifactor Stress Functional Testing of Electrical Insulation Systems,” *IEEE Std 1064-1991*, **1991**, vol., no., pp.1-.
- [33] Densley. J., “Ageing and diagnostics in extruded insulations for power cables,” *In Proceedings of 1995 IEEE 5th International Conference on Conduction and Breakdown in Solid Dielectrics*, **July 1995**. 1-15. IEEE.
- [34] Densley. J., “Ageing mechanisms and diagnostics for power cables-an overview,” *IEEE electrical insulation magazine*, **2001**, 17(1), 14-22.
- [35] Gazdzinski. R. F., Denny. W. M., Toman. G. J., Butwin, R. T., “Aging management guideline for commercial nuclear power plants—electrical cable and terminations,” *Sandia Labs report, SAND96-0344*, **1996**.
- [36] Mo, S. J., Zhang, J., Liang, D., & Chen, H. Y., “Study on pyrolysis characteristics of cross-linked polyethylene material cable.” *Procedia engineering*, **2013**, 52, 588-592.
- [37] Langlois, V., Meyer, M., Audouin, L., & Verdu, J., “Physical aspects of the thermal oxidation of crosslinked polyethylene.” *Polymer degradation and stability*, **1992**, 36(3), 207-216.
- [38] Boukezzi. L., Boubakeur. A., Laurent. C., Lallouani. M., “DSC study of artificial thermal aging of XLPE insulation cables,” *In 2007 IEEE International Conference on Solid Dielectrics*, **2007**. 146-149. IEEE.

- [39] International Atomic Energy Agency (IAEA), "Assessing and managing cable aging in nuclear power plants," *IAEA Nuclear Energy Series*, **2012**, No. NP-T-3.6.
- [40] Billingham. N. C., Bott. D. C., Danke. A. S., "Chapter 3," *In Developmental Polymer Degradation*, **1981**, p. 63ff.
- [41] Dole. P., Chauchard. J., "Determination of oxidation profiles of elastomeric materials. Part II. Correlation of macro (swelling) with micro (pinpoint DMA)," *In Polymer Degradation and Stability*, **1995**, Vol. 41.
- [42] Wise. J., Gillen. K. T., Clough. R. L., "Quantitative model for the time development of diffusion-limited oxidation profiles," *Polymer*, **1997**, 38(8), 1929-1944.
- [43] Howard. J. B., Gilroy. H. M., "Some observations on long-term behavior of stabilized polyethylene," *Polym. Eng. Sci.*, **1975**, 15, 268-271.
- [44] Board. B. L., Ruddell. H. J., "Investigation of Premature Depletion of Stabilizers from Solid Polyethylene Insulation," *International Wire and Cable Symposium Proceedings*, **1982**, 300-312.
- [45] Celina, M., & George, G. A., "A heterogeneous model for the thermal oxidation of solid polypropylene from chemiluminescence analysis." *Polymer degradation and stability*, **1993**, 40(3), 323-335.
- [46] Bowler. N., Liu, S., "Aging Mechanisms and Monitoring of Cable Polymers," *In International Journal of Prognostics and Health Management*, **2015**.
- [47] Seguchi. T., Tamura. K., Ohshima. T., Shimada. A., Kudoh. H., "Degradation mechanisms of cable insulation materials during radiation-thermal ageing in radiation environment," *Radiation Physics and Chemistry*, **2011**, 80(2), 268-273.
- [48] Seguchi. T., Tamura. K., Shimada. A., Sugimoto. M., Kudoh. H., "Mechanism of antioxidant interaction on polymer oxidation by thermal and radiation ageing," *Radiation Physics and Chemistry*, **2012**, 81(11), 1747-1751.
- [49] Haruna. T. B. A. A. D. K., "Aspects of stabilization with phosphorous antioxidants in polymers. Die Angewandte Makromolekulare Chemie," *Applied Macromolecular Chemistry and Physics*, **1995**, 232(1), 119-131.
- [50] Seguchi. T., Tamura. K., Shimada. A., Sugimoto. M., Kudoh. H., "Mechanism of antioxidant interaction on polymer oxidation by thermal and radiation ageing," *Radiation Physics and Chemistry*, **2012**, 81(11), 1747-1751.
- [51] Conley. R.T., "Thermal Stability of Polymers," New York: Marcel Dekker, **1970**.
- [52] Osawa. Z., "Degradation and stabilization of polymers," Musashino Kurieito, Co., Ltd. **1992**.
- [53] Sugimoto. M., Shimada. A., Kudoh. H., Tamura. K., Seguchi. T., "Product analysis for polyethylene degradation by radiation and thermal ageing," *Radiation Physics and Chemistry* **2013**, 82, 69-73.
- [54] Seguchi. T., Tamura. K., Ohshima. T., Shimada. A., Kudoh. H., "Degradation mechanisms of cable insulation materials during radiation-thermal ageing in radiation environment," *Radiation Physics and Chemistry*, **2011**, 80(2), 268-273.
- [55] Zhang. C. C., Li. Y. F., Hu. M. Y., Ma. F. L., Zhao. H., Han. B. Z., "Conductivity properties of XLPE insulation used for HVDC cable after accelerated thermal ageing," *In 2018 12th International Conference on the Properties and Applications of Dielectric Materials (ICPADM)*, **2018**, 500-503. IEEE.
- [56] Kang. S. D., Kim. J. H., "Investigation on the insulation resistance characteristics of low voltage cable," *Energies*, **2020**, 13(14), 3611.
- [57] Mecheri. Y., Bouazabia. S., Boubakeur. A., Lallouani. M., "Effect of thermal ageing on the properties of XLPE as an insulating material for HV cables," *In Proceedings of the International Electrical Insulation Conference*, IET Centre, Birmingham, UK, 2013, 29-31.

- [58] International Atomic Energy Agency (IAEA), "Assessing and managing cable aging in nuclear power plants," *IAEA Nuclear Energy Series*, No. NP-T-3.6. **2012**.
- [59] Mazzanti, G., "The combination of electro-thermal stress, load cycling and thermal transients and its effects on the life of high voltage ac cables." *IEEE Transactions on Dielectrics and Electrical Insulation*, **2009**, 16(4), 1168-1179.
- [60] Zhang, Y., Gu, G., Liu, J., Jiang, F., Fan, Y., & Zha, J., "Evaluation of Non-Uniform Thermal Aging of XLPE Cable Based on Modified Debye Model." *Frontiers in Materials*, **2022**, 9, 838792.
- [61] C. Zhou., H. Yi, X. Dong., "Review of recent research towards power cable life cycle management," *IET High Voltage*, **2017**, vol. 2, no. 3, pp. 179-187.
- [62] IEEE Std 43: IEEE recommended practice for testing insulation resistance of electric machinery, **2013**.
- [63] Tamus. Z. Á., Csányi. G. M., Tomon. G., "Investigation of temperature dependence of dc diagnostic tests on lv pvc insulated cables," *In Jicable*, **2015**. Vol. 15, p. 2015
- [64] Boukezzi. L., Boubakeur. A., "Effect of thermal aging on the electrical characteristics of XLPE for HV cables," *Transactions on Electrical and Electronic Materials*, **2018**, 19(5), 344-351.
- [65] Mecheri. Y., Boukezzi. L., Boubakeur. A., Lallouani. M. "Dielectric and mechanical behavior of cross-linked polyethylene under thermal aging," *In 2000 Annual report conference on electrical insulation and dielectric phenomena (Cat. No. 00CH37132)*, **2000**, Vol. 2, pp. 560-563.
- [66] Verdu, J., "Vieillissement des plastiques", *AFNOR Technique*. Eyrolles ,**1984**.
- [67] Nedjar. M., "Effect of thermal aging on the electrical properties of crosslinked polyethylene," *Journal of applied polymer science*, **2009**, 111(4), 1985-1990.
- [68] Ghorbani, H., Abbasi, A., Jeroense, M., Gustafsson, A., & Saltzer, M. (2017). Electrical characterization of extruded DC cable insulation—The challenge of scaling. *IEEE Transactions on Dielectrics and Electrical Insulation*, 24(3), 1465-1475.
- [69] H. Ghorbani, T. Christen and H. Edin, "Role of thermal and electrical relaxations for the long-term conduction current in polyethylene", *IEEE Int. Conf. Dielectr. (ICD)*, Montpellier, France, **2016**, pp. 1106-1109.
- [70] Somsak. T., Suwanasri. T., Suwanasri. C., "Condition Assessment of Underground Cable System Using Health Index and Conditional Multiplying Factor," *In Proceedings of the 21st International Symposium on High Voltage Engineering, Springer International Publishing*, **2020**, Volume 1 (pp. 763-776).
- [71] ABD HALIM, H. S., RAHMAN, M. A. A., GHOSH, P. S., "CONDITION ASSESSMENT OF IN SERVICE MEDIUM VOLTAGE UNDERGROUND PILC CABLES USING PARTIAL DISCHARGE MAPPING AND POLARIZATION INDEX TEST RESULTS," *In 19th International Conference on Electricity Distribution*, **2007**.
- [72] Zuluaga Castro. J. D., Escobar Ardila. C. H., Cely Rey. L. A., Trujillo Artunduaga. J. E., "Empirical and Theoretical Electrical Integrity Analysis Based on Polarization Index, Dielectric Absorption Ratio and Insulation Measurements," *In SPE Artificial Lift Conference and Exhibition-Americas*, **2022** (p. D031S010R001). SPE.
- [73] Dey. J., Dutta. S., Baral. A., Kiran. A., Kumar; D., "Estimation of Insulation Condition Sensitive Parameters from Polarization Current using DFA," *In 2022 2nd International Conference on Emerging Frontiers in Electrical and Electronic Technologies (ICEFEET)*, **2022**, (pp. 1-6). IEEE.
- [74] Andjelković. D., Rajaković. N., "A new accelerated aging procedure for cable life tests," *Electric power systems research*, **1996**, 36(1), 13-19.
- [75] Ponniran. A., Kamarudin. M. S., "Study on the performance of underground XLPE cables in service based on tan delta and capacitance measurements," *In 2008 IEEE 2nd International*

- Power and Energy Conference, 2008*, (pp. 39-43). IEEE.
- [76] Fothergill. J. C., Dodd. S. J., Dissado. L. A. Liu. T., Nilsson. U. H., “The measurement of very low conductivity and dielectric loss in XLPE cables: a possible method to detect degradation due to thermal aging,” *IEEE Transactions on dielectrics and electrical insulation*, **2011**, 18(5), 1544-1553.
- [77] Kocatepe. C., Kumru. C. F., Ayaz. R., Arıkan. O., Akça. H., “The influence of voltage and frequency variations on insulation quality of a high voltage cable,” *In Eurocon 2013*, **2013**, pp. 964-968. IEEE.
- [78] Yang. K., Yang. G., “Degradation reliability assessment using severe critical values,” *International Journal of Reliability, Quality and Safety Engineering*, **1998**, 5(01), 85-95.
- [79] Meeker. W. Q., LuValle. M. J., “An accelerated life test model based on reliability kinetics,” *Technometrics*, **1995**, 37(2), 133-146.
- [80] Zhang. C., Chuckpaiwong. I., Liang. S. Y., Seth, B. B., “Mechanical component lifetime estimation based on accelerated life testing with singularity extrapolation,” *Mechanical Systems and Signal Processing*, **2002**, 16(4), 705-718.
- [81] Alghamdi. A. S., Desuqi. R. K., “A study of expected lifetime of XLPE insulation cables working at elevated temperatures by applying accelerated thermal ageing,” *Heliyon*, **2020**, 6(1).
- [82] C. Kim, Z. Jin, X. Huang, P. Jiang, Q. Ke, “Investigation on water treeing behaviors of thermally aged XLPE cable insulation,” *Polym. Degrad. Stabil*, **2007**. 92 (4), 537–544.
- [83] B.S. Bernstein, W.A. Thue, M.D. Walton, J.T. Smith., “Accelerated aging of extruded dielectric power cables. II. Life testing of 15 kV XLPE-insulated cables,” *IEEE Trans. Power Deliv*, **1992**. 7 (2) 603–608.
- [84] Z. Yang, N. Hirai, Y. Ohki., “Evaluation of aging status of flame-retardant cross-linked polyethylene by measuring indenter modulus,” *in 2019 2nd International Conference on Electrical Materials and Power Equipment (ICEMPE)*, **2019**, Guangzhou, China, pp. 57–60.
- [85] Li. J., Yan. N., Deng. Z., Wang. X., Jia. Z., “Thermal Aging State Evaluation of 10kV Polypropylene Cable,” *In 2023 IEEE 4th International Conference on Electrical Materials and Power Equipment (ICEMPE)*, **2023**, (pp. 1-4). IEEE.
- [86] Mustafa. E., Afia. R. S., Tamus. Z. Á., “Investigation of electrical and mechanical properties of low voltage power cables under thermal stress,” *In 2020 International Conference on Diagnostics in Electrical Engineering (Diagnosticska)*, **2020**, (pp. 1-4). IEEE.
- [87] Hughes. T. J., “Environmental controls on the state of HV cables under the seafloor,” Doctoral dissertation, University of Southampton, **2016**.
- [88] IEEE Standard. IEEE Standard Power Cable Ampacity Tables, IEEE Std 835-1994, **1994**, vol., no., pp.1-3151.
- [89] IEC 60287-1-1 Electric cables-calculation of the current rating, part 1: current rating equations (100% load factor) and calculation of losses, section 1: general, **2006**.
- [90] Vahidi. B., Mahmoudi. A., “Determination of the Ampacity of Buried Cable in Non-Homogenous Environmental Condition by 3D Computation,” *Journal of Electrical Engineering and Technology*, **2012**, 7(3), 384-388.
- [91] Liang, Y., “Steady-state thermal analysis of power cable systems in ducts using streamline-upwind/ Petrov-Galerkin finite element method,” *IEEE Transactions on Dielectrics and Electrical Insulation*, **2012**, 19(1), 283-290.
- [92] Anders. G. J., “Institute of Electrical and Electronics Engineers. Rating of electric power cables in unfavorable thermal environment,” (pp. 1-73). *Hoboken, NJ, USA: Wiley*. **2005**.
- [93] Nahman. J., Tanaskovic. M., “Determination of the current carrying capacity of cables using the finite element method,” *Electric Power Systems Research*, **2002**, 61(2), 109-117.
- [94] Jeong. W., Seong, J., “Comparison of effects on technical variances of computational fluid

- dynamics (CFD) software based on finite element and finite volume methods,” *International Journal of Mechanical Sciences*, **2014**, 78, 19-26. 2014.
- [95] Anders. G. J., “Rating of electric power cables: ampacity computations for transmission, distribution, and industrial applications,” **1997**.
- [96] Vahidi. B., Mahmoudi. A., “Determination of the Ampacity of Buried Cable in Non-Homogenous Environmental Condition by 3D Computation,” *Journal of Electrical Engineering and Technology*, **2012**, 7(3), 384-388.
- [97] Boukezzi. L., Saadi. Y., Boubakeur. A., “The radial distribution of temperature in XLPE cable: An analysis with the Finite Volume Numerical Method (FVM),” *In 2010 Annual Report Conference on Electrical Insulation and Dielectric Phenomena*, **2010**, (pp. 1-4). IEEE.
- [98] Hwang. C. C., Jiang. Y. H., “Extensions to the finite element method for thermal analysis of underground cable systems,” *Electric Power Systems Research*, **2003**, 64(2), 159-164.
- [99] Brakelmann. H., Stammen. J., “Thermal analysis of submarine cable routes: LSM or FEM?,” *In 2006 IEEE International Power and Energy Conference*, **2006**, (pp. 560-565). IEEE.
- [100] Hughes. T. J., Henstock. T. J., Pilgrim. J. A., Dix. J. K., Gernon. T. M., Thompson. C. E., “Effect of sediment properties on the thermal performance of submarine HV cables,” *IEEE Transactions on Power Delivery*, **2015**, 30(6), 2443-2450.
- [101] Zhang. Y., Chen. X., Zhang. H., Liu. J., Zhang. C., Jiao. J., “Analysis on the temperature field and the ampacity of XLPE submarine HV cable based on electro-thermal-flow multiphysics coupling simulation,” *Polymers*, **2020**, 12(4), 952.
- [102] Luitel. M., “Statistical approach for predicting remaining life of crosslinked polyethylene insulated cables,” Wichita State University, **2005**.
- [103] Hectors K, De Waele W., “Cumulative Damage and Life Prediction Models for High-Cycle Fatigue of Metals: A Review.” *Metals*, **2021**, 11(2):204.
- [104] Han. Y. J., Lee., H. M., Shin. Y. J., “Thermal aging estimation with load cycle and thermal transients for XLPE-insulated underground cable,” *In 2017 IEEE Conference on Electrical Insulation and Dielectric Phenomenon (CEIDP)*, **2017**, (pp. 205-208). IEEE.
- [105] Heggås. M., “Dynamic rating of power cables based upon transient temperature calculations,” Master's thesis, NTNU. **2019**.
- [106] Hughes. T. J., Henstock. T. J., Pilgrim. J. A., Dix. J. K., Gernon. T. M., Thompson. C. E., “Effect of sediment properties on the thermal performance of submarine HV cables,” *IEEE Transactions on Power Delivery*, **2015**, 30(6), 2443-2450.
- [107] Klimenta, J. L., “Thermal aging management for electricity distribution networks: FEM-based qualification of underground power cables.” *Thermal Science*, **2022**, 26(4 Part B), 3571-3586. .
- [108] Klimenta. D., Panić. M., Klimenta. J., Stojanović. M., “FEM-based Arrhenius modeling of the thermal effects of a heating pipeline and pavements on underground power cables,” *Energy Reports*, **2022**, 8, 183-191.
- [109] IEEE 1407-2007, “IEEE Guide for Accelerated Aging Tests for Medium-Voltage (5kV – 35kV) Extruded Electric Power Cables Using Water-Filled Tanks,” IEEE Power Engineering Society, Sponsored by the Insulated Conductors Committee, New York, NY.
- [110] Product Specification EPM37843, Cabelte, Arcozelo, Portugal, **2016**.
- [111] Sarma. H., “Accelerated life tests on a new water tree retardant insulation for power cables,” *IEEE transactions on power delivery*, **1997**, 12(2), 551-559.
- [112] International Electrotechnical Commission. “IEC 60584-2: Thermocouples—Part 2: Tolerances.” *International Electrotechnical Commission*. **1993**.
- [113] Yamamoto. T., Minakawa. T., “The final report of the project of assessment of cable aging for nuclear power plants,” *Japan Nuclear Energy Safety Organization*, Tokyo, Japan, **2009**.

- [114] Chang. Y. S., Mosleh. A., “Predictive Model on the Degradation of the Electrical Resistance of Cable Insulation,” *Probabilistic Safety Assessment and Management PSAM 14*, **2018**.
- [115] R. Nath, T. Kaura, M.M. Perlman., “Steady-state conduction in linear low-density polyethylene with Poole-lowered trap depth,” *IEEE Trans. Electr. Insul.*, **1990**, Vol. 25, pp. 419-425.
- [116]K.R. Bambery, R.J. Fleming, J.T. Holboll., “Space charge profiles in low density PE samples containing a permittivity/conductivity gradient,” *J. Phys. D: Appl. Phys.*, **2001**, Vol. 34, pp. 3071-3077, 2001.
- [117]F. Frutos, M. Acedo, M. Mudarra, J. Belana, J. Orrit, J.A. Diego, J.C. Cañadas, J. Sellarès., “Effect of annealing on conductivity in XLPE mid-voltage cable insulation,” *J. Electrostatics*, **2007**, Vol. 65, pp. 122-131.
- [118]Diego. J. A., Belana. J.; Orrit. J., Cañadas. J. C., Mudarra. M., Frutos. F., Acedo. M., “Annealing effect on the conductivity of XLPE insulation in power cable,” *IEEE Transactions on Dielectrics and Electrical Insulation 2011*, 18(5), 1554-1561. **2011**.
- [119]N.F. Mott and E.A. Davis, “Electronic Processes in Non-Crystalline Materials”, Oxford University Press, Oxford, Great Britain, pp. 32-37, **1979**.
- [120]Meng. X. K., Wang. Z. Q., Li. G. F., “Dynamic analysis of core temperature of low-voltage power cable based on thermal conductivity,” *Canadian Journal of Electrical and Computer Engineering*, **2016**, 39(1), 59-65.
- [121]Lee. K. Y., Yang. J. S., Choi. Y. S., Park. D. H., “Specific heat and thermal conductivity measurement of XLPE insulator and semiconducting materials,” *In 2006 IEEE 8th International Conference on Properties & applications of Dielectric Materials*, **2006**, (pp. 805-809). IEEE.
- [122]Jia. Y., Mao. Z., Huang. W., Zhang. J., “Effect of temperature and crystallinity on the thermal conductivity of semi-crystalline polymers: A case study of polyethylene,” *Materials Chemistry and Physics*, **2022**, 287, 126325.
- [123]The Engineering Toolbox (2003), Air - Density, Specific Weight and Thermal Expansion Coefficient vs. Temperature and Pressure. [online] Available at: https://www.engineeringtoolbox.com/air-density-specific-weight-d_600.html, Accessed 16 Nov 2021.
- [124]Issa, R. I., “Solution of the implicitly discretised fluid flow equations by operator-splitting,” *Journal of computational physics*, **1986**, 62(1), 40-65.
- [125]H. Li, Y. C. S., Liu. G., Lei. C., “Study on relationship between thermal conductivity and core temperature of power cable,” *In Asia-Pacific Power and Energy Engineering Conference 2011*, pp. 1-4. IEEE Computer Society.**2011**.
- [126]Bergman, T. L., “Fundamentals of heat and mass transfer,” *John Wiley & Sons*. **2011**.
- [127]Nellis, G., and Klein, S., “Heat transfer,” Cambridge university press. **2008**.
- [128]Gouda. O. E., Farag. A. A. E., “Factors Affecting the Sheath Losses in Single-Core Underground Power Cables with Two-Points Bonding Method,” *International Journal of Electrical & Computer Engineering*, **2012**, (2088-8708), 2(1).
- [129]Xie. M., Wang. H., Zhang. X., Gao. Z., Li. W., “Study on impedance characteristic of aircraft cables,” *In 2014 17th International Conference on Electrical Machines and Systems (ICEMS)*, **2014**, (pp. 645-650). IEEE.
- [130]Shafiei, M. A. Ahmadi, S. H. Zaheri, A. Baghban, A. Amirfakhrian, R. Soleimani, “Estimating hydrogen sulfide solubility in ionic liquids using a machine learning approach,” *6e Journal of Supercritical Fluids*, **2014**, vol. 95,pp. 525–534.
- [131]S.S.Haykin., “Neural Networks A Comprehensive Foundation,” Prentice Hall, Upper Saddle

River, NJ, **1999**.

- [132]Burden, F., & Winkler, D., Bayesian regularization of neural networks. Artificial neural networks: methods and applications, 23-42. **2009**.
- [133]S. R. Moosavi, D. A. Wood, M. A. Ahmadi, A. Choubineh., “ANN-based prediction of laboratory-scale performance of CO₂-foam flooding for improving oil recovery,” *Natural Resources Research*, **2019**, vol. 28, no. 4, pp. 1619–1637.
- [134]Gouravaraju. S., Narayan. J.; Sauer. R. A.; Gautam. S. S. A Bayesian regularization-backpropagation neural network model for peeling computations. *The Journal of Adhesion* 2023, 99(1), 92-115.
- [135]MacKay. D. J. Bayesian interpolation. *Neural computation* 1992, 4(3), 415-447.
- [136]Yue. Z.; Songzheng. Z., Tianshi. L., “Bayesian regularization BP Neural Network model for predicting oil-gas drilling cost,” *In 2011 International Conference on Business Management and Electronic Information*, **2011**, (Vol. 2, pp. 483-487). IEEE.
- [137]Mosleh. A., Al-Sheikhly. M., Chang. Y. S., Reister. R., “Physics-based probabilistic model of the effects of ionizing radiation on polymeric insulators of electric cables used in nuclear power plants,” (No. 15-8258). Univ. of California, Los Angeles, CA (United States).**2019**.
- [138]DeCarlo. R. A., “Linear systems: A state variable approach with numerical implementation,” Prentice-Hall, Inc. **1989**.
- [139]Serway, R.A., Jewett. J. W., “Current and resistance. In *Physics for scientists and engineers with modern physics*,” 10th ed.; Cengage: Boston, MA, USA,**2018**; pp. 691-712.
- [140]Rodríguez-Valverde. M. Á., Tirado-Miranda. M., “A simpler derivation of the integral formula of electrical resistance,” *European journal of physics* **2009**, 30(4), L47.
- [141]Navidi, W. C., “Statistics for engineers and scientists (Vol. 2),” New York: McGraw-Hill. **2006**.
- [142]Stojanović, M., Klimenta, J., Panić, M., Klimenta, D., Tasić, D., Milovanović, M., & Perović, B. (2023), “Thermal aging management of underground power cables in electricity distribution networks: a FEM-based Arrhenius analysis of the hot spot effect,” *Electrical Engineering*, 105(2), 647-662.**2023**.
- [143]D. Andjelkovi, N. Rajakovikb, “A new accelerated aging procedure for cable life tests,” *Elect. Power Syst. Res.* **1996**, vol. 36, pp. 13–9.
- [144]E. Da Silva, J. Ramirez, J. Rodriguez, J. Bermudez, J. Ren, A. Ferraz, S. Davila., “Diagnosis of XLPE Insulated cables aged under conditions of multiple stresses: Thermoelectric and humidity,” *Proc. IEEE Int. Symp. Elect. Insul.***1998**, pp. 117–121.
- [145]Banks. V, Faremo. H, Steenis. E. F., “An accelerated ageing test on the basis of 500Hz for water treeing in Cables,” *Jicable95*, **1995**: 347-356.
- [146]F. E. Fendell., “Laminar natural convection about an isothermally heated sphere at small Grashof number,” *Journal of fluid Mechanics*, **1968**, 34.1: 163-176.
- [147]N. Rott, “Note on the history of the Reynolds number,” *Annual review of fluid mechanics* 1990, 22.1: 1-12.**1990**.

Appendix A (reference section 3.4)

Thermocouples and PICO data logger

TC-08 thermocouple data logger is shown as Figure A.1. One PICO data logger has 8 channels for linking with 8 thermocouples. Then PICO data loggers are connected with PC.

Software Picolog Recoder is used for data collection setup. The recording rate of collected data is 1S/60s, it means one temperature data would be recoded by Pico data logger in every minute. Filter fatcor in Picolog Recoder is set as 6 .The sampling rate is 1 sample per 10s, as it equals to recoding rate times filter factor. Therefore, one temeperature data is sampled in every 10 seconds, there are 6 data are sampled in a minute so that they would be averaged and recorded.



Figure A.1. TC-08 thermocouple data logger

More detailed information about TC-08 thermocouple data logger could be found in following link: <https://www.picotech.com/data-logger/tc-08/thermocouple-data-logger>

Figure A.2 shows the thermocouple type T. Type-T thermocouples are more accuracy but have a narrower temperature measurement range than type-K. For the thermocouple used in this experiment, it could measure temperature in range of -75°C to $+260^{\circ}\text{C}$. The accuracy of thermocouple is $\pm 0.5^{\circ}\text{C}$ in -40°C to $+125^{\circ}\text{C}$ range.

The cable part is protected by PTFE insulation, the probe is an exposed wired tip. The total length is 3m.



Figure A.2. Thermocouple type T

More detailed information about type-T thermocouple can be accessed in following link:

<https://www.picotech.com/accessories/type-t-thermocouple/thermocouple-type-t-ptfe-3-m>

Appendix B (reference section 3.5.1)

Instrument and diagrams of IR measurements

The Megger MIT1025 is instrument used in the experiment for testing IR1, IR10, PI and DAR periodical. Figure B.1 shows the MIT 1025, it can be seen that there are three terminals in the instrument: positive(red), negative(black) and guard(blue). The MIT 1025 has multiple test modes, including IR tests, PI, DAR tests, Dielectric Discharge test, step voltage test and ramp voltage test. Voltage levels could be selected in range from 500V to 10kV. The MIT1025 is provided with calibration certificate which is automatically produced as a part of the final test procedures of Megger.

It should be made sure that the circuit for insulation test is under de-energized condition and fully discharged before measurement executed.



Figure B.1. Megger MIT1025

The blue cable is for the guard terminal which enhances the testing capabilities by acting as a shut for more information on the guard terminal. PowerDB is software used for the collection and reporting data by connecting PC with working Megger equipment. The connection between cable sample, Megger MIT1025 and PC is illustrated by Figure B.2. Positive (red) lead connect to conductor of cable sample, while negative (black) lead connect

to metal shield of cable. The measurement accuracy of Megger MIT1025 is listed in Table B.1.

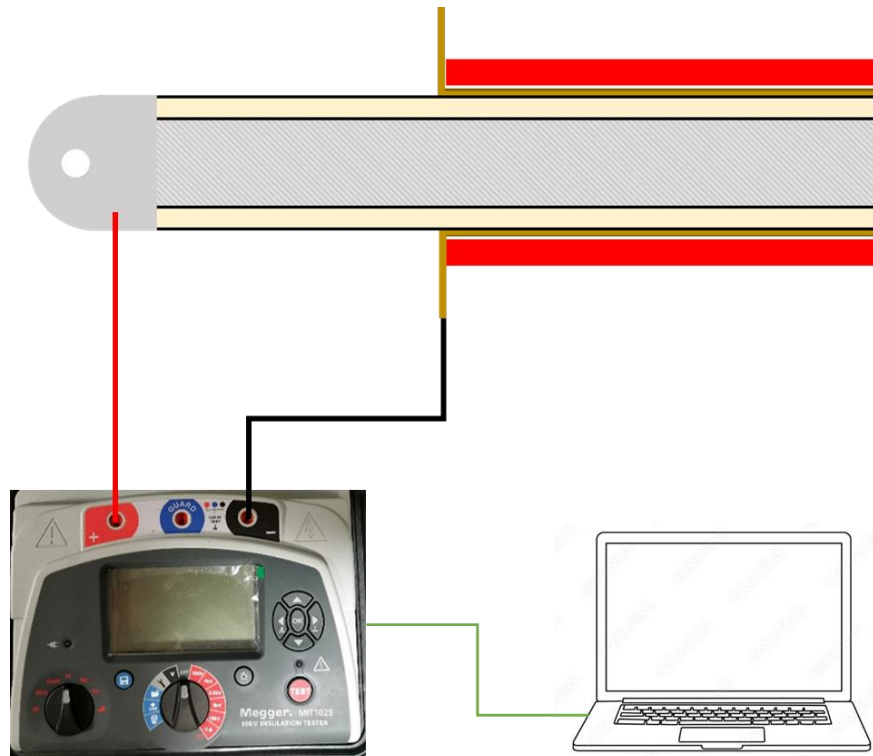


Figure B.2. Connection diagram of Megger MIT1025 measuring cable sample

The measurements procedure of power cable insulation by MIT 1025 is:

1. Select measurement modes
2. Install the test leads, locking test leads for additional safety: Positive to cable core (Red); Negative to cable metal sheath (Black)
3. Select voltage based on the rated operating voltage of the test item
4. Depress the test button for a safety interval

Table B.1. MIT1025 measurement accuracy in different measurement ranges

Testing voltages Accuracy	10kV	5kV	2.5kV	1kV	500V
5%	1M Ω to 2T Ω	1M Ω to 1T Ω	1M Ω to 500G Ω	1M Ω to 200G Ω	1M Ω to 100G Ω
20%	1M Ω to 20T Ω	1M Ω to 10T Ω	1M Ω to 5T Ω	1M Ω to 2T Ω	1M Ω to 1T Ω

Appendix C (reference section 3.5.4)

Instrument and diagrams of $\tan\delta$ measurement

The instrument used for testing $\tan\delta$ and capacitance of cable samples in the experiment is shown as Figure C.1. This equipment contains precision digital bridge, power unit, reference capacitor, step-up transformer, and other electronic circuits. It could be used in laboratory for high accuracy test. It's running automatically when it started and then results would display on the LCD screen and printed automatically. The accuracy of the instrument output is presented by Table C.1.



Figure C.1. WGSOL-4C Tan delta tester

Table C.1. Accuracy of $\tan\delta$ tester

Testing items	Accuracy
Capacitance	$\pm (\text{reading} \times 1\% + 1\text{pF})$
Dissipation Factor	$\pm (\text{reading} \times 1\% + 0.00040)$

Figure C.2 presents the connection of $\tan\delta$ tester on the cable samples, UST mode is test used in this case. Test voltage level could be selected in range of 200V to 10kV. The test voltage frequency could be selected from 45Hz, 50Hz, 55Hz, 60Hz and 65Hz.

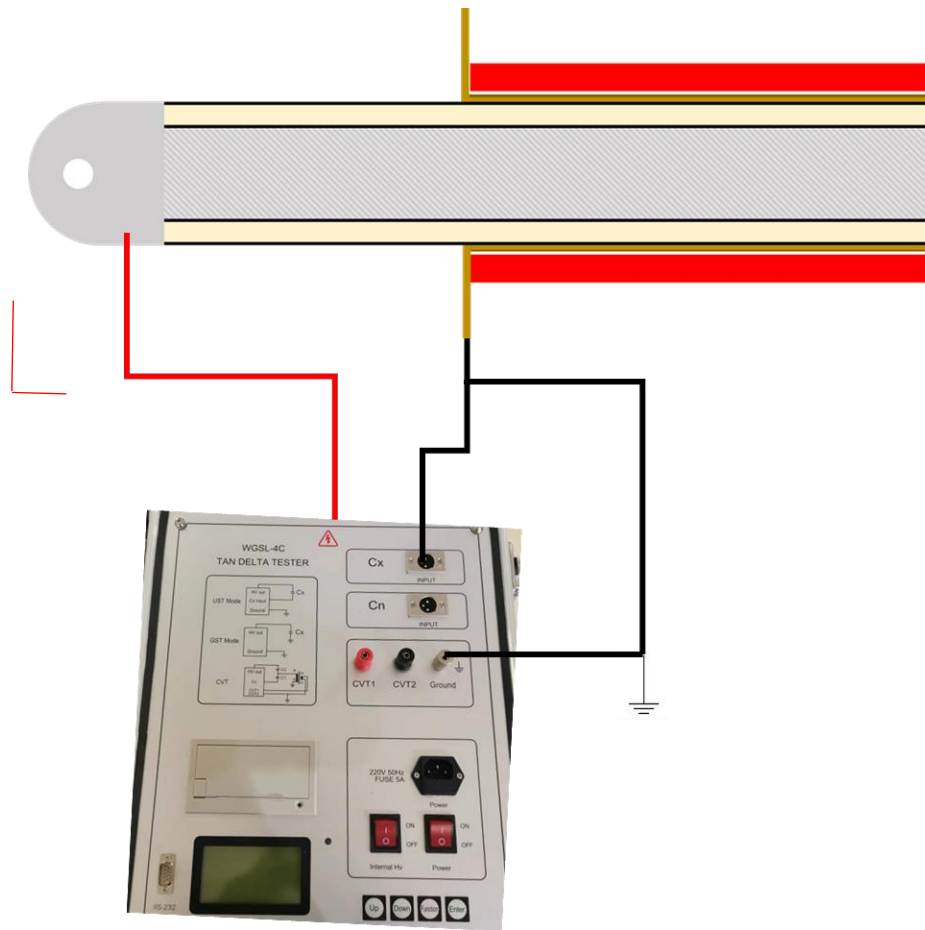


Figure C.2. Sketch of connection between Tan δ tester with power cable sample

Appendix D (reference section 4.2)

FVM simulation results of cables in chamber

Temperature distribution on cable, insulation and conductor surfaces from 0h to 8h in FVM modelling results are presented in this appendix.

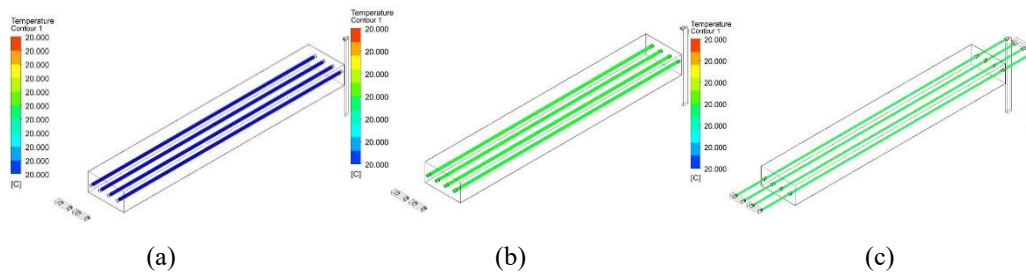


Figure D.1. Temperature distribution on (a) cable; (b) insulation and (c) conductor surfaces at 0h in FVM modelling results

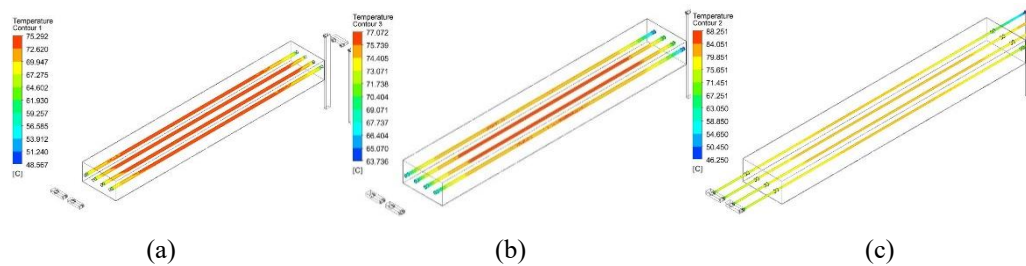


Figure D.2. Temperature distribution on (a) cable; (b) insulation and (c) conductor surfaces at 1h in FVM modelling results

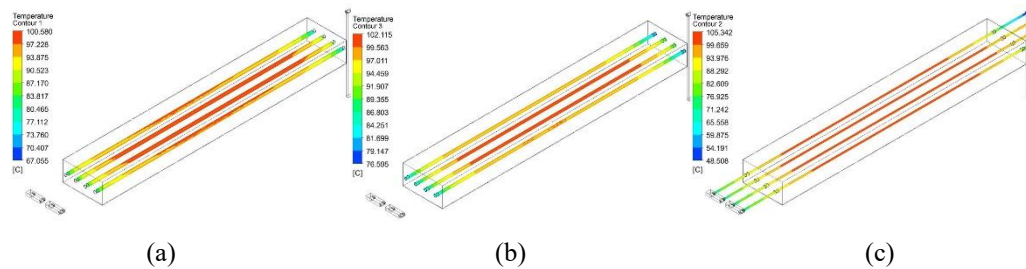


Figure D.3. Temperature distribution on (a) cable; (b) insulation and (c) conductor surfaces at 2h in FVM modelling results

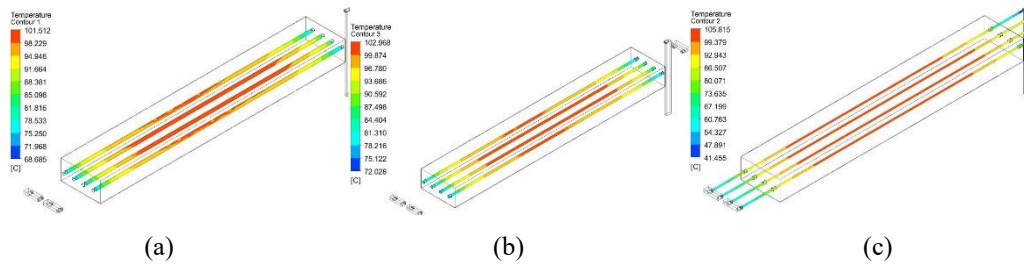


Figure D.4. Temperature distribution on **(a)** cable; **(b)** insulation and **(c)** conductor surfaces at 3h in FVM modelling results

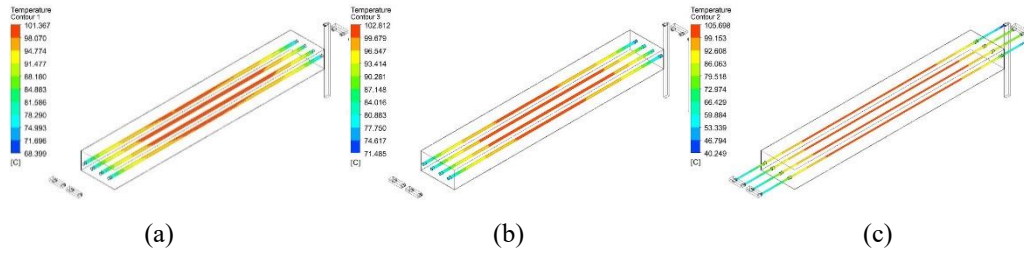


Figure D.5. Temperature distribution on **(a)** cable; **(b)** insulation and **(c)** conductor surfaces at 4h in FVM modelling results

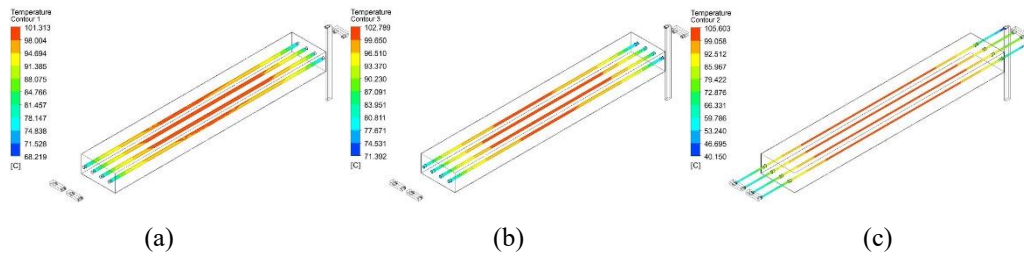


Figure D.6. Temperature distribution on **(a)** cable; **(b)** insulation and **(c)** conductor surfaces at 5h in FVM modelling results

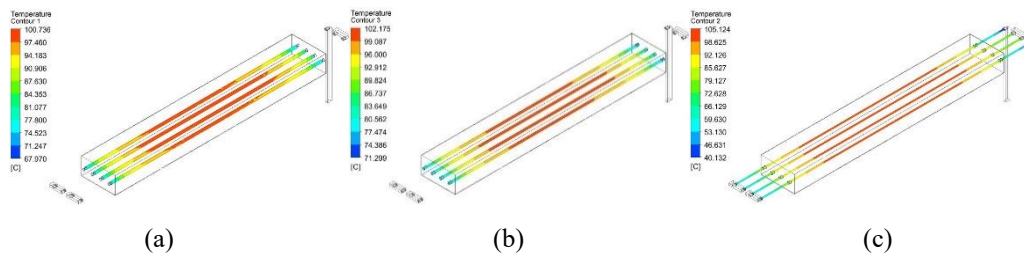


Figure D.7. Temperature distribution on **(a)** cable; **(b)** insulation and **(c)** conductor surfaces at 6h in FVM modelling results

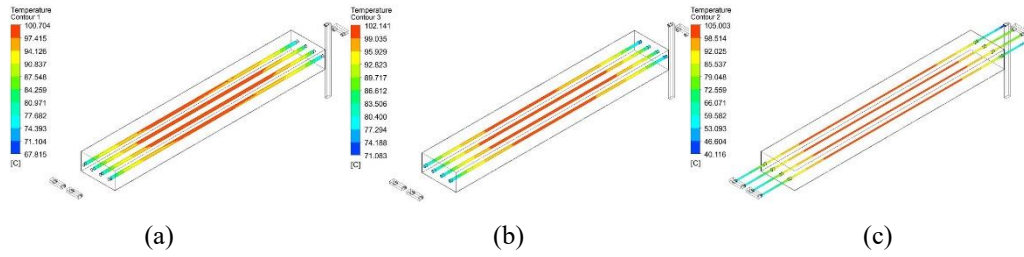


Figure D.8. Temperature distribution on (a) cable; (b) insulation and (c) conductor surfaces at 7h in FVM modelling results

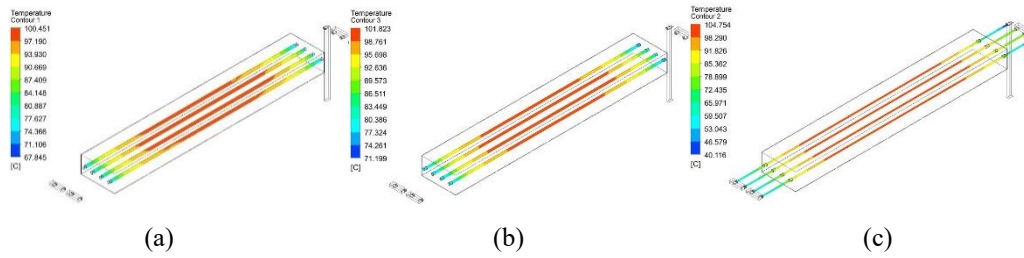


Figure D.9. Temperature distribution on (a) cable; (b) insulation and (c) conductor surfaces at 8h in FVM modelling results

Appendix E (reference section 4.3.2)

ANN model performance

Presented herein are graphs of training performances for ANN models trained by different cable's temperature profiles referenced in section 4.3.2.

- Figure E.1: mean squared errors of ANN models
- Figure E.2 to E.5: error histograms of ANN models for cables' insulation
- Figure E.6 to E.9: correlation coefficient of ANN models for cables' insulation

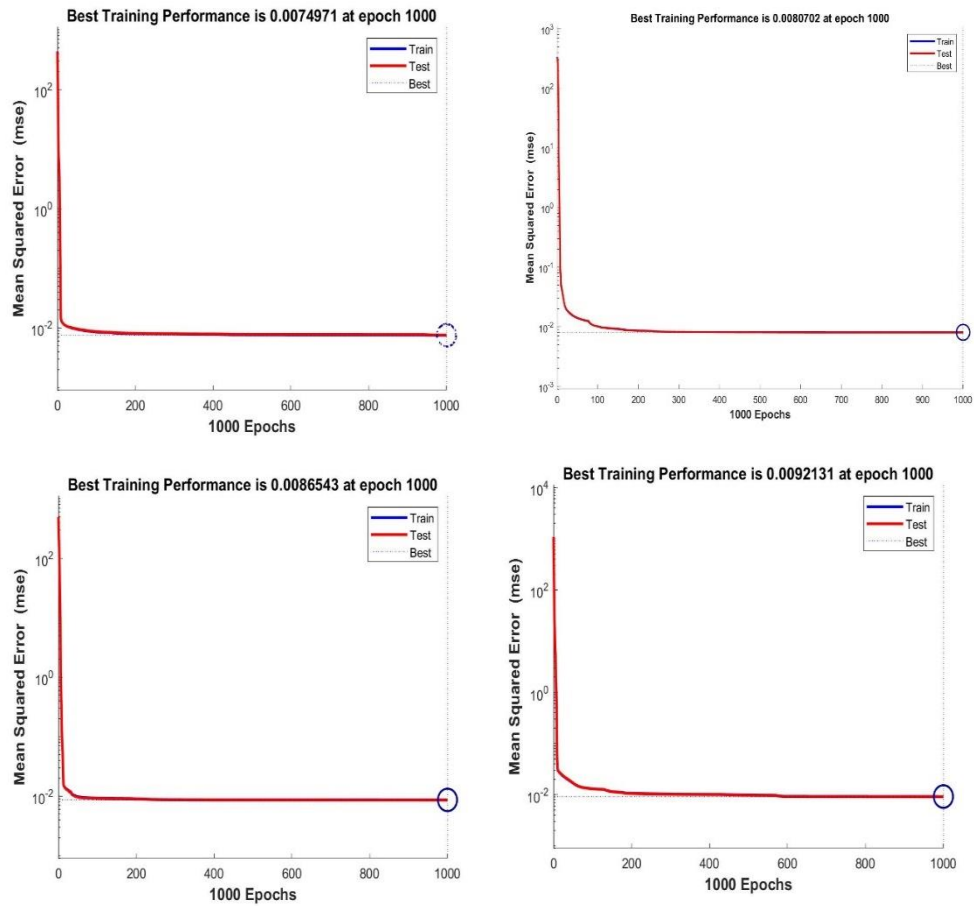


Figure E.1. Mean Squared Errors of ANN models along with training epochs for insulation of (a) cable1, (b) cable2, (c) cable3 and (d) cable4

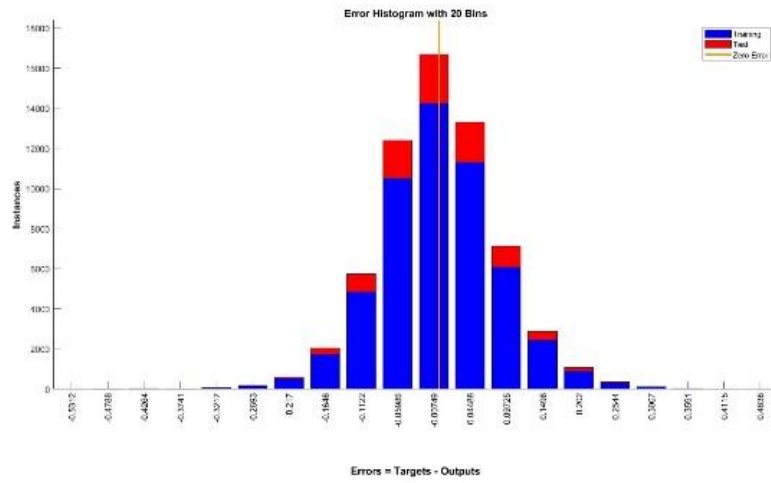


Figure E.2. Error histogram of ANN for cable 1 insulation

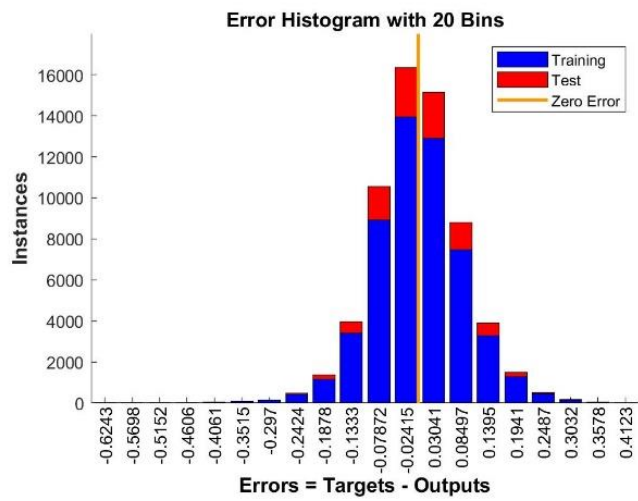


Figure E.3. Error histogram of ANN for cable 2 insulation

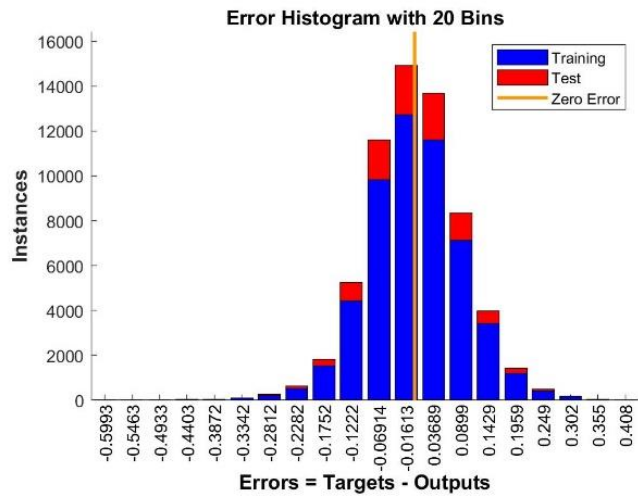


Figure E.4. Error histogram of ANN for cable 3 insulation

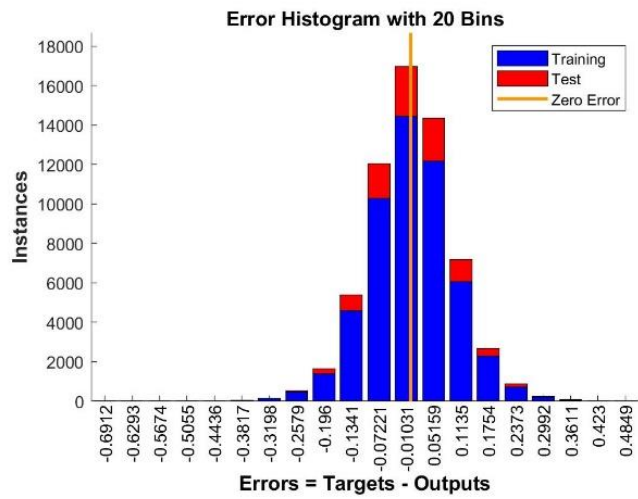


Figure E.5. Error histogram of ANN for cable 4 insulation

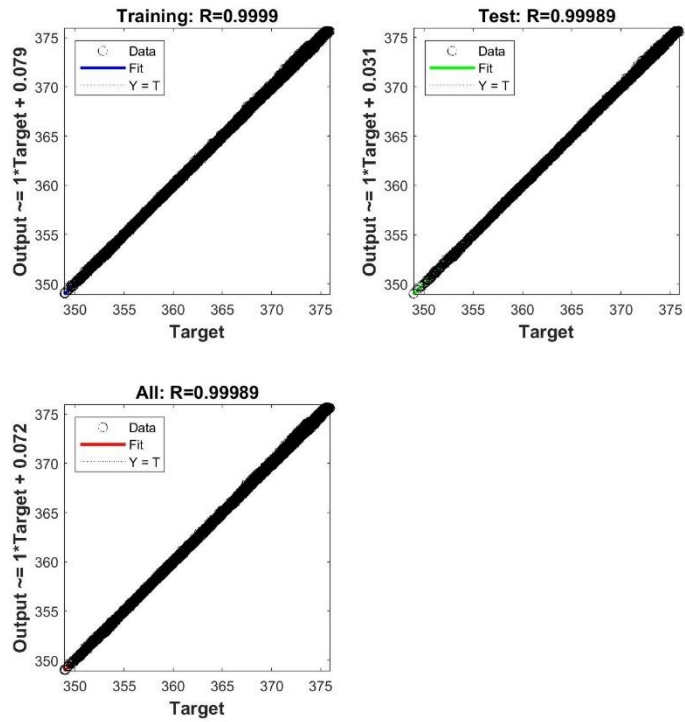


Figure E.6. Correlation coefficient of ANN model for cable 1

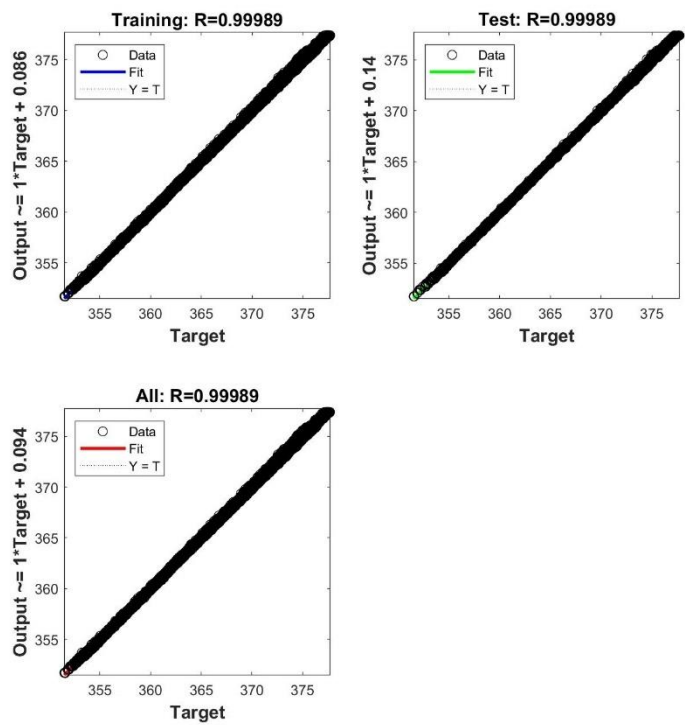


Figure E.7. Correlation coefficient of ANN model for cable 1

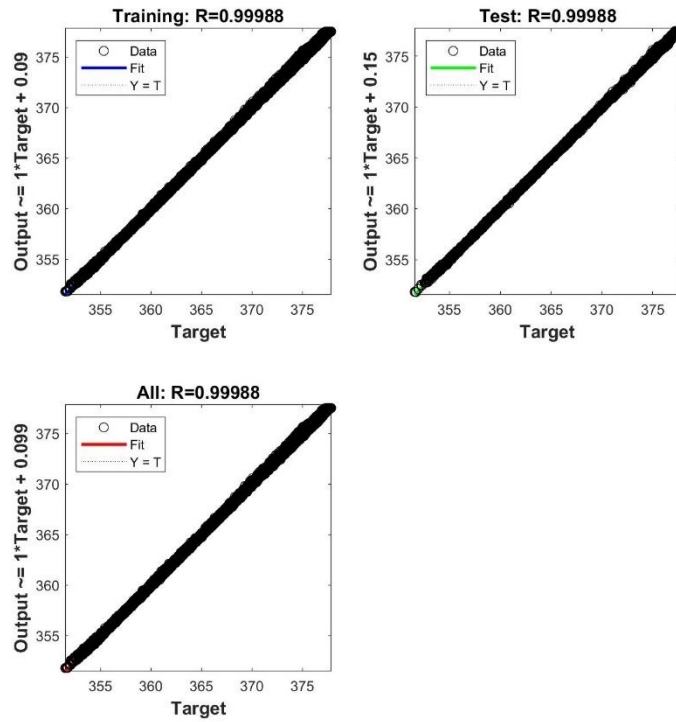


Figure E.8. Correlation coefficient of ANN model for cable 1

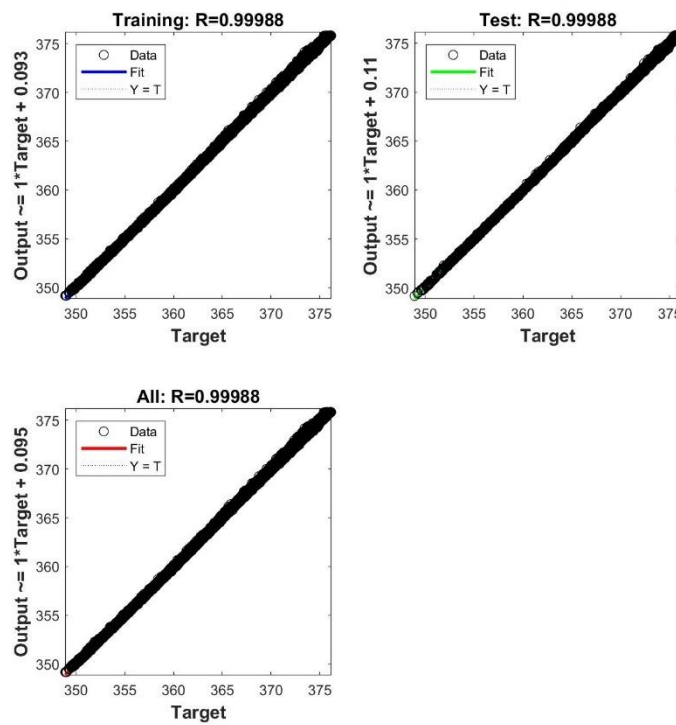


Figure E.9. Correlation coefficient of ANN model for cable 1